The Dissertation Committee for Lucas Alejo Cieza-Gonzalez
certifies that this is the approved version of the following dissertation:

Structure and Evolution of Circumstellar Disks, a Spitzer View

Committee:

Paul Harvey, Supervisor

William Cochran

Neal Evans

Daniel Jaffe

John Lacy

Karl Stapelfeldt

Structure and Evolution of Circumstellar Disks, a Spitzer View

by

Lucas Alejo Cieza-Gonzalez, B.S.,M.A.

Dissertation

Presented to the Faculty of the Graduate School of

The University of Texas at Austin

in Partial Fulfillment

of the Requirements

for the Degree of

Doctor of Philosophy

The University of Texas at Austin

August 2007

To my grandfather, Dr. Alberto Rex Gonzalez
and Vicky, my love.

Acknowledgments

On February 28, 2002, one day before I received my official admission letter from UT, I received an e-mail from Paul Harvey telling me about the research opportunities at the department in the areas of star and planet formation. That is how I learned about the future NASA mission called the Space Infrared Telescope Facility and about the Legacy Project “From Molecular Cores to Planet Forming Disks (c2d)”. Working for the c2d project seemed like a unique opportunity and Paul’s e-mail was probably the main reason I decided to come to Texas. However, I could not anticipate the full extent of the impact that such an opportunity would have on my entire graduate career and beyond. Five years later, I can confidently say that being part of the c2d team has provided me the best environment any graduate student can hope for to cultivate his/hers research interests. I will *always* be grateful to Paul Harvey for giving me a place in the c2d project and to Neal Evans for leading the team in such a productive way.

I would also like to express my gratitude for the many c2d members, faculty, postdocs, and students, that one way or another have contributed to my scientific formation and success in graduate school. Similarly, I would like to thank the over 25 collaborators, outside and inside the c2d team, that have contributed to the projects presented in this dissertation. Without them, this dissertation could not be possible. A special thanks goes to Nairn Baliber, the sole coauthor of two of the chapters. I would also like to thank the other members of my Committee, William

Cochran, Dan Jaffe, John Lacy, and Karl Stapelfeldt for their comments and advise.

I am grateful for the immense support that the entire Astronomy Department and University have shown for my graduate career. I have been honored with an excessive number of awards and fellowships, and I know I haven't done enough in graduate school to deserve all of them. I am in debt and hope that some future work could make up the difference!

I was one the lucky few whose graduate career overlapped completely with Stephanie Crouch's service as Graduate Coordinator in the department. I would like to give special thanks to her for making the life of graduate students much easier than it would otherwise be without her invaluable help. She will be greatly missed and I wish her well in her new endeavour.

Last but not least, I would like to express my gratitude for my family's unconditional support to my career and every other aspect of my life. They, together with my friends, remind me that the most important things of the universe are smaller and much closer than the stars.

Lucas Alejo Cieza-Gonzalez

The University of Texas at Austin
August 2007

Structure and Evolution of Circumstellar Disks, a Spitzer View

Publication No. ____________________

Lucas Alejo Cieza-Gonzalez, Ph.D.
The University of Texas at Austin, 2007

Supervisor: Paul Harvey

This dissertation is the sum of five studies of the structure and evolution of circumstellar disks, the birthplace of planets. These studies are all based on Infrared data from the *Spitzer* Space Telescope, and taken together trace the evolution of disks from the optically thick primordial stage to the optically thin debris disk stage. The five projects included in this dissertation are diverse but they are all interconnected and have a common underlying motivation: to impose observational constraints on different aspects of planet formation theories. In the first project, we study the near and mid-IR (1.2-24 μm) emission of Classical T Tauri Star (CTTS), which are low-mass pre-main sequence (PMS) stars that show clear evidence for accretion. We discuss the implications of our results on the structure of their inner disks and their estimated ages. In the second project, we study the incidence as a function of age of disks around weak-line T Tauri stars (low-mass PMS stars that are mostly coeval with CTTS but that do not show clear evidence for accretion) and explore the structure of these disks. We estimate the dissipation timescale of the planet-forming region of primordial disks and discuss the implications for planet formation theories. The third and fourth projects deal with the evolution of angular momentum of PMS stars. We search for observational evidence for the connection between stellar rotation and the presence of a disk predicted by the current disk-braking paradigm, according to which the rotational evolution of PMS stars is regulated through magnetic interactions between the stellar magnetosphere and the inner disk. The last project deals with debris disks, which are second-generation disks where the dust is continuously replenished by collisions between planetesimals. We search for debris disks in the far-IR (24-160 μm) around a sample of Hyades Cluster members. We discuss the implications of our results on the evolution of debris disks and on the Late Heavy Bombardment in the Solar System.

Contents

List of Tables

List of Figures

Chapter 1

Introduction

1.1 General Context

Over the last couple of decades, evidence that circumstellar disks are common products of star formation has greatly accumulated. This evidence ranges from the IR excess detected in most T Tauri stars observed by the IRAS (Cohen 1983) and ISO (Habing et al. 2001) satellites, to direct HST images of disks (McCaughrean & O'Dell 1996) seen as silhouettes in front of the Orion Nebula. Also, even though there is not direct proof that planets actually grow from circumstellar material, it has become increasingly clear that they are potential birthplaces of planets since their masses, sizes, and compositions are consistent with the assumed pre-planetary solar nebula (Hillenbrand 2003). More recently, the discovery of exo-planets orbiting nearby main sequence stars has confirmed that the formation of planets is a common process and not a rare phenomenon exclusive to our Solar System. Thus, any theory of planet formation should be robust enough to account for this fact and can not rely on special conditions or on unlikely processes.

Star and planet formation are intimately related. Standard low-mass star formation models (e.g. Shu et al. 1987) describe the free fall collapse of a slowly rotating molecular cloud core followed by the development of a hydrostatic proto-star surrounded by an envelope and a disk of material whose residual angular momentum prevented it from falling into the star. This early phase is expected to occur on a timescale of about 10^5 years (Beckwith 1999) and results in an optically revealed classical T Tauri star (low-mass PMS stars that show clear evidence for accretion (Hα EW > 10 $\mathring{A}$). This stage is characterized by intense accretion onto the star, strong winds, and bipolar outflows. As the system evolves, presumably into a weak-lined T Tauri star (PMS stars that occupy the same region of the H-R diagram as CTTSs but do not show clear evidence for accretion (Hα EW < 10 $\mathring{A}$), accretion ends, and the dust settles into the mid-plane of the disk where the solid particles are believed to stick together and to grow into planetesimals as they collide. Once the objects reach the kilometer scale, gravity increases the collision cross-section of the most massive planetesimals, and runaway accretion occurs (Lissauer 1993). In the standard core accretion model (e.g. Pollack 1996), massive enough proto-planets still embedded in the disk can accrete the remaining gas and produce giant planets. The early stages are the most uncertain, and many people suspect that grains will not grow into planetesimals by collisions alone at the rate necessary to go through all stages of giant planet formation before the gas nebula has dissipated. However, since current statistics of extra-solar planets (e.g. Butler et al. 2001) seem to indicate that giant planets are common, this has led some people (i.e. Boss 2000 and Youdin & Shu 2002) to revisit an alternative mechanism that had been put aside for several decades, namely, gravitational instability. Thus while the existence of planets around a significant fraction of all the stars is considered verified, the mechanism of planet formation still remains an open question. So far, none of the proposed theories has proven satisfactory. On one hand, the standard model of continuous accretion of solid particles relies on doubtful sticking properties of rocks, a special mass distribution, and a variety of initial conditions. On the other hand, gravitational instability, relies on unclear mechanisms to enhance the surface density of the disk's mid-plane to trigger the process of planet formation. Clearly, more observational constraints are necessary to help the theoretical work proceed forward. Providing such constraints is the main motivation of most of the projects presented in this dissertation.

1.2 Primordial Circumstellar disks

Direct detection of forming planets is well beyond our current capabilities, but disks are easier to detect and study since the surface area of a planetary mass dispersed into small grains is many orders of magnitude greater than the surface area of a planet. For this reason, most of the information about the properties of circumstellar disks such as size, mass, density, and evolution timescales has been obtained by observing the thermal emission of the dust gains. These particles absorb and re-radiate the light mostly in the 1 μm - 1 mm range. Since the temperature of the disk decreases with radius, different wavelengths probe different radii; therefore, the spectral energy distribution (SED) of a circumstellar disk contains considerable information about the physical properties of the system. Many models of circumstellar disks have been constructed in order to try to reproduce the observed SED's. Most of these models include an inner cavity and a flared disk (e.g. Chiang & Goldereich 1997; Beckwith 1999; Dullemond et al. 2001). Even though the models do not produce a unique fit to the data, they provide important constraints on the physical and geometrical properties of disks.

Chapters 2 through 5 deal with the structure and evolution primordial disks, and therefore have different implications for planet formation theories. In Chapter 2, we argue that CTTSs possess significant non-photospheric excess in the J- and H-bands. We also argue that deriving the stellar luminosities of CTTS by making bolometric corrections to the J-band fluxes, which is the "standard" procedure, systematically overestimates these luminosities. Overestimated luminosities translate into underestimated ages when stars are placed in the H-R diagram; therefore, our results have important implications for the dissipation timescale of inner accretion disks. We propose that this near-IR excess originates at a hot inner rim, analogous to those suggested for Herbig Ae/Be stars.

In Chapter 3, we determine the frequency of circumstellar disks around WTTS as a function of age and study the properties and evolutionary status of these disks, which was one of the central goals of the c2d *Spitzer* Legacy Project. Since *Spitzer* observations probe planet-forming regions of the disk (r ∼0.1–10 AU), our results impose much stronger constraints on the time available for the formation of planets than those provided by previous near-IR studies.

In Chapters 4 and 5 we take advantage of the unprecedented disk identification capabilities of *Spitzer* to test the predictions of the disk-braking paradigm. In Chapter 4, we obtain new photometric rotation periods in the young cluster IC 348 and combine all published periods in this cluster with *Spitzer* photometry in order to search for a correlation between slow rotation and the presence of a disk. We find some indication that the disk fraction decreases significantly for stars with very short periods ($P < 2$ d), but no general correlation between period and IR-excess was found, mainly because of the small size of the sample. In Chapter 5, we combine stellar rotation periods of NGC 2264 and the Orion Nebula Cluster from the literature with *Spitzer* observations and show that a very clear correlation between period and the presence of a disk can be seen across the entire period range in both clusters when the study is restricted to a clean and unbiased sample of stars with estimated masses ≥ 0.25 $M_\odot$ (lower mass stars are much fainter and have very biased *Spitzer* data). Our results represent the strongest evidence to date supporting the disk-braking paradigm.

1.3 Debris disks around MS stars

Soon after circumstellar disks were discovered by the Infrared Astronomical Satellite (IRAS) around MS stars like Vega, which was older than any star previously known to have a disk, it was realized that these disks were gas poor and could not be made of primordial material. Since, in a gas poor environment, the survival time of dust to dissipation processes such as the Poynting-Robertson effect is *much* smaller than the ages of these stars, these disks are believed to be debris disks where dust is continuously produced by collisions between planetesimals which motions are stirred up by larger bodies, such as planets. Because of their apparent connection with planetary systems, debris disks rapidly became the subjects of many studies.

Chapter 6, describes the only project in this dissertation that deals with debris disks around MS stars. We study a sample of 45 FGK-type Hyades Cluster members (from our GO Cycle-1 *Spitzer* proposal, W. Cochran PI) to search for debris disks in the far-IR (24-160 μm). The age of the Hyades, 650 Myrs, corresponds to the epoch of the late heavy bombardment in the Solar System (Thera 1973), an epoch at which the Solar System is thought to have had a major debris disk. However, we find that none of the Hyades stars in our sample shows a significant far-IR excess. If the Hyades stars resemble the Sun at 650 Myrs of age, our result is more consistent with the idea that the late heavy bombardment was a spike in the impact rate rather than the end of an exponential decrease in the bombardment rate from the formation of the terrestrial planets.

Chapter 2

Evidence for J and H-band excess in classical T Tauri stars and the implications for disk structure and estimated ages

2.1 Abstract

[1] We argue that classical T Tauri stars (cTTs) possess significant non-photospheric excess in the J and H bands (1.25 μm an 1.66 μm respectively). We first show that normalizing the spectral energy distributions (SEDs) of cTTs to the J-band leads to a poor fit of the optical fluxes (which are systematically overestimated), while normalizing the SEDs to the I_C-band (0.8 μm) produces a better fit tothe optical bands and in many cases reveals the presence of a considerable excess at J and H. Near-infrared spectroscopic veiling measurements from the literature support this result. We find that J and H-band excesses correlate well with the K-band (2.2

---

[1] based on Cieza, L., Kessler-Silacci, J., Jaffe, D., Harvey, P., & Evans, N. 2005, ApJ, 635, 422

μm) excess, and that the J-K and H-K colors of the excess emission are consistent with that of a black body at the dust sublimation temperature ($\sim$ 1500-2000 K). We propose that this near-IR excess originates at a hot inner rim, analogous to those suggested to explain the “near-IR bump” in the SEDs of Herbig Ae/Be stars. To test our hypothesis, we use the model presented by Dullemond et al. (2001) to fit the photometry data between 0.5 μm and 24 μm of 10 cTTs associated with the Chamaeleon II molecular cloud. We find that simple models that include luminosities calculated from I_C-band magnitudes and an inner rim may account for the reported J and H-band excesses. The models that best fit the data are those where the inner radius of the disk is larger than expected for a rim in thermal equilibrium with the photospheric radiation field alone. In particular, we find that large inner rims are necessary to account for the mid infrared fluxes (3.6–8.0 μm) obtained bythe Spitzer Space Telescope (Spitzer). The large radius could be explained if, as proposed by D’Alessio et al. (2003), the UV radiation from the accretion shock significantly affects the sizes of the inner holes in disks around cTTs. Finally, we argue that deriving the stellar luminosities of cTTs by making bolometric corrections to the J-band fluxes, which is the “standard” procedure for obtaining cTTs luminosities, systematically overestimates these luminosities. The overestimated luminosities translate into underestimated ages when the stars are placed in the H-R diagram. Thus, the results presented herein have important implications for the dissipation timescale of inner accretion disks.

2.2 Introduction

Some of the first near-infrared observations of pre-main sequence (PMS) stars revealed ~2-5 μm fluxes well above predicted photospheric values (e.g., Mendoza 1966 and 1968). This near-IR excess was soon recognized as evidence of heated dust in circumstellar disks, well before disks were physically resolved at millimeter wavelengths (e.g., Kitamura et al. 1996), and later in the near-IR by interferometric observations (e.g., Akeson et al. 2000). Over the last decades, evidence has accumulated supporting the idea that circumstellar disks are the birthplaces of planets since the disk masses, sizes, and compositions are consistent with the presumed pre-planetary solar nebula (e.g., Hillenbrand 2003). For this reason, the study of the structure and evolution of circumstellar disks has become crucial to our understanding of the formation of planetary systems, a field that has been greatly stimulated by the newly discovered exoplanets orbiting nearby main sequence stars (e.g., Marcy & Buttler 1998).

Classical T Tauri stars (cTTs), which are low mass PMS stars still accreting circumstellar material, have large ultraviolet (UV), optical, and infrared (IR) excesses that can dominate the photospheric emission at many wavelengths (e.g., Hartigan et al. 1991). These excesses are produced by a variety of mechanisms, all of which are associated with the presence of a disk around the young central source. The current paradigm for the structure of circumstellar disks associated with T Tauri stars (e.g., Hartmann 1998) describes the observed SEDs in terms of the superposition of several components: the star itself, a flared disk, possibly with a hot atmosphere, and magnetospheric accretion columns through which the circumstellar material is channeled onto the surface of the star. Each component contributes a different percentage of the total flux of the system at different wavelengths, and it is usually difficult to disentangle each contribution since degeneracies arise among many of the parameters that go into modeling the SEDs (Chiang et al. 2001). The broad wavelength range of the non-photospheric emission and the frequent presence of significant circumstellar reddening in cTTs makes it difficult to find a wavelength at which to obtain photometry of the star itself from which to estimate the stellar luminosity. The method used most frequently to derive bolometric luminosity of the stellar photosphere includes applying a bolometric correction to a single-band measurement corrected for extinction (e.g., Kenyon & Hartmann 1995 and Hartigan et al. 1994). It is usually argued that the J-band, at 1.25 μm is the best representation of the photospheric emission. The ratio of the radiation from the photosphere to that from the hot accretion shock (UV-excess) reaches a maximum here, while the effects of extinction are less important than at shorter wavelengths and the emission from the circumstellar dust is less prominent than at longer IR wavelengths. A detailed discussion supporting this argument can be found in Kenyon & Hartmann (1990). They investigate from a theoretical point of view, the change in apparent luminosity of K1-M1 cTTs due to several effects: the occultation of the star by the disk, the accretion and reprocessing luminosity of the disk, and the radiation from the boundary layer between the disk and the stellar photosphere. They conclude that the emission from the hot boundary layer will contaminate the photospheric emission at wavelengths < 0.8 μm, while the disk emission will affect wavelengths > 2 μm; and therefore, that the I and J-band are the best representations of the true stellar fluxes. The same is true for models that replace the boundary layers with magnetospheric accretion columns (Johns-Krull & Valenti, 2001; Calvet & Gullbring, 1998). Even though the presence of significant J-band excess in cTTs has been reported in the past (e.g., Folha & Emerson, 1999), the J-band is still considered to be the best representation of the photospheric emission and is commonly used, without veiling corrections, to calculate the stellar luminosity of cTTs and to derive their ages. Here we present additional results that suggest that classical T Tauri stars (cTTs) possess significant non-photospheric excesses in the J and H bands. In section 2.3, we describe our SED fitting method and show that normalizing the photospheres of cTTs to the J-band leads to a poor fit of the optical fluxes (which are systematically overestimated). We show that normalizing the SEDs to the I_C-band [2] produces a better fit in the optical bands, BVR_CI_C,

---

[2] I_C denotes the I Cousins band at 0.80 μm as defined by Bessel (1979)

and in many cases reveals the presence of considerable J and H-band excesses. In section 2.5, we describe near-IR veiling measurements from the literature that provide independent evidence supporting our results, and in section 2.6 we calculate the J-K and H-K colors of the excess emission, which are consistent with black body emission at ∼1500–2000 K. In section 2.7, we fit the photometry data between 0.4 μm and 24 μm of 10 cTTs associated with the Chamaeleon II molecular cloud and show that the reported J-band excess can be accounted for by the emission of an inner rim at the dust sublimation temperature. Then, in section 2.8 we investigate the effects of the J-band excess on estimating stellar ages. Finally, our conclusions are summarized in section 2.9.

2.3 SED fitting

2.3.1 J and H-band excesses from SED fitting

We were motivated to investigate the possibility of significant J and H-band excesses when trying to estimate the luminosities of a sample of 15 cTTs in the Chamaeleon II molecular cloud. The sample was taken from Hughes & Hartigan (1992), and the goal was to obtain stellar ages by placing the objects in the H-R diagram, following the "standard procedure" (e.g., Kenyon & Hartmann, 1995, hereafter, KH95). This procedure involves applying a bolometric correction, appropriate to the spectral type of the object, to a single-band measurement corrected for extinction. According to the current paradigm, luminosities obtained from the J-band and I-band should produce similar results. This is certainly the case, to within ∼5 %, when the method is applied to weak-lined T Tauri stars (see sections 2.3.2 and 2.8). However, we find that when we apply this method to cTTs, the luminosities obtained from the J-band were systematically higher, by a factor of ∼1.35, than those obtained from the I_C-band. In order to investigate this discrepancy, we plot the entire SEDs of the stars in the Chamealeon II sample using broad band photometry, and try to separate the photospheric contribution from the rest of the SED. Table 2.1 lists the fluxes used to construct these SEDs. The BV$R_C I_C$ photometry and spectral types were taken from Hughes & Hartigan (1992), the JHK values come from the 2-Micron all Sky Survey (2MASS, Kleinmann, 1992), and the mid and far IR photometry was obtained as part of the Spitzer Legacy Project "From Molecular Cores to Planet-forming Disks (c2d)" (Evans et al. 2003). A detailed discussion of the Spitzer observations is presented by Porras et al. (2005) and Young et al. (2005).

As a first step in our SED fitting approach, extinction is estimated from the R_C-I_C color excess. As discussed in section 2.2, at least some cTTs are known to have important non-photospheric V-band excess emission, and we argue that J and H-band excesses are also present; therefore, of all the available colors, R_C-I_C should provide the most reliable measurement of the true photospheric colors of cTTs. Following the extinction curve provided by the Asiago database of photometric systems1 (Fiorucci & Munari 2002) [3] , we adopt A_V = 4.76[(R_C–I_C)–(R_C–I_C)$_o$] (for R_V = A_V//E(B–V) = 3.1). Where (R-I)$_o$ is the expected color of a dwarf main sequence star (from KH95) with the same spectral type as the given Chamaeleon II cTTs. Then, we calculate the extinctions for all the other bands using the relations listed in Table 2.2, also derived using the Asiago database of photometric systems. The expected optical and near-IR fluxes are then obtained from the I_C or J-band photometry corrected for extinction and the broad-band colors of main-sequence stars taken from KH95. Similarly, the predicted stellar fluxes in the Spitzer bands were obtained from the Spitzer Science Center online tool, Stellar Pet1, which computes the mid and far-infrared fluxes using Kurucz models (Kurucz 1993) given the K magnitude and spectral type of the star. Since cTTs are known to have K-band excess, we used the predicted K-band photospheric fluxes calculated as described

---

[3] http://ulisse.pd.astro.it/Astro/ADPS/

above as the input for Stellar Pet, rather than the observed K-band fluxes. Finally, all the optical and near-IR magnitudes are converted to flux densities in units of Jansky using the zero-points listed in Table 2.2.

The left column of Figure 2.1 shows that, if the SEDs are normalized to the J-band (i.e., the de-reddened J-band flux is assumed to accurately represent the photospheric flux), the BVRI fluxes are significantly overestimated. Normalizing the SED to the I_C-band, as shown in the right column of Figure 2.1 leads to a considerably better fit of the optical bands while revealing significant J and H-band excess for many of the sources. This behavior in the SEDs is not consistent with random errors and seems to be systematic. If our SED fitting procedure is correct, either the J-band excess is real, or the BVR_CI_C fluxes are suppressed. The facts that the J and H-band excess are accompanied by excesses at longer wavelengths and that in general the observed (extinction-corrected) optical colors match the expected photospheric colors, suggest that the J and H-band excesses are real. We note that the accretion shock emission can easily account for the B and V-band excesses seen in some of the SEDs in Figure 2.1, which are in fact expected (Hartigan et al. 1991).

2.3.2 Testing the SED fitting procedure

In plots such as those in Figure 2.1, photometric uncertainties (usually around 3% in the optical and the near-IR) are small compared to other sources of error, which include errors in the spectral types, the adopted colors, and extinction corrections. To estimate the internal errors in the SED fitting approach, we applied the same procedure to a sample of 71 weak-lined T Tauri stars (wTTs) associated with the Taurus molecular cloud. Thirty nine stars of this sample were Taurus wTTs observed by the Spitzer Space Telescope (SST) as part of the Legacy project c2d (Evans et al. 2003) and are listed in Table 2.3. The rest of the stars in the sample were wTTs studied by Strom et al. (1989) and are listed in Table 2.4. It is currently believed that the main difference between cTTs and wTTs is the presence in cTTs of an inner accretion disk (Hartmann 1998) and the accompanying phenomena: strong winds and bipolar outflows, near-IR excess, UV excess, strong Hα emission, spectral veiling, etc. All these phenomena are directly connected to the excess radiation at near-IR and shorter wavelengths; therefore, it is reasonable to assume that the fluxes of wTTs at wavelengths shorter than ~ 2 μm are a good representation of the underlying photospheres of cTTs of the same spectral type. This assumption is not valid at wavelengths longer that $\sim$2 μm where some wTTs also possess an IR excess (Padgett et al. 2005 and Cieza et al. 2005). Following the idea that cTTs and wTTs have similar photospheres, the difference between the observed SEDs of classical and weak-lined T Tauri stars of the same spectral type can be attributed to a non-photosperic component in the cTTs fluxes for $\lambda < 2$ μm . Tables 2.3 and 2.4 list the broad band photometry and spectral types used to fit the SEDs of our sample of wTTs. Some of the wTTs SEDs (normalized to the I_C-band) are shown in Figure 2.2 as an illustration of the good agreement between expected and extinction-corrected observed fluxes for stars of different spectral types. The solid line indicates the expected stellar photosphere (calculated as described in section 2.3.1. i.e, based on expected broad band colors normalized to the I_C band) and is not a fit to the extinction-corrected data points. The excellent agreement between the expected and extinction-corrected fluxes gives us confidence in the stellar intrinsic colors and extinction corrections that we use. The optical photometry for the wTTs listed in Table 2.3 comes from Cieza et al. (2005), while the spectral types for these wTTs were taken from Herbig & Bell (1988) and Wichmann et al. (2000). The optical photometry and spectral types of the wTTs in Table 2.4 are taken from Strom et al. (1989). For consistency, all the JHK fluxes are from 2MASS.

In the case of wTTs, we find that all bands fit noticeably better than for cTTs, and normalizing the SEDs to either the J or I_C-band leads to essentially the same fluxes. Figure 2.3a shows the J-band excess for the Taurus wTTs when the photosphere is normalized to I_C. We define the J-band excess, J_x , as $J_x = J_{obs}/J_{exp}–1$, where J_{obs} and J_{exp} are the extinction-corrected observed fluxes and expected fluxes respectively. The mean and the median of the J_x distribution for our sample of wTTs are 0.07 and 0.06 respectively, and the standard deviation is 0.14. This is consistent with wTTs having no J-band excess. Given the large number of wTTs in our sample, we believe that the 6% deviation of the median of the distribution from 0 might reflect a small, but measurable difference between the colors of T Tauri stars and those of dwarf MS stars. Such a difference in the colors is not surprising because T Tauri stars have lower photospheric gravities than dwarf MS stars of the same spectral type. We take this difference in the mean colors into account when we calculate the J-band excess of cTTs by folding in the offset of the wTTs distribution into our calculations. Thus, for each cTTs the J-band excess is calculated as $J_x = J_{obs}/1.06J_{exp}–1$. The standard deviation of the distribution of J_x for wTTs is a measurement of the errors introduced by our SED fitting procedure. These errors include: errors in the spectral types, errors in the extinction correction applied, and errors introduced by the photospheric variability of wTTs (the optical and near-IR photometry correspond to different epochs). We use the standard deviation of the J_x distribution for wTTs as an estimate of the 1σ error in our procedure when we calculate the J-band excess of cTTs. However, we caution that the UV-excess produced by the accretion shock provides an important additional source of error when our procedure is used to calculate the near-IR excess of cTTs. First, the optical veiling due to the accretion shock is likely to affect the photospheric colors and the extinctions derived from the observed color excesses. We discuss this problem in Section 2.3.3. Second, the optical veiling introduces a much larger variability in cTTs than in wTTs. Since we use optical and near-IR data corresponding to different epochs, the variability of cTTs willl increase the uncertainty in the near-IR excesses derived for individual sources. However, in the context of our procedure, photometric variability should only introduce random errors in the determination of the near-IR excess, and it is equally likely to increase the derived near-IR excesses as it is to decrease them. Therefore, given a large enough sample of cTTs, it should be possible to establish whether or not cTTs, as a group, present significant J and H-band excesses.

To extend our sample of cTTs we include in our analysis 44 additional cTTs associated with the Taurus-Auriga molecular complex. These objects, with BVR$_C$I$_C$JHK photometry and spectral types also from Strom et al. (1989) are listed in Table 2.5. For consistency with the Chamaeleon II cTTs, we use the JHK photometry from 2MASS. Figure 2.3b shows the distribution of J$_x$ for the sample of Taurus wTTs and the combined sample of Taurus cTTs: the 15 Chamaeleon II objects from Hughes & Hartigan (1992) plus the 44 Taurus objects from Strom et al. (1989). Defining 1σ and J$_x$ as above, 65 % of the cTTs have J-band excesses larger than 1σ, 48 % larger than 2σ, and 32 % larger than 3σ. The mean J-band excess for the sample of cTTs,$\langle$J$_x\rangle$, is 0.35. Figures 2.3c and 2.3d are analogous to Figure 2.3b, but show the excess in the H and K-bands. The statistics of the J$_x$, H$_x$, and K$_x$ distributions for our sample of wTTs and cTTs are listed in Table 2.6. The second, third and fourth columns show the statistics of the distributions of J, H and K-band excess for wTTs. In all cases, the distributions are consistent with wTTs having no near-IR excess. The standard deviations listed in the fourth column are used as an estimate of the errors of our procedure. These errors are used to calculate the percentage of cTTs with excess larger than, 1σ, 2σ and 3σ (last 3 columns). The main conclusions that can be drawn from Figures 2.3b-c and Table 2.6 are that, for cTTs $\langle K_x\rangle > \langle H_x\rangle > \langle J_x\rangle$ and that these mean excesses are statistically significant in all cases.

Significant K-band excesses are expected for cTTs, and have traditionally been used as a diagnostic for the presence of circumstellar disks (e.g., Strom et al. 1989). However, J and H-band excesses are not expected, and are difficult to explain by using current standard models of circumstellar disks around cTTs (Chiang & Goldreich 1997, 1999). It could be argued that this discrepancy between the near-IR SEDs of cTTs and wTTs is due to the fact that, in general, the SEDs of cTTs were much more strongly corrected for extinction. In that case, an anomalous extinction law could be responsible for the mismatch between the expected and observed fluxes at different wavelengths. However, we find no significant correlation between extinction and J or H-band excess, as illustrated by Figure 2.4. We have tested the effect of the extinction further by using a different extinction law, characterized by R_V=5.0 (See Table 2.2), to correct the stellar fluxes. Since the amplitudes of the observed J-band excesses are smaller than those of the H-band, and since the J-band is more affected by extinction, we concentrate our analysis on the result at the J-band. From the extinction relations listed in Table 2.2, we find that E(J-I_C)Rv=3.1 = 0.32 A_V and E(J-I_C)Rv=5.0=0.36 A_V. This implies that in the context of our SED fitting approach, going from an extinction curve with Rv=3.1 to shallower extinction curve with Rv=5.0, would change the observed J-band fluxes by

$$\Delta J = -J_x = E(J - I_C)_{Rv=3.1} - E(J - I_C)_{Rv=5.0} = -0.04A_V \qquad (2.1)$$

Thus, an extinction law characterized by Rv=5.0, could only account for the J-band excesses of the handful of objects to the left of the line Jx/A_V=0.04 drawn in Figure 2.4 (left panel), all of which have insignificant J-band excesses ($< 1\ \sigma$). The same argument applies to the H-band excesses. An extinction law characterized by Rv=5.0 could only account for the H-band excesses for the objects also to the left of the line Hx/A_V=0.04 drawn in Figure 2.4 (right panel). Thus, we conclude that our results regarding J and H-band excesses are not significantly affected by the choice of extinction law. This very weak dependence of our results on the extinction law is due to two factors: First, since we estimate the extinction from the R$_C$-I$_C$ color excess, the difference in extinction obtained from the two different extinction laws is less than 5%. Second, in order to estimate J-band excesses, we are effectively comparing observed extinction-corrected J-I$_C$ colors to expected J-I$_C$ colors. Since different extinction curves start to converge at these wavelengths, they predict very similar J-I$_C$ color changes for a given A$_V$.

We have also investigated the propagation of the spectral type uncertainties into the derived near-IR excesses. We find that adopting spectral types that are one sub-class later (i.e,. lower effective temperatures) than the spectral types tabulated in Tables 2.1 and 2.4 for every cTTs in our sample leads to an increase of ∼0.1 and ∼0.15 in the calculated mean J and H-band excesses respectively with respect to the excesses shown in Table 2.5. Similarly, adopting spectral types that are one sub-class earlier (i.e., higher effective temperature) than those shown in Tables 2.1 and 2.5, leads to a decrease of ∼0.1 and ∼0.15 in the mean J and H-band excesses respectively. We conclude that, unless we have systematically underestimated the stellar temperatures by 3 spectral type sub-classes, the J-band excess can not be attributed to uncertainties in the spectral types. To account for the H-band excesses, an even larger systematic error in spectral types is needed.

2.3.3 Revisiting initial assumptions

In order to estimate the J, H, and K-band excesses in section 2.3.2, we implicitly made two assumptions that are necessary to estimate the extinction and normalize the expected fluxes to a particular band. Namely, we assumed (1) that the observed extinction-corrected I$_C$-R$_C$ colors of cTTs correspond to photospheric colors, and (2) that the extinction-corrected I$_C$-band fluxes of cTTs are an accurate representation of the underlying photospheres. Then, we calculated the J, H, and K-band excesses by computing the flux ratios, $F_{obs}/F_{expected}$ where F stands for the J, H or K-band fluxes. In the context of our procedure, this is equivalent to calculating I_C-J, I_C-H, and I_C-K color excesses according to $m_{col-exc}$ = (I_{Cobs}–m_{obs})–(I_C–m_{exp}), where m stands for J,H,K magnitudes. If both assumptions (1) and (2) are correct, then the color excess accurately measures the true non photospheric excess, m_{excess}. However, since the emission from the accretion shock and the inner disk will also contribute to the I and R-band total fluxes, these two assumptions are only approximations. In order to test their validity, we take the case of a M0 cTTs, the most common type of star in our sample, with a J-band excess equal to the mean J-band excess reported in section 2.3.2 (rJ = 0.35), and a V-band excess equal to the mean V-band excess (rV=0.60) reported by Gullbring et al. (1998) and Hartmann & Kenyon (1990) for a sub-sample of the objects in Table 2.5. Using the mean colors of main-sequence stars from KH95 and assuming that the emission from the accretion shock and the inner rim can be characterized as black body emission at 10,000 K and 1,700 K, respectively, we derived the expected veiling at the I_C and R_C-bands shown in Table 2.7. The last column shows the total change in apparent magnitude due to the veiling produced by the accretion shock (second column) and the rim (third column) emission. The values are for a M0 star with typical J and V-band veiling of 0.60 and 0.35 respectively. We find that the R_C and I_C-bands contain a non-photospheric contribution of 28% and 19% respectively 1. Since we normalized the photosphere to the I_C-band, a zero color excess,$m_{color-excess}$ =0, for a given band, would actually imply: = rIc = 0.19 (i.e., it seems that we underestimate the J, H and K-band excesses by 0.19). However, there is another effect that compensates for the fact that we ignore the veiling at I_C. Since rIc = 0.19 and rRc = 0.28, the I_C-R_C colors of the stellar photosphere appear bluer by 0.09 magnitudes, and we underestimate the extinction, A_V, by 0.56 magnitudes. If the extinction is underestimated, the shortest wavelengths of the SED are under-compensated with respect to the longer wavelengths, and an artificial color excess is produced. Using the extinction relations from Table 2.2, we convert the underestimated extinctions into the apparent color excesses shown in Table 2.8. The second column lists the amount by which the extinction is underestimated due to the change in R_C-I_C colors produced by the veiling listed in Table 2.7. The third column shows the amount by which the color excess is overestimated due to the underestimated extinctions, $\Delta(I_C\text{–m})_{AV}$, The fourth column shows the net effect of ignoring both rIc and rRc on the apparent excesses at the BVR_CI_CJHK bands (for a M0 star with rV=0.60 and rJ=0.35). For the J, H and K-bands, the end result is that $m_{excess} \sim m_{color-excess}$ to within 5%, which was the original assumption.

Also, we find that the change in the apparent I_C magnitude due to the veiling, mIc, is well compensated by the underestimation in extinction in that band, AIc. In fact, $\Delta AI_C - \Delta mI_C \sim 0.05$ mag, which implies that assuming no I_C and R_C excess only affects the apparent luminosity by $\sim$5 %.

The last column in Table 2.8 also shows that, in this example, we underestimate the R_C and I_C-band excesses by exactly the same amount as the assumed veiling (0.28 and 0.19 magnitudes, respectively). Similarly we underestimated the V-excess by 0.37 magnitudes which is equivalent to underestimating the veiling by 0.4. Since the assumed V-band veiling was 0.6, this means that the SED fitting approach will typically reveal only 30% of the V-band excess due to the accretion shock. This compensating effect of the underestimated extinction on the optical excess explains why the optical SEDs shown in the left panel of Figure 2.1 match the expected photospheres so well, even though excess emission is likely to be present at all wavelengths. This interplay between the UV-excess and the apparent extinction prevents us from obtaining the V-band or B-band excess from the SED and improving the fit recursively by taking into account the effect of the veiling on the apparent colors.

2.4 Comparison with previous works

We arrive at the conclusion that cTTs possess significant J and H-band excesses by analyzing photometric data that are available in the literature. Thus, we were motivated to compare our procedure and assumptions against those found in the original papers from which most of the data were taken (i.e., Strom et al. 1989 and Hughes & Hartigan 1992). We also compare our procedure with that followed by Meyer et al. (1997), who present a detailed analysis of the near-IR colors of cTTs.

Strom et al. (1989, S89 hereafter), present SEDs for 16 of the T Tauri stars in our Table 2.4 and Table 2.5. Their SEDs are normalized to the R_C-band, and as a photospheric model, they use SEDs of dwarf stars of a spectral type corresponding to that of the T Tauri stars. Even though the presence of significant J and H-band excesses is not heavily emphasized by S89, these excesses are clearly seen in most of their SEDs. In fact, S89 mentions that in some cases the spectral energy distribution of the excess emission can be characterized as black body emission at a temperature of T $\sim$2000-2500 K and suggest that the most likely origin of this emission is the inner edge of the disk at the dust sublimation temperature. This conclusion is one of the main results presented herein (see section 2.6.2), but it has been for the most part neglected by subsequent literature. Possibly, the large uncertainties in their procedure and the high temperatures derived from the excess emission prevented S89 from making a stronger case for the presence of significant J and H-band excesses. Several factors may have contributed to a larger uncertainty in the SED fitting procedure used by S89 when compared to our procedure. First, S89 calculate the extinction from the (V-R_C) color excess which is more sensitive to the veiling produced by the accretion shock luminosity and to the extinction law than is the (R_C-I_C) color excess we use. Second, they use intrinsic colors from Johnson (1964) which are on the Johnson system, not on the Cousins system as the observations they report. The transformation between photometric systems introduces an additional source of error. Finally, S89 use J, H and K-band photometry compiled from the literature, while we use the 2MASS catalog which provides a more uniform data set.

Hughes & Hartigan (1992, HH92 hereafter) present SEDs for all the objects shown in Figure 2.1. They normalize the SEDs to the J-band (i.e., they assume zero J-band excess as we do for the SEDs shown in the right column of Figure 2.1.). However, their SEDs do not show the clear systematic underestimation of the optical fluxes seen in our SEDs when they are normalized to the J-band. It is likely that the systematic underestimation of the optical fluxes is masked by the large uncertainties in their procedure. HH92 calculate the extinction, as we do, from the (R_C-I_C) color excess of the objects, but do not specify the extinction law used. They adopt intrinsic colors taken from Bessel (1979) who only reports intrinsic colors for a very limited set of spectral types (i.e., F5, G0, G6, K2, K4, K7, M2); therefore, they probably had to interpolate in order to obtain intrinsic colors for stars of intermediate spectral types. Also, and more importantly, they use a black body curve as the stellar model, which provides only a very rough approximation of the photospheric fluxes.

Meyer et al. (1987, M97 hereafter), follow a procedure very similar to ours in order to calculate the near-IR excess of cTTs. However, they made the crucial assumption that the non-photospheric contribution to the J-band flux comes exclusively from tail of the UV-excess produced by the accretion shock (i.e., there is no contribution from the disk). With this assumption, they estimate that the J-band veiling is 10% of the V-band veiling and calculate the J-band excess from the V-band veiling values provided by Hartigan et al. (1995). They find that the mean of the J-band veiling calculated in this way is $\langle J_x \rangle \sim 0.0$. M97 analyze the same sample of cTTs reported by S89 (Table 2.4 in this paper), but they use the original near-IR fluxes provided by S89 rather than the 2MASS fluxes used by us. They calculate the extinction from the (R_C-I_C) color excess and use extinction corrections identical to ours (i.e., E(R_C-I_C)=0.21 A_V, E(J-H) = 0.11AV, and E(H-K)=0.06AV). However, M97 adopt intrinsic colors from Bessel (1979), which has the limitations mentioned above. With this assumption that $\langle J_x \rangle \sim$0.0, they estimate the H and K-band excess from the J-H and J-K color excesses. M97 find a median H and K-band excess of 0.2 and 0.6 respectively, but caution that the reported values are only lower limits because of the assumption of zero J-band excess. In fact, they state that if they normalize the photospheres to the I_C-band, the calculated mean J-band excess becomes 0.23. In section 2.3.2 we found median J-band, H-band, and K-band excesses of 0.28, 0.54, 1.1, respectively, for our combined sample of Chameleon and Taurus cTTs. We conclude that, once the M97 excesses are corrected for the assumption of zero J-band excess (by adding $\langle J_x \rangle \sim 0.25$ to the $\langle H_x \rangle$ and $\langle K_x \rangle$ excesses), their values agree well with our calculated J,H, and K-band excesses. K-band veiling measurements from the literature support larger K-band excess values than the 0.6 reported by M97 (closer to our 1.45 calculated mean value). Folha et al. (1999) obtain a mean K-band veiling, $\langle rK \rangle \sim 1.3$ for a sample of 30 Taurus cTTs and Doppmann et al. (2003) calculates $\langle rK \rangle \sim$2.0 for a sample of 10 Ophiuchus cTTs, while Muzerolle et al. (2003) finds $\langle rK \rangle \sim$1.2 for a sample of 9 Taurus cTTs. In the next section we discuss more spectroscopic veiling measurements that support our conclusion that classical T Tauri stars present significant J and H-band excesses calculated using our SED fitting approach (Jx SED). The tabulated Jx SED values, defined as in section 2.3.2, can be directly compared with the veiling values obtained by FE99. Figure 2.5 shows the J-band excesses obtained by the two different methods. Since the data points cluster on the upper-right quadrant of the figure, both methods show clear evidence of J-band excess for cTTs as a group. We note that the average and range of the J-band excesses measured by these two different methods are in good agreement, even though the agreement for individual objects is relatively poor. The spectroscopic and photometric data correspond to different epochs, however, and variability might be responsible for some of the scatter. Comparison of the J-band magnitudes reported by Strom et al. (1989) and those from 2MASS show an average difference of ∼0.2 magnitudes and a maximum deviation of up to a factor of 2 in flux, but no systematic variation. Also, The 1σ error bars shown for Jx (SED) correspond to the standard deviation of the Jx in wTTs listed in Table 2.5, and do not include the errors introduced by the interplay between the UV excess and the apparent extinction discussed in section 2.3.3. These errors are difficult to quantify, but are likely to weaken the expected correlation between Jx (SED) and Jx (Spectroscopy).

Other somewhat less direct, but still compelling, evidence for J-band excess is presented by Doppmann et al. (2003). They obtained K-band veiling measurements of 10 cTTs associated with the Rho Ophiuchus dark cloud from high resolution spectra (R = 50,000) centered around 2.207 μm. In this case, the veiling is obtained using spectral synthesis models as templates. They compare stellar luminosities from dereddened K-band magnitudes corrected for veiling against luminosities derived from dereddened J-band magnitudes assuming zero J-band veiling. They find that the J-band luminosities are systematically higher by a factor ∼2. This implies an average J-band veiling of ∼1, which is higher than the average J-band veiling of ∼0.6 found by FE99 for the Taurus cTTs, and the average J-band excesses of ∼0.4 from the SED fitting obtained in this work for the cTTs in Taurus and Chamaeleon II. However, the cTTs in the Doppmann Rho Oph sample were selected based on their large K-band luminosities. Since K-band excess usually dominates the photosphere (they found $\langle K_x \rangle \sim 2.0$), the sample is probably biased toward large K-band and J-band excesses.

2.5 Spectroscopic evidence for J-band excess

In order to test our results from the previous section indicating the presence of significant J and H-band excesses, we analyze a sub-sample of the cTTs in the Taurus-Auriga complex with spectroscopic J-band veiling measurements available in the literature. These measurements provide a test that is independent of any assumptions regarding reddening, extinction or broad-band colors. Spectral veiling,r_λ, is defined as the ratio of any non-photospheric flux to the photospheric flux at a given wavelength,λ. This excess flux is usually estimated by comparing the equivalent widths of the lines of the program objects to those of unveiled stars used as templates, or to synthetic models. Perhaps because J and H-band excesses are not expected, we find no H-band veiling measurements of cTTs in the literature, and only a few works reporting J-band measurements. However, Folha & Emerson (1999), FE99 hereafter, report J-band veiling measurements for 45 cTTs, 33 of which have BVR_CI_CJHK photometry from Strom et al. (1989). This data set provides a sample to test directly our results from previous sections. The FE99 veiling measurements, listed in Table 2.5 as "rJ Spectra", were obtained from high resolution spectra (R ~20,500) around the Pa β line (1.28215 μm) using Main Sequence dwarfs of similar spectral types as templates. Also listed in Table 2.5 are the J-band

SED fitting and spectral veiling measurements independently provide compelling, but not conclusive, evidence for the existence of J-band excesses in cTTs. The combination of these two independent lines of evidence, however, provides a very strong case for the presence of significant non-photospheric J and H-band excesses in cTTs. The existence of a J-band excess has important implications for the study of the structure and evolution of cTTs disks and should be investigated further.

2.6 The physical origin of the ner-IR excess

2.6.1 J and H-band excess vs. K-band and V-band excesses.

In order to explore the nature of the J and H-band excesses, we investigate their correlation with the two known sources of non-photospheric radiation: the accretion shock and the disk emission. If the J and H-band excesses are related to the accretion shock, they should correlate with optical veiling, rV, as measured by spectral veiling (i.e, rJ $\sim$ 0.1 rV for late K and early M stars). Figure 2.6 shows our J-band excess measurements versus the rV from Gullbring et al. (1998). We do not find any strong correlation with this small data set, but clearly, rJ $>>$ 0.1 rV, instead of rJ $\sim$ 0.1 rV, as would be expected if both originated directly at the accretion shock (Hartigan et al. 1995). In addition, the emission from the accretion shock should be negligible at the H-band, but we find that $\langle H_{exc} \rangle > \langle J_{exc} \rangle$. Thus, we discard this explanation.

If the J and H-band excesses come from the circumstellar disk itself, one might expect them to correlate with the excess at longer wavelengths. Figure 2.7 shows our calculated K-band excess vs. J and H-band excesses (left and right panel respectively) for both the Chamaeleon II and Taurus cTTs from Tables 2.1 and 2.5. The Spearman's ranks of these correlations are 0.65 and 0.92 with probabilities of being drawn from a random distribution of 1.5E-8 and 6.3E-26 respectively. These are robust correlations, and they strongly suggest that the J, H and K-band excesses have a common source.

2.6.2 The color temperature of the near-IR excess

.

If J, H and K-band excesses have a common source, and this source is optically thick, then its characteristic temperature can be estimated from the J-K and

H-K colors of the excesses, or equivalently the ratio of the J to K and H to K excess fluxes. Our SED fitting approach allows a straightforward calculation of the J-K and H-K colors of the excess. Following the discussion in section 2.3.2, we obtain: $J_{EXC} \sim J_{obs} - 1.06J_{exc}$, $H_{EXC} \sim H_{obs} - 1.03H_{exc}$, $K_{EXC} \sim K_{obs} - 1.06K_{exc}$, where, J_{EXC}, H_{EXC} and K_{EXC}, are the absolute J,H, and K-band excesses fluxes in Jy, as opposed to the dimensionless excess J_x, H_x, and K_x discussed so far. Figure 2.8 shows J_{EXC} vs. K_{EXC} and H_{EXC} vs. K_{EXC} in units of flux of the expected stellar photospheres at 2.2 μm. The *flux* ratios J_{EXC}/K_{EXC} and H_{EXC}/K_{EXC} shown in Figure 2.8 are both consistent with black body emission at a relatively narrow range of temperatures, T ~1750 K. The right panel of Figure 2.8 reveals a tighter correlation than the left panel. This is expected however, because the percentage error in J_{EXC} is about twice the percentage error in H_{EXC}. The 1σ error bars shown in the top-left of both panels correspond to the standard deviation of wTTs listed in Table 2.6. For the reasons discussed in section 2.3.3, the actual error bars are probably larger, suggesting that uncertainties in our procedure are responsible for a significant fraction of the scatter in the observed excesses.

Depending on the density and composition, the sublimation temperature of dust grains is also ~1500-2000 K (e.g., Pollack et al 1994). Thus, we argue that the near-infrared excess of T Tauri stars is produced at the inner edge of the disk whose temperature is set by the dust sublimation temperature.

2.6.3 The color Temperature of the IRAC excesses

Following the procedure outlined in section 2.6.2, we obtain the color temperature of the mid-IR excess of the cTTS from the Chamaeleon II sample (Table 2.1) by computing the ratios of the flux excesses at the IRAC [4] (3.6 μm) and IRAC-3 bands (5.8 μm) (Porras et al. 2005). At these wavelengths, the excess emission largely

---

[4] The Infra-Red Array Camera on the Spitzer Space Telescope

dominates over the photospheric emission, and the uncertainties in the expected fluxes are likely to dominate the errors in deriving color temperatures. Figure 2.9 shows that the color temperatures of the IRAC excess are T ~1400 ±200 K). This temperature is similar to the black body temperature derived by Muzerolle et al. (2003) (T ~ 1400 K) in which they used high resolution spectroscopy of three spectral regions between 2.1 and 4.8 μm to probe the shape of the excess emission of 9 cTTs. These temperatures are significantly lower than those obtained from the near-IR colors of the excess (T ~1750 ±250 K). We discuss a possible explanation for this difference in the following section.

2.6.4 The inner disks of PMS stars

Herbig Ae/Be stars (Herbig 1960) are pre-main sequence intermediate mass (mass > 2 $M_\odot$ stars analogous to cTTs (mass < 2 $M_\odot$). The mid- and far-IR regions of the SEDs of Herbig Ae/Be stars are well fitted by standard models of passive flared disks (e.g., CG97 & CG99); however, these models fail to explain the near-IR excess, known as the "near-IR bump" observed in most Herbig Ae/Be stars. According to these simple models, the disk flares outward at large radii due to the vertical hydrostatic equilibrium, but is physically thin near the star. Thus, the grazing angle of the incident radiation is small at small radii, and the inner disk is heated very inefficiently and extends to a few stellar radii before reaching the dust sublimation temperature. When the vertical structure of the inner disk is taken into account (Natta et al. 2001 and Dullemond et al. 2001), the very inner edge of the disk, which becomes an inner rim, is irradiated normal to the surface and heated more efficiently. Thus, the dust sublimation radius moves farther away from the star. Farther away from the star, gravity becomes weaker, and the disk's scale height increases. The effect is that the surface area of the region emitting at the dust sublimation temperature becomes much larger than that predicted by simple standard disk models. With this modification, the radiation from the inner rim can account for the observed near-IR bump. Naturally, we investigate the possibility of an analogous inner rim in cTTs to explain the observed 2MASS and IRAC excesses. The idea that cTTs might present inner rims analogous to those of Herbig Be/Ae stars has already been proposed by Muzerolle et al. (2003) based on the black body shape of their 2.1-4.8 μm excess emission and by Allen et al. (2004) based on the IRAC colors of cTTs in young clusters.

For simplicity, current circumestellar disks models usually adopt a single dust sublimation temperature. Natta el al. (2001) assume a dust sublimation temperature of 1700 K, while Dullemond et al. (2001) adopt a temperature of 1500 K to fit their models. However, recent detailed models of the shape of the inner rim (Isella & Natta 2005) show that, when the dependence of the dust sublimation temperature on gas density is taken into account, the inner rim becomes rounded, and its surface has a vertical temperature gradient which is several hundreds of K wide. Such an inner rim would present a hotter color temperature at shorter wavelengths, and a cooler color temperature at longer wavelengths, and could help to explain the discrepancy between the color temperatures we derived from the 2MASS and IRAC observations (section 2.6.2 and 2.6.3, respectively).

2.7 Disk modeling and implication of the near-IR excess for disk structure

In order to quantify the contribution from the inner rim to the total flux at different wavelengths, we model the SED of 10 cTTs from the Chamaeleon II sample (Table 2.1) using the disk model presented by Dullemond et al. (2001). The model is based on the flared disk model of Chiang & Goldreich (1997 and 1999) and includes a disk with three distinct components: a cool disk interior, a warm surface layer, and a hot inner rim located at the dust sublimation radius. The main parameters of the models are listed in Table 2.9. For all models, we assume a single dust sublimation temperature of 1400 K, corresponding to the typical color temperature of the IRAC excess found in section 2.6.3. To estimate the stellar effective temperatures (Teff), we adopt the spectral type-Teff relations from KH95. The stellar luminosities are obtained from the extinction-corrected I_C-band (0.8 μm) magnitudes and the bolometric corrections, appropriate for the spectral type, from Hartigan et al. (1994). Following Hughes & Hartigan (1992), we adopted a distance of 200 pc for all the objects. Finally, the stellar masses are estimated using the evolutionary tracks presented by Siess et al. (2000). For our objects, we find that Siess et al. models yield masses that are intermediate between those derived from the models by D'Antona et al. (1998) and those obtained from the models by Baraffe et al. (1998). The photospheric luminosity of the star, the stellar mass, and the dust sublimation temperature determine the radius and scale height of the rim. This predicted inner rim is labeled "inner rim A" on the disk models in Figure 2.10.

We find that the models for most of the stars systematically underestimate the near and mid-IR excesses. However, a good fit can be obtained simply by scaling the contribution from the predicted inner rim by a factor,Ω , that ranges from ~1 to ~7. This "scaled-up" rim is labeled as "Inner rim B" in Figure 2.10. We interpret this result as an indication that the area of the inner rim is larger, by a factor of Ω, than predicted by the models. i.e., $\Omega = A_{rimB}/A_{rimA}$, where A_{rim} is the area of the rim. Since $A_{rim} \propto R_{rim}H_{rim}$, and according to our adopted model $R_{rim} \propto {H_{rim}}^{2/3}$, where R_{rim} and H_{rim} are the radius and the scale height of the rim, then $A_{rim} \propto {R_{rim}}^{5/2}$. Thus, the radius of the inner rimB can be calculated as $R_{rimB}=R_{rimA}\Omega^{2/5}$.

The masses of the disk models shown in Figure 2.10 were adjusted to try to match the observed 24 μm fluxes. The adopted disk masses range from 5E-2 to 5E-4 solar masses. In all cases, the out disk radius was set to 400 AU, and the disk's surface density, Σ is given by $\Sigma(R)(g\ cm^{-2}=2\times10^3(R/AU)^{-2}$. Since our simple approach of scaling the inner rim does not take into account the effects of the modifications in the inner disk on the disk structure at larger radii, we do not try to constrain the physical parameters of the outer disks. However, we keep the outer disk models in the SEDs shown in Figure 2.10 only to show that the 2MASS and IRAC fluxes are completely dominated by the emission from the inner rim with very minor contributions from the rest of the disk.

The fact that the energy eradiated (i.e., the area under the curve in Figure 2.10) by rim B is larger than that eradiated by rim A suggests that the inner rim is powered by more than the stellar photosphere. We argue that the most likely "source of missing energy" is the UV emission from the accretion shock produced as material from the star is channeled onto the stellar surface. The accretion shock emission has already been recognized by D'Alessio et al. (2003) as an important heating source of the inner disks of cTTs. Unfortunately, as discussed in section 2.3.3, it is very difficult to estimate the UV-excess from the SED alone, and it needs to be obtained independently, e.g., from UV spectroscopy. However, most accretion luminosity estimates based on optical spectroscopy involve an extinction correction. Gullbring et al. (1998) estimate accretion luminosities for a sample of cTTs from UV spectroscopy and compare their results with those presented by Hartigan et al. (1995), for the same sample of stars, following a similar method. The accretion luminosities derived by these two groups systematically differ by up to an order of magnitude. According to Gullbring et al. (1998), most of the discrepancy can be traced back to a large systematic difference in the extinction corrections. The large variability typical of the UV excess makes it even harder to obtain an accurate estimate of the accretion luminosity unless the observations involved in the analysis are made simultaneously. An estimate of the UV-excess is necessary to test whether the energy from the accretion shock luminosity is enough to account for the observed mid-IR excesses seen in the Chamaeleon II objects; however, for the reasons mentioned above, we leave such a test for future work.

We note that the degeneracy between the UV-excess and the extinction can eventually be disentangled by measuring the veiling at the wavelengths corresponding to the BVRCIC band passes using high resolution spectroscopy from 0.4 to 0.9 μm and obtaining simultaneous optical photometry. With that information, the R_C-I_C colors can be corrected for veiling in order to estimate the extinction more accurately, and the UV excess can be estimated directly from the B-band veiling or the U photometry corrected for extinction. We plan to follow that procedure in a follow-up paper in order to study self-consistently the effect of the UV-excess on the SEDs of cTTs at near-IR and Spitzer wavelengths. However, even without the veiling information from spectroscopy, we do find indirect evidence that supports the idea that the UV excess significantly affects the sizes of the inner holes in disks around cTTs. First, if the inner rim is larger than expected because it is significantly powered by accretion shock luminosity, a correlation between the K-band excess and the accretion luminosity is expected. For a sub-sample of the Taurus cTTs, we use the accretion luminosities, derived from UV photometry and spectroscopy, from Muzerolle et al. (1998) to investigate the correlation between K-band excesses and accretion luminosity. This correlation is evident in Figure 2.11, which also shows that, for some cTTs, accretion shock luminosity can dominate the stellar luminosity. The Spearman's rank of the correlation between K-band excesses and accretion luminosity is 0.81 with a probability of being drawn from a random distribution of 1.01E-6. A similar correlation between accretion luminosity and near-IR excess has been reported by Muzerolle et al. (2003) for a smaller sample or cTTs. Also, D'Alessio et al. (2003) demonstrate that including the UV radiation in the circumstellar disk models can significantly increase the size of the inner hole. In particular, they find that, when the UV excess is included, the dust sublimation radius of the "continuum star" DG Tau (0.2 AU) is ∼3 times larger than the radius inferred when neglecting the UV excess emission (0.07 AU), and is in good agreement with the inner radius derived from K-band interferometric observation of DG Tau (Colavita et al. 2003). For our objects, $R_{rimB}/R_{rimA} \leq 2$; thus we conclude that the UV-excess from the accretion shock could in principle account for the sizes of all the inner rims reported herein.

We were motivated to investigate the possibility of large inner rims in cTTs while trying to find an explanation for the J and H-band excesses calculated in section 2.3. However, we emphasize that our results from the IRAC bands, which suggest the presence of large inner rims, are independent of any assumptions made about the presence of J or H-band excesses. In section 2.3.2, we found that the J-band excess is at the ∼35 % level. Using the J-band to obtain the photospheric luminosity, rather than the I_C-band, increases the expected IRAC fluxes only by ∼35%. But in some cases, at IRAC wavelengths, the flux discrepancy between disk models with small inner rims heated only by the stellar photosphere and the observations is an order of magnitude larger than the J-band excess. This discrepancy between the models and the observed IRAC fluxes is well beyond any observational errors and uncertainties in the expected photospheric fluxes. We have followed the same procedure described in section 2.3.1 to calculate the IRAC excesses of a large sample of wTTs (Cieza et al. 2005). For wTTs showing no IR-excess, the expected photospheric fluxes agree with the observed fluxes to within ∼5%. Since the existence of large inner rims in cTTs is also supported by interferometric observations (Colavita et al. 2003), and its presence could account for both the IRAC and 2MASS excesses, it is tempting to conclude that the J and H-band excesses calculated in section 2.3.2 are mainly, even if not exclusively, produced by the tail of the inner disk emission.

2.8 Implications of the J-band excess for stellar ages and disk evolution

The presence of significant J-band and H-band excess has important implications not only for the structure of circumstellar disks, but also for estimations of stellar ages. Since cTTs are usually placed in the H-R diagram using luminosities derived from the J-band (e.g., KH95 and Hartigan et al. 1994), a systematic error in the J-band luminosities translates into a systematic error in the derived ages. In order to investigate the effect of the J-band excess on the derived luminosities and ages, we calculate the luminosities of our entire sample of cTTs and wTTs from the extinction-corrected I_C and J-band magnitudes and bolometric corrections appropriate for the spectral types from Hartigan et al. (1994), and then compare the results. We adopted distances of 140 pc and 200 pc for objects in Taurus and Chameleon II, respectively (Kenyon et al. 1994, and Hughes & Hartigan, 1992). For our sample of 59 cTTs (Tables 2.1 and 2.5), we find that luminosities derived from the J-band are systematically higher by a factor of $\sim$1.35 on average with respect to luminosities obtained from the I_C-band. However, for wTTs, we find no systematic difference between the two methods. This systematic difference in the luminosities obtained for cTTs is a direct consequence of the J-I_C color excesses reported in section 2.3.2; therefore, the uncertainties in the J-band excess determination propagate directly into the uncertainties in the luminosity difference between luminosities derived from the I_C-band and those derived from the J-band. In section 2.3.3, we conclude that these color excesses are a good measurement of the non-photospheric J-band contributions (i.e. $J_x \approx J_{col-exc}$). Thus, we believe that the photospheric luminosities obtained from the I_C-band are more accurate than those obtained from the J-band. As discussed in Section 2.7, if optical spectroscopic veiling measurements were available, this conclusion could be tested by combining photometry and spectroscopic veiling measurements at the R_C and I_C bands. The extinction can then be obtained from the veiling corrected R_C-I_C colors and the I_C fluxes can be corrected for extinction and veiling independently rather than assuming that the effects cancel each other.

If the luminosities obtained from the I_C band are in fact more accurate that those obtained from the J-band as a general rule, the luminosities of cTTs have been systematically overestimated by most studies. Since low-mass PMS stars (mass < 1 $M_\odot$) contract roughly at constant temperature, overestimated luminosities translate into underestimated ages when the stars are placed in the H-R diagram. This effect is shown in Figure 2.12, which plots the ages of cTTs and wTTs obtained from I_C-band luminosities vs. those obtained from J-band luminosities for 3 different sets of evolutionary tracks. We find that, in general, models by D'Antona et al (1998) (a) yield younger ages, models by Baraffe et al. (1998) (c) yield older ages, while models by Siess et al. (2000) (b) yield intermediate ages. In all cases, cTTs appear systematically younger when the ages are derived from the J-band luminosities instead of the I_C-band luminosities. Since wTTs have no J-band excess, no systematic effect is seen for their ages, and using J-band or I_C luminosities yields essentially the same age.

In Figure 2.13, we plot the age distribution of cTTs and wTTs when the stellar luminosities are estimated from the J-band (left panel) and from the I_C-band (right panel) using the models from Siess et al. (2000). The mean, median and standard deviation of the logarithmic age distribution (in million of years) are 0.32, 0.27, and 0.35 respectively when the ages are derives from J-band luminosities and 0.50, 0.47, and 0.37 respectively when the ages are derived from I_C-band luminosities.

The right panel of Figure 2.13 shows that, when the ages are derived from the I_C-band, the overlap of the age distribution of cTTs and wTTs increases significantly with respect to the age distributions obtained from the J-band luminosities. Most wTTs are likely to be evolutionary descendants of cTTs, since all low-mass PMS are likely to go through a cTTs phase, even if this phase is short. Strong winds and star-disk interactions are the main mechanisms through which PMS stars are believed to dissipate angular momentum; therefore, without a T Tauri phase it becomes very difficult to explain the angular momentum evolution of young stellar objects (Rebull et al. 2004). If wTTs are in fact evolutionary descendents of cTTs, a large overlap in their age distributions implies a wide distribution in the duration of the cTTs stage. In this context, the right panel of Figure 2.13 suggests that the inner accretion disk, the presence of which defines the cTTs phase, dissipates on a time scale that ranges from 1 to 10 Myr.

The diversity in the dissipation time-scale of the inner accretion disks might be related to the presence of sub-stellar companions or to the formation of giant planets within the disks. The presence of planets is usually invoked to account for the large inner holes (∼1-10 AU wide) inferred from the SEDs of several wTTs and cTTs (e.g., Calvet et al. 2002 and D′Alessio 2004). Mid and far-IR properties of a statistically significant sample of young wTTs (i.e., coeval with cTTs) are needed to test this idea. Spitzer observations will soon reveal the fraction of wTTs with (non-accreting) circumstellar disks as a function of age, which will help to constrain the dissipation timescale of the planet-forming region of the disk.

2.9 Summary and conclusions

1) In section 2.3, we showed that cTTs present significant J and H-band color excesses in addition to the well studied K-band excess. We interpreted these color excesses as evidence for non-photospheric emission.

2) In sections 2.6.2 and 2.6.3, we estimated the color temperature of the excess emission at 2MASS and IRAC wavelengths, respectively. We found that the color temperature of the excess emission is T ∼1750 ± 250K at 2MASS wavelengths and T ∼1400 ± 200 at IRAC wavelengths. We suggested that this emission origi-

nates at an inner rim which is physically narrow but has a gradient of temperatures several hundreds of degrees wide.

3) In section 2.7, we modeled the SED of 10 cTTs from 0.4 to 24 μm and found that the 2MASS and IRAC fluxes are dominated by the emission from the inner rim. The models that best fit the data are those where the inner radius of the disk is larger than expected for a rim in thermal equilibrium with the stellar radiation field alone. We found that the K-band excess correlates with accretion luminosity. As proposed by D$'$Alessio et al. (2003), the UV radiation from the accretion shock could explain the larger than expected inner holes.

4) Finally, in section 2.8, we calculated stellar luminosities from the I_C and J-band, and used these luminosities to estimate stellar ages from 3 different sets of evolutionary tracks. We argued that normalizing the luminosity of cTTs to the J-band systematically overestimates their luminosities. These overestimated luminosities translate into underestimated ages when the stars are placed in the H-R diagram. When the ages are derived from I_C-band luminosities, cTTs and wTTs show a larger age overlap with respect to ages derived from the J-band. If wTTs are descendants of cTTs, this large overlap implies a wide diversity in the duration of the cTTs phase.

2.10 Acknowledgments

Support for this work, part of the Spitzer Legacy Science Program, was provided by NASA through contracts 1224608 and 1256316 issued by the Jet Propulsion Laboratory, California Institute of Technology, under contract 1407. This publication makes use of data products from the Two Micron All Sky Survey, which is a joint project of the University of Massachusetts and the Infrared Processing and Analysis Center/California Institute of Technology, funded by the NASA and the NSF.

Table 2.1. Chamaeleon II CTTS from HH92

		B	V	R_C	I_C	J	H	K	IRAC-2	IRAC-2	IRAC-3	IRAC-4	MISP-1
Star ID	Spectral Type				(mag)						(mJy)		
Sz 46	M3	17.66	16.19	14.74	13.18	11.25	10.26	9.75	8.14E+1	7.33E+1	6.37E+1	5.55E+1	5.16E+1
Sz 48	M1	19.17	18.05	16.17	14.36	11.44	10.10	9.45	1.33E+2	...	8.97E+1	...	8.40E+1
Sz 50	M3	17.64	16.01	14.30	12.50	10.31	9.32	8.85	1.38E+2	1.37E+2	1.31E+2	1.71E+2	3.56E+2
Sz 51	M0	15.38	14.50	13.47	12.38	10.61	9.85	9.35	1.91E+2	1.64E+2	1.30E+2	1.18E+2	1.08E+2
Sz 53	M1	17.85	16.59	15.20	13.66	11.73	10.58	9.92	9.39E+1	8.72E+1	7.32E+1	7.62E+1	8.47E+1
Sz 54	K7	13.88	12.53	11.58	10.61	9.05	8.15	7.59	3.87E+2	4.05E+2	3.08E+2	2.71E+2	2.61E+2
Sz 55	M0	18.90	17.49	15.95	14.41	12.54	11.55	10.92	2.98E+1	...	2.09E+1	...	2.69E+1
Sz 56	M4	18.53	17.08	15.41	13.47	11.49	10.78	10.41	3.52E+1	...	2.17E+1	...	5.04E+1
Sz 57	M4	19.56	17.70	15.64	13.48	10.95	10.22	9.80	6.05E+1	...	4.12E+1	...	3.26E+1
Sz 58	K5	17.89	16.01	14.44	13.00	10.84	9.58	8.75	2.72E+2	...	2.52E+2	...	3.49E+2
Sz 59	M0	16.37	14.80	13.42	12.08	10.51	9.26	8.38	3.98E+2	...	3.07E+2	...	2.38E+2
Sz 60a	M1	17.56	16.21	14.88	13.45	11.19	10.22	9.54	6.40E+1	...	4.74E+1	...	5.66E+1
Sz 60b	M4	18.16	16.80	15.32	13.60	11.51	9.74	9.46	5.09E+1	...	3.97E+1	...	...
Sz 61	K4	16.77	15.13	13.69	12.38	9.88	8.76	7.94	5.94E+2	6.12E+2	5.04E+2	5.32E+2	6.50E+2
Sz 62	M2	16.99	15.55	14.03	12.56	10.52	9.65	9.12	1.35E+2	1.13E+2	9.33E+1	1.03E+2	1.16E+2

Note. — Five of the 20 PMS stars presented in Table 2.5 of HH92 were excluded from our analysis. Sz 47 and Sz 49 were excluded because they are heavily veiled and their spectral types are very uncertain. IRAS 12496-7650 was excluded because it is a highly embedded Herbig Be/Ae star. Sz 63 and Sz 64 were excluded because of the lack of Spitzer data. Even though the spectral type of Sz 55 is marked as uncertain, this star was kept on the sample because we were able to obtain a reasonable star + disk model to fit the optical, near-IR, and Spitzer data (see Fig. 2.10).

Table 2.2. Adopted Extinction Relations and Zero Points

Band	λ (μm)	$A_V/A\lambda$ (R_V=3.1)	$A_V/A\lambda$ (R_V=5.0)	Zero Point (Jy)
B	0.44	1.31	1.20	4130
V	0.55	1.00	1.00	3781
R_C	0.65	0.79	0.84	3080
I_C	0.80	0.58	0.62	2550
J	1.25	0.26	0.26	1594
H	1.66	0.15	0.15	1024
K	2.2	0.09	0.09	667

Note. — Extinction curves and optical zero points are from the Asiago database of photometric systems (http://ulisse.pd.astro.it/Astro/ADPS; Fiorucci & Munari 2003). The 2MASS zero points are from the 2MASS All Sky data release web document (http://www.ipac.caltech.edu/2mass/releases/allsky/doc/sec6_4a.html).

Table 2.3. Taurus WTTS from the c2d Legacy Project

Star ID	Spectral Type	V	R_C	I_C	J	H	K
FX Tau	M4	13.50	12.37	10.98	9.39	8.40	7.92
HD 283572	G2	9.05	8.56	8.07	7.41	7.01	6.87
IW Tau	K7	12.51	11.57	10.51	9.24	8.48	8.28
Lk 19	K0	10.94	10.35	9.75	8.87	8.32	8.15
LkCa 4	K7	11.69	10.97	10.28	9.34	8.71	8.58
LkCa 1	M4	13.73	12.63	11.05	9.64	8.87	8.62
LkCa 21	M3	13.43	12.32	10.88	9.46	8.67	8.45
LkCa 3	M1	12.06	11.04	9.76	8.36	7.62	7.42
LkCa 5	M2	13.54	12.54	11.29	9.97	9.29	9.05
LkCa 7	K7	12.52	11.60	10.46	9.13	8.38	8.26
NTTS 032641+2420	K1	12.20	11.64	11.13	10.32	9.86	9.70
NTTS 040234+2143	M2	14.77	13.72	12.31	10.95	10.29	10.06
NTTS 041559+1716	K6	12.23	11.56	10.88	10.03	9.42	9.27
NTTS 042417+1744	K1	10.35	9.89	9.47	8.78	8.39	8.30
NTTS 042835+1700	K5	12.57	11.86	11.18	10.28	9.71	9.50
NTTS 042916+1751	K7	12.01	11.26	10.53	9.70	9.06	8.85
NTTS 042950+1757	K7	13.11	12.20	11.27	10.16	9.46	9.31
RX J0405.3+2009	K1	10.67	9.96	9.41	8.69	8.19	8.09
RX J0409.2+1716	M0	13.44	12.11	11.15	9.96	9.25	9.05
RX J0409.8+2446	M1	13.51	12.55	11.35	10.10	9.45	9.25
RX J0412.8+1937	K6	12.47	11.68	10.85	9.99	9.43	9.24
RX J0420.3+3123	K4	12.60	11.96	11.30	10.45	9.88	9.73
RX J0432.8+1735	M2	13.66	12.60	11.32	10.00	9.23	9.02
1RX J0438.2+202	K2	12.18	11.52	10.90	10.07	9.53	9.36
RX J0438.6+1546	K1	10.89	10.31	9.73	8.90	8.36	8.24
RX J0439.4+3332A	K5	11.54	10.79	10.13	9.18	8.57	8.42
RX J0445.8+1556	G5	9.29	8.84	8.41	7.85	7.46	7.34

Table 2.3 (cont'd)

Star ID	Spectral Type	V	R_C	I_C	J	H	K
RX J0452.5+1730	K4	11.97	11.08	10.58	9.97	9.41	9.25
RX J0452.8+1621	K6	11.74	10.81	10.05	9.10	8.48	8.28
RX J0457.2+1524	K1	10.21	9.67	9.13	8.38	7.91	7.75
RX J0457.5+2014	K3	11.34	10.73	10.15	9.28	8.82	8.69
RX J0458.7+2046	K7	11.95	11.05	10.43	9.59	8.96	8.80
RX J0459.7+1430	K4	11.71	11.10	10.53	9.66	9.09	8.95
UX Tau A	K2	11.93	11.11	10.16	8.62	7.96	7.55
V807 Tau	K7	11.44	10.56	9.58	8.15	7.36	6.96
V836 Tau	K7	13.99	12.93	11.74	9.91	9.08	8.60
V927 Tau	M5	14.70	13.39	11.43	9.73	9.06	8.77
V928 Tau	M0	14.04	12.77	11.33	9.54	8.43	8.11
Wa Tau 1	K0	10.30	9.76	9.24	8.42	7.93	7.80

Table 2.4. Taurus WTTS from S89

Star ID	Spectral Type	B	V	R_C	I_C	J	H	K
347	K1	12.95	12.05	11.52	11.01	10.32	9.86	9.70
351	K5	13.38	12.25	11.55	10.84	9.80	9.21	9.07
352	G0	12.71	11.85	11.34	10.82	10.08	9.71	9.58
353	G5	13.25	12.31	11.75	11.18	10.45	10.01	9.86
354	K3	14.90	13.79	13.10	12.47	11.79	11.23	11.09
355	K2	13.59	12.67	12.13	11.60	10.81	10.34	10.21
357	K2	13.96	12.91	12.28	11.67	10.84	10.32	10.16
358	M2	15.99	14.52	13.40	11.85	10.27	9.70	9.46
359	M2	15.07	14.17	13.09	11.74	10.37	9.75	9.53
360	M3	16.54	14.97	13.72	12.24	10.80	10.17	9.97
361	M3	16.61	15.09	13.92	12.41	10.94	10.35	10.10
362	M2	16.04	14.67	13.60	12.30	10.95	10.29	10.06
365	M4	15.22	13.73	12.52	11.07	9.64	8.87	8.62
368	M1	13.61	12.10	11.01	9.78	8.36	7.62	7.42
370	K7	13.96	12.49	11.54	10.56	9.25	8.52	8.32
371	M2	15.06	13.56	12.51	11.33	9.98	9.29	9.05
372	K5	14.37	13.26	12.60	11.99	11.18	10.60	10.46
376	K7	13.41	12.28	11.59	10.92	10.03	9.42	9.27
378	K7	14.81	13.24	12.24	11.16	9.50	8.65	8.42
379	K7	13.94	12.55	11.63	10.58	9.13	8.33	8.26
380	G5	9.87	9.04	8.34	7.83	7.41	7.01	6.87
385	M1	14.50	13.04	12.06	11.09	9.78	8.89	8.35
388	K1	11.13	10.34	9.88	9.45	8.78	8.39	8.30
392	K5	13.71	12.53	11.81	11.15	10.28	9.71	9.50
397	K7	13.29	12.06	11.31	10.61	9.70	9.06	8.85
399	K7	13.58	12.18	11.29	10.34	9.17	8.49	8.23
400	K7	13.51	12.11	11.23	10.35	9.07	8.43	8.25

Table 2.4 (cont'd)

Star ID	Spectral Type	B	V	R_C	I_C	J	H	K
403	K7	14.72	13.22	12.28	11.37	10.16	9.46	9.31
407	F8	13.70	12.67	12.04	11.43	10.58	10.08	9.90
408	K0	11.33	10.37	9.80	9.27	8.42	7.93	7.80
415	G0	12.46	11.07	10.21	9.36	8.10	7.50	7.23
419	K5	13.41	12.09	11.31	10.57	9.42	8.60	8.16
420	K7	14.04	12.51	11.51	10.51	9.24	8.48	8.28
426	K0	11.87	10.85	10.25	9.68	8.87	8.32	8.15
427	K7	12.88	11.60	10.81	10.05	8.96	8.32	8.13
429	K7	14.66	13.13	12.19	11.21	9.91	9.08	8.60

Table 2.5. Taurus WTTS from S89

Star ID	Spectral Type	B	V	R_C	I_C	J	H	K	J_x SED	r_J Spectra	σ_{rJ}[1]
23	M0	15.01	14.30	13.50	12.40	10.32	9.39	8.71	1.01	1.02	0.52
25	K3	13.59	12.36	11.42	10.60	9.00	7.87	6.86	-0.01	1.2	LL
26	M2	15.46	13.91	12.78	11.39	9.96	9.15	8.84	0.04	0.80	LL
27	M2	15.24	13.67	12.57	11.27	9.87	9.05	8.81	...	...	...
28	M0	15.03	14.11	13.09	11.55	9.56	8.62	7.97	0.05	0.43	0.21
30	M2	15.03	14.11	13.09	11.55	9.56	8.62	7.97	0.04	0.99	0.21
32	K7	13.07	12.06	11.23	10.39	9.30	8.42	8.05	0.45	0.52	0.14
33	M2	14.31	12.95	11.87	10.66	9.15	8.26	7.71	0.32	0.41	0.15
34	K1	11.86	10.92	10.28	9.63	8.00	6.78	5.74	3.15	0.80	LL
35	K0	11.07	9.89	9.11	8.45	7.15	6.18	5.40	0.22	0.78	0.15
36	M1	13.17	12.08	11.08	9.94	8.17	7.25	6.73	...	...	...
37	K7	13.09	12.27	11.33	10.48	8.96	7.81	6.73	1.25	2.50	LL
38	M0	15.32	13.92	12.80	11.53	9.77	8.82	8.18	...	...	...
41	M0	15.08	13.53	12.43	11.27	9.66	8.64	8.00	0.52	0.12	0.12
44	M1	15.54	13.90	12.71	11.25	9.55	8.57	8.06	0.15	0.35	0.16
45	K7	13.77	12.45	11.47	10.48	8.88	7.82	7.03	0.82	0.72	0.20
46	M4	15.76	14.28	13.04	11.29	9.52	8.78	8.54	0.10	0.60	0.22
48	M1	17.48	15.75	14.29	12.73	10.33	9.08	8.37	0.47	0.43	0.21

Table 2.5 (cont'd)

Star ID	Spectral Type	B	V	R_C	I_C	J	H	K	J_x SED	r_J Spectra	σ_{rJ}[1]
49	M0	15.92	14.55	13.47	12.36	10.21	8.67	7.10	0.47	2.50	LL
50	M3	16.37	14.94	13.59	11.81	9.34	8.16	7.17	0.58	0.8	LL
51	K7	15.20	13.65	12.46	10.99	8.98	8.81	8.52	...	...	...
54	K7	13.75	12.35	11.36	10.38	8.79	7.85	7.25	0.61	0.38	0.14
55	M2	14.48	12.95	11.90	10.61	9.30	8.38	7.86	0.20	0.11	0.18
56	K6	14.27	13.09	12.08	11.05	9.16	8.22	7.55	0.50	0.40	0.17
57	K7	13.64	12.37	11.45	10.53	9.00	8.01	7.32	0.54	0.72	0.22
58	K7	14.19	13.05	12.11	11.15	9.69	8.77	8.12	0.51	0.7	LL
61	K7	14.72	13.37	12.32	11.22	9.48	8.43	7.79	...	...	...
62	M1	15.42	13.99	12.99	11.85	10.44	9.76	9.52	...	...	...
63	K7	14.23	12.96	12.05	11.01	9.67	8.76	8.29	0.42	0.21	0.08
65	M0	13.72	12.33	11.40	10.44	9.16	8.37	8.03	0.21	0.08	0.10
66	K3	14.83	13.16	12.07	11.00	9.34	8.24	7.47	-0.10	1.06	0.36
67	K7	15.70	14.30	13.11	11.79	9.64	8.44	7.49	0.90	1.07	0.28
68	M0	15.26	13.75	12.71	11.53	9.85	9.10	8.79	0.37	-0.04	0.09
69	K7	16.51	14.74	13.32	11.96	9.58	8.40	7.94	...	...	...
70	M1	15.65	14.31	13.20	12.05	10.99	9.69	8.76	...	...	...
71	M0	16.35	14.89	13.62	12.30	10.71	9.77	9.33	...	...	...

Table 2.5 (cont'd)

Star ID	Spectral Type	B	V	R_C	I_C	J	H	K	J_x SED	r_J Spectra	σ_{rJ}[1]
72	M0	15.14	13.55	12.41	11.25	9.56	8.63	8.08	0.91	0.15	0.19
73	K6	14.98	13.42	12.28	11.09	9.24	7.99	7.31	...	...	...
74	K6	12.23	11.57	10.91	10.25	8.54	7.46	6.45	0.24	2.50	LL
75	K6	12.78	11.90	11.16	10.46	9.33	8.59	8.16	0.32	0.57	0.19
76	K7	13.61	12.37	11.39	10.46	8.91	7.89	7.05	0.24	0.84	0.20
77	K3	13.22	12.03	11.22	10.50	9.34	8.60	8.28	...	...	...
80	K1	11.84	11.09	10.42	9.68	8.54	7.62	6.87	0.23	0.5	LL
367	K3	12.02	10.65	9.80	8.94	7.63	6.83	6.48	0.12	1.37	0.40

[1] LL stands for lower limits

Table 2.6. Statistics on the Near-IR colors of T Tauri Stars

Band (1)	WTTS Mean Excess (2)	WTTS Median Excess (3)	WTTS Standard Deviation = 1-σ (4)	CTTS Mean Excess 5)	CTTS Median Excess (6)	CTTS Excess > 1-σ % (7)	CTTS Excess > 2-σ % (8)	CTTS Excess > 3-σ % (9)
J	0.07	0.06	0.14	0.35	0.28	63	48	32
H	0.06	0.03	0.18	0.69	0.54	78	64	52
K	0.10	0.06	0.24	1.45	1.10	79	74	67

Table 2.7. Expected Veiling

Band (1)	Veiling (Accretion Shock) (2)	Veiling (Inner Rim) (3)	Δm (r_V=60, r_J=0.35) (4)
R_C	0.50r_V	0.05r_J	0.28
I_C	0.23r_V	0.15r_J	0.19

Table 2.8. Apparent Color Excess

Band (1)	ΔA (mag) (2)	Δ(I$_C$-m)$_{Av}$ (mag) (3)	ΔExcess[1] (mag) (4)
B	0.56	-0.31	-0.50
V	0.43	-0.18	-0.37
R$_C$	0.34	-0.09	-0.28
I$_C$	0.25	0.00	-0.19
J	0.11	0.14	-0.05
H	0.06	0.19	0.00
K	0.04	0.21	+0.02

[1] ΔExcess = Δ(I$_C$ - m)$_{Av}$, where Δm$_{Ic}$=0.19

Table 2.9. Apparent Color Excess

Star ID	L_* ($L_\odot$)	T_{eff} (K)	M_* ($M_\odot$)	R_{rimA} (AU)	Ω^1	$R_{rimB}{}^1$ (AU)
Sz 47	0.19	3470	0.35	0.04	4.1	0.07
Sz 51	0.35	3850	0.60	0.05	5.8	0.10
Sz 53	0.26	3720	0.50	0.04	3.5	0.07
Sz 55	0.18	3850	0.60	0.04	1	0.04
Sz 56	0.23	3370	0.30	0.04	1	0.04
Sz 57	0.40	3370	0.30	0.05	1	0.05
Sz 58	0.51	4350	0.60	0.05	6.0	0.10
Sz 59	0.41	3850	0.40	0.06	6.7	0.13
Sz 61	1.66	4590	1.40	0.11	4.5	0.20
Sz 62	0.42	3580	0.40	0.05	3.6	0.08

[1] Rim area scaling factor

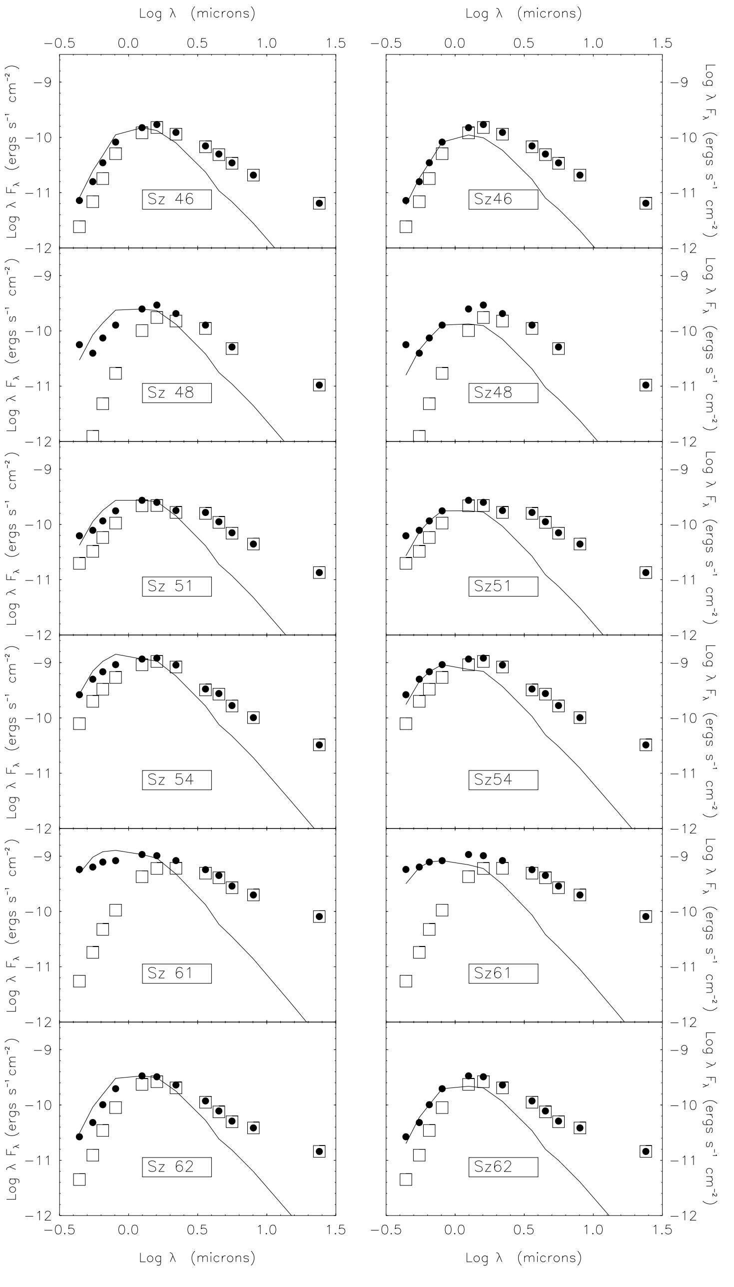

Figure 2.1 Optical and IR SEDs of 6 Chamaeleon II cTTs with the stellar photosphere normalized to the J-band (left column) and to the I$_C$ band (right column). In the first case, the BVRI fluxes are significantly overestimated. Normalizing the SED to the I$_C$-band leads to a better fit of the optical bands and reveals significant J and H-band excess for many of the sources. The open squares represent observed fluxes while filled circles denote extinction corrected fluxes. The solid lines indicate the expected stellar photospheres. Photometric uncertainties (usually around 3% in the optical and the near-IR, and 5% in IRAC wavelengths) are small compared to other sources of error, which include errors in the spectral types, the adopted colors, and extinction corrections. We try to quantify these errors in sections 2.3.2 and 2.3.3.

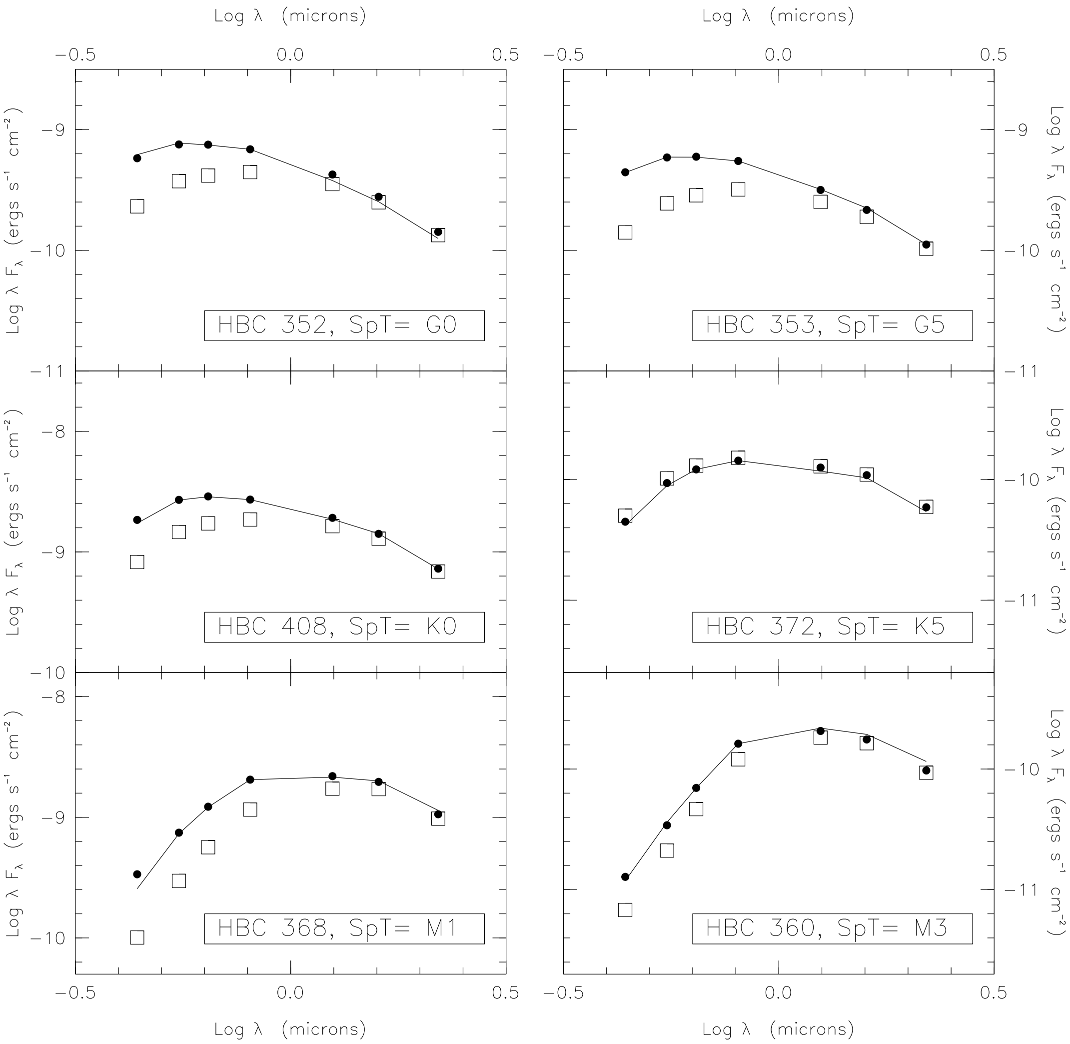

Figure 2.2 SEDs of 6 Taurus wTTs illustrate the very good agreement between expected and extinction-corrected observed fluxes for stars of different spectral types. The open squares represent observed fluxes while filled circles denote extinction corrected fluxes. The solid line indicates the expected stellar photosphere (calculated as described in section 2.3.2. i.e, based on expected broad band colors normalized to the I$_C$ band) and is not a fit to the extinction-corrected data points. The excellent agreement between the expected and extinction-corrected fluxes gives us confidence in the stellar intrinsic colors and extinction corrections that we use.

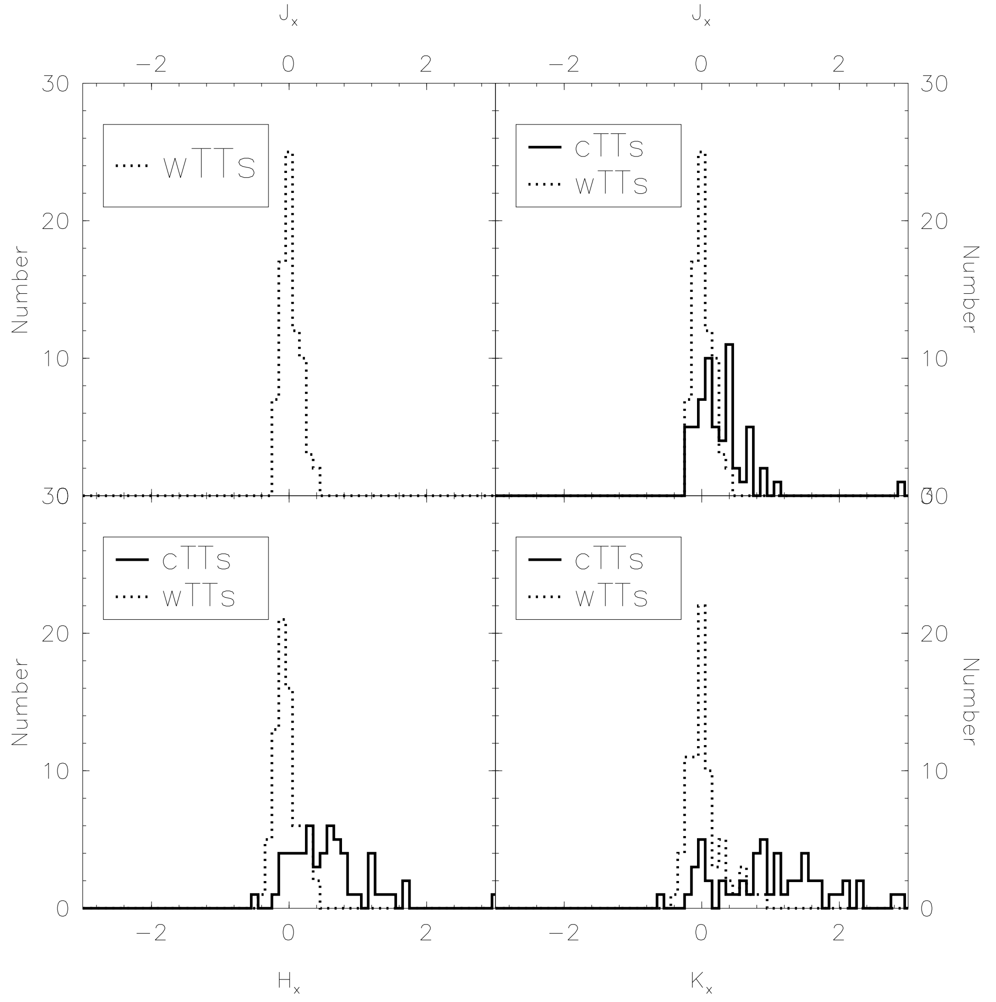

Figure 2.3 Histograms of the excess at the J-band (a and b), H-band (c), and K-band (d) for wTTs (dotted lines) and cTTs (solid lines). The excesses shown for cTTs have been corrected for the median excesses found for wTTs (third column in Table 2.6). The distributions shown are consistent with wTTs having no near-IR excess. Significant excess is seen in all three 2MASS bands for cTTs.

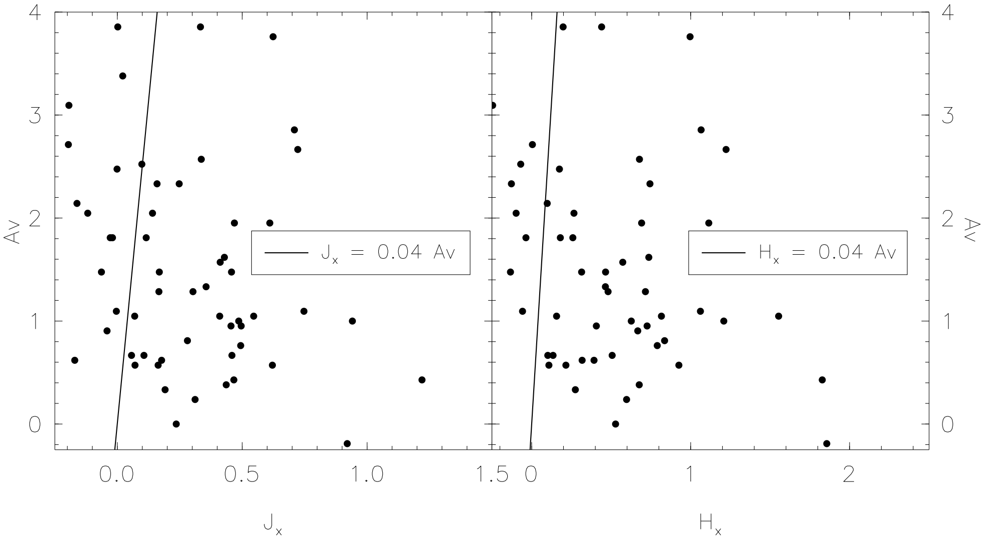

Figure 2.4 Extinction (A_V) vs. J-band excess (left panel) and H-band excess (right panel). No significant correlation is seen in the figures. A shallower extinction curve with R_V=5.0 can only account for the IR excess for the objects left to the shown solid lines.

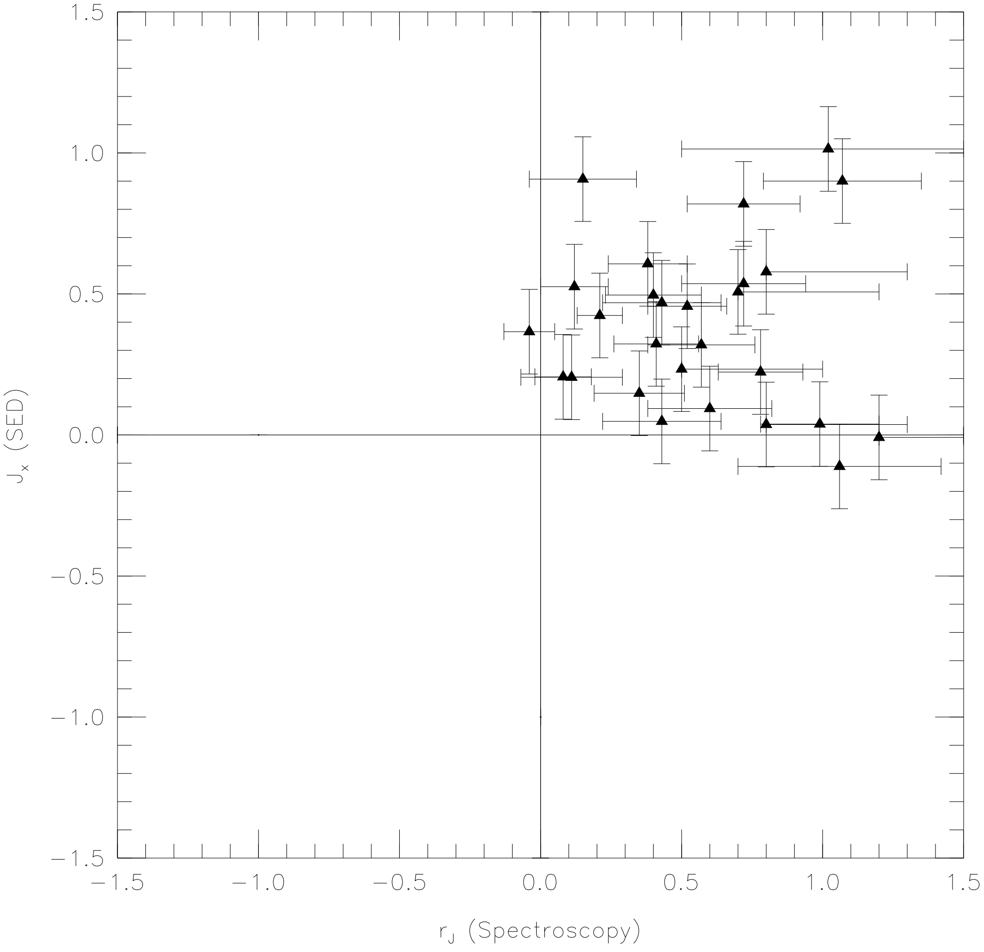

Figure 2.5 J-band excess calculated using our SED fitting vs. the J-band excess derived spectroscopically by FE99. The data points cluster in the upper-right quadrant of the figure; therefore, both methods show clear evidence of J-band excess for cTTs as a group.

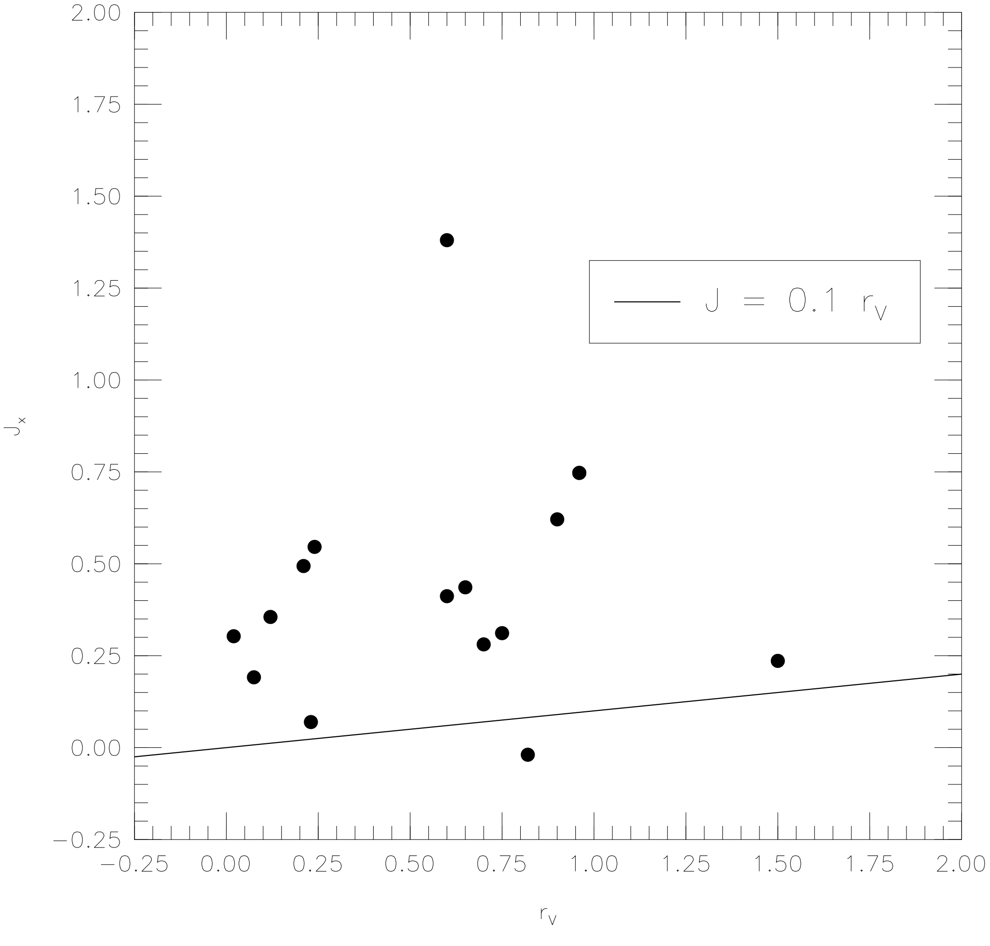

Figure 2.6 J-band excess calculated using our SED fitting vs. rV from Gullbring et al. (1998). No significant correlation is seen with this small data set, but clearly, rJ >> 0.1 r$_V$, instead of r$_J$ $\sim$ 0.1 r$_V$, as would be expected if both originated directly at the accretion shock. The r$_J$ $\sim$ 0.1 r$_V$ relation is represented by the solid line.

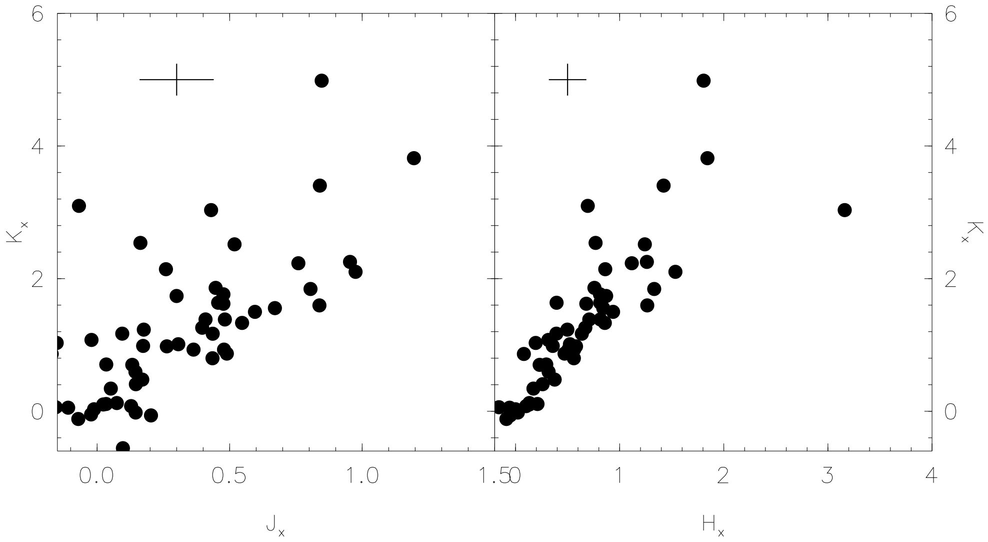

Figure 2.7 K-band excess vs. J-band excess (left panel) and H-band excess (right panel). K-band excess correlates strongly with both, J and H-band excesses. The 1-σ error bars shown at the upper left corner of the figures correspond to the standard deviation of wTTs listed in Table 2.6. The Spearmans ranks of these correlations are 0.65 and 0.92 with probabilities of being drawn from a random distribution of 1.5E-8 and 6.3E-26 respectively. These robust correlations suggest that the J, H, and K-band excesses have a common source.

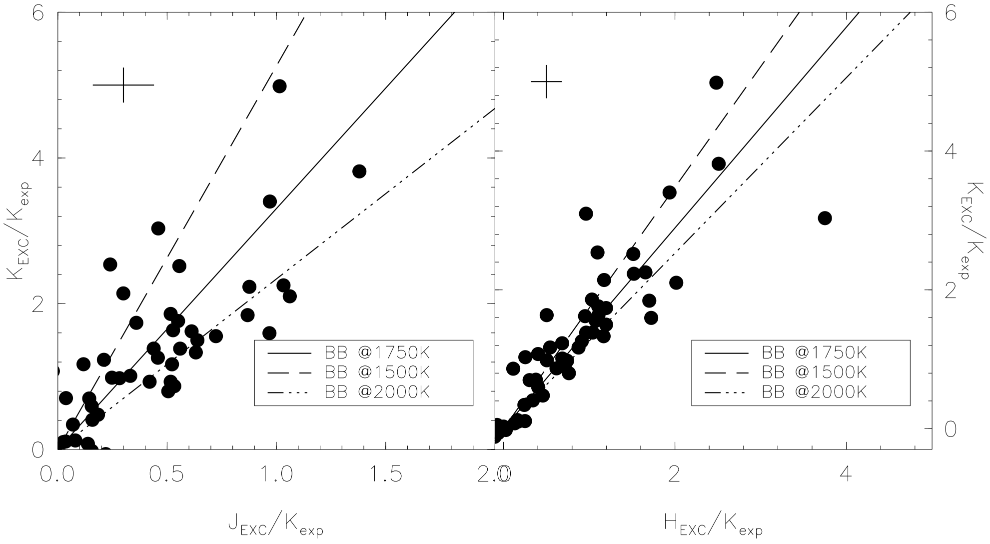

Figure 2.8 K-band excess flux vs. J-band excess flux (left panel) and H-band excess flux (right panel) in units of the expected photosphere at 2.2 μm. The flux ratios shown are consistent with black body emission at a relatively narrow range of temperatures, T ∼1750 K. The lines shown correspond to black bodies at 1500, 1750, and 2000 K. The 1σ error bars shown at the upper left corner of the figures correspond to the standard deviation of wTTs listed in Table 2.6. For reasons discussed in section 2.3.2, the actual error bars are probably larger (see text).

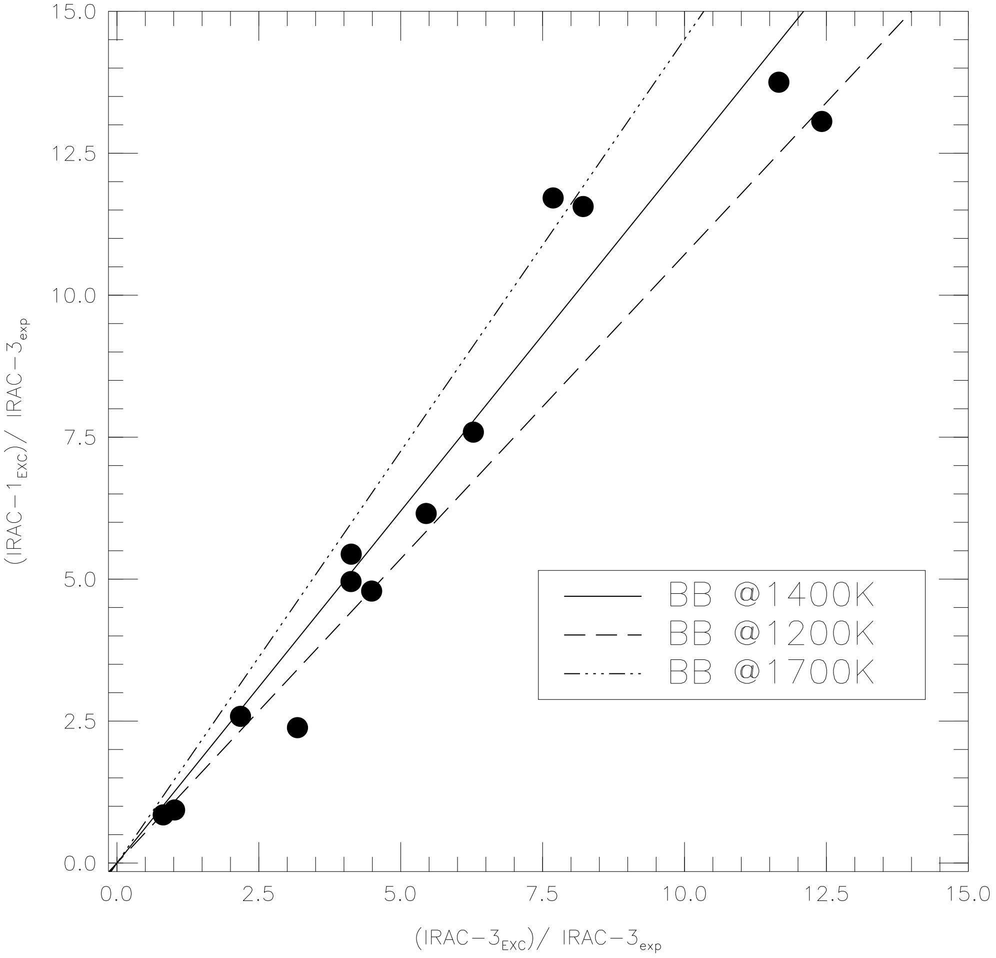

Figure 2.9 IRAC-1 excess flux vs. IRAC-3 excess flux, in units of the expected photosphere at 5.8 μm. The flux ratios shown are consistent with black body emission at T ~1400 K. The lines shown correspond to black bodies at 1200, 400, and 1700 K.

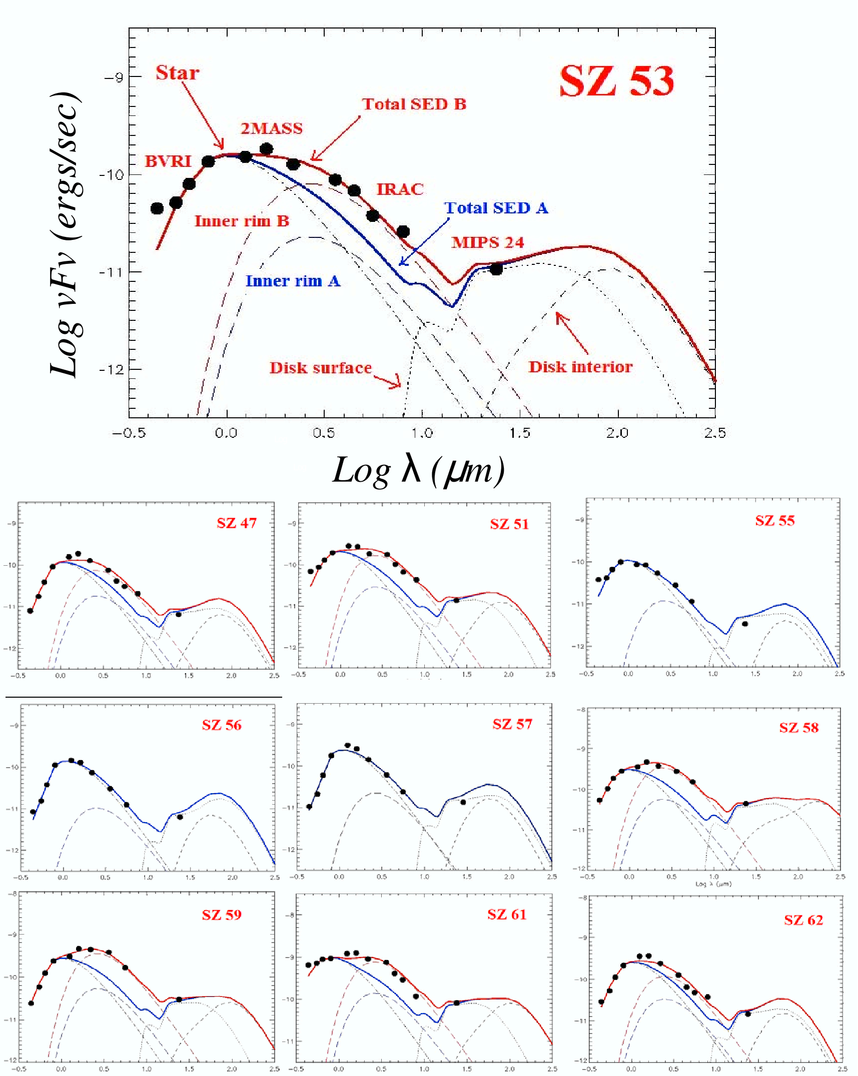

Figure 2.10 Disk models for 10 chamaeleon II cTTs. The solid blue line (Total SED A) corresponds to the total SED when the inner rim is irradiated only by the photosphere of the central star (rim A). The solid red line (Total SED B) corresponds to the total SED when the emission from the inner rim is scaled by the factor listed in Table 2.9 (rim B). According to the models, the near and mid-IR SED of the cTTs is largely dominated by the emission from the inner rim at the dust sublimation temperature T ∼ 1750 K. Also, in most cases, the area of the inner rim is larger than expected for a rim in thermal equilibrium with the stellar radiation field alone. Thus, an additional source of energy is needed. We argue that as proposed by DAlessio et al. (2003), the UV radiation from the accretion shock significantly affects the sizes of the inner holes in disks around cTTs increasing the area of the inner rim.

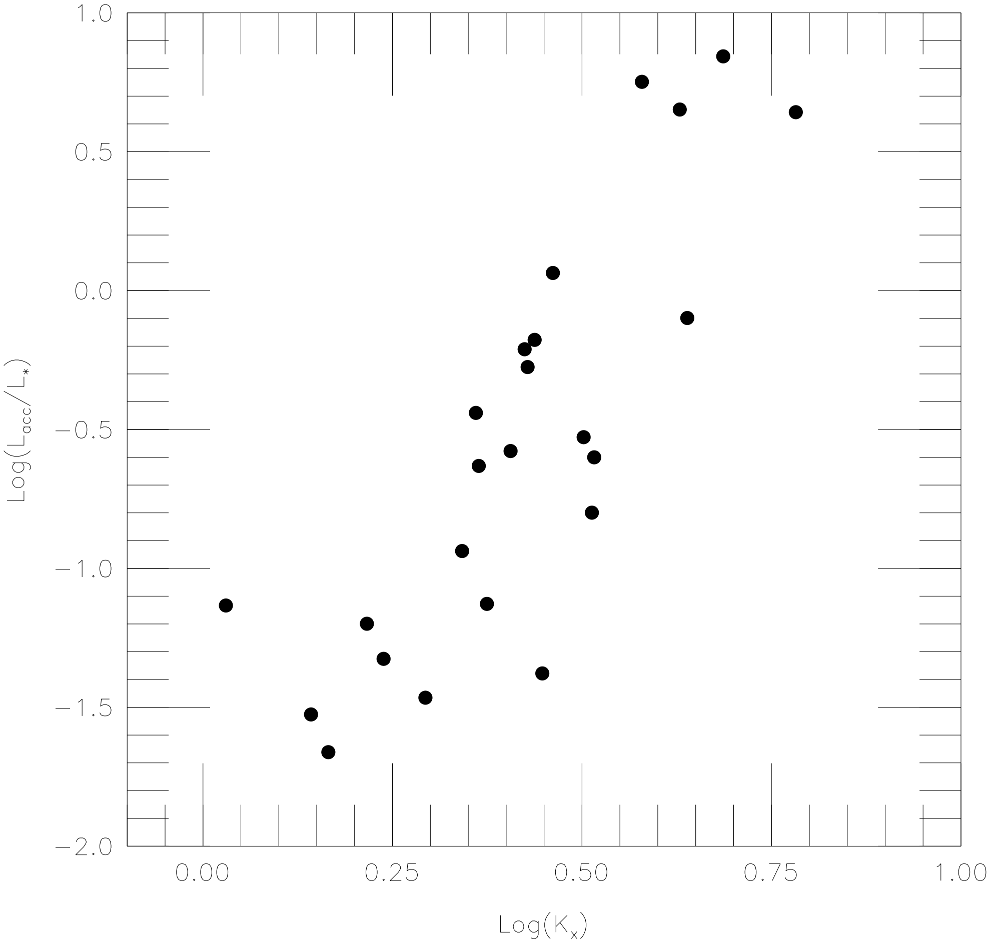

Figure 2.11 Accretion luminosity (L$_{acc}$) vs. K-band excess. The plot shows that K-band excess correlates well with accretion shock luminosity. The Spearmans rank of the correlation is 0.81 with a probability of being drawn from a random distribution of 1.01E-6. The figure also shows that, for some cTTs, the accretion luminosity can dominate the stellar luminosity.

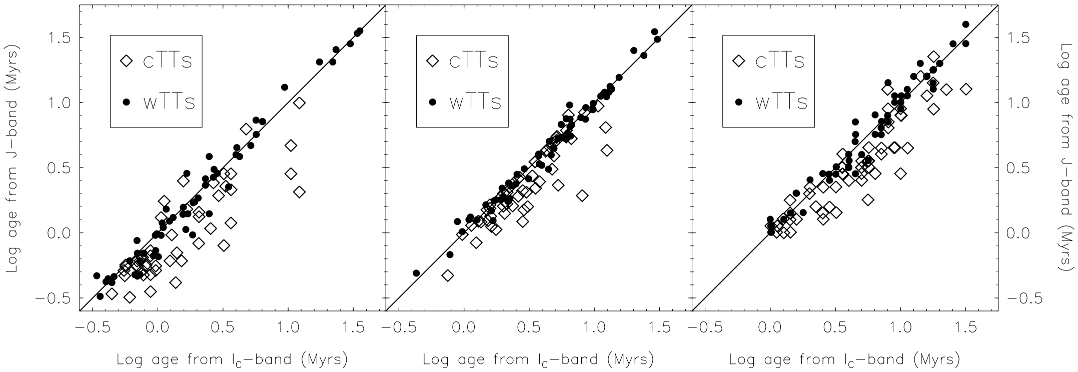

Figure 2.12 Stellar ages derived from J and I$_C$-band luminosities for 3 different sets of evolutionary tracks: D'Antona et al (1998) (a), Siess et al (2000) (b) and Beraffe et al. (1998) (c). In all cases, cTTs appear systematically younger when the luminosities are derived from the J-band with respect to ages obtained from the I$_C$-band luminosities. No systematic effect is seen on the derived ages of wTTs.

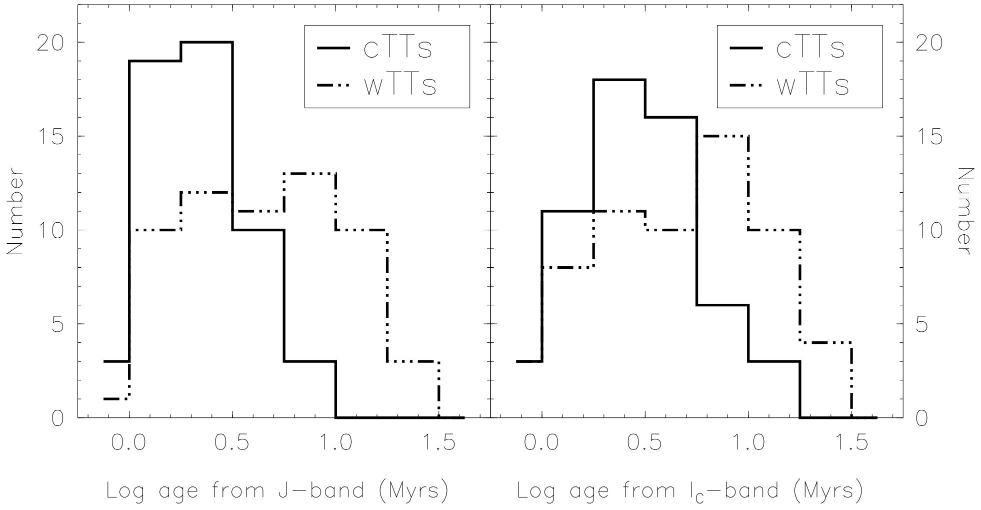

Figure 2.13 Age distribution of cTTs and wTTs when the ages are estimated from J-band luminosities (left panel) and when the ages are derived using I$_C$-band luminosities (right panel). The ages correspond to the models by Siess et al (2000).We suggest that, when J-band luminosities are used, the J-band excess artificially narrows the apparent age distribution of cTTs, and displaces its mean age to a younger value.

Chapter 3

The *Spitzer* c2d Survey of Weak-line T Tauri Stars II: New Constraints on the Timescale for Planet Building

3.1 Abstract

[1] One of the central goals of the *Spitzer* Legacy Project "From Molecular Cores to Planet-forming Disks" (c2d) is to determine the frequency of remnant circumstellar disks around weak-line T Tauri stars (wTTs) and to study the properties and evolutionary status of these disks. Here we present a census of disks for a sample of over 230 spectroscopically identified wTTs located in the c2d IRAC (3.6, 4.5, 4.8, and 8.0 μm) and MIPS (24 μm) maps of the Ophiuchus, Lupus, and Perseus

---

[1] based on Cieza, L., Padgett, D., Stapelfeldt, K., Augereau, J.C., Harvey, P., Evans, N, Merín, B., Koerner, D., Sargent, A., van Dishoeck, E., Allen, L., Blake, G., Brooke, T., Chapman, N., Huard, T., Lai, J.P., Mundy, L., Myers, P., Spiesman, W., Wahhaj, Z. 2007, in press, accepted by ApJ, astro-ph:/0706.0563

Molecular Clouds. We find that $\sim$20% of the wTTs in a magnitude limited subsample have noticeable IR-excesses at IRAC wavelengths indicating the presence of a circumstellar disk. The disk frequencies we find in these 3 regions are $\sim$3-6 times larger than that recently found for a sample of 83 relatively isolated wTTs located, for the most part, outside the highest extinction regions covered by the c2d IRAC and MIPS maps. This discrepancy in the disk fraction of these two different groups of wTTs (on cloud vs. off-cloud targets) supports the idea that samples of wTTs distributed *around* molecular clouds (nominally 1-10 Myrs old) represent a somewhat older population of stars. The disk fractions we find are more consistent with those obtained in recent *Spitzer* studies of wTTs in young clusters such as IC 348 and Tr 37. From their location in the H-R diagram, we find that, in our sample, the wTTs with excesses are among the younger part of the age distribution. Still, up to $\sim$50% of the apparently youngest stars in the sample show no evidence of IR excess, suggesting that the circumstellar disks of a sizable fraction of pre-main-sequence stars dissipate in a timescale of $\sim$1 Myr. We also find that none of the stars in our sample apparently older than $\sim$10 Myrs have detectable circumstellar disks at wavelengths $\leq$ 24 μm. Our result on the survival time of primordial disks is very similar to those obtained by studies based on K-band identified inner disks (r $<$ 0.1 AU). Also, we find that the wTTs disks in our sample exhibit a wide range of properties (SED morphology, inner radius, L_{DISK}/L_*, etc) which bridge the gaps observed between the cTTs and the debris disk regimes. This strongly suggests that wTTs disks are in fact the link between the massive primordial disks found around cTTs and the debris disks observed around main-sequence stars.

3.2 Introduction

Over the last couple of decades, it has been clearly established that circumstellar disks are an integral part of the star formation process. Even though there is currently no direct evidence that planets actually grow from circumstellar material, it has become increasingly clear that disks are potential birthplaces of planets because their masses, sizes, and compositions are consistent with those of the assumed pre-planetary solar nebulae (Hillenbrand 2003). More recently, the discovery of exo-planets orbiting nearby main sequence stars has confirmed that the formation of planets is a common process and not a rare phenomenon exclusive to the Solar System.

Direct detection of forming planets is well beyond our current capabilities and observing molecular hydrogen, which largely dominates the mass of primordial disks, is particularly challenging (Thi et al. 2001, Richter et al. 2002). However, the thermal emission from circumstellar dust is much easier to detect and study. For this reason, the study of the evolution of circumstellar dust has been a natural first step toward providing observational constraints on planet formation theories.

Strom et al. (1989) studied a sample of 83 classical T Tauri stars (cTTs) and weak-line T Tauri stars (wTTs) located in the Taurus-Auriga star-forming region in order to determine the fraction of objects with K-band (2.2 μm) and IRAS excesses indicating the presence of a circumstellar disk. WTTs are low-mass pre-main sequence stars that occupy the same region of the H–R diagram as cTTs but do not show clear evidence of accretion. The distinction between the two is usually made based on the $H\alpha$ equivalent width (EW). The H_α EW of cTTs is > 10 $\AA$, while the $H\alpha$ EW of wTTs is < 10 $\AA$. Since there is a very strong correlation between spectroscopic signatures of gas accretion and the presence of near-IR excess (Hartigan et al. 1995), most CTTS show near-IR excess while most wTTs lack such an excess. Strom et al. (1989) found that 60% of their stars younger than 3 Myrs showed a K-band excess, indicating the presence of a circumstellar disk, while only 10% of the stars older than 10 Myrs years did so. Based on these numbers, they estimated a disk dissipation timescale of $<$ 3-10 Myrs and claimed that their result was, at the time, “the best astrophysical constraint on the time available for planet building”. It has been argued that individual star-forming regions such as Taurus lack the intrinsic age spread necessary to investigate the dissipation timescale of circumstellar disks from individually derived ages (Hartmann 2001). However, similar disk lifetimes studies based on the disk frequency of clusters with different mean ages and extending to the 3.4 μm L-band (e.g. Haisch et al. 2001) have led to results similar to those presented by Strom and collaborators (see Hillenbrand (2006) for a review on the frequency of near-IR excesses based on a sample of $\sim$3000 PMS). The K-band excess, when used as a disk indicator, is only sensitive to dust in the innermost part of the disk; therefore, K-band studies only constrain the dissipation timescale of a region of the disks that is much closer to the star than the locations corresponding to the orbits of any of the planets in the Solar System (Mercury’s semi-major axis is 0.39 AU). The dissipation timescale of the dust in the planet-forming regions might or might not be the same. Since the dynamical timescale is shorter and the surface density is higher closer to the central star, circumstellar disks are expected to evolve from the inside out. Most wTTs, which by definition present little or no evidence for accretion, also show little or no near-IR excess (Hartigan et al. 1995). However, even after the inner accretion disk has dissipated, it is entirely possible that wTTs to still have enough material at larger radii to form terrestrial and giant planets. In fact, millimeter-wave observations show that at least 10 % of wTTs have disks with estimated masses in the 10^{-1}–10^{-3} $M_{\odot}$ range (Osterloh & Beckwith 1995, Andrews and Williams 2005).

While the existence of planets around a significant fraction of all MS stars has been verified (e.g., Marcy & Butler 1998), the fundamentals of the planet formation process still remain open questions, especially for giant planets. There are currently three main theories for the formation of giant planets: core accretion, gravitational instability, and hybrid models that combine aspects of both theories.

See Lissauer & Stevenson (2007) and Durisen et al. (2007) for two recent reviews of the core accretion and gravitational instability models and a discussion of the many upstanding questions.

Although it is unlikely that an observational estimate of the disk's dissipation timescale by itself can distinguish between the competing theoretical models mentioned above, estimates of the dissipation timescale of the planet forming regions can impose valuable constraints on current theoretical models. In order to probe the planet-forming regions of disks around pre-main sequence (PMS) stars, mid- and far-IR observations are required. Unfortunately, these spectral regions are not easily observable from the ground, and past space IR telescopes such as IRAS and ISO were only sensitive enough to detect very bright optically thick disks in low-mass stars at the distance of nearest star-forming regions. These instruments lacked the sensitivity needed to detect the modest IR-excesses expected for optically thin disks and faint optically thick disks. Thus, *Spitzer*'s sensitivity is required to establish whether most wTTs have optically thin disks, disks with inner holes, which are to cold to be detected in the near-IR from the ground, disks too faint to be detected by IRAS and ISO, or no disks at all. One of the main goals of the *Spitzer* Legacy Project "From Molecular Cores to Planet-forming Disks" (c2d; Evans et al. 2003) is to determine whether or not most wTTs have circumstellar disks and to characterize their properties and evolutionary status. Preliminary results from the c2d Legacy Project (Padgett et al. 2006, P06 hereafter) showed that disks are rare (∼6%) among the population of wTTs distributed *around* nearby molecular clouds. However, other recent *Spitzer* studies have reported significantly larger disk fractions (∼30%) among wTTs in young clusters such as IC 348 and Tr 37 (Lada et al. 2006; Sicilia-Aguilar et al 2006). Here we study a sample of over 230 spectroscopically identified wTTs located in the c2d IRAC and MIPS maps of the Lupus, Ophiuchus, and Perseus Molecular Clouds in order to investigate the frequency of circumstellar disks as a function of stellar age. In Section 3.3, we describe the c2d survey of molecular clouds and our sample of wTTs. In Section 3.4, we identify IR excesses and investigate the properties of their disks. In Section 3.5, we compare our results to previous *Spitzer* results and discuss the evolutionary status of wTTs disks. Also in Section 3.5, we derive the ages of the wTTs in our sample from their location in the H-R diagram. We investigate the disk frequency as a function of stellar age and use our results to impose constraints on the timescale for planet building. Finally, our conclusions are summarized in Section 3.6.

3.3 Observations

3.3.1 C2D large molecular clouds and GTO observations

As part of the c2d Legacy Project, *Spitzer* has mapped 13.0 sq. deg. of 3 nearby star-forming regions, Perseus, Ophiuchus, and Lupus, with IRAC (3.6, 4.5, 5.8, and 8.0 μm) and 22.1 sq. deg. with MIPS (24 μm). MIPS 70 and 160 μm observations were also taken, but due to sensitivity considerations, we do not include these observations in most of our analysis. The IRAC maps consist of two dithers of 10.4 sec observations, each obtained at two epochs (41.6 sec total) separated by several hours. The second epoch observations were taken in the High Dynamic Range mode, which includes 0.4 sec observations before the 10.4 sec exposures, allowing photometry of both bright and faint stars at the same time. MIPS observations were taken with the fast scan mode, also in two different epochs of 15 sec exposures each. See Jorgensen et al. (2006) and Young et al. (2005) for a detailed description of the observing strategy used for the c2d IRAC and MIPS survey of nearby molecular clouds.

In addition to the data from the c2d legacy project, we use observations of IC 348 taken as part of the IRAC and MIPS Guaranteed Time Observer (GTO) programs (Program ID 36 and 58, respectively). The IRAC GTO observations cover a $15' \times 15'$ field of view centered in the cluster and consists of two pairs of 8 dithers of 96.8 sec exposures for the 3.6, 4.5, and 5.8 μm observations (e.g. 1549 sec exposures per pixel). The 8.0 μm observations consist of four pairs of 8 dithers of 46.8 sec exposures [2]. The MIPS 24 μm GTO observations of IC 348 were taken in the medium scan mode resulting in an average exposure time of 80 seconds per pixel. For consistency, we processed the Basic Calibrated Data from the GTO programs and produced point source catalogs using the c2d pipeline (Evans et al. 2005). The c2d pipeline uses the c2d mosaicking/source extraction software c2dphot (Harvey et al. 2004), which is based on the mosaicking program APEX developed by the *Spitzer* Science Center, and the source extractor Dophot (Schechter et al. 1993).

Flux uncertainties in c2dphot are calculated in a standard way from a numerical estimate of the Hessian matrix (Press et al. 1992; Silvia 1996). This procedure for estimating uncertainties, although statistically correct, appears to underestimate the uncertainty as measured by the repeatability of flux measurements of the same objects at different epochs. For bright sources, there appears to be a random error floor to the best uncertainty possible with our observing techniques of 0.05 mag for the IRAC bands and 0.09 mag for the MIPS bands. The absolute calibration uncertainties are not included in our uncertainties. They are 5 and 10% for IRAC and MIPS, respectively (see data handbook for the instruments). As in most *Spitzer* surveys, the intrinsic sensitivity of the c2d observations is not uniform across the clouds due to variations in the total exposure time at different positions in the sky, in the amount of extended cloud emission, and in the source confusion level. Based on the cumulative fraction of all sources detected in both epochs of the c2d observations, the overall 90 % completeness levels of the c2d survey have been estimated to be 0.07, 0.12, 0.5, 0.4, and 1.0 mJy for 3.6, 4.5, 5.8, 8.0, and 24 μm. See Evans

---

[2] The longest integration time of the 8.0 μm array, nominally 100 secs, consists of 2 exposures of 46.8 sec each (See IRAC handbook, http://ssc.spitzer.caltech.edu/irac/dh/).

et al. (2005) for a detailed discussion of the uncertainties and sensitivity limits of the c2d survey.

The IRAC observations are sensitive enough to allow robust detections of stellar photospheres in all four IRAC bands for our entire sample of wTTs in Ophiuchus and Lupus (distance ∼125 pc and ∼150–200 pc, respectively) and in ∼85% of the objects in Perseus (distance ∼320 pc). MIPS 24 μm observations are not deep enough to reach the stellar photosphere of some low mass objects (especially in Perseus, which is the most distant cloud we consider), but, in general, they are deep enough to detect optically thick disks in our entire sample. The different completeness levels of our disk census due to sensitivity considerations are discussed in more detail in Section 3.4.1.

3.3.2 Sample Selection

The c2d maps contain several hundred young stars identified by their X-ray and $H\alpha$ brightness that have been spectroscopically classified as wTTs stars. Our sample was selected from the literature and is distributed as follows: 69 objects in Ophiuchus (Bouvier & Appenzeller 1992; Martin et al. 1998), 33 in Lupus (Hughes et al. 1994; Krautter et al. 1997), and 130 objects in Perseus (Luhman et al. 2003). The Lupus and Ophiuchus objects are distributed across the cloud maps, while the targets in Perseus are located exclusively in the IC 348 cluster. Of the 33 Lupus objects, 27 are located in the c2d maps of Lupus III and 6 lie within the c2d maps of Lupus I.

Spitzer SEDs of the wTTs in IC 348 have already been presented by Lada et al. (2006, L06 hereafter). We include these objects in our sample because they increase the statistical significance of our results and allow us to compare a clustered population to the more distributed population of stars in Lupus and Ophiuchus. Also, we adopt a different disk identification criterion than L06, which results in a lower disk fraction than that obtained by the Lada group (see Section 3.5.1).

Furthermore, L06 adopt a single age (2-3 Myrs) for the stars in the IC 348 cluster and do not attempt to study the disk fraction as function of age, which is one of the main goals of our paper.

All the objects in our sample, which are listed in Table 3.1, have known spectral types and small $H\alpha$ EWs. The spectral types are necessary to estimate stellar ages from the position of the targets in the H-R diagram and the contribution of the stellar photospheres to the observed SEDs, while the $H\alpha$ EWs are required to establish wTTs status. The nominal division between cTTs and wTTs is $H\alpha$ EW = 10 $\AA$; however, since the $H\alpha$ EW due to chromospheric activity alone can reach this value for late M stars (e.g., Martin 1997), we have included in our study 18 M2-M7 stars ($<$ 8 % of our sample) with $H\alpha$ EW up to 15 $\AA$. Also, ~8% of the stars in our sample show $H\alpha$ in absorption rather than in emission.

We note that even though there is a strong correlation between Hα emission and other accretion signatures such as optical veiling, a single-epoch low-resolution measurement of Hα equivalent width is not enough to rule out active accretion for at least two reasons. First, even when a narrow range of spectral types is considered, the distribution of Hα EWs of T Tauri stars does not show a clear gap between accreting and not accreting objects (e.g., the $H\alpha$ EWs of weakly accreting PMS overlap with those of chromospherically active non-accreting stars). Second, accretion itself is a highly variable process and some objects constantly move across the wTTs–cTTs Hα EW boundary. Therefore, we consider our sample to be composed of mostly non-accreting objects but do not rule out the presence of actively accreting interlopers.

3.3.3 Complementary data

In order to construct more complete SEDs of our wTTs, we have collected the 2MASS photometry for our entire sample and the V, R_C, I_C-band photometry reported by Hughes et al. (1994) and Wichmann et al. (1997) for 24 of our 33 Lupus objects. Also we have obtained our own V$R_C I_C$ optical observations for 52 of our 69 Ophiuchus targets and R$_C$ and I$_C$-band observations for 115 of the 130 objects in IC 348 with the 0.8 m telescope at McDonald Observatory. The Ophiuchus targets were observed in 7 different $46.\!'2$ x $46.\!'2$ fields of view during the photometric nights of June 20^{th}-21^{st} 2005 with exposures times of 30, 50, and 100 seconds for the V, R_C, and I_C-band respectively. The objects in IC 348 were observed in a single field of view with 200 and 150 second exposures in the R$_C$ and I_C-band, respectively. In addition to the program stars, on each night, 3 fields of Landolt standards (∼5 standards per field) were observed at different airmasses. The seeing ranged from $1.5''$ to $2''$ when the observations were made. We reduced the data and perform aperture photometry using the standard IRAF packages CCDRED and DAOPHOT. We used a $5.4''$ (4-pixel) aperture and a sky annulus with inner and outer radii of $16.2''$ and $22.95''$ respectively.

The rms scatter of the photometric solutions applied to the programs stars was < 0.02 mag in all three filters. We adopt a conservative *minimum* photometric error of 0.03 mag. We report the magnitudes and the uncertainties for all the objects with estimated photometric error less than ∼0.2 mag. The *Spitzer* photometry for our entire sample is listed in Table 3.1. The non-*Spitzer* data: optical and 2MASS photometry, along with the spectral types and H$_\alpha$ equivalent widths from the literature, is listed in Table 3.2.

3.4 Results

3.4.1 Disk Identification

In order to identify the stars with disks, we compare the extinction-corrected *Spitzer* colors of our targets, to those predicted by NextGen Models (Hauschildt et al.

1999), convolved with the *Spitzer* bandpasses, for the photospheres of stars of the corresponding spectral types. The broader the wavelength baseline of the color used, the larger is the expected excess of the stars with disks; therefore, the available color that provides the most clear disk identification is [3.6]–[24]. However, since both *Spitzer's* sensitivity and the photospheric fluxes decrease with increasing wavelength, not all sources are detected at wavelengths longer than 5.8 μm.

In Figure 3.1a, we plot [3.6] vs EX([3.6]–[24]), for the 98 stars with 3.6 and 24 μm fluxes available, where EX([3.6]–[24]) is ([3.6]–[24])$_{OBSo}$-([3.6]–[24])$_{Model}$, ([3.6]–[24])$_{OBSo}$ are the observed colors corrected for extinction, and ([3.6]–[24])$_{Model}$ are the photospheric colors predicted by the NextGen Models. We estimate the extinction, A_V, using $A_V = 4.76 \times E(R-I) = 4.76 \times ((R_C - I_C)_{OBS} - (R_C - I_C)_O)$. The intrinsic stellar colors, (R$_C$-I$_C$)o, come from Kenyon & Hartmann (1995). For objects without R$_C$ and I$_C$ fluxes available, we use A_V=5.88×E(J-K$_S$). We note that this will result in an overestimated extinction for objects with significant K-band excess. The extinction at 8 and 24 μm are calculated according to Table 3.3.

We consider objects with [3.6]–[24] $<$ 0.7 to be those without excess whose emission arises solely from the stellar photosphere. The mean EX([3.6]–[24]) value for this group is not zero but 0.07 mag with a 1-σ dispersion of 0.17 mag. The 0.07 mag offset of the observed stellar photospheres with respect to the models is probably due to a combination of the systematic errors in the absolute flux calibrations, the stellar models, and the extinction corrections. In Figure 3.1a, we treat this offset by subtracting 0.07 mag from all the EX([3.6]–[24]) values. We find that 40 objects have a [3.6]–[24] excesses larger than 5-σ. These are very robust disk identifications. One object, RXJ1622.6-2345, has [3.6]–[24] excess just over 3-σ. We consider this object to be a good disk candidate, but warn the reader of its lower significance. Since the c2d MIPS maps cover a larger area than the IRAC maps, 24 μm is the only *Spitzer* flux available for 5 stars in our sample. In these cases, we use [K]–[24] colors for disk identification. None of the 5 objects for which MIPS 24 μm is the only available *Spitzer* flux show a significant K–24 μm excess. Of the 127 stars without measured [3.6]–[24] or [K]–[24] colors, 112 have [3.6]–[8.0] colors available. Figure 3.1b is analogous to Figure 3.1a, but here we plot [3.6] vs EX([3.6]–[8.0]) for all the stars with measured [3.6]–[8.0] colors, including the ones from Figure 3.1a, which are shown as open diamonds. Following Cieza & Baliber (2006), objects with [3.6]–[8.0] < 0.7 are considered stellar photospheres. In this case, the mean color offset with respect to the models is 0.05 mag. The standard deviation of the stellar photospheres is 0.16 mag, but the error clearly increases with decreasing brightness. We find that only 6 objects not detected at 24 μm show a clear evidence ($>$ 5-σ) for 8 μm excess. Two objects, IC348-76 and IC348-67, show excesses between 3 and 5-σ. Since the SEDs of these two objects show a hint of IR-excess at 4.5 and 5.8 μm, we consider these two objects to be good disk candidates. We find that none of the 15 objects without [3.6]–[24], [K$_S$]–[24], or [3.6]–[8.0] colors available shows a significant [3.6]–[5.8] excess.

The SEDs of the wTTs disks in Lupus, Ophiuchus, and IC 348 are shown in Figures 3.2, 3.3, and 3.4, respectively. The open squares represent the observed optical, 2MASS, IRAC and MIPS-24 μm fluxes, while the dots correspond to the extinction corrected values. The A$_V$'s are estimated as described above for Figure 3.1, while the extinctions at other wavelengths are calculated according to Table 3.3. NextGen model photospheres, corresponding to published spectral types and normalized to the extinction-corrected J-band, are shown for comparison.

Disk Census Completeness

Following the procedure described above, we identify a total of 46 wTTs disks and 3 disk candidates. For definiteness, we consider these 3 disk candidates to be real in the rest of the paper. However, we note that the completeness of our disk census is lower for our IC 348 sample than it is for the sample of Lupus and Ophiuchus wTTs.

The IRAC observations are sensitive enough to allow robust detections of stellar photospheres in all four IRAC bands for wTTs in the sample from Lupus and Ophiuchus (102 objects in total). Also, the 5 objects in Lupus and Ophiuchus that fall outside the c2d IRAC maps all have 24 μm fluxes consistent with stellar photospheres, which rules out the presence of any significant IRAC excess in these objects. Therefore, the census of IRAC excesses in our sample of Lupus and Ophiuchus wTTs is likely to be complete (i.e. only 17 out of the 102 wTTs in Lupus and Ophiuchus have significant IRAC excesses). At 24 μm, we detect [3] 80% (82/102) of the Lupus and Ophiuchus objects. Thus, it is possible that some of the 20 wTTs from the Lupus and Ophiuchus sample that are not detected at 24 μm have SEDs that start to diverge from their photospheres longward of 8.0 μm but remain bellow our sensitivity at 24 μm.

We find that all the objects with IRAC excess are detected at 24 μm, and that only 2 of the 82 objects detected at 24 μm have excesses that only become evident at this wavelength. However, some of these 14 wTTs could have SEDs that start to diverge from their photospheres longward of 8.0 μm but remain bellow our sensitivity at 24 μm.

In our IC 348 sample, 11% (14/130) of the objects are not detected at 8.0 μm and 82 % (107/130) are not detected at 24 μm. The longer integration times of the GTO IRAC observations of IC 348 with respect to the c2d observation of Lupus and Ophiuchus (1548 vs. 46.8 secs) more than compensates the effect of the distance (320 vs. 125–200 pc) on the expected sensitivities. However, the high background

---

[3] by detect we mean that the flux of the object has been measured regardless of whether or not the star has an excess. All the objects have been observed at 24 μm;therefore, a non detection implies that the flux of the object is below our 24 μm sensitivity limit.

of the IC 348 cluster becomes the limiting factor for the detection of faint sources at 8.0 μm. At 24 μm, the depth of the GTO observations only partially compensates for the greater distance of IC 348, and the effect of the background becomes even larger than it is at 8.0 μm. The combination of these two factors explains the very low detection rate of IC 348 members at 24 μm. None of the 14 objects without a 8.0 or 24 μm*detection* shows a significant 5.8 μm excess that would indicate the presence of a circumstellar disks. However, some of these 14 wTTs could have SEDs that start to diverge from their photospheres longward of 5.8 μm but remain bellow our sensitivity at 8.0 and 24 μm. Finally, we find that 91% (21/23) of the objects detected at 24 μm also show significant IRAC excesses, which is consistent with the results for Lupus and Ophiuchus. Obviously, in IC 348, we are likely to have missed most of the stars for which the onset of the IR-excess occurs longward of 8.0 μm.

Disk fraction statistics

In section 3.4.1 we tried to present a disk census as complete as possible given the available data. However, since the sensitivity of our disk survey is not uniform across all wavelengths and varies from region to region due to distance and background level effects, we derive disk fraction statistics from the number of objects with excess at IRAC wavelengths (IRAC disk fraction, hereafter) in a magnitude limited subsamples that is not likely to be affected by sensitivity variations.

As discussed in the previous section, we consider our census of IRAC excesses in our sample of Lupus and Ophiuchus wTTs to be complete. Excluding the disks that are only detected longward of 10 μm (ROXs 36, and RX J1622.6-2345), we derive the following IRAC disk fractions: 27%±7% (9/33) for Lupus, 13%±4% (9/69) for Ophiuchus. For IC 348, we restrict our sample to the 96 objects with 3.6 μm fluxes greater than 3.2 mJy, a level above which we also detect at 8.0 μm every object in our sample. We find that 22 of these 96 objects show significant

IRAC excess, which leads to a disk fraction of 23±4%. Combining the objects in Lupus, Ophuichus, and IC 348, we derive an overall IRAC disk fraction of 20±3% (40/198). The IRAC disk fractions of wTTs in Lupus and Ophiuchus bracket that of the IC 348 cluster. This suggest that the disk fraction in IC 348 wTTs targets is not strongly affected by the cluster environment.

At 24 μm, the sensitivity of our survey is significantly less uniform than at IRAC wavelengths. We find that even some of our brightest objects lack 24 μm detections due to the strong background emission surrounding them. This prevent us from deriving robust MIPS disk fractions statistics even from a magnitude limited sample.

3.4.2 Disk Properties

Selected Color-Color Diagrams

In this section, we place our sample of wTTs in *Spitzer* color-color diagrams as our first attempt to explore the diversity of wTTs disks. For comparison, we also include in these diagrams two samples of 83 and 66 cTTs from Taurus and IC 348, respectively. We used the Hα EW from Luhman et al. (2003) to select the sample of cTTs in IC 348. For these objects we use our own photometry. The *Spitzer* fluxes of the Taurus cTTs come from Hartmann et al. (2005). In Figures 3.7 and 3.8, we show an A_V=10 extinction vector based on Table 3.3; however, we note that for most of the stars in our sample the extinction is *significantly* smaller. The mean A_V we derive for our Lupus, Ophiuchus, and IC 348 wTTs samples are 0.64, 2.7, and 1.7 mag respectively. Also, 93% of our sample has A_V < 5 mag, and the remaining 7 % has 10 mag < A_V < 5 mag.

Figure 3.7a shows the [3.6]–[24] vs. [3.6]–[8.0] colors of our sample of wTTs stars. Based on the colors shown, we identify three different groups. The first group consists of objects with [3.6]–[24] < 0.7 and [3.6]–[8.0] < 0.4, which are consistent with bare stellar photospheres. The second group consists of stars with [3.6]–[24] > 0.7 and [3.6]–[8.0] < 0.4 (i.e. their SEDs start to diverge from their stellar photospheres longward of 8.0 μm). The 4 stars in this group are RXJ1622.6-2345, ROXs 36, IC348-56, and IC348-124. In Section 3.4.2, we find that the objects in this second group have the lowest fractional disk luminosities of the sample. In fact, all four objects have $L_{DISK}/L_{*} < 10^{-3}$, which suggest the presence of optically thin disks. The last group of objects has [3.6]–[24] > 0.7 and [3.6]–[24] > 0.4 (i.e. they show excess at both IRAC and MIPS wavelengths). Most of these objects are likely to be optically thick disks. Figure 3.7b shows our sample of wTTs combined with the sample of cTTs. We note that the cTTs populate exclusively the region of the diagram we associate with optically thick disks and that both wTTs and cTTs populations are very well mixed in this region of the diagram.

In Figure 3.8a, we show the [3.6]–[4.5] vs. [5.8]–[8.0] colors of wTTs. In general, the populations of stars with and without an excess are clearly separated. Stars in the upper right corner of the diagram have both 4.5 and 8.0 μm excesses. Stars in the lower right corner of the diagram are stars with 8.0 μm excess but no 4.5 μm excess. These objects are usually interpreted as "transition disks" with inner holes (e.g. Calvet et al. 2002; D'Alessio et al. 2005). In fact, Sicilia-Aguilar et al. (2006) define transition disks as objects with 8.0 μm excess but no 4.5 μm excess. They find that only ∼10% of the T Tauri disks in the 4-Myrs old cluster Tr 37 fall into this category. In contrast, we find that ∼30 % of the wTTs are in fact "transition disks" according the working definition stated above. This is in good agreement with the idea that wTTs disks represent a more evolved evolutionary state than cTTs disks. In Figure 3.8b, we combine wTTs and cTTs in the same color-color diagram.

$EW(H_\alpha)$ dependence?

Since the distinction between cTTs and wTTs is based on the H_α EW, and cTTs show a much higher disk fraction than wTTs, we investigate the dependence of the IRAC disk fraction on $H\alpha$ EW within our sample of wTTs. We restrict our analysis to the 198 objects in the magnitude limited subsample discussed in Section 3.4.1. Figure 3.9a shows a histogram of the $H\alpha$ EW of stars with and without a disk, while Figure 3.9b shows the disk fraction vs. $H\alpha$ EW. We find that (1) the disk fraction is highly correlated with $H\alpha$, and (2) the disk fraction is a smooth function of $H\alpha$ EW, increasing from ∼5% for the stars with $H\alpha$ observed in absorption to >50 % for the stars with 15 $\mathring{A} > H\alpha$ EW > 10 $\mathring{A}$.

Since a strong correlation between the presence of a disk and Hα emission of chromospheric origin would be difficult the explain, the correlation observed in Figure 3.9 is likely to be driven by the presence of weakly accreting stars in our sample of wTTs. Muli-epoch high-resolution spectroscopy of the sample of wTTs with disks would be highly desirable to establish, from their Hα velocity profiles, which objects are in fact actively accreting (White & Basri 2003).

Disk fraction dependence on spectral type?

Lada et al. (2006) find that the "optically thick" disk fraction in the entire populations of PMS stars (cTTs/wTTs) in IC 348 seems to be a function of spectral type. They argue that the disk fraction peaks around K6–M2 stars, which at the age of the cluster corresponds to stars with masses similar to that of the Sun, and conclude that circumstellar disks might last longer around solar type stars than around both less and more massive stars. Similarly, Carpenter et al. (2006) studied a sample of over 200 PMS star in the 5 Myrs old Upper Scorpius OB association with masses between ∼0.1 and 20 $M_\odot$ and found that stars with K-M spectral types have a significantly larger disk fraction than stars with G-A spectral types.

In order to investigate the possibility of a disk fraction dependence on spectral type for wTTs, we restrict our analysis to the 198 objects in the magnitude limited subsample discussed in Section 3.4.1 and divide our sample into the same 3 spectral types bins studied by Lada et al. (2006). We find the following IRAC disk fractions for the 3 bins: 28%±7% (12/42) for stars with spectral types K6 and earlier, 16%±5% (10/62) for K7–M2 stars, and 19%±4% (18/94) for M2–M6 stars. Our result is inconsistent with a disk fraction of wTTs peaking around K6-M2 stars and suggests that the disk fraction dependence on spectral type found by Lada et al. 2006, if real, is likely to be driven by the cTTs population, which would imply that the duration of the *accretion phase* is a function of spectral type. Given the very different mass range of our sample, our result does not contradict those presented by Carpenter et al. (2006).

Fractional Disk Luminosity

The ratio of the disk luminosity to the stellar luminosity, L_{DISK}/L_{*}, is a measurement of the fraction of the star's radiation that is intercepted and re-emitted by the disk plus any accretion luminosity. This quantity is intimately related to the evolutionary status of a circumstellar disk. On the one hand, the primordial, gas rich, disks around cTTs have typical L_{DISK}/L_{*} values $> 10 - 20\%$. On the other hand, L_{DISK}/L_{*} values for optically thin, gas poor, debris disks around MS stars range from 10^{-3} to 10^{-6} (Beichman et al. 2005). In order to characterize L_{DISK}/L_{*} for wTTs disks, we estimate this quantity for all the wTTs disks in our sample except for the few disks in IC 348 for which 24 μm fluxes are not available. These objects are below our 24 μm sensitivity limits, and the disk luminosities obtained from the IRAC excesses alone would be highly uncertain.

We estimate the disk luminosity according to the following procedure. We first calculate the IR-excess at IRAC wavelengths and at 24 μm by subtracting from the observed fluxes the expected photospheric contributions predicted by the stellar models shown in Figures 3.2, 3.3, and 3.4. Then, the IR-excess at 24 μm is extrapolated to longer wavelengths assuming the emission of a black body peaking at 24 μm (i.e., T = 121 K) and diluted by an emissivity proportional to λ^{-1}. Also, the IR emission of the shortest *significant* IRAC excess is extrapolated to shorter wavelengths assuming black body emission. The temperature of the adopted black bodies ranges from 1400 to 500 K depending on the IRAC band from which the IR-excess is extrapolated. Finally, we calculate the total disk luminosities by integrating the observed and extrapolated IR-excesses over frequency. Similarly, the stellar luminosities are calculated by integrating the fluxes of the stellar models shown in Figures 3.2, 3.3, and 3.4 over frequency. The distribution of L_{DISK}/L_* for our sample of wTTs is shown in Figure 3.10. The L_{DISK}/L_* values calculated using the same procedure for a sample of cTTs (From Cieza et al. 2005) and debris disks (from Chen et al. 2005) are shown for comparison. The L_{DISK}/L_* values we derive for our sample should be considered lower limits because our assumption that the flux density peaks at 24 μm may underestimate the flux contribution of cool material in the outer disk. However, since none of our disks are detected at 70 μm, we can constrain the flux contribution of the outer disks that may be missing in our disk luminosity estimates. For each object, we approximate the outer disk as a diluted black body peaking at 70 μm (i.e., T = 41 K) with a flux density equal to 45 mJy, the estimated 3-σ limits of the c2d observations at 70 μm (Evans et al. 2005). For objects in Lupus and Ophiuchus, this approach constrains the luminosities of the outer disks to the 10^{-5}–10^{-4} L_* range. For objects in IC 348, this range is 10^{-3}–10^{-4} L_*. Thus, we conclude that, for objects with warm disks for which we derive $L_{DISK}/L_* > 10^{-3}$, the flux contribution of the outer disks is a small fraction of the total disk luminosity. For the objects we derive L_{DISK}/L_* $< 10^{-3}$, the contribution of an unseen outer disk could, in principle, dominate the total disk luminosity. However, the disk luminosities of such cold disks would still remain in the debris disk range.

Figure 3.10 shows that only one object, Sz 96, has a L_{DISK}/L_* value characteristic of cTTs. This object is a M2 border line cTTs/wTTs with a $H\alpha$ EW of 11 $\AA$. As shown in Figure 3.2, the SED of Sz 96 shows strong IR-excess at 2MASS wavelengths and is indistinguishable from that of a cTTs. This object is likely to be one of the actively accreting interlopers discussed in Sections 3.3.2 and 3.4.2. Similarly, only 4 objects have $10^{-3} > L_{DISK}/L_* > 10^{-6}$, the range characteristic of optically thin debris disks. However, we note that the low luminosity and low optical depth of a disk do not necessarily warrant debris disk status, which requires the presence of second generation of dust produced by the collision of planetesimals in a gas poor environment. The lowest luminosity, and presumably optically thin, disks in our sample are RXJ1622.6-2345, ROXs 36, IC348-56, and IC348-124. We model the SEDs of these disks in Section 3.5.3. If these objects are in fact debris disks, at an age of ∼1–3 Myrs, they could be some of the youngest debris disks observed to date. However, the confirmation of debris disk status would require information on the grain size distribution and gas content of their disks. The main conclusion that can be drawn from Figure 3.10 is that the bulk of the wTTs disks have L_{DISK}/L_* values that bridge the gap between the cTTs and the debris disk range. This supports the idea that wTTs disks represent an intermediate evolutionary stage linking primordial disks around cTTs and debris disks around MS stars.

3.5 Discussion

3.5.1 Comparison to recent Spitzer results

Comparison to Padgett et al. 2006

The IRAC disk fractions we found in Section 3.4.1 are ∼3–6 times larger than those recently found for a sample of 83 relatively isolated wTTs (Padgett et al. 2006, P06 hereafter). P06 find that 3 of their objects show IR-excess both at IRAC and MIPS wavelengths, while 2 objects show IRAC fluxes consistent with photospheric emission and small excesses at 24 μm. Most of these stars in the P06 sample are members of the extended population of Li rich wTTs discovered by the ROSAT X-ray satellite around nearby molecular clouds and are, for the most part, located outside the high extinction regions mapped by the c2d project, but within ∼6 degrees of the centers of the c2d cloud maps.The P06 observations were sensitive to the stellar photospheres of the entire sample at both IRAC wavelengths and 24 μm. Given the size of the samples involved, the discrepancy in the IRAC disk fraction of the off-cloud wTTs studied by P06, 4±2%, and that of the on-cloud wTTs studied in this paper, 20±3%, is significant at the 4-σ level.

Follow up spectroscopic studies of ROSAT targets (e.g. Covino et al. 1997; Martin et al. 1999; Wichmann et al. 2000) used the strength of the Li I 6707 absorption line to discriminate bona-fide PMS from young active MS stars (possibly ∼100 Myrs old) sharing the same X-ray properties. P06 selected their sample from ROSAT wTTs with Li I 6707 absorption lines stronger than that of a Pleiades star of the same spectral type. These objects were suspected to be 1–10 Myr-old because the age distribution of the ROSAT wTTs, derived from their position in the H-R diagram, is not significantly different from that derived for the on-cloud TT Tauri stars (Alcala et al. 1997; see also Section 3.5.4 of this paper). This age estimate assumes that the ROSAT sources are located at the same distances as their adjacent molecular clouds. However, the distance and pre-main sequence status of the extended population of ROSAT sources has been called into question. Feigelson (1996) and Briceno et al. (1997) argue that the distributed population of ROSAT sources consist of mostly foreground post-T Tauri and active young ($\sim$100 Myrs old) MS stars which are not necessarily associated with regions of current star formation (i.e. they are old enough to have moved far away from their birth sites) and that the presence of Li I 6707 does not warrant PMS status since it is highly dependent on stellar mass, convection, and angular momentum history. The low disk fraction of the distributed population of ROSAT sources studied by P06 with respect to that of the sample of on-cloud wTTs studied here supports the idea that the ROSAT sources found *around* molecular clouds represent a significantly older population of stars than that of the $<$ 1-10 Myrs old cTTs and wTTs found *within* molecular clouds. The age estimate of the extended population of Li rich ROSAT sources depends on whether or not the P06/ROSAT targets are at the same distances as their adjacent molecular clouds. The luminosities of stars closer to us than the molecular clouds themselves could be considerably overestimated, translating into underestimated ages when the stars are placed in the H-R diagram. If the P06 sources are in fact associated with the molecular cloud and the sample has been biased toward foreground stars, the wTTS in P06 sample could be somewhat older than their nominal age of 1–10 Myr. It is reasonable to assume that such a bias toward foreground objects exists because P06 favored bright objects when selecting their sample in order to increase the number of wTTs that could be observed at a given sensitivity. If the P06 sources are not associated with their adjacent molecular clouds, then the only age constraints are Li I 6707 EW and X-ray brightness, and ages of the order of 100 Myrs could not be ruled out.

Comparison to Lada et al. 2006

In a recent study of ∼300 confirmed members of IC 348 (wTTs and cTTs) Lada et al. (2006, L06 hereafter) find an IRAC disk fraction of ∼35% among IC 348 members classified as wTTs. The sample of wTTs studied by L06 is virtually the same sample of IC 348 wTTs included in this paper, for which we derive a disk fraction of $23\% \pm 4\%$. In what follows, we attempt to account for the difference in these results. L06 use a disk identification criterion based on the slope, α, of a power law fit to the four IRAC bands. From the comparison to disk models, they identify objects with $\alpha > -1.8$ as optically thick disks. Based on the predicted slope of an M0 star and the typical uncertainty in the power law fit, they identify objects with $\alpha < -2.56$ as stellar photospheres and objects with intermediate slopes, $-2.56 > \alpha > -1.8$. as "anemic disks". Cieza & Baliber (2006) suggest that many of the objects identified as "anemic disks" by the L06 are more consistent with stellar photosphere of late M stars than with circumstellar disks. Based on a large sample (> 400) of cTTs and wTTs from the literature with photometric uncertainties smaller than 0.1 mag, Cieza & Baliber (2006) find that cTTs and wTTs disks occupy a well defined locus in the [3.6]–[8.0] vs [3.6]–[5.8] diagram with [3.6]–[8.0] > 0.7, while bare stellar photospheres have [3.6]–[8.0] < 0.5. In fact, only ∼1 % of the their sample have 0.7 > [3.6]–[8.0] > 0.5. As seen in Figure 8, faint objects in IC 348, most of which are M4–M7 stars, have very uncertain [3.6]–[8.0] colors.

We suggest the possibility that the combined effect of slightly redder stellar photospheres and larger photometric uncertainties in late M stars with respect to brighter stars with earlier spectral types resulted in a large fraction of M4–M7 stellar photospheres being classified as "anemic" disks by L06. L06 find that the ratio of "anemic" disks to optically thick disks increases from ∼1/5 to ∼1/1 from K6–M2 to M2–M6 stars, which is consistent with the idea that some of the anemic disks around late type stars may be of questionable significance.

We find that most of the wTTs below [3.6]–[8.0] = 0.7 (the disk identification boundary suggested by Cieza & Baliber 2006) that are classified as "anemic" disks by L06 are objects with spectral types M5 or later, which tend to have very uncertain IRAC colors due to the strong IR background of the IC 348 cluster. These low-mass objects account for the difference in the disk fraction derived by us and L06 for the wTTs in IC 348.

In Table 3.4 we list the 18 objects classified as anemic disks by L06 that do not satisfy our disk identification criterion discussed in Section 3.4.1. We find that, for objects in Table 3.4, the [3.6]–[8.0] colors obtained by L06 are ~0.15 mag redder in the mean than our colors. However, this is a selection effect due to the fact that we are only considering the objects that have [3.6]–[8.0] colors from L06 that are red enough to be classified as anemic disks. In fact, when the entire sample of IC 348 wTTs is considered, our photometry gives [3.6]–[8.0] colors that are ~0.05 mag *redder* than those obtained by L06. We note that even using the colors from L06, only one of the objects satisfies [3.6]–[8.0] > 0.7, the disk identification criterion proposed by Cieza & Baliber (2006). Also, for 12 of the 18 objects listed in Table 3.4, L06 derive α's that are consistent with the expected stellar photosphere within the errors (i.e. $(\alpha+2.66)/\sigma_\alpha < 3$, where -2.66 is the slope of an M0 photosphere adopted by L06). Finally, two of the objects for which $(\alpha+2.66)/\sigma_\alpha > 3$ have no 8.0 μm fluxes measured by us or by L06, which renders the disk identification less reliable. We conclude that an accurate identification of weak IRAC excesses requires careful consideration of the photometric uncertainties involved, especially in regions with strong extended emission such as the IC 348 cluster.

3.5.2 The diversity and evolutionary status of wTTs disks

For late type stars, the IRAC and MIPS fluxes originate from the inner ~20 AU of the disk. For this reason, observations at these wavelengths are especially suited to study the evolution of the planet-forming region of the disk. According to models of the evolution of circumstellar disks, dust growth and settling take place very efficiently in the circumstellar disks soon after their formation (Weidenschilling 1997, Dullemond & Dominik 2005). Numerical models also predict that the growth of dust will reduce the opacity of the disk to the stellar radiation causing the disk to become flatter and the excesses in the mid infrared to decrease with time proceeding from the shortest to the longest wavelengths. There is mounting evidence of such phenomena in the IRAC colors of T Tauri stars and lower mass objects (D'Alessio et al. 2001, Furlan et al. 2005, Sicilia-Aguilar et al. 2005, Muzerolle et al. 2006).

In this section, we try to explore observational consequences that could be related to dust grain growth and/or settling toward the mid-plane for the sample of wTTs with disks. To this end, we estimate the longest wavelength *without* significant infrared excess from the dereddened SEDs, $\lambda_{\rm turn-off}$ (in μm), and the slope of the SED longward of $\lambda_{\rm turn-off}$, $\alpha_{\rm excess}$ for all the wTTs stars with disks in the sample. We compare these values for our sample of wTTs to those we obtain for a sample of cTTs in Chamaeleon from Cieza et al. (2005) and a sample of debris disks from Chen et al. (2005). Figure 3.11 shows the ranges of mid-IR slopes $\alpha_{\rm excess}$ versus the wavelength of disk emission turn off $\lambda_{\rm turn-off}$. Systems with $\lambda_{\rm turn-off} \leq 2.0$ μm show some excess in the near-IR JHK bands and are probably actively accreting (see e.g. Hartmann et al. 2005 and Muzerolle et al. 2003). Objects with $\lambda_{\rm turn-off}$ in the IRAC range are likely to be purely irradiated disks with increasing degree of settling and/or larger inner holes with increasing $\lambda_{\rm turn-off}$. Finally, those stars with $\lambda_{\rm turn-off} \geq 8.0$ μm are likely to have cleared inner disks with radii of several AU (e.g. Calvet et al. 2002) or alternatively have dust in the inner disk which has grown to sizes large enough not to produce any detectable excess above the photospheric level.

A simple disk evolution scenario based solely on dust grain growth and settling predicts smaller $\alpha_{\rm excess}$ slopes for longer $\lambda_{\rm turn-off}$ or larger cleared inner regions (Dullemond & Dominik 2005, D'Alessio et al. 2005). However, Figure 3.11 suggests that the *range of possible excess slopes increases with the process of inner disk clearing.* The actively-accreting cTTs stars all cluster around $\alpha_{\rm excess}$ values of -1. For these objects, the onset of the IR excess occurs near 2.2 μm. We find that wTTs show a richer distribution of SED morphologies than cTTs. Some of the wTTs show SEDs that are indistinguishable from those of cTTs, while others show a wide range of $\lambda_{\rm turn-off}$ $\alpha_{\rm excess}$ values. Finally, the debris disks, with ages 12 and 200 Myrs (Chen et al. 2005) show detectable excess only longward of 8.0 μm, but also present a great variety of spectral slopes.

In general, the diagram suggests an evolutionary sequence in which most actively accreting cTTs have similar near to mid-IR SEDs, dominated by optically thick emission of the inner disk. This similarity is probably due to the fact that, in most cases, their inner disks extend to the dust sublimation radius (Muzerolle et al. 2003). On the other hand, if disks evolve from the inside out, wTTs disks are likely to have a wider range of of inner disk radii and temperatures than cTTs. This diversity of inner disks, together with possible grain grown and grain settling to the disk mid-plane may explain the large ranges of $\alpha_{\rm excess}$ and $\lambda_{\rm turn-off}$ found. Finally, the debris disks populate the right part of the plot with large cleared inner disks and emission from cool optically thin dust.

3.5.3 Comparison to Optically Thin Disk Models

As discussed in Section 3.4.2, four stars in our sample show SEDs and L_{DISK}/L_* consistent with optically thin disks. These are ROXs 36, RXJ1622.6-2345, IC348-56 and IC348-124.In this section, we modeled these four objects using the optically thin disk model developed by Augereau et al. (1999).

We limited the exploration of the parameter space to the disk parameters that affect most the global shape of an SED, namely the minimum grain size $a_{\rm min}$, the peak surface density position r_0 and the total dust mass $M_{\rm dust}$ (or, equivalently, the surface density at r_0). We adopted a differential grain size distribution proportional to $a^{-3.5}$ between $a_{\rm min}$ and $a_{\rm max}$, with $a_{\rm max} = 1300\,\mu$m, a value sufficiently large to not affect the SED fitting in the wavelength range we consider. Following Augereau et al. (1999), the disk surface density $\Sigma(r)$ is parametrized by a two power-law radial profile $\Sigma(r) = \Sigma(r_0)\sqrt{2}\left(x^{-2\alpha_{\rm in}} + x^{-2\alpha_{\rm out}}\right)^{-1/2}$ with $x = r/r_0$, and where $\alpha_{\rm in} = 10$ and $\alpha_{\rm out} = -3$ to simulate a disk peaked around r_0, with a sharp inner edge, and a density profile decreasing smoothly with the distance from the star beyond r_0. The optical properties of the grains were calculated for astronomical silicates (optical constants from Weingartner & Draine (2001)), and with the Mie theory valid for hard spheres. The grain temperatures were obtained by assuming the dust particles are in thermal equilibrium with the central star. NextGen model atmosphere spectra (Hauschildt et al. 1999) scaled to the observed dereddened K-band magnitude, were used to model the stellar photospheres.

For each star, we calculated 15000 SEDs ($0.3\,\mu$m$\leq \lambda \leq 950\,\mu$m), for 75, logarithmically-spaced values of $a_{\rm min}$ between $0.05\,\mu$m and $100\,\mu$m, and for 200 values of r_0, logarithmically-spaced between 0.02 AU and 300 AU. For each model, the dust mass was adjusted by a least-squares method, assuming purely photospheric emission (within the uncertainties, 10%) in the four IRAC bands, and by fitting the measured MIPS 24 μm flux density. Models with flux densities in the MIPS 70 μm and 160 μm bands, larger than the estimated 2σ upper limits of 0.03 Jy and 0.5 Jy, respectively, were eliminated. The results are summarized in Table 3.5, and the SEDs are displayed in Figure 3.12. Results in Table 3.5 are listed for two different regimes of minimal grain sizes, namely, $a_{\rm min} > 10$ μm and $a_{\rm min} < 0.5$ μm. The first regime accounts for a scenario where all grains have grown to sizes > 10 μm and where smaller grains are not replenished by collisions, while the second regime accounts for a case where grains smaller than 0.5 μm remain in the system, either because they are collisionally replenished, or because pressure forces are inefficient to expel grains. However, assuming a gas poor environment (i.e. the dust dynamics is not controlled by the gas), dissipation processes acting on small grains will limit the size of the smallest grains that are likely to populate the disk. For ROX 36, an A2 star, the blow-out size is of the order of a few microns. Thus, grains significantly smaller than 0.5 μm are unbound and unlikely to be present in the disk. For the three M-type stars, radiation pressure is not high enough to overcome the gravitational force and expel grains. In this case, and provided the star mass loss rate is high enough, the pressure force expected from the stellar wind will set the lower limit for $a_{\rm min}$ (Augereau & Beust 2006, Strubbe & Chiang 2006).

In most cases, neither the position of the peak surface density r_0, nor the minimum grain size $a_{\rm min}$, can be uniquely determined with so few observational constraints, but some models can be eliminated. In particular, the lack of excess in the IRAC bands imposes the disk to be significantly dust-depleted within ~1, AU from the star. The best fits to the SEDs of the three low-mass stars (RXJ1622.6-2345, IC348-56 and IC348-124) are indeed obtained for r_0 values around 2–5 AU, while in the case of ROXs 36, the inner hole could be ten times larger. The properties of the ROXs 36 disk are in fact those of a typical β Pic-like disk: a dust mass in the 10^{-4}–10^{-2} M$_\oplus$ range, a low fractional luminosity $L_{\rm IR}/L_*$ of about 10^{-4}, and typical minimum collision time-scales (as calculated using the formula given by Backman et al. 1993) one to three orders of magnitudes smaller than the star age. Also, as it is the case for virtually all β Pic-like disks, the disk around ROXs 36 seems to be collisional dominated because collisions occur much faster than Poynting-Robertson (P-R) drag (as calculated using the formula given by Augereau & Beust 2006) for all grains larger than the blow-up size. The best fits to the observed excesses around the three low-mass wTTs (RXJ1622.6-2345, IC348-56 and IC348-124) are also consistent with optically thin disks observed around other young M-type stars such as AU Mic (Liu et al. 2004). These three objects have low luminosity ratios, $L_{\rm IR}/L_{*} < 2\times10^{-2}$, and dust masses between 10^{-4} and $10^{-3}\,{\rm M}_{\oplus}$, with an upper limit of about $0.5\,{\rm M}_{\oplus}$. The collision time-scales for these three objects are extremely small (of the order of 100 yr).

The preliminary models described above suggest that the disks around ROXs 36, RXJ1622.6-2345, IC348-56, and IC348-124 *could* be younger analogs of the β Pic and AU Mic debris disks, and thus some of the youngest debris disks ever observed. However, this interpretation depends on the assumption that these four wTTs disks are gas poor (as their older counterparts are). The timescale over which gas clearing occurs is still poorly constrained observationally and it is even unclear whether gas and dust are lost simultaneously as disks evolve from the massive optically thick to the debris disk phase. High-resolution *Spitzer*-IRS observations, such as those presented by Pascucci et al. (2007), to constrain the amount of gas present in these extremely young (1-3 Myrs) optically thin disks could provide crucial information on the gas evolution in the transition from the primordial to the debris disk stage.

In Section 3.4.1, we found that most wTTs (∼80 %) show no evidence for a disk. Since *Spitzer* observations are capable of detecting very small amounts of dust in the planet-forming regions of the disk (r ∼0.1–10 AU), the absence of mid-IR excess imposes very stringent limits on the amount of dust available for planet formation around "disk-less" wTTs (i.e. most wTTs). In this section, we use the optically thin disk models discussed above to constrain the maximum amount of dust that could remain undetected within the first few tens of AU of the wTTs in our sample. Since the 24 μm observations are the most constraining, we restrict our analysis to Lupus and Ophiuchus objects that have 24 μm fluxes consistent with stellar photospheres and exclude the objects that remain undetected at this wavelength. Objects in IC 348 are also excluded because we detect the stellar photospheres of only a couple of them.

Since none of our "diskless" wTTs are detected in the c2d 70 and 160 μm maps, for the purpose of our models, we adopt nominal upper limits of 15 and 250 mJy at 70 and 160 μm, respectively. For each model we calculated the mass encompassed within a radius r, as a function of this radius. With this approach, we can estimate the maximum dust mass in the inner regions of the wTTs with no detectable, or marginally detected, emission in excess to the photospheric emission. The results are displayed in Figure 3.13 for the Lupus and Ophiuchus clouds , assuming distances to the Sun listed in Table 3.6. For the Lupus and Oph clouds, the c2d Spitzer observations constrain the observed wTTs to have less than a few $10^{-6}\,\mathrm{M}_\oplus$ of dust within 1 AU from the central star, and less than a few $10^{-4}\,\mathrm{M}_\oplus$ within 10 AU. These mass upper limits, obtained for minimum grain sizes between 10 and 100 μm, drop by about an order of magnitude when $a_{\mathrm{min}} \leq 0.5\,\mu$m.The Lupus and Oph wTTs with no (or marginal) excess at 24 μm, have then inner disks that are strongly depleted, and only extremely cold disks with large inner holes are still theoretically possible because of the relatively large MIPS 70 μm and 160 μm upper limits. Such belts would resemble the dust rings resolved about nearby young Main Sequence stars (e.g. HD 181327, Schneider et al. 2006 and ref. therein). Of course, our observations only constrain the mass of dust and can not rule out the presence of much larger planetesimals or planets because once dust grains grow into larger bodies (r $\gg \lambda$), most of the solid mass never interacts with the radiation, and the opacity function, k_ν (cm^2/gr), decreases dramatically.

3.5.4 Circumstellar Disks and Stellar Ages

In Section 3.4.1, we studied the overall disk fraction of our sample of wTTs. In this section, we derive stellar ages from two different evolutionary tracks and estimate the disk frequency as a function of stellar age. In order to derive stellar ages from theoretical evolutionary tracks, it is necessary to obtain the effective temperatures and luminosities of all the targets. We estimate the effective temperatures directly from the spectral type of the objects according to the scale provided by Kenyon & Hartmann (1995). We derive the stellar luminosities by applying a bolometric correction (appropriate for each spectral type) to the 2MASS J-band magnitudes corrected for extinction and assuming the nominal cloud distance listed in Table 3.6. The J-band was chosen because the effects of extinction is less important than at shorter wavelengths ($A_J \sim 0.26\ A_V$) and the emission from the disk is less prominent that at longer wavelengths. The bolometric corrections were taken from Hartigan, Strom & Strom (1994) and the J-band extinction, A_J, was calculated using $A_J = 1.24 \times E(R_C - I_C) = 1.24 \times ((R_C - I_C)_{OBS} - (R_C - I_C)_O)$. The intrinsic stellar colors, (R_C-I_C)o, come from Kenyon & Hartmann (1995). For objects without R_C and I_C fluxes available, we use A_J=5.88×E(J-K).

Estimation of Age Uncertainties

In order to estimate the error bars associated with the ages we derive, we first estimate the observational uncertainties that need to be propagated through the H-R diagram. Fortunately, the T_{eff}'s and luminosities of wTTs are easier to determine than those of cTTs. The interplay between extinction and veiling introduces a large uncertainty in determining stellar luminosities of cTTs, and different results are obtained depending on the band to which the bolometric correction is applied (Cieza et al. 2005). In fact, the luminosities obtained from the J-band are systematically larger (by ∼35%) than those obtained from the I_C band. For wTTs, Cieza et al. (2005) show that the luminosities derived from the I_C and J bands agree to within 5%; therefore, distance is probably the dominant uncertainty in calculating their luminosity. The distance uncertainties listed in Table 3.6 translate into ∼20–30% luminosity uncertainties. Similarly, the spectral type classification of wTTs (and therefore their temperatures) is usually more accurate than that of cTTs. This is because the spectra of cTTs are affected by veiling, and their photospheres are highly heterogeneous in terms of temperature due to the presence of hot accretion columns. To estimate the effective temperature uncertainty of the wTTs in our sample, we adopt one spectral type subclass as the classification accuracy. For the reasons mentioned above, we regard the T_{eff}'s and the luminosities (and therefore the ages) of wTTs as being more accurate than those derived for cTTs using the same procedure.

A study of the disk fraction as a function of age can only yield meaningful results if the intrinsic age spread of the sample is larger than the age uncertainties attributable to observational errors. We verify that our sample satisfies this condition by comparing the spread of the ages we derive to that expected solely from observational errors. Based on an error budget similar to the one described above, Hartman (2001) estimated that observational errors will introduce an age spread of σlog(age) = 0.18 in the logarithmic age distribution derived for wTTs in Taurus. In Figure 3.14, we plot the derived age distribution of our sample as calculated from two different evolutionary tracks. The mean age and the age spread are model dependent. According the models presented by D'Antona & Mazzitelli (1994, 1998, D98 hereafter) [4] the logarithmic age distribution of our sample can be characterized as a Gaussian centered around log(age)=6.3 with σ(log age) = 0.57. Similarly, according to the models presented by Siess et al. (2000, S00 hereafter) [5], the logarithmic age distribution of the sample can be characterized as a Gaussian centered around log(age)=6.6 with σ(log age) = 0.40. The age spreads derived are 2.2-3.2 times the value attributed by Hartmann (2001) to observational errors, which is also shown in Fig 13 for comparison.

---

[4] Available at http://www.mporzio.astro.it/ dantona/prems.html.

[5] Available at http://www-astro.ulb.ac.be/ siess/database.html.

Evolutionary Tracks and Stellar Ages

In order to evaluate the degree to which ages we derive depends on the models, we compare the individual ages derived from the D98 and S00 models. We choose these two particular evolutionary tracks because they provide the appropriate mass and age range and are both widely used, which allows a direct comparison of our results to those from other papers. Figure 3.15a shows the ages derived for our sample using both sets of evolutionary tracks. The error bars for every object have been calculated by propagating into the evolutionary tracks the *observational* uncertainties computed as described in the previous section (e.g. a T_{eff} uncertainty equal to one spectral type subclass and a luminosity uncertainty dominated by the distance uncertainty). Stellar ages of PMS stars are very difficult to estimate due to the large observational and model uncertainties involved (Hillenbrand & White, 2004) and they are often taken with a high degree of (healthy) skepticism. However, even though the error bars in the individual ages are large, the total age spread in the sample is significantly larger than the typical (observational) error bar. This is consistent with the analysis of Figure 3.14. Also, even though D98 and S00 evolutionary tracks show some systematic differences (e.g. D98 tracks yield significantly younger ages than S00 models), the relative ages agree fairly well.

Figure 3.15a shows that ∼40% of the wTTs that are both younger than 1.5 Myrs according to the S00 models *and* younger than 0.6 Myrs according to the D98 models have circumstellar disks. In contrast, none of the targets that are older than 10 Myrs according to the D98 *or* S00 models has a disk. The decrease in the disk fraction with stellar age is clearly seen Figure 3.15b, where we restrict our analysis to the 198 objects in the magnitude limited subsample discussed in Section 3.4.1 and divide the ages we derive using the D98 and S00 models into 4 age bins. Very similar conclusions can be drawn if our sample is combined with that of P06. Including the P06 samples considerably increases the statistical significance of the last age bin. Taken both samples together, none of the ~40 stars that are older than 10 Myrs according to either of the tracks have an IR excess indicating the presence of a circumstellar disk.

3.5.5 Constraint on the Timescale of Planet Building

Figure 3.15 suggests that circumstellar disks, as defined by the presence of IR excesses at $\lambda \leq$ 10-24 μm, are very rare or nonexistent around wTTs with ages $\gtrsim$10 Myrs. This timescale is very similar to that obtained by studies of the frequency of circumstellar disks detected in the near-IR (See Hillenbrand 2006 for a review). However, our results impose much stronger constraints on the time available for the formation of planets than those provided by previous studies. Past results based on near-IR excesses always left room for the possibility that stars without near-IR excess had enough material to form planets at larger radii not probed by near-IR wavelengths. IRAS and ISO had the appropriate wavelengths range to probe the planet-forming regions of the disk but lacked the sensitivity needed to detect all but the strongest mid- and far-IR excesses in low-mass stars at the distances of nearest star-forming regions. *Spitzer* provides, for the first time, the wavelength coverage and the sensitivity needed to detect small amounts of dust in the planet-forming regions of a statistically significant number of low-mass PMS stars. In particular, the results from Section 3.5.3 suggest that 24 μm fluxes consistent with stellar photospheres constrain the amount of *warm* dust (T ~100 K) in the disks of our sample of wTTs to be much less than an Earth mass. Even though our 24 μm observations are not sensitive to the stellar photospheres of all the targets, taking the P06 sample and our sample together, there are at least ~40 wTTs with estimated ages > 10 Myrs showing photospheric fluxes at 24 μm. This number is likely to be a lower limit because, as discussed in Section 3.5.1, we suspect that the ages of many of the stars in the P06 sample have been underestimated. This seems to imply that after

$\sim$10 Myrs wTTs have to be in a relatively advanced stage of the planet formation process if they are to form planets at all.

Since the cTTs disks older than 10 Myrs are also very infrequent, 10 Myrs seems to be a general upper limit for the survival of primordial disks around PMS stars. This conclusion is also supported by recent results from the "Formation and Evolution of Planetary Systems" (FEPS) project. Silverstone et al. (2006, S06 hereafter) search for IRAC excesses in a sample of 74 young (age $<$ 30 Myr old) Sun-like ($0.7 < M_*/M_\odot$) stars. They divided the sample into two age bins, 3-10 Myrs and 10-30 Myrs. S06 find IRAC excesses for 4 of the 29 stars in the youngest age bin and for 1 of the 45 stars in the older age bin. The FEPS objects were selected based on their ages ($<$ 30 Myrs), masses ($\sim 1\ M_\odot$), distances ($<$ 170 pc), and low infrared backgrounds, without a bias with respect to their Hα EW or IR properties. The five objects with IRAC excess have SEDs consistent with those of CTTS, and given the age uncertainties, it entirely possible that they are all younger than 10 Myrs. In fact, the only object with IRAC excess for which S06 adopts an age older than 10 Myrs is PDS 66. S06 adopted an age of 17 Myrs for PDS 66 based on the mean age of the Lower Centaurus Crux, but its formal age is 7-17 Myrs depending on the evolutionary track used (Mamajek et al. 2002). Recent sub-millimeter results extend the conclusions on the survival time of the material in the inner disk ($r < 0.1$ AU) and the planet-forming region of the disk ($r \sim 1$–10 AU) to the outer disk ($r \sim$100 AU). Andrews & Williams (2005) observed over 150 YSOs in Taurus and found that $<$ 10 % of the object lacking inner disk signatures were detected at sub-mm wavelengths. Given the high sensitivity of their survey (3σ $\sim$10 mJy at 850 μm) they conclude that dust in the inner and outer disk dissipate nearly simultaneously.

Figures 3.15 also suggests that the disks of some wTTs dissipate in timescales $\lesssim$1 Myrs[6]. Are these apparently very young disk-less objects as young as the evo-

---

[6] This assumes that all wTTs had a disk at some point of their evolution. It is possible that

lutionary tracks suggest or is their apparent youth just a product of the large age uncertainty? Several factors can introduce very large errors in the age determination. For instance, the luminosity of foreground field stars can be grossly overestimated if the nominal cloud distances are used, leading to grossly underestimated ages. Also, large errors in the spectral type classification might lead to large errors in the extinction and luminosities. To check for these possibilities, we plotted the SEDs of the objects classified as the youngest disk-less wTTs in our sample.

Their SEDs look consistent with stellar photospheres and the overall quality of the fits suggests that both the spectral types and the extinction corrections are reasonably accurate. Still, some of these objects are ∼0.5 Myrs old according to the DM98 models and ∼1.0 Myrs old according to the S00 models, and ∼15 times more luminous than main-sequence stars of the corresponding spectral types.

In Section 3.5.4 we found that the dissipation timescale or "survival time" of wTTs circumstellar disks ranges from less than 1 to 10 Myrs. A related timescale is the transition timescale from optically thick accretion disks to undetectable disks. Assuming that wTTs disks are the link between cTTs disks and "disk-less" wTTs, then the transition timescale, τ, can be estimated as $\tau = \frac{N_{TRAN}}{N_{PMS}} \times$ <age>, where N_{TRAN} is the number of wTTs disks, N_{PMS} is the total number of PMS stars (wTTs+cTTs), and <age> is the mean age of the sample. Adopting the wTTs/cTTs ratio of IC 348 (∼3/2) and a mean age of 3 Myrs, the overall IRAC disk fraction in wTTs of 20% we find in Section 3.4.1 implies τ ∼0.4 Myrs. This timescale is very similar to that found for the transition timescale between an optically thick disk and an optically thin disk by Skrutskie et al. (1990) and Wolk & Walter (1996) based on the number of "transition objects", which they define as targets without K-band excess but with strong IRAS excesses. The fact that the transitional timescale is

---

some disks dissipate very early (t << 1 Myrs), even before the star is optically revealed and can be classified as a wTTs. However, accretion through a disk is considered an unavoidable step of the star formation process.

significantly shorter than the mean disk-lifetime is inconsistent with traditional viscous evolution (Hartmann et al. 1998) or magnetospheric clearing models (Armitage et al. 1999), which predict a steady disk evolution, and thus similar timescales for disk lifetimes and disk dispersal times. Non-steady disk evolution scenarios are required to explain the short transitional timescales inferred after significantly longer disk lifetimes. Such scenarios include the ultraviolet-switch model (Alexander et al. 2006) and the presence of gap forming planets (e.g. Quillen et al. 2004).

Our results from Section 3.5.4, constrain not only the dissipation timescale of the dust during the planet formation process, but also the amount of second generation dust that is produced during this process (Section 3.5.3). Numerical models presented by Kenyon & Bromley (2004) predict the amount of 10 and 20 μm excess as a function of time produced by the formation of terrestrial planets. Detailed comparison between these kind of models with predictive power and the new observational constraints *Spitzer* is now providing could be highly valuable for our understanding of planet formation.

Particularly intriguing and potentially very important objects are the $\sim$1 Myrs old wTTs without any measurable IR excess (for $\lambda \leq 24$ μm) discussed above. One possible explanation for the very early dissipation of their disks is that these stars have already formed planets through gravitational instability, which is expected to occur at extremely young ages when disks are most massive (Boss 2000). Another possibility for the fast dissipation of these disks is the presence of close companions that could have disrupted their disks. This possibility can be tested with a combination of radial velocity and adaptive optics observations to search for companions. Initial conditions could also be responsible for the early dissipation of the disk, although this hypothesis is not easily testable observationally. We note that the Space Interferometry Mission should be able to establish whether or not these very young disk-less wTTs do in fact harbor planets. The presence of planets around these ∼1 Myrs old stars would set the tightest constraints to date for the planet formation timescale.

The properties of wTTs with disks such as their age, SED morphology, L_{DISK}/L_*, etc, strongly suggests that wTTs disks are the link between the massive primordial disks found around cTTs and the debris disks observed around young MS stars. They could be arguably the best places to study ongoing planet formation. Before the end of its mission, *Spitzer* is likely to identify hundreds of wTTs disks in nearby star-forming regions. These objects will most likely be the main targets of many follow-up observations. Deep far-IR and sub-mm observations with *Spitzer*, Herschel, and Alma will allow the study of the outer regions of these wTTs disks and estimates of their masses. Follow-up *Spitzer*/IRS observations of the 10 and 20 μm silicate features will provide important information on the evolutionary state of the circumstellar dust around these objects. Finally, high resolution searches for H_2 and atomic lines, such as those presented by Hollenbach et al. (2005) and Pascucci et al. (2007), would be highly desirable to constrain the amount of gas available for the formation of giant planets in wTTs disks.

3.6 Summary of results

We present a census of circumstellar disks and report the disk frequency as a function of stellar age for a sample of over 230 spectroscopically identified wTTs located in the c2d IRAC and MIPS maps of the Ophiuchus, Lupus and Perseus Molecular Clouds. Our main results can be summarized as follows:

1) In Section 3.4.1, we find from a magnitude limited subsample of wTTs that ∼20% of the wTTs have noticeable IR-excesses at IRAC wavelengths indicating the presence of a circumstellar disk.

2) The disks frequencies we find in the 3 clouds we consider are ∼3-6 times larger than that recently found by P06 for a sample of 83 relatively isolated wTTs

projected outside the boundaries of nearby molecular clouds. This discrepancy in the disk fractions supports the idea that samples of wTTs (nominally 1-10 Myrs old) located a few degrees away from their parent molecular clouds represent an older population of stars. The disk fractions we find are more consistent with those obtained in recent *Spitzer* studies of wTTs in young clusters such as IC 348 and Tr 37. However, in Section 3.5.1, we suggest that Lada and colleagues might have overestimated the disk fraction of wTTs in IC 348 by classifying as "anemic disks" a fraction of disk-less M4-M7 stars with large photometric uncertainties.

3) In Section 3.4.2. we find that the disk fraction of wTTs is a smooth function of $H\alpha$ EW. In Section 3.4.2, we show that the fractional disk luminosities of wTTs disks bridge the gap between the cTTs and the debris disk range.

4) In Section 3.5.3, we estimate mass upper limits of dust within the inner 10 AU of $10^{-4}M_{\oplus}$ for the objects in our sample with 24 μm fluxes consistent with stellar photospheres.

5) In Section 3.5.4, we place our sample of wTTs in the H-R diagram and find that the stars with excesses are among the younger part of the age distribution. However, we also find that up to ∼50% of the apparently youngest stars in the wTTs sample show no evidence of IR excess. This suggests that the circumstellar disks of a sizable fraction of pre-main-sequence stars dissipate before the stars reach an age of ∼1 Myr.

6) Also in Section 3.5.4, we find that none of the stars in our sample apparently older than ∼10 Myrs have detectable circumstellar disks. Since *Spitzer* observations probe planet-forming regions of the disk (r ∼0.1-10 AU) and are capable of detecting IR excesses produced by very small amounts of dust, our results impose stronger constraints on the time available for the formation of planets than those provided by previous studies based on detections of disks in the near-IR.

7) Finally, in Section 3.5.5 we estimate a transition timescale of ∼0.4 Myrs

between optically thick accretion disks and disks that are undetectable shortward of ~10 μm, in good agreement with previous results.

3.7 Acknowledgments

We thank the anonymous referee for his/her many detailed comments, which have helped to improve the paper. Support for this work, which is part of the *Spitzer* Legacy Science Program, was provided by NASA through contracts 1224608, 1230782, and 1230799 issued by the Jet Propulsion Laboratory, California Institute of Technology under NASA contract 1407. B.M. acknowledges the Fundación Ramón Areces for financial support. Astrochemistry in Leiden is supported by a NWO Spinoza and NOVA grant, and by the European Research Training Network ”The Origin of Planetary Systems” (PLANETS, contract number HPRN-CT-2002-00308). We thank the Lorentz Center in Leiden for hosting several meetings that contributed to this paper. This publication makes use of data products from the Two Micron All Sky Survey, which is a joint project of the University of Massachusetts and the Infrared Processing and Analysis Center funded by NASA and the National Science Foundation. We also acknowledge use of the SIMBAD database.

Table 3.1. *Spitzer data*

ID	R.A (J2000.0)	Dec (J2000.0)	$F_{3.6}$	$Error_{3.6}$	$F_{4.5}$	$Error_{4.5}$	$F_{5.8}$ (mJy)	$Error_{5.8}$	$F_{8.0}$	$Error_{8.0}$	F_{24}	$Error_{24}$
IC348-1	55.8837	32.1048	1.06e+01	1.51e-01	7.09e+00	8.78e-02	4.81e+00	5.52e-02	2.79e+01	4.68e-02	—	—
IC348-2	55.8903	32.0293	4.96e+00	7.22e-02	3.42e+01	4.89e-02	2.52e+00	3.64e-02	1.42e+01	2.89e-02	—	—
IC348-3	55.9526	32.2308	3.23e+00	4.64e-02	2.39e+00	2.82e-02	1.65e+00	2.96e-02	9.38e-01	3.05e-02	—	—
IC348-4	55.9532	32.1259	9.01e+00	1.75e-01	6.51e+00	8.82e-02	4.13e+00	5.04e-02	2.34e+00	4.26e-02	—	—
IC348-5	55.9558	32.1778	7.47e+00	1.13e-01	5.55e+00	6.76e-02	3.57e+00	4.47e-02	2.13e+00	4.04e-02	—	—

Note. — [The complete version of this table is in the electronic edition of the Journal. The printed edition contains only a sample to illustrate its content.]

Table 3.2. non-*Spitzer data*

ID	R.A (J2000.0)	Dec (J2000.0)	SpT	H_α ($\AA$)	V	$Error_V$	R_C	$Error_{R_C}$	I_C (mag)	$Error_{I_C}$	J	*H*	K_S
IC348-1	55.8837	32.1048	M0.75	1.0	—	—	14.81	0.03	13.73	0.03	12.18	11.38	11.13
IC348-2	55.8903	32.0293	M5	5.0	—	—	17.93	0.03	15.91	0.03	13.36	12.57	12.22
IC348-3	55.9526	32.2308	M5	6	—	—	17.92	0.03	16.05	0.03	13.59	12.98	12.64
IC348-4	55.9532	32.1259	M1.5	0	—	—	15.44	0.03	14.16	0.03	12.44	11.59	11.34
IC348-5	55.9558	32.1778	M3.5	11	—	—	16.36	0.03	14.76	0.03	12.58	11.80	11.54

Note. — [The complete version of this table is in the electronic edition of the Journal. The printed edition contains only a sample to illustrate its content.]

Table 3.3. Adopted Extinction Relations

Band	λ (μm)	A_V/A_λ[1]
V	0.55	1.00
R_C	0.65	0.79
I_C	0.80	0.58
J	1.25	0.26
H	1.66	0.15
K_S	2.2	0.09
IRAC-1	3.6	0.04
IRAC-2	4.5	0.03
IRAC-3	5.8	0.02
IRAC-4	8.0	0.01
MIPS-1	24	0.002

[1] The extinction relations for the optical and 2MASS wavelengths come the Asiago database of photometric systems (http://ulisse.pd.astro.it/Astro/ADPS/enter.html ; Fiorucci & Munari 2003), while those for the *Spitzer* bands come from Huard et al. (2006, in prep.

Table 3.4. Objects classified as anemic disks by L06 that do not satisfy our disk identification criterion

Ra (J2000.0)	Dec (J2000.0)	ID L06	SpT	α L06	σ_α L06	$(\alpha+2.66)/\sigma_\alpha$ L06	[3.6]-[8.0] L06	[3.6]-[8.0] C2D	Δ([3.6]-[8.0]) L06-C2D
55.9526	32.2308	261	M5	-2.560	0.048	2.0	0.29	0.26	0.03
55.9742	32.1251	254	M4.25	-2.549	0.081	1.3	0.30	0.29	0.01
56.0185	32.0817	303	M5.75	-2.197	0.125	3.7	0.61	—	—
56.0740	32.0799	169	M5.25	-2.440	0.099	2.2	0.41	0.36	0.05
56.0816	32.0403	322	M4.25	-2.426	0.046	5.0	—	—	—
56.0971	32.0318	1684	M5.75	-1.811	0.500	1.6	—	—	—
56.1203	32.0730	385	M5.75	-2.183	0.350	1.3	0.71	—	—
56.1309	32.1915	226	M5.25	-2.233	0.265	1.6	0.60	0.38	0.22
56.1358	32.1451	33	M2.5	-2.483	0.157	1.1	0.32	0.16	0.16
56.1365	32.1544	88	M3.25	-2.355	0.081	3.7	0.46	0.48	-0.02
56.1460	32.1269	8024	K7	-2.213	0.218	2.0	0.62	0.25	0.37
56.1590	32.1727	353	M6	-2.251	0.178	2.2	0.61	0.16	0.45
56.1794	32.1709	217	M5	-2.312	0.043	8.0	0.52	0.43	0.09
56.1822	32.1800	360	M4.75	-2.303	0.064	5.5	—	—-	—
56.1861	32.1251	218	M5	-2.294	0.049	7.4	0.54	-0.04	0.58
56.1902	32.1864	413	M4	-2.398	0.500	0.5	—	0.31	—
56.2035	32.2228	178	M2.75	-2.520	0.080	1.7	0.31	0.23	0.08

Table 3.4 (cont'd)

Ra (J2000.0)	Dec (J2000.0)	ID L06	SpT	α L06	σ_α L06	$(\alpha+2.66)/\sigma_\alpha$ L06	[3.6]-[8.0] L06	[3.6]-[8.0] C2D	Δ([3.6]-[8.0]) L06-C2D
56.2527	32.1387	344	M5	-2.376	0.229	1.2	0.49	0.45	0.04

Table 3.5. Optically thin disk properties, for two different regimes of minimal grain sizes, a_{min}.

		($a_{min} < 0.5$ μm)			($a_{min} > 10$ μm)		
Star	r_0(AU)	M_{dust}($10^{-3}M_{\oplus}$)	t_{coll}(yr)	r_0(AU)	M_{dust}($10^{-3}M_{\oplus}$)	t_{coll}(yr)	$L_{IR}/L_{*}\times10^3$
ROXs 36	82^{+100}_{-73}	$6.7^{+25}_{-6.5}$	$77000^{+110000}_{-74000}$	$17^{+2.8}_{-10}$	$5.3^{+5.9}_{-4.9}$	7400^{+1900}_{-5200}	$0.11^{+0.015}_{-0.023}$
RXJ1622.6-2345	$4.0^{+51}_{-3.5}$	$0.13^{+280}_{-0.13}$	310^{+2000}_{-300}	$1.9^{+6.1}_{-1.4}$	$0.35^{+85}_{-0.34}$	130^{+79}_{-110}	$0.60^{+5.4}_{-0.11}$
IC348-56	$5.2^{+59}_{-4.4}$	$0.53^{+570}_{-0.52}$	190^{+1300}_{-190}	$2.5^{+6.7}_{-1.8}$	$1.5^{+180}_{-1.5}$	86^{+52}_{-70}	$1.4^{+9.7}_{-0.27}$
IC348-124	$4.1^{+27.}_{-3.2}$	$0.74^{+170}_{-0.69}$	65^{+330}_{-61}	$1.8^{+2.4}_{-0.94}$	$1.8^{+33}_{-1.6}$	24^{+15}_{-14}	$3.1^{+8.6}_{-0.65}$

Table 3.6. Adopted Distances

Cloud	Distance (pc)	Reference
Ophiuchus	125±20	de Geus et al. (1989)
Lupus I	150±20	Comeron et al. (2006), in prep.
Lupus III	200±20	Comeron et al. (2006), in prep.
IC348	320±30	Herbig (1998)

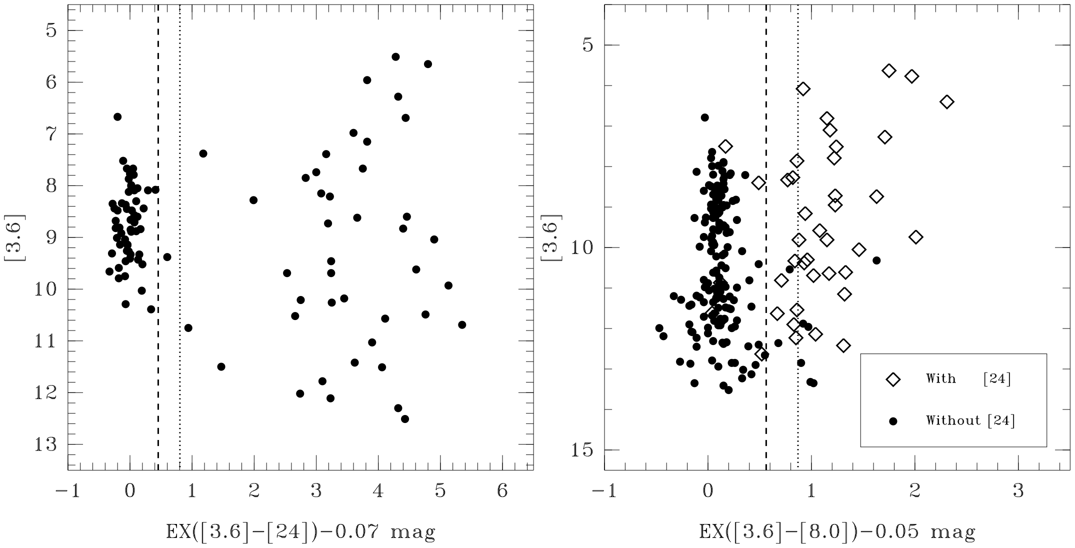

Figure 3.1 [3.6] vs EX([3.6]–[24]) (left) and [3.6] vs EX([3.6]–[8.0]) (right) diagrams for our sample of wTTs used for disk identification. See text for definitions. The 3 and 5-σ dispersion of the stellar photospheres are shown as dashed and dotted lines, respectively. Most of the disks are detected at 24 μm.

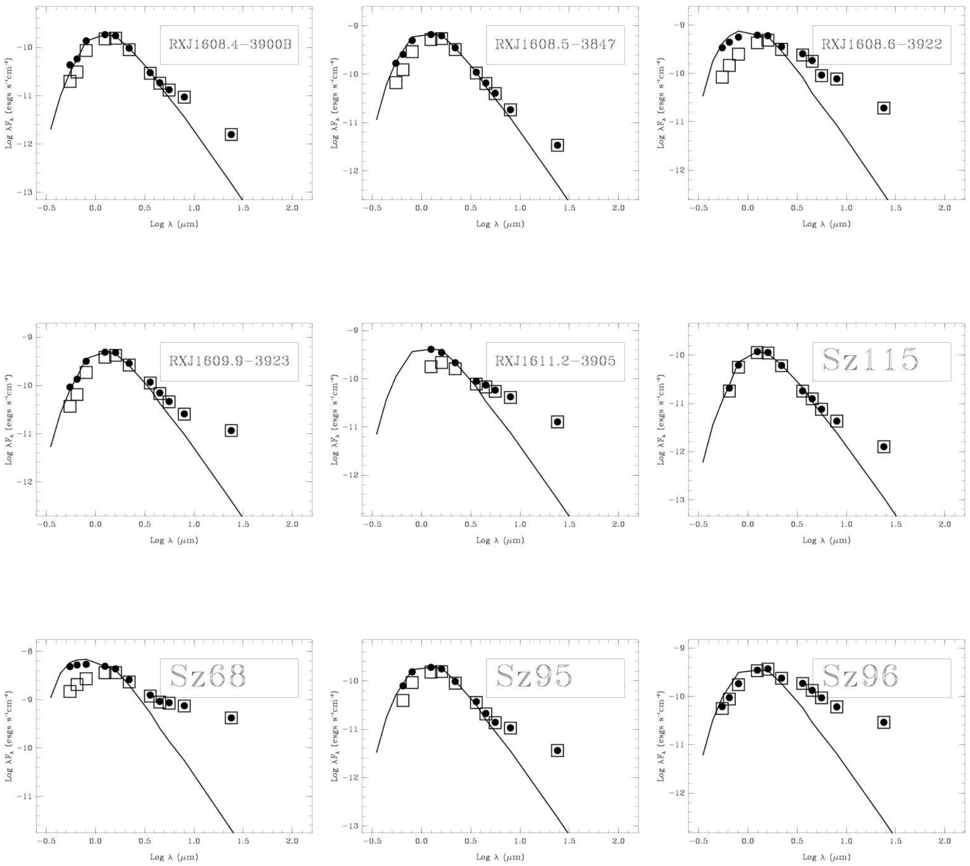

Figure 3.2 SEDs of wTTs disks in Lupus. The open squares represent the observed optical, 2MASS, IRAC and MIPS-24 μm fluxes, while the dots correspond to the extinction corrected values. Model photospheres corresponding to published spectral types are shown for comparison.

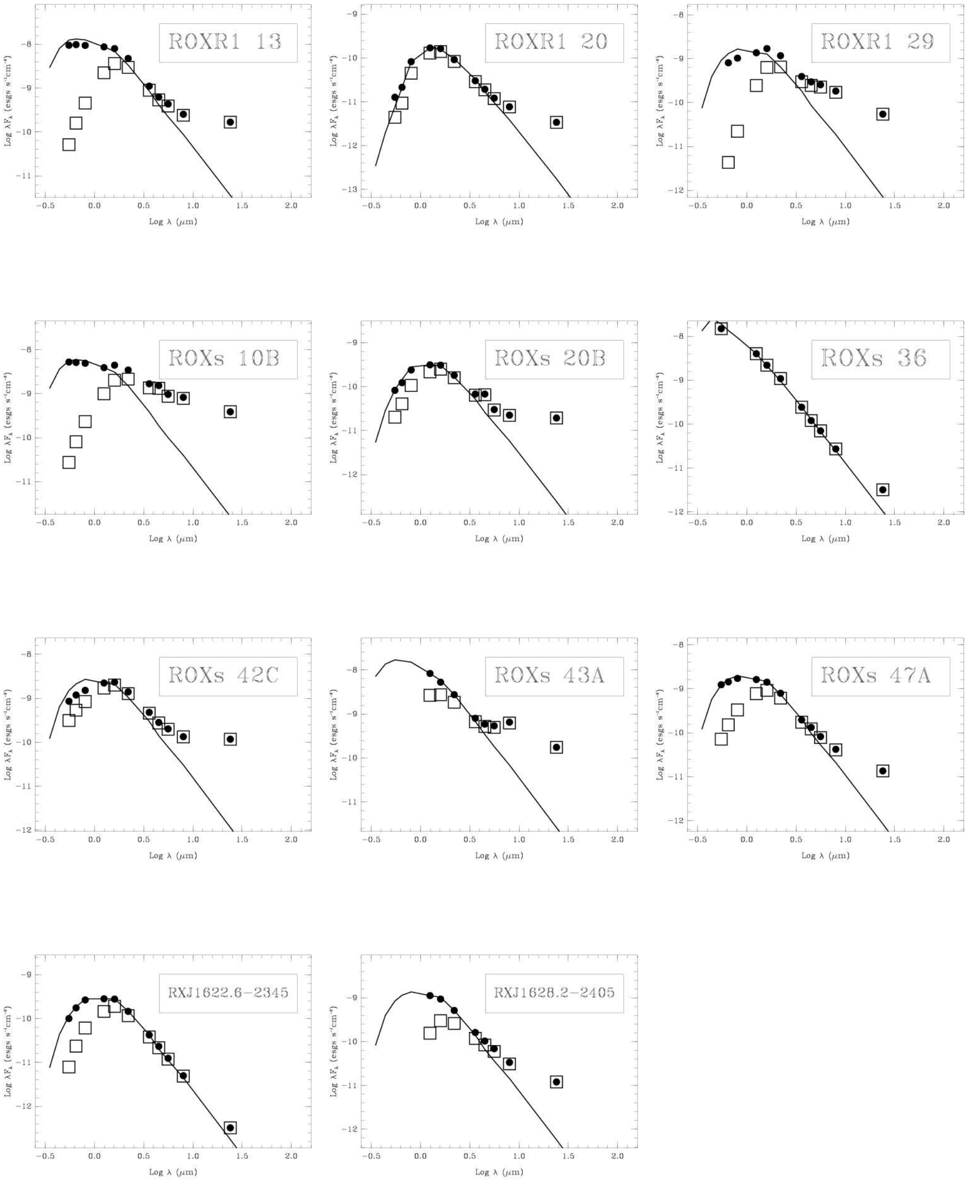
ROXR1 13

ROXR1 20

ROXR1 29

ROXs 10B

ROXs 20B

ROXs 36

ROXs 42C

ROXs 43A

ROXs 47A

RXJ1622.6−2345

RXJ1628.2−2405

Figure 3.3 SEDs of wTTs disks in Ophiuchus.

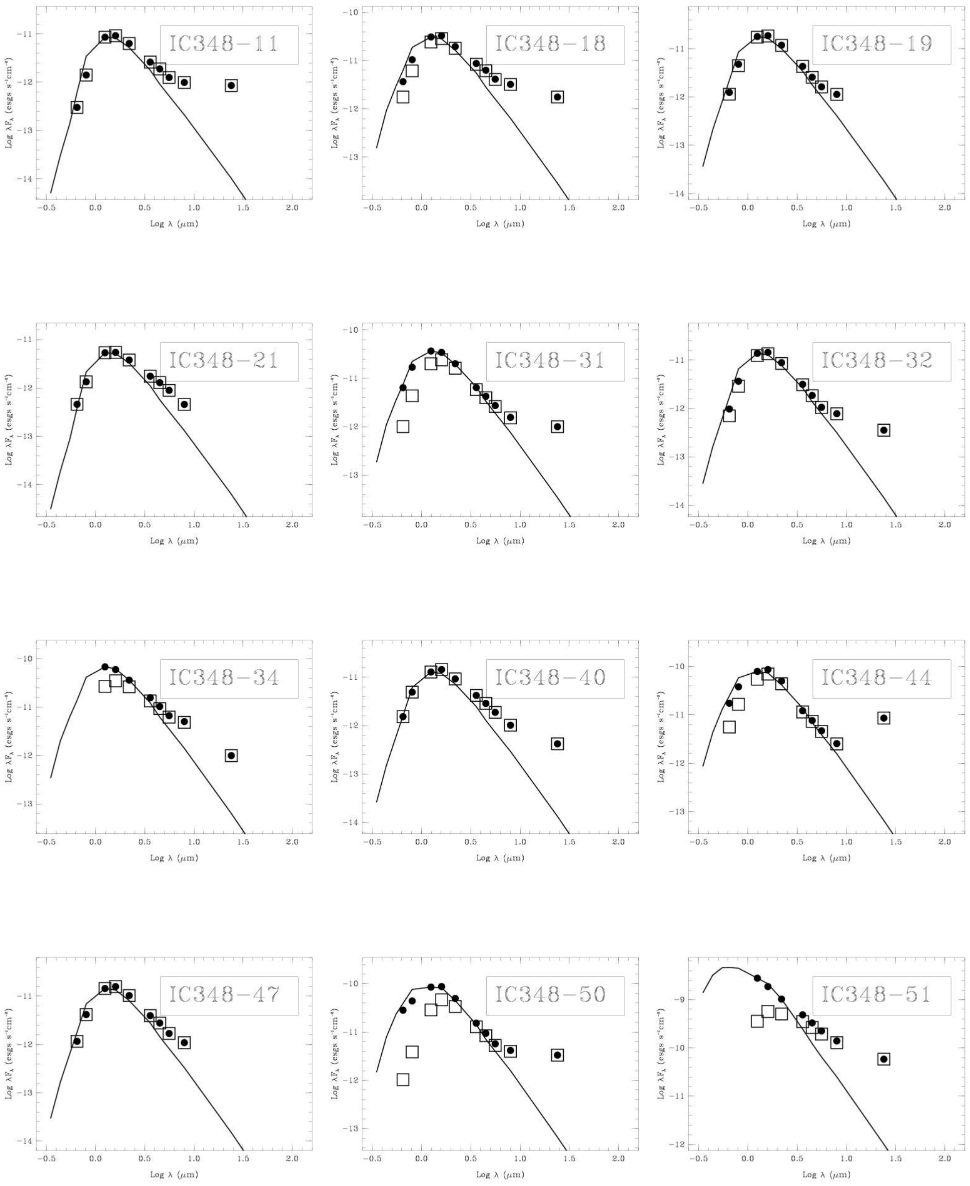

Figure 3.4 SEDs of wTTs disks in IC 348.

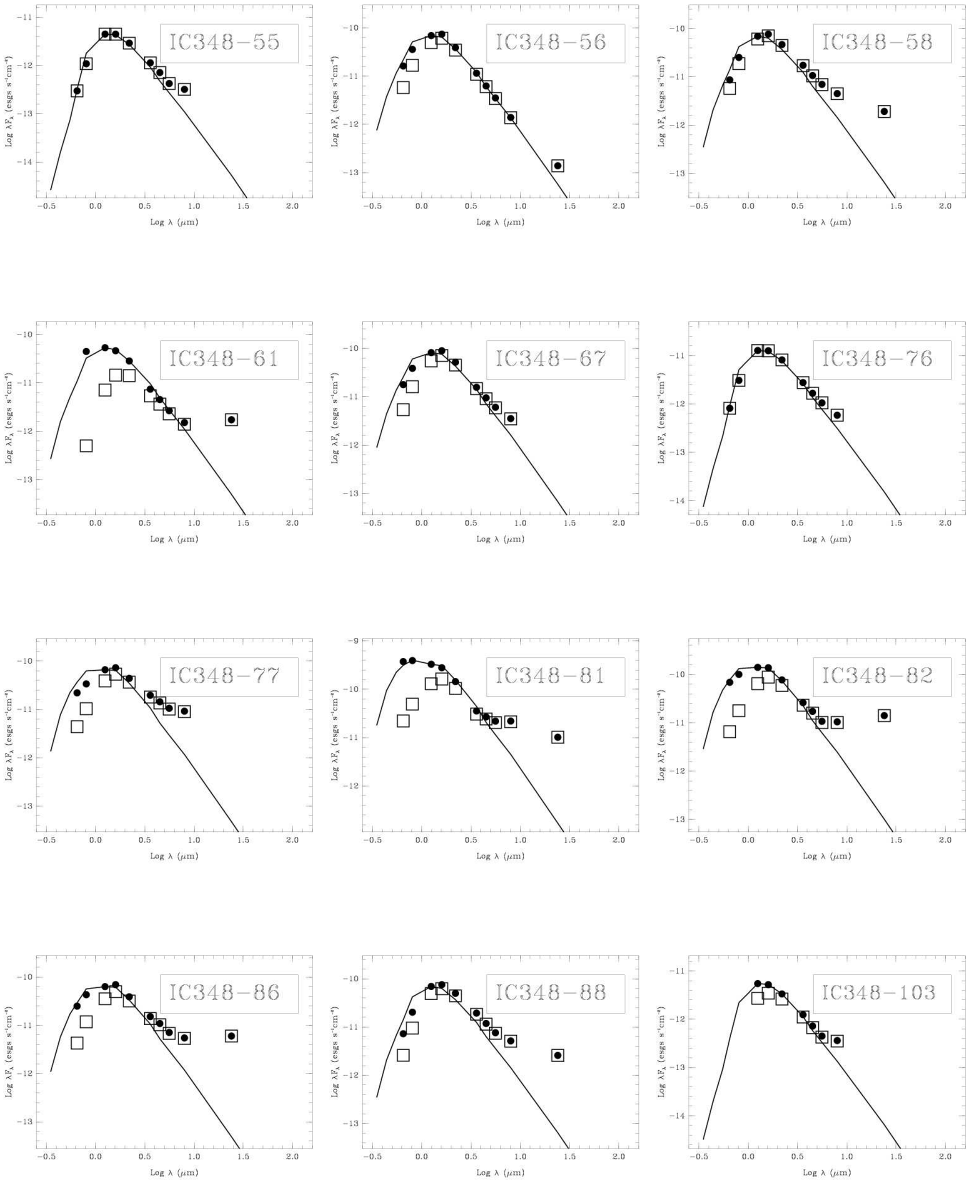

Figure 3.5 SEDs of wTTS disks in IC 348 — Continued.

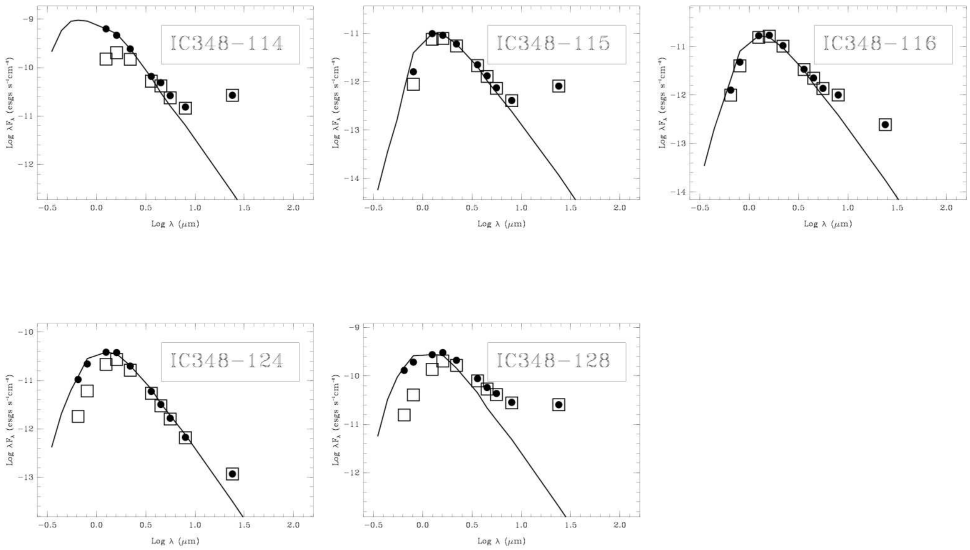

Figure 3.6 SEDs of wTTs disks in IC 348 — Continued.

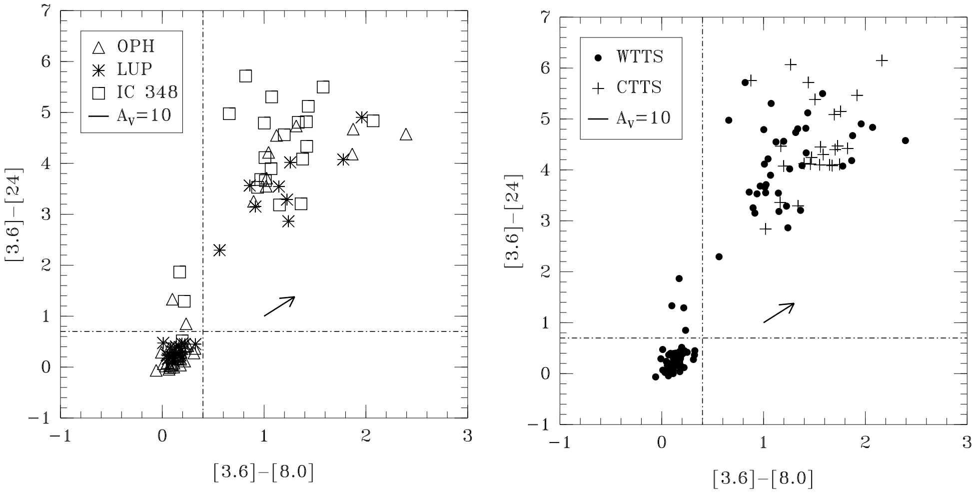

Figure 3.7 The Figure on the left shows the [3.6]–[24] vs. [3.6]–[8.0] colors of our sample of wTTs stars. Based on this diagram, we identify three different groups: (1) stellar photosphere with [3.6]–[24] $<$ 0.7 and [3.6]–[8.0] $<$ 0.4, (2) Objects with [3.6]–[24] $>$ 0.7 and [3.6]–[8.0] $<$ 0.4 which show significant 24 μm excess but no evidence for 8.0 μm excess, and (3) objects with [3.6]–[24] $>$ 0.7 and [3.6]–[8.0] $>$ 0.4 which show evidence for both IRAC and MIPS excesses. Objects in the second group are likely to have optically thin disks (see Section 3.4.2). The Figure on the right combines our sample of wTTs with a sample of cTTs from Hartmann et al. (2005) and Lada et al. (2006).

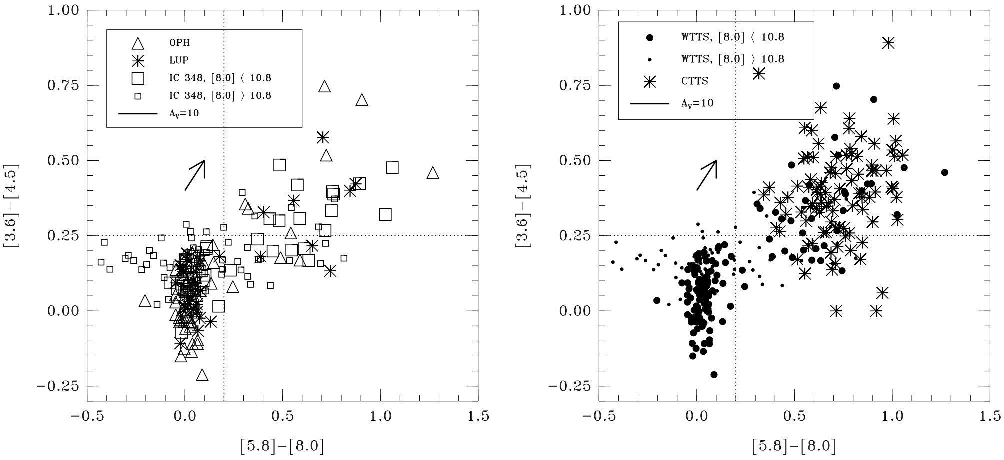

Figure 3.8 The Figure on the left shows the [3.6]–[4.5] vs. [5.8]–[8.0] colors of our sample of wTTs. Faint IC 348 members ([8.0] $>$ 10.8 mag, 3 mJy) tend to have more uncertain colors than the rest of the sample and are shown as smaller open boxes. The dotted lines represent the approximate boundaries of the color of the stellar photospheres. Stars in the upper right corner of the diagram have both, 4.5 and 8.0 μm, excesses. Stars in the lower right corner of the diagram are stars with 8.0 μm excess but no 4.5 μm excess. The Figure on the right combines our sample of wTTs with cTTs from Hartmann et al. (2005) and Lada et al. (2006).

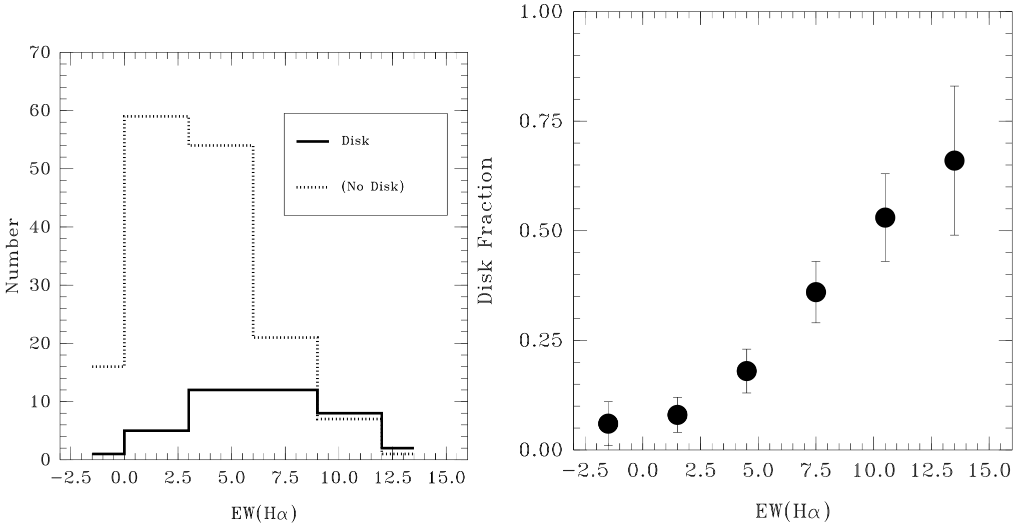

Figure 3.9 Histogram of the $H\alpha$ equivalent width for stars with and without a disk (a), and the disk fraction of wTTs vs. $H\alpha$ equivalent width (b). The disk fraction of wTTs seems to be a smooth function of $H\alpha$ equivalent width.

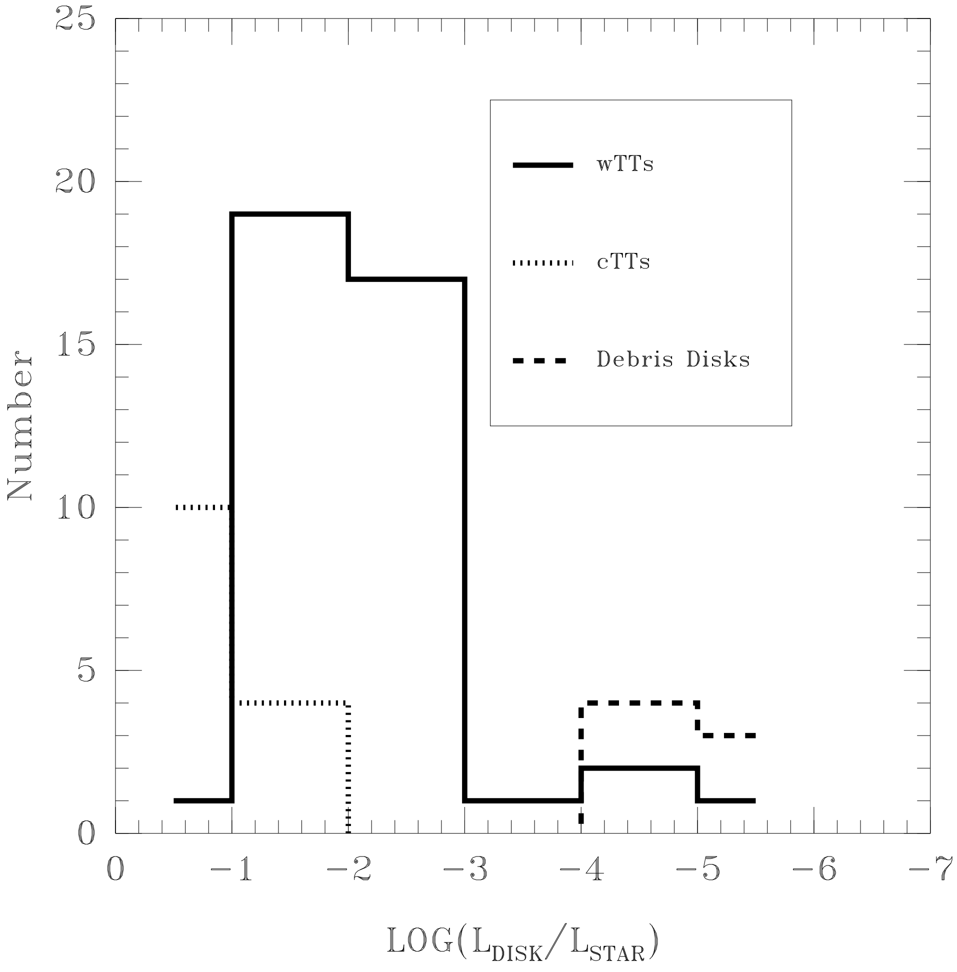

Figure 3.10 The fractional disk luminosities, L_{DISK}/L_*, derived for our sample of wTTs disks. The L_{DISK}/L_* values calculated using the same procedure for a sample of cTTs (From Cieza et al. 2005) and debris disks (from Chen et al. 2005) are shown for comparison. The L_{DISK}/L_* values of of wTTs disks fill the gap between the ranges observed for typical cTTs and debris disks, which are shown for comparison.

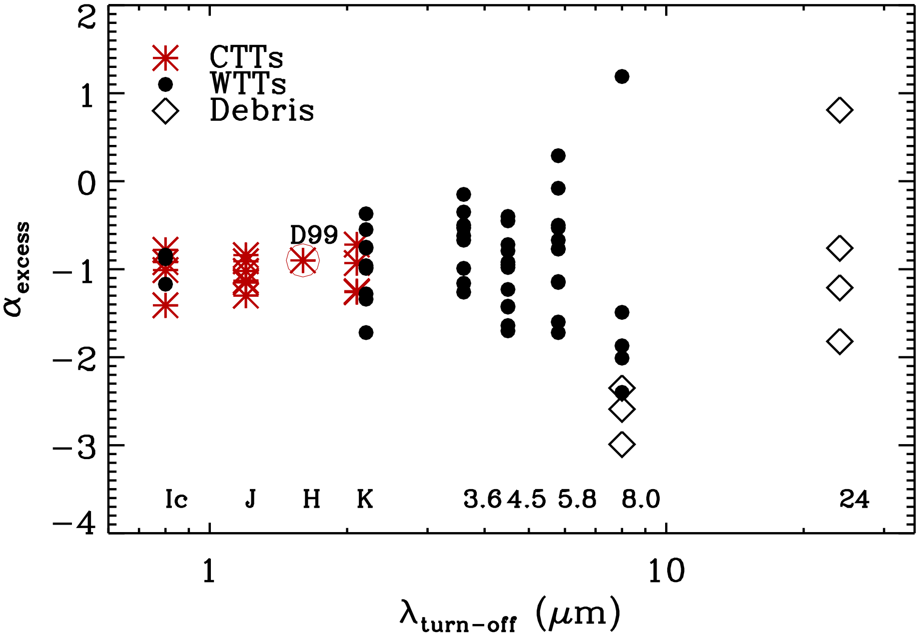

Figure 3.11 Distribution of excess slopes $\alpha_{\rm excess}$ vs. the wavelength at which the infrared excess begins $\lambda_{\rm turn-off}$ for the sample of wTTs (solid dots), a sample of cTTs in Chamaeleon from Cieza et al. (2005), the median SED of cTTs in Taurus from D'Alessio et al. (1999) in asterisks (marked as D99), and a sample of Debris disks from Chen et al. (2005) in diamonds. The diagram shows a much larger spread in inner disk morphologies of wTTs with respect of those of cTTs.

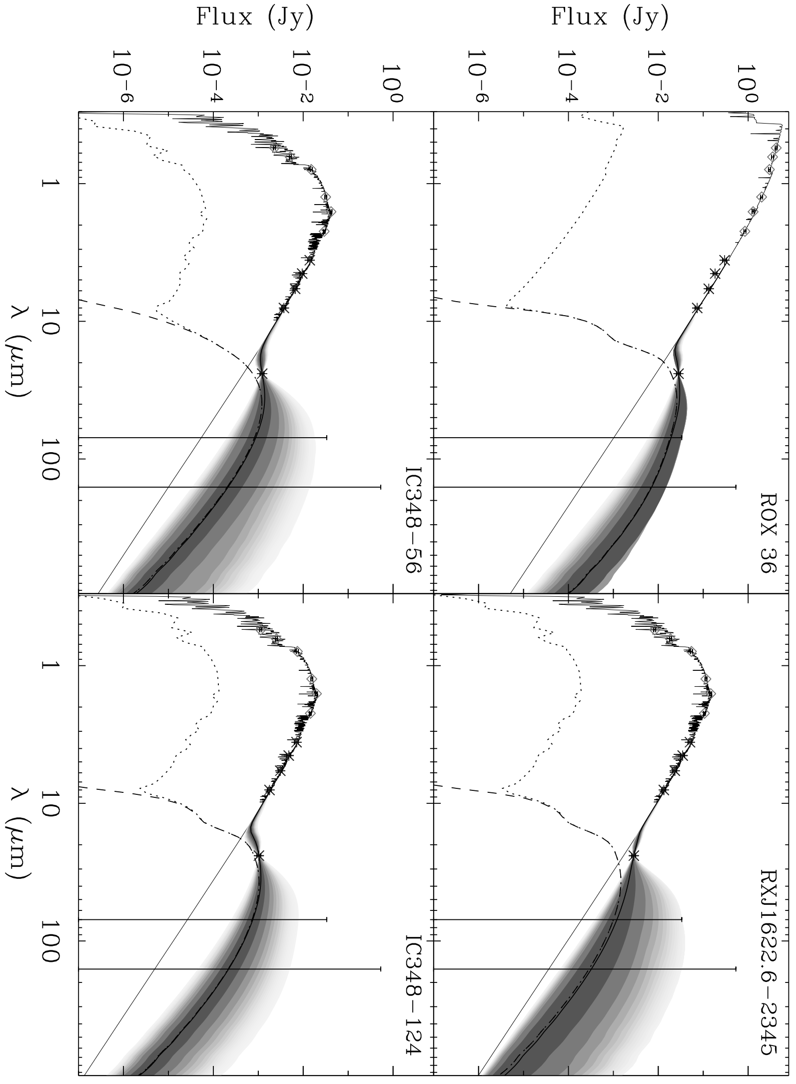

Figure 3.12 wTTs with 24 μm excess consistent with optically thin disks. On each plot, the darkest regions correspond to the most likely fits to the SEDs. The dashed line shows the thermal emission for the best-fit model, while the dotted line corresponds to the total disk emission (i.e. including scattered light emission.)

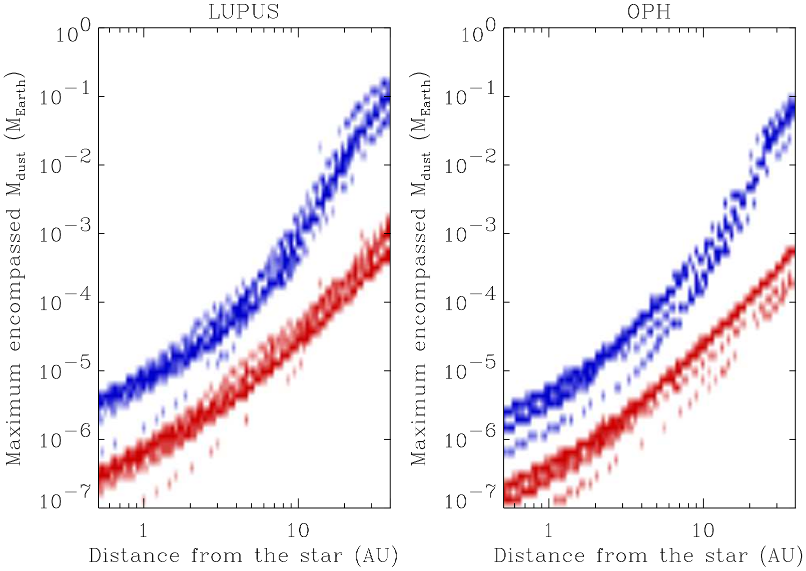

Figure 3.13 Maximum encompassed dust mass as a function of the distance from the star for the Lupus and Ophiuchus clouds (respectively left and right panels). The red area corresponds to mass upper limits when minimum grain sizes $a_{\rm min}$ between $0.05\,\mu$m and $0.5\,\mu$m are considered, while the blue area corresponds to $10\,\mu\text{m} < a_{\rm min} < 100\,\mu$m.

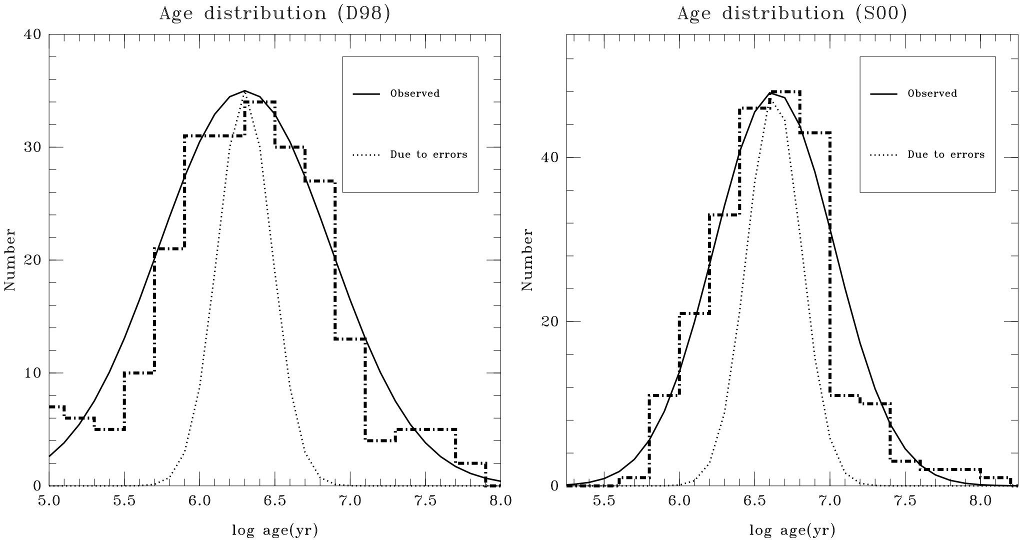

Figure 3.14 The distributions of stellar ages obtained for our sample using the D98 and S00 evolutionary tracks (left and right panels, respectively). The observed age distributions (solid lines) are significantly wider than what is expected from the propagation of observational errors into derived stellar ages (dotted lines).

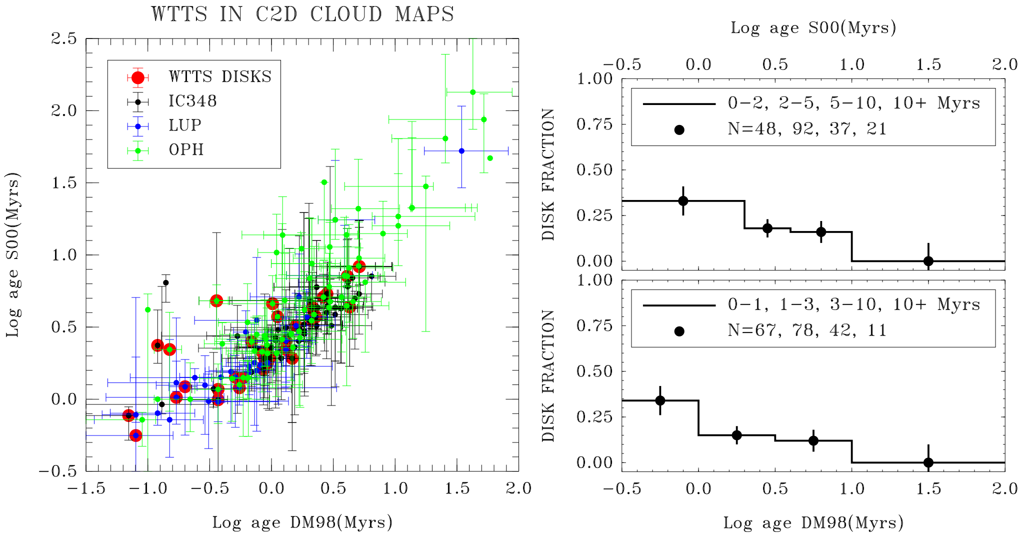

Figure 3.15 The stellar ages derived for our sample of wTTs using two different sets of evolutionary tracks (D98 and S00). The error bars have been calculated adopting a T_{eff} uncertainty equal to one spectral type subclass and a luminosity error calculated from the uncertainty in the distance (a). A clear decrease in the disk fraction is seen with increasing age. ∼40% of the targets that are both younger than 1 Myrs according to D98 tracks and younger than 2 Myrs according to S00 tracks have disks. None of the stars that are older than ∼10 Myrs according to either of the models have disks (b).

Chapter 4

Testing the Disk Regulation Paradigm with Spitzer Observations. I. Rotation Periods of Pre-main Sequence Stars in the IC 348 Cluster

4.1 Abstract

[1] We present 106 stellar rotation periods in the young cluster IC 348, 74 of which are new detections, increasing the total number of known periods in this cluster to 145. The period distribution resembles that seen in the heart of the Orion Nebula

---

[1] based on Cieza, L. & Baliber, N. 2006, ApJ, 649, 862

Cluster by Herbst and colleagues. Stars estimated to be less massive than $0.25\,M_\odot$ show a unimodal distribution of fast rotators (P $\sim$ 1–2 days), while stars estimated to be more massive than $0.25\,M_\odot$ show a bimodal distribution with peaks at $\sim$ 2 and $\sim$ 8 days. We combine all published rotation periods in IC 348 with *Spitzer* mid-IR (3.6, 4.5, 5.8, and 8.0 μm) photometry, which provides an unprecedented efficient and reliable disk indicator in order to test the disk-braking paradigm. We find no evidence that the tail of slow rotators in low-mass stars or the long period peak in high-mass stars are preferentially populated by objects with disks as might be expected based on the current disk-braking model. Also, we find no significant correlation between period and the *magnitude* of the IR-excess, regardless of the mass range considered. Given the significant improvement of *Spitzer* observations over near-IR indicators of inner disks, our results *do not* support a strong correlation in this cluster between rotation period and the presence of a disk as predicted by disk-braking theory. Rather, they are consistent with the suggestion that the correlation between period and the amplitude of the (I − K) excess reported in the past is a secondary manifestation of the correlation between the amplitude of near-IR excess and mass. By comparing our sample with a recent *Spitzer* census of IC 348, we find that the disk properties of our sample are indistinguishable from the overall disk properties of the cluster. We conclude that it is very unlikely that the lack of a correlation between rotation period and IR excess is due to a bias in the disk properties of our sample. Finally, we find some indication that the disk fraction decreases significantly for stars with very short periods (P $\lesssim$ 1.5 days). The fact that very fast rotators tend to have little or no excess has already been recognized by Rebull and colleagues for stars in the Orion Nebula Cluster. This is the only feature of our sample that could *potentially* be interpreted as evidence for disk braking. There is currently no alternative model to disk braking to explain the evolution of the angular momentum of pre-main-sequence stars. It has been proposed that the observational signatures of disk braking might be significantly masked by the intrinsic breadth of the initial period distribution. We argue that a more rigorous and quantitative analysis of the observational data is required before the disk-braking model can be regarded as inconsistent with observations.

4.2 Introduction

The evolution of the angular momentum of pre-main-sequence (PMS) stars is one of the longest-standing problems in star formation and is currently a controversial topic. As low-mass ($\sim$0.1–1.2 $M_\odot$) PMS stars evolve along their convective tracks, conservation of angular momentum dictates that they should spin up considerably. Low-mass PMS stars are believed to contract by a factor of $\sim$2–3 during their first 3 Myrs of evolution. If these stars were to conserve their specific angular momentum, j (where $j \propto R^2/P$), their rotation periods would be expected to decrease by a factor of $\sim$ 4–9. Using the models by D'Antona & Mazzitelli (1994, 1998, D98, hereafter),[2] and assuming angular momentum conservation and homologous contraction, Herbst et al. (2000) show that, given a starting period of 10 days,[3] all low-mass stars should rotate with periods shorter than $\sim$2 days by an age of 2 Myrs. However, observations show a large population of slow rotators (P $\sim$ 8.0 days) in clusters that, according to the same evolutionary tracks, are $\sim$2 Myrs old or older (Luhman et al., 2003). Also, the *very* broad distribution of rotation periods in the zero-age main sequence (ZAMS) suggests a very broad range of angular momentum loss between the birth line and the ZAMS.

Proposed mechanisms to explain the presence of slow rotators come in the form of magnetic-field interaction between the PMS star and material in its inner

---

[2] Available at http://www.mporzio.astro.it/ dantona/prems.html

[3] Adopting an initial period of 10 days is a conservative choice because recent observations (e.g. Covey et al., 2005) show that deeply embedded PMS stars tend to rotate *faster* than optically revealed PMS stars.

disk, locking the star's rotation to the Keplerian velocity of the disk's inner edge (Königl, 1991; Shu et al., 1994) and/or creating an accretion-driven wind (Shu et al., 2000), thereby transferring angular momentum from the star to material from the disk, preventing it from spinning up, unchecked. "Disk locking" and "disk braking" have become essential features of virtually every model of the angular momentum evolution of PMS stars.

The first order prediction of disk-locking and disk-braking models is that, as a group, stars with disks should rotate slower than stars that have already lost their disks and are free to spin up. However, finding an observational correlation between the presence (or lack) of a circumstellar disk and the rotation period of PMS stars has proven a difficult task. It has been repeatedly argued that one of the main difficulties in finding this predicted correlation is the lack of an appropriate disk indicator (Rebull, 2001; Herbst et al., 2002). *Spitzer*'s unprecedented mid-IR sensitivity allows, for the first time, an unambiguous identification of disks in a statistically significant sample of PMS stars with known rotation periods.

Here we report 74 previously unidentified rotation periods detected in the young cluster IC 348 which is situated in the East side of the Perseus Molecular Cloud. Our new periods, when combined with the periods in the literature, increase the total number of known periods in this cluster to 145. IC 348 is 315 pc away, young (2–3 Myrs), relatively compact (∼400 members, D ∼ 20 arcminutes), and has low extinction ($A_V < 4$) (Luhman et al., 2003). We combine all published rotation periods in IC 348 with *Spitzer* photometry to investigate the disk-braking scenario. This paper is organized as follows. In Section 4.3, we summarize previous observational attempts to identify a period–disk correlation. In Section 4.4, we describe our time series photometry and the observed rotation period distribution. In Section 4.5, we combine the rotation periods with the disk identification from *Spitzer* observations in order to search for the period–disk correlation predicted by the disk-braking paradigm. In Section 4.6, we discuss the implication of our results in the context of the disk-braking scenario. Finally, we summarize our results in Section 4.7.

4.3 Previous Observational Results

4.3.1 Rotation Periods and Disks in Other Clusters

Rotation periods of young stars with late spectral types can efficiently be obtained via precise differential photometry due the brightness modulation produced by the rotation of cool star spots and hot accretion columns reaching their surfaces. Fifteen years ago, the number of PMS stars with photometrically measured rotation periods was less than 100. This number is currently approaching 2000 (see Stassun & Terndrup (2003) for a recent review of observations). As the number of available rotation periods of PMS stars in young stellar clusters has increased, some groups have found apparent observational signatures of the disk-locking model. Attridge & Herbst (1992) report a bimodal distribution in the period of 35 PMS stars in the Orion Nebula Cluster (ONC), peaking at ~2 and ~8 days. This bimodal distribution has been confirmed by Herbst et al. (2000, 2002, H00 and H02, hereafter), who find it to be restricted to samples of stars with masses $> 0.25\,M_{\odot}$. H02 find that very low-mass stars ($\mathrm{M} < 0.25\,M_{\odot}$) exhibit a unimodal period distribution dominated by fast rotators with periods of 1–2 days. H00 and H02 also report a positive correlation between the presence of a circumstellar disk (as indicated by the presence of K-band excess) and slow rotation. The long-period peak in the bimodal distribution has been interpreted by these authors as being populated by disk-locked stars.

However, observations by several other groups do not confirm the bimodal nature of the period distribution of PMS stars in the ONC. Based on a sample of 254 stars, Stassun et al. (1999) find that the distribution of rotation periods between 0.5

and 8.0 days is statistically consistent with a constant distribution and that there is no apparent correlation between rotation period and near-IR excess. H00 argue that the Stassun et al. (1999) results do not show the expected bimodal distribution because their sample is dominated by stars of very low mass (i.e. $\mathrm{M} < 0.25\,M_{\odot}$). Still, based on 281 periods of stars in four fields *around* (but not including) the heart of the ONC, Rebull (2001) finds that the distribution of periods is statistically indistinguishable for stars less and more massive than $0.25\,M_{\odot}$. Herbst & Mundt (2005) argue that the "Flanking Fields" observed by Rebull (2001) represent a very heterogeneous sample in terms of age in which any structure in the period distribution would be wiped out. Rebull (2001) also finds no clear correlation between the presence of a circumstellar disk and three different disk indicators ($\mathrm{I_C}$–K, H–K, and U–V color excesses). Rebull (2001) and Hillenbrand et al. (1998) show that the correlation between near-IR excess and disk presence is far from perfect, leading to many disks being missed and false identification of disks. Rebull (2001) does conclude, however, that, given the lack of any observable correlation, disk locking is probably not the complete solution to the period distribution of PMS stars.

More recently, a statistically significant number of rotation periods in NGC 2264 have become available. In this cluster, Lamm et al. (2005) find a bimodal distribution for a sample of 184 stars with estimated masses $> 0.25\,M_{\odot}$. They find that the peaks in the period distribution observed in NGC 2264 are shifted toward shorter periods with respect to the ones found in the ONC. These shifts are interpreted as evidence of angular momentum evolution between the age of the ONC (~ 1 Myrs) and that of NGC 2264 (~ 2–4 Myrs). Using $\mathrm{R} - \mathrm{H}\alpha$ color criteria for disk identification, they argue that stars with disks tend to rotate slower than stars without disks. However, 60% of their sample have no disk-indicator measurements. Makidon et al. (2004) report periods for 118 stars in NGC 2264 with estimated masses $> 0.25\,M_{\odot}$. They find no evidence for a statistically significant bimodal distribution or a disk–

period correlation, regardless of the disk indicator used: EW(Hα), U–V, I–K, or H–K color excesses. Clearly, despite the categoric claims made by some authors (e.g. Herbst & Mundt, 2005), both the existence of a bimodal distribution in the rotation periods of PMS stars and the presence of a disk–rotation period correlation still await independent confirmation.

4.3.2 Rotation Periods and Disks in IC 348

All of the currently known periods for IC 348 can be collected from three papers (prior to this one): Cohen et al. (2004), Littlefair et al. (2005), and Kızıloğlu et al. (2005). Based on an observing campaign spanning more than 5 years, Cohen et al. (2004) report the rotation periods of 28 PMS stars in IC 348. The observations were taken in the I_C band with the 0.6 m telescope at the Van Vleck Observatory, which has a field of view of $10\rlap{.}'2$ on a side. Littlefair et al. (2005) report 32 additional periods based on I_C observations performed with the 1.0 m Jocobus Katelyn Telescope, which has a usable field of view of $9'$ on a side. Cohen et al. (2004) and Littlefair et al. (2005) only report 18 periods in common (partially because the Littlefair et al. (2005) observations are considerably deeper than those presented by Cohen et al. (2004)), but the periods in common show excellent agreement. Finally, Kızıloğlu et al. (2005) present 35 periods based on observations taken with the 0.45 m ROTSE-IIId robotic telescope which has a field of view of 1.85 degrees on a side and operates without a filter. Of these 35 periods, 17 were previously detected by Cohen et al. (2004), one was reported by Littlefair et al. (2005), and 18 were new detections. Kızıloğlu et al. (2005) calculated the confidence level of their rotation periods assuming white noise as the only source of error; however, as we discuss in Section4.4.2, that is a very optimistic assumption. Therefore, we only use the rotation periods from their work which have confidence levels greater than $5\,\sigma$.

Cohen et al. (2004) do not have enough stars to fully explore the presence of a bimodal distribution or the disk–period correlation in their sample but argue that the period distribution hints at the bimodality seen in the ONC. Littlefair et al. (2005) also see a hint of a period bimodality in the "high" mass stars but argue that it is not statistically significant given the small number of stars in the appropriate mass range. They did explore the possibility of an observable disk–period correlation in their sample. However, they find no correlation of period with K − L color excess (available for 30 stars) or Hα equivalent width (available for 43 stars). Also, Littlefair et al. (2005) suggest that the rotation period − (I–K) excess correlation reported by H02 might be due to a secondary correlation arising from the fact that (I–K) excess is easier to detect in stars more massive than $0.25\,M_\odot$ than it is to detect in lower-mass stars (Hillenbrand et al., 1998). The Kızıloğlu et al. (2005) paper focuses on an X-ray luminosity–period correlation and does not discuss the shape of the period distribution or any possible correlation between period and disk indicators.

4.4 Optical Observations and Data Reduction

4.4.1 Time Series Photometry

For our photometric measurements of IC 348 stellar rotation periods, data were collected using the McDonald Observatory 0.76 m Telescope and its Prime Focus Corrector (PFC) (Claver, 1992), which provides a 1° field of view, $46\farcm2$ x $46\farcm2$ of which is covered by a 2048 x 2048 CCD. I_C-band time-series photometry was performed on data collected during 3 observing runs: 2003, December 6th–22nd; 2004, January 4th–8th; and 2004, January 24th–30th. Ten slightly overlapping fields were used to cover the entire IRAC map of the Perseus Molecular Cloud obtained as part of the *Spitzer* Legacy Project "From Molecular Cores to Planet-forming Disks," (c2d) (Evans et al., 2003). Two of these fields are centered on the IC 348 and NGC 1333 clusters and are referred as 'cluster fields' in the following discussion. Three frames were taken for every pointing of the cluster fields: a 15 sec exposure followed by two 150 sec exposures. For the rest of the fields, only two frames were taken, namely, a 3 sec exposure followed by a 15 sec exposure. From the 3 observing runs, a total of ∼140 useful data points were obtained for each star of the cluster fields and ∼50 data points for stars in the rest of the fields. Typical rotation periods of PMS stars range from ∼0.2 to ∼15 days. therefore, the observations obtained provide both an appropriate sampling rate and baseline to be sensitive to all expected rotation periods.

We tested the range of periods recoverable in our data by inserting sine waves of several different amplitudes into data from nonvarying stars of various magnitudes in the IC 348 field. The model variations ranged in period from 0.3 to about 19 days. Using the same detection method in identifying rotation periods in IC 348 PMS stars, recovery rates for the model variations were about 71% for periods between 0.4 and 0.5 days and 52% for periods between 0.5 and 0.6 days, although most of the periods that were not accurately identified in this regime were a factor of 2 away from the actual period, which would not affect the overall rotation period distribution significantly. Nearly 100models with periods of 0.6 days and above were correctly identified. Therefore, we conclude that the observations obtained provide both an appropriate sampling rate and baseline to be sensitive to all expected rotation periods.

After standard CCD reductions were performed with the IRAF imred.ccdred package, photometry is performed using a combination of the ISIS image subtraction software (Alard & Lupton, 1998; Alard, 2000) and our own code. After residual images are generated by ISIS, our code measures aperture sums for stars in the residual images and produces light curves measured in percent flux normalized to a reference image. Here we present the rotation periods found in the field covering the IC 348 cluster. Rotation periods for stars in the rest of the Perseus cloud, including those in the cluster NGC 1333, will be presented in a future paper.

4.4.2 Finding the Rotation Periods

To search for periodic signals in the light curves of our targets, we used the standard periodogram technique discussed by Scargle (1982) for analyzing periodic signals of unevenly spaced data and the prescription given by Horne & Baliunas (1986) to select the optimum number of independent frequencies used to inspect the data. The initial period range of the periodogram was set to 0.1–50 days, but, since the number of independent frequencies inspected is heavily weighted toward higher frequencies, low frequencies are not well sampled in this range, which produces a large uncertainty for long periods. For this reason, a new periodogram was produced for every star. In this new periodogram, the shortest period sampled was set to 0.75 times the period found in the first pass. For our data set, the normalized power spectrum (PS) peak of the Scargle periodogram corresponding to a false alarm probability (FAP, as defined by Horne & Baliunas, 1986) of 1% is ∼10. This threshold corresponds to the 1% probability that a power spectrum peak reaches a given high by pure fluctuations of white, uncorrelated noise, and is clearly too optimistic.

The assumption that the data points are statistically uncorrelated and that noise can be characterized as white is usually not valid for time series photometry of PMS stars (see Rebull, 2001, and references therein). The distribution of PS peaks for the entire sample of ∼3600 stars in the IC 348 field is shown in Figure 4.1. The left side of the peak can be characterized as a Gaussian centered at 6.4 with a FWHM of 1.5. Rightward of the peak, the PS distribution has a tail corresponding to light curves with real periodic signals combined with spurious signals produced by non-white noise. The shape of the distribution of the PS peaks suggests that periods become unreliable for PS peaks lower than ∼20. Since our field contains over 60 stars with known rotation periods from the literature, we can also estimate our PS confidence threshold by plotting the agreement of our periods with published values from Cohen et al. (2004), Littlefair et al. (2005), and Kızıloğlu et al. (2005) as a function of the peak of the PS (Figure 4.2).

Figure 4.2 shows that even though some of our periods agree with published values down to a PS peak of ∼10, many values start to diverge when the peak is ∼20. Above a PS peak of 20, the periods we find disagree with published periods for only 5 objects, labeled A through E in Figures 4.2 and 4.3. In what follows we analyze these objects one by one. Object A (ID 92) has a PS peak of 41.9. We find a period of 4.55 days while Kızıloğlu et al. (2005) finds a period of 1.28 days. Figure 4.3 shows that the period found by Kızıloğlu et al. (2005) can be explained as the beating of our period and a 1 day sampling interval (i.e. a relation of the form $1/\mathrm{P}_{\mathrm{beating}} = \pm 1 \pm (1/\mathrm{P})$, denoted by the solid line). Object B (ID 104) has a PS peak of 32.5, and we find a rotation period of 8.57 days. Kızıloğlu et al. (2005) assign to this object a rotation period of 32.28 days, which is much longer that the typical rotation periods of PMS stars. Since the period found by them is close to a factor of four larger than our period, it is likely to be an harmonic of the real period.

For object C (ID 100), which has a PS peak of 30.8, we find a period of 19.8 days, while Littlefair et al. (2005) find a period of 13.4 days. Both cases represent an unusually long rotation period and the discrepancy is likely to be due to the increasing uncertainty with increasing period for relatively short observing campaigns. Since our observations span 52 days and Littlefair et al. (2005) observations span only 26 days, our period is more likely to be correct. For object D (ID 125), we find a PS peak of 26.0 and a period of 10.64. Kızıloğlu et al. (2005) find a period of 22.51 which is also likely to be an harmonic of the real period. Finally, for object

E, we find a PS peak of 21.6 and a period of 18.3 days. Littlefair et al. (2005) find a period of 8.4 days. In this case, it is likely that our period is an harmonic of the real period found by the other group. The contamination of rotation-period distributions by harmonics and "beat periods" at the 10% level has already been seen by many groups (e.g. H02 and Lamm et al., 2005) when comparing their results to previously published data. In addition to a change in the beating of a period within the sampling rate (which would be different for each observing run), the periods themselves may change between observing runs (as seen in Rebull, 2001). Clearly, the lower the adopted PS threshold, the larger the contamination fraction. For definitiveness, based on Figures 4.1 through 4.3 and the above discussion, we adopt a PS peak of 22.0 as the criteria to consider the periodic signal to be an accurate representation of the rotation period. This corresponds to the highest PS peak of an object showing a significant discrepancy with published periods that we believe is due to our own incorrect period (object E in Figures 4.2 and 4.3).

4.4.3 The Rotation Period Distribution

Inspecting the periodograms of the ∼3600 stars detected in our field, we find 106 objects with PS peaks higher than 22, the adopted detection threshold. Of these 106 objects, only 32 had previously known rotation periods. Thus, we have obtained 74 new rotation periods. Our periods more than double the number of previously known rotation periods in the IC 348 cluster and increase the total number to 145; a comprehensive list of all known stars with periods in IC 348 appears in Table 4.1. The coordinates of each periodic stars listed are those of the closest counterpart identified in the 2MASS survey. Figure 4.4 shows the histogram of all the rotation periods listed in Table 4.1. The period distribution extends to almost 30 days; however, for the rest of the paper, we restrict our analysis to the 133 stars listed in Table 4.1 with periods shorter than 15 days. We decided to make this cut because stars with periods > 15 days (less than 5% of the total sample) are likely to be more contaminated by harmonics than the rest of of stars (in the previous section we found that periods longer than 15 days account for 3 out the 5 stars with PS peaks larger than 22 which have a period disagreement with previously published values). Also, any MS star contaminating our sample is likely to have a rotation period > 15 days.

4.4.4 The Periodic Sample

The stellar population of IC 348 and their disk properties are very well characterized. Luhman et al. (2003) present a spectroscopic census of the cluster members of the central $16' \times 14'$ area of the cluster. This census is nearly complete for stars with spectral types M8 and earlier and yields a sample of 288 objects whose membership has been established based on their proper motions, positions in the H–R diagram, A_V's, and spectroscopic signatures of youth. More recently, Lada et al. (2006) present *Spitzer* observations of all the 288 objects identified by Luhman et al. (2003) as IC 348 members. These results are based on the the same IRAC GTO observations we use for disk identification, and will be discussed further in Section 4.6.1.

Of the 145 periodic stars listed in Table 4.1, 94 are identified by Luhman et al. (2003) as members of the cluster, and each of them have measured spectral types. We note that the 51 stars in our sample which are *not* identified by Luhman et al. (2003) as IC 348 members fall outside the $16' \times 14'$ field for which they present a complete membership census. However, Cambrésy et al. (2006) present an extinction map of the IC 348 region and conclude that the cluster extends up to $25'$ from its center, placing all the objects in our sample within those cluster boundaries. Most of the periodic stars in our sample turned out to be known members of IC 348, while only 8% of all of the stellar light curves we inspected correspond to the 288 known members identified by Luhman et al. (2003). More importantly, none of our periodic stars are identified by Luhman et al. (2003) as foreground or background non-members of the cluster. This indicates that periodicity is a very efficient selector for PMS stars, and we conclude that it is therefore likely that most, if not all, of the periodic stars falling outside the region studied by Luhman et al. (2003) are in fact members of the IC 348 cluster.

4.4.5 Mid-IR Observations and Data Reduction

As part of the c2d Legacy Project (Program ID 178), *Spitzer* has mapped 3.8 sq. deg. of the Perseus Molecular Cloud with the Infrared Array Camera (IRAC, 3.6, 4.5, 5.8, and 8.0 μm) containing the IC 348 cluster and its surroundings. The IRAC maps consist of four dithers of 10.4 sec observations divided into two epochs (i.e. a total of 41.6 sec exposures per pixel) separated by several hours. The second-epoch observations were taken in the High Dynamic Range mode, which includes 0.4 sec observations before the 10.4 sec exposures, allowing photometry of both bright and faint stars at the same time. See Jorgensen et al. (2006) for a detailed discussion of the c2d IRAC observations of the Perseus Molecular Cloud. Also, *Spitzer* has obtained deep observations IC 348 as part of the Guaranteed Time Observer program (GTO) “Deep IRAC imaging of Brown Dwarfs in Star Forming Clusters” (Program ID 36). These observations cover a $15' \, \mathrm{x} \, 15'$ field of view centered in the cluster and consists of two pairs of 8 dithers of 96.8 sec exposures for the 3.6, 4.5, and 5.8 μm observations (e.g. 1600 sec exposures per pixel). A characteristic of this observing mode only splits each $\sim$100 sec IRAC4 exposure into two equal exposures. As a result, the 8.0 μm observations consist of four pairs of 8 dithers of 46.8 sec exposures.

The results of the *Spitzer* observations of the entire population of IC 348 members is presented in Lada et al. (2006). For consistency, we processed the Basic Calibrated Data from the GTO program and produced point source catalogs using the c2d pipeline. The c2d pipeline uses the c2d mosaicking/source extraction software, c2dphot (Harvey et al., 2004), which is based on the mosaicking program APEX developed by the *Spitzer* Science Center and the source extractor Dophot (Schechter et al., 1993). See Evans et al. (2006) for a detailed description of the c2d data products. We searched the c2d and GTO IRAC point source catalogs and found fluxes for 129 of the 145 objects listed in Table 4.1 (i.e., 16 of the periodic objects fall outside the c2d/GTO IRAC maps of Perseus).

4.4.6 Complementary data

In addition to the rotation periods and the IRAC photometry, we have collected the following complementary data for our stars in Table 4.1. First, with the same telescope used to obtain the time series photometry, we obtained RI absolute photometry for our field. We performed PSF fitting photometry with the standard IRAF implementation of the DAOPHOT (Stetson, 1987) and used Landolt standards for calibration (Landolt, 1992). We report RI data for all but a few stars listed in Table 4.1 that fall outside the field due to a small pointing error. Also, we have collected the 2MASS J, H and K magnitudes for all but 3 very faint stars. Finally, we have collected all the spectral types available for our sample, covering 93 objects from Luhman et al. (2003). All the complementary data are also listed in Table 4.1.

4.5 Testing the Disk Regulation Paradigm

4.5.1 Identification and Classification of Mid-IR Excess

In recent *Spitzer* studies of circumstellar disks, different groups adopt different disk identification criteria. An effective and reliable method of disk identification is crucial to this type of survey, especially when dealing with a small sample size, such as is the case with the IC 348 rotation periods. A near-100% recovery of disks with few or no false positives using IRAC photometry is possible. Here we discuss the disk-identification criteria used in two studies particularly relevant to this paper: The study of the correlation between stellar rotation and IRAC excess in Orion (Rebull et al., 2006) and the *Spitzer* observations of all the confirmed members of IC 348 (Lada et al., 2006). Bare stellar photospheres have an IRAC color ~ 0.0, while stars with an IR excess have positive colors. The broader the color baseline used, the larger the mean IR excess of the stars with disks; therefore, the IRAC color that provides the clearest separation between stars with and without disks is [3.6]–[8.0]. For their study of periodic stars in the ONC, Rebull et al. (2006) adopt the color $[3.6]–[8.0] > 1.0$ as the criterion for disk identification. This boundary is chosen based on the shape of the [3.6]–[8.0] histogram of their sample, which shows a clear deficit of periodic stars around this color. Lada et al. (2006) use a criterion based on the slope, α, of a power law fit to the four IRAC bands. From the comparison to disk models, they identify objects with $\alpha > -1.8$ as optically thick disks. Based on the predicted slope of an M0 star and the typical uncertainty in the power law fit, they identify objects with $\alpha < -2.56$ as bare stellar photospheres. Objects with intermediate slopes, $-2.56 > \alpha > -1.8$ are termed “anemic disks” and are interpreted as optically thin disks or disks with inner holes.

We find that the disk criteria adopted by the Lada and Rebull groups identify a slightly different set of stars. In this section, we propose alternative disk identification criteria and explore the differences between our criteria and those adopted by the other groups. In order to construct our disk-identification criteria, we first collect IRAC colors for a large sample of PMS stars with high signal to noise ratios (S/N) from the literature. We construct our sample from the classical and weak-lined T Tauri stars (cTTs and wTTs) studied by Hartmann et al. (2005), Lada et al. (2006), Padgett et al. 2006, and Cieza et al. (2006, in prep). To minimize the uncertainties, we restrict the sample to the 435 objects for which reported photometric errors are less than 0.1 mag and explore the location of this sample in different color-color diagrams. We find that the [3.6]–[8.0] *vs.* [3.6]–[5.8] diagram shown in the left panel of Figure 4.5 provides the best separation of stars with an without a disk. This combination of colors results in a well-defined locus of stellar photospheres and of cTTs wTTs disks. We identify the stars with [3.6]–[8.0] $>$ 0.7 located along the dash-dotted line as stars with disks and stars with [3.6]–[5.8] $<$ 0.5 and [3.6]–[8.0] $<$ 0.5 as diskless stellar photospheres. Only ∼1% of the sample (5/435) have 0.7 $>$ [3.6]–[8.0] $>$ 0.5, where the colors of the weakest disks seem to overlap with the colors of the redder stellar photospheres. We note that the few photospheres slightly redder than the main clump correspond, for the most part, to M2–M6 stars.

Incidentally, a linear fit to the sample of stars with disks yields

$$([3.6] - [8.0])_{\mathrm{DISKS}} = 1.39 \pm 0.05 \times ([3.6] - [5.8])_{\mathrm{DISKS}} + 0.43 \pm 0.03$$

This relationship extends over one magnitude in the [3.6]–[5.8] color and two magnitudes in the [3.6]–[8.0] color with a $1\,\sigma$ dispersion (i.e. $([3.6]\text{–}[8.0])_{\mathrm{FIT}}\,/\,([3.6]\text{–}[8.0])$ of 0.15 mag). The tightness of this *IRAC locus of T Tauri star disks* is comparable to that of the loci of cTTs in the near-IR defined by Meyer et al. (1997). Therefore, one can use this convenient IRAC locus of disks as an initial tool to identify wTTs and cTTs candidates in any IRAC field. One might expect contamination from galaxies with IRAC colors similar to stars in this locus. However, in the fields observed by the Spitzer Wide-area InfraRed Extragalactic survey (SWIRE), only about ∼15% of the galaxies fell within a 3σ distance from this IRAC locus.

In order to compare our disk-identification criteria to those adopted by Lada et al. (2006) and Rebull et al. (2006), we plot the [3.6]–[8.0] *vs.* [3.6]–[5.8] colors reported by the Lada group for their entire sample of IC 348 objects (288 stars) with different symbols, indicating the classification given in their study (Figure 4.5, right panel). This figure shows that the disk-identification criterion adopted by Rebull and collaborators (i.e. [3.6]–[8.0] $>$ 1.0) selects a sample of stars which has an almost one-to-one correspondence with the objects classified as optically thick disks by the Lada group, meaning the Rebull criterion misses disks with weaker mid-IR signatures. On the other hand, Lada and collaborators classify as anemic disks both objects that belong to our IRAC locus of T Tauri star disks and some objects which have colors consistent with bare stellar photospheres (i.e., the Lada criteria overestimate the number of anemic disks). We believe this is a consequence of adopting criteria for disk identification which are independent of spectral type. In fact, most of the objects classified as anemic disks by Lada et al. (2006) which do not satisfy our disk identification criteria are late M stars. In addition, the scatter in the right panel of Figure 4.5 is dominated by the photometric error in 8.0 μm fluxes of the faintest stars, which also comprise the handful of objects with nonphysical negative [3.6]–[8.0] colors.

Figure 4.6 shows the [3.6]–[8.0] *vs.* [3.6]–[5.8] colors of our periodic sample in IC 348, restricted to the 111 stars in Table 4.1 with 3.6, 5.8, and 8.0 μm fluxes and periods $<$ 15 days. We find that 41 stars have a color [3.6]–[8.0] $>$ 0.7, indicating the presence of a disk, and that only 3 stars have borderline colors, 0.7 $>$ [3.6]–[8.0] $>$ 0.5. Two of the objects with intermediate colors (ID= 73 and 113) are faint M4.75–M5 stars; therefore, we classify them as diskless stars. The other object (ID=89) is of unknown spectral type. We searched the catalogs from the c2d Legacy Project and found that this object has a 24 μm flux of 23.1 mJy, which corresponds to a 24 μm excess of over 4 magnitudes. Thus, we classify this object as possessing a disk, leading to a total number of disks in our sample of 42 and a disk fraction of 38% ±4% (42/111).

Given the fact that only 3 objects in our sample have a somewhat ambiguous disk identification, we estimate our disk census to be both complete and reliable at the ∼97% level. In contrast, Hillenbrand et al. (1998) show that color-color diagrams combining optical and near-IR data can only identify $< 70\%$ of the accretion disks in a given sample and that this efficiency decreases for very low-mass stars (e.g. spectral types later than M2). Also, *Spitzer* can identify stars with low accretion rates and disks with inner holes which have no near-IR excess, making *Spitzer* data (combined with effective disk-identification criteria, as described above) a more effective tool for disk identification than any ground-based near-IR observations.

Having accurately determined which stars have disks, one can then conduct a comprehensive search for any correlation between stellar rotation period and the presence of a disk. The period distributions for stars with and without a disk are shown in Figure 4.7, while Figure 4.8 shows the [3.6]–[8.0] color as a function of rotation period. The most striking feature of Figure 4.7 is that stars with disks show a bimodal distribution even more-clearly defined than that seen in the entire sample. This fact goes directly against the first order prediction of the current disk-locking paradigm in which the bimodal distribution itself is a manifestation of two populations of stars, one with disks (slow rotators) and another without disks (fast rotators). Similarly, Figure 4.8 shows no evidence of any correlation between period and the *magnitude* of the IR excess. A standard Spearman test yields over an 84% chance that the quantities are completely uncorrelated. However, before drawing any further conclusions from Figures 4.7 and 4.8, we would like to explore and attempt to disentangle another variable which has been claimed to correlate with rotation period: Stellar mass.

4.5.2 Mass Dependence

Following H00, most authors have divided their rotation period distributions into “high mass” and “low mass” stars. The H00 masses come from Hillenbrand (1997) and were obtained using the evolutionary tracks by D98. The $0.25\,M_\odot$ division should be regarded as a nominal value throughout the paper since PMS stellar masses are highly model dependent. We point out that D98 models yield systematically lower masses than other widely used evolutionary models such as those presented by Baraffe et al. (1998) and Siess et al. (2000). According to the D98 models, for ages less than several million years, the $0.25\,M_{\odot}$ division corresponds to the M2 spectral type. Therefore, other authors (e.g Rebull, 2001) have used spectral type as a proxy for stellar mass. Optical colors ($\mathrm{R_C}$–$\mathrm{I_C}$) have also been used to differentiate between low- and high-mass stars (e.g. Lamm et al., 2005).

Ever since a statistically significant number of rotation periods became available, it has been suggested that rotation periods are highly dependent on mass. H00 argued that stars more massive than $\sim 0.25\,M_{\odot}$ show a bimodal distribution, while lower-mass stars show a more uniform distribution and a lack of fast rotators ($\mathrm{P} < 2$ days). H00 attributed the lack of low-mass fast rotators to a deuterium-burning phase that temporarily halts the contraction of low mass stars. However, deeper observations of the ONC (e.g. H02) later showed a large population of fast-rotating, low-mass stars. In fact, H02 argue that low-mass stars rotate significantly faster than high-mass stars and that the period distribution of low-mass stars peaks at $\sim$2 days (i.e. the apparent lack of low-mass fast rotators previously reported was a selection effect). Using $\mathrm{R_C}$–$\mathrm{I_C}$ color criteria, Lamm et al. (2005) also find that low-mass ($\mathrm{R_C}$–$\mathrm{I_C} > 1.3$) stars rotate, on average, faster than “high” mass ($\mathrm{R_C}$–$\mathrm{I_C} < 1.3$) stars. However, other authors have cast doubts on this conclusion. Rebull (2001) finds that the periods of high-mass stars (spectral type earlier than M3) and low-mass stars (spectral types M2 and later) in the Orion Flanking Fields are statistically consistent with each other. However, as mentioned earlier, Herbst & Mundt (2005) regard the Rebull (2001) sample as too heterogeneous in terms of age for any period dependence on disk properties or mass to be observable.

Naturally, we would like to explore the mass dependence in our period distribution. In order to divide our sample into "high" and "low" mass stars, we take advantage of the large amount of information collected in Table 4.1. Most of the stars in our sample (94/145, 64%) have spectral types from Luhman et al. (2003). We classify stars with spectral type M2 and later as low-mass stars and stars with spectral types earlier than M2 as high-mass stars. For stars without spectral types, we adopt the following procedure. First, we classified the objects based on their [3.6]–[4.5] *vs.* [3.6]–[8.0] colors. Sources with [3.6]–[4.5] < 0.2 and [3.6]–[8.0] < 0.5 are consistent with bare stellar photospheres. For these objects, we obtain photometric approximations of spectral types by fitting the RIJHK and IRAC magnitudes to stellar models of different spectral types corrected for extinction.

The stellar models were constructed as in Cieza et al. (2005), from optical and near-IR broadband colors from Kenyon & Hartmann (1995) tied to IRAC colors based on Kurucz models (Kurucz, 1993). We adopt the extinction corrections also listed in Cieza et al. (2005). For stars with [3.6]–[4.5] < 0.2 and [3.6]–[8.0] > 0.5 (e.g. stars without $4.5\,\mu$m excess but with significant $8.0\,\mu$m excess), we follow the procedure describe above, but without fitting the $8.0\,\mu$m or $5.6\,\mu$m data points (in practice, the weights of the IRAC data points in the fit are set by the corresponding "excess"). We tested our procedure with 58 stars with spectral types and [3.6]–[4.5] < 0.2 and find that, remarkably, our photometric spectral types typically agree with those reported by Luhman et al. (2003) to within a spectral subtype. Namely, $\mathbf{MEAN}(\mathrm{Spt}_{\mathrm{Luhman}} - \mathrm{Spt}_{\mathrm{phot}}) = 0.26$ and $\mathbf{MEAN}(\mathrm{ABS}(\mathrm{Spt}_{\mathrm{Luhman}} - \mathrm{Spt}_{\mathrm{phot}}))=0.69$, where one spectral type subclass equals unity and spectral types are ordered from early to late.

Finally, objects with [3.6]–[4.5] > 0.2 and [3.6]–[8.0] > 0.5 are likely to be cTTs with thick inner disks (e.g. Lada et al., 2006). Meyer et al. (1997) show that cTTs occupy a very-well-defined locus in the *dereddened* H–K *vs.* J–H diagram. We take advantage of this fact and estimate the $\mathrm{A_V}$ of the few objects with [3.6]–

[4.5] < 0.2 and unknown spectral types by dereddening them to the locus defined by Meyer et al. (1997). Using the $\mathrm{A_V}$'s estimated in this way, we deredden their $\mathrm{R_C - I_C}$ colors. We classified stars with $\mathrm{(R_C - I_C)_o} < 1.3$ as high-mass stars and stars with $\mathrm{(R_C - I_C)_o} > 1.3$ as low-mass stars (where a $\mathrm{R_C - I_C}$ color of 1.3 corresponds to a spectral type of M2). The period distributions for low- and high-mass stars are shown in Figures 4.9. We find that the period distributions are remarkably similar to those presented by H02 for the heart of the ONC. Stars estimated to be less massive than $0.25\,M_\odot$ show a unimodal distribution dominated by fast rotators (P ∼ 1–2 days) and a tail of slow rotators, while stars estimated to be more massive than $0.25\,M_\odot$ show a bimodal distribution with peaks at ∼2 and ∼8 days. Thus, our results confirm the strong dependence of stellar rotation on mass, as observed by H02 in the heart of the ONC and by Lamm et al. (2005) in NGC 2264.

As mentioned in section 4.3, Lamm et al. (2005) find that the peaks in the period distribution observed in NGC 2264 are shifted toward shorter periods with respect to those seen the ONC. These shifts are interpreted as evidence of angular momentum evolution between the ONC (age ∼1 Myrs) and NGC 2264 (age ∼ 2–4 Myrs). Do we see the same angular momentum evolution between the ONC and IC 348 (age ∼3 Myrs)? On one hand, the location of the peaks in the period distribution of the high-mass stars in IC 348 suggests that they have spun down with respect to those in the ONC. On the other hand, the median period of the low-mass stars in IC 348 seems to suggest that these stars have spun up with respect to the low-mass stars in the ONC. However, given the size of the sample and the magnitude of the changes, none of the differences are statistically significant.

4.5.3 IR Excess–Rotation Period Correlation?

Taking the low- and high-mass stars separately, is there any evidence that stars with disks rotate slower, as a group, than stars without disks? Given the substantial improvement in the disk identification efficiency using IRAC observations over near-IR indicators, the disk–period correlation reported by H00 and H02, if real, should be readily-detectable in our data. Figure 4.10 shows the [3.6]–[8.0] color *vs.* period for both low- and high-mass stars. A standard Spearman test shows that there is a 68% chance that the period of high-mass stars is completely uncorrelated with IR excess. This chance drops to 23% for low-mass stars, but the significance level is not anywhere near the level found by H02 for the correlation between period and (I–K) excess in Orion stars (H02 find that there is a 10^{-10} chance that period and (I–K) excess are uncorrelated quantities). Our results support the claim made by Littlefair et al. (2005) that the correlation between period and (I–K) is a secondary manifestation of the correlation between near-IR excess and mass. Most of the power in the weak correlation between period and IRAC excess comes from the fact that the 5 fastest rotators (all of them low-mass objects) show little or no excess. We discuss this point in Section 4.6.2.

Low-mass stars show a unimodal distribution peaking at ∼1–2 days and a tail of slow rotators. According to the disk-braking model, one would expect stars without disks to be concentrated around the 1–2-day peak and stars with disks to be concentrated in the long-period tail. We find no evidence of that being the case. If anything, we find the opposite to be true. The median period of the sample of low mass objects is 3.58 days. The disk fraction of the objects rotating faster than the median is 38% ±8% (11/29), while the disk fraction of the objects rotating slower than the median is 21% ±7% (6/29). High-mass stars show a bimodal distribution peaking at ∼2 days and ∼8 days. In the context of the disk-braking model, one would expect, for the most part, stars populating the short-period peak to be objects without disks and the stars populating the long-period peak to be stars with disks. Again, we find no significant evidence for disk braking. We find that 38% ±10% (9/24) of the high-mass stars rotating faster than the median (P = 6.9 days) have disks, while a marginally higher fraction of stars rotating slower than the median, 52% ±10 (13/25), have disks.

4.6 Discussion

The fact that we find no evidence for a correlation between period and the presence of IR excess represents a serious challenge to the current paradigm of the evolution of angular momentum of PMS stars, which relies heavily on disk braking to explain the presence of slowly rotating PMS and ZAMS stars. It could be argued that the $8.0\,\mu$m excess is *too good* a disk indicator, enabling detection of disks with inner holes too large for the disk to still be locked to the star. However, disk models show that stars with inner holes have lower $8.0\,\mu$m excesses than stars with disks extending inward to the dust sublimation temperature (e.g. **?** models of wTTs *versus* Cieza et al. (2005) models of cTTs). Therefore, even if a diversity of inner hole sizes were responsible for masking the disk–period correlation in the histograms in Figure 4.7, one would expect periods to correlate with the *magnitude* of the $8.0\,\mu$m excess (one would expect stars with strong $8.0\,\mu$m excess to rotate slower than stars with weak or no $8.0\,\mu$m excess). As illustrated by Figure 4.8, we find no evidence of such a correlation either. Throughout the paper, we use the $8.0\,\mu$m excess as a disk indicator because, as discussed in Section 4.5.1, it provides the best separation between stars with and without disks; however, we see no period–IR excess correlation using the excess at any of the IRAC bands as a disk indicator.

There is currently no quantitative theory for disk braking; however, some authors have tried to make some quantitative analysis based on the derived distributions of angular momentum for stars of different ages. Herbst & Mundt (2005) construct the distributions of the specific angular momentum of the ONC, NGC 2264, and a sample of main sequence (MS) stars, combining objects from the Pleiades, α Per, and the IC 2602 clusters. Specific angular momentum, j, is obviously a more relevant quantity than period to study the evolution of angular momentum of PMS stars. However, its calculation requires the knowledge of the stellar radius (e.g. $j \propto R^2/\mathrm{P}$). To that end, Herbst & Mundt (2005) assume a mean radius of $2.09\,\mathrm{R}_\odot$ for stars in the ONC and of $1.7\,\mathrm{R}_\odot$ for stars in NGC 2264. They argue that the ONC, NGC 2264, and MS clusters represent a clear sequence in the evolution of angular momentum corresponding to 3 different ages, nominally: 1, 2 and 50 Myrs.

Herbst & Mundt (2005) suggest that the broad distribution of angular momentum observed in their sample of MS stars can be explained by assuming that 40–50% of the PMS stars conserve angular momentum when they contract while the remainder of the stars, *which should already be slow rotators by the ages of the ONC and NGC 2264*, must stay disk-locked for up to 5 Myrs in order to account for the slow rotators in the ZAMS sample (this is consistent with the findings of (Rebull et al., 2004)). Were this the case, we should see strong evidence for disk locking in our sample of PMS stars with rotation periods and IR-excess measurements. Since we see no such evidence, our results are inconsistent with the Herbst & Mundt (2005) claim, unless, for some reason, our sample is severely biased against disk-locked stars. We investigate the possibility of such a bias in the next section.

4.6.1 Sample bias?

A critical point regarding the validity of the conclusions of this paper is to what degree our sample of stars with rotation periods is representative of the entire population of IC 348 members. Fortunately, the stellar population of IC 348 and its disk properties are very well characterized. As discussed in Section 4.4.4, Luhman et al. (2003) present a detailed spectroscopic census of IC 348 cluster members, complete for spectral type M8 and earlier, and Lada et al. (2006) have recently presented *Spitzer* observations of all the 288 objects identified by Luhman et al. (2003) as IC 348 members. Because the Lada results are based on the same IRAC GTO observations we use for disk identification, they provide a perfect test to investigate the possibility of any strong disk fraction bias in our sample of IC 348 members with rotation periods with respect to the entire cluster population.

Cohen et al. (2004) argue that, since none of the 28 periods they report correspond to known cTTs, rotation period samples are heavily biased against accreting objects, where disk braking is more likely to occur. In contrast, Littlefair et al. (2005) report that 43% of their periods correspond to cTTs, a result which is not significantly different from the overall cTTs fraction among IC 348 members ($\sim 40\%$). They argue that the drastic improvement in the efficiency for obtaining rotation periods of cTTs in their work with respect to the Cohen et al. (2004) results is due to the high sampling density of their observations; cTTs are highly non-periodic on time scales larger than a few days or weeks. Cohen et al. (2004) periods come from an observing campaign spanning several years with a very low temporal density, while Littlefair et al. (2005) observations come from a 26-night campaign with a typical sampling rate of one frame every 10 minutes. Our observations also had very high temporal density and yield a cTTs fraction of $\sim$40%.

Using the same disk identification criteria ($[3.6]–[8.0] > 0.7$) for the entire sample of IC 348 members studied by Lada et al. (2006) and for the periodic sample listed in Table 4.1, we find the disk fractions to be the same within statistical errors, $41\% \pm 2.7\%$ vs. $38\% \pm 4.5\%$, respectively. Since there is no evidence that our sample is biased against stars with disks, we conclude that our sample of stars with rotation periods is representative of the entire population of IC 348 members in terms of their disk properties. Rebull et al. (2006) reach the same conclusion for the stars in Orion by noting that the [3.6]–[8.0] color distribution of the periodic stars is statistically indistinguishable from that of the entire population of Orion members. Therefore, we argue that it is very unlikely that the lack of correlation between rotation period and IR excess is due to a bias in the disk properties of our sample.

4.6.2 Previous Spitzer Results and Very Fast Rotators

Previous to this paper, the analysis of the periodic stars in Orion by Rebull et al. (2006) is the only study that combines rotation periods and *Spitzer* observations. They study a sample of 464 stars with known rotation periods and [3.6]–[8.0] colors. They note that the cumulative distribution function of periods for stars with disks (i.e., [3.6]–[8.0] > 1) shows an inflection point around 1.8 days. Based on this inflection point, they divide their sample into "short" and "long" period stars. They find that stars with short periods are *significantly* less likely to have a disk than stars with long periods. However, they also find that for periods > 1.8 days, the period distributions for stars with and without disks are statistically *indistinguishable.*

Our results are consistent with those of the Rebull group. Although at a lower significance level, due to the smaller size of our sample, our results also suggest that there is a significant decrease in the disk fraction at very short periods. As mentioned in Section 4.5.3, most of the power in the weak correlation between period and 8.0 μm excess for low-mass stars in IC 348 arises from the fact that the 5 fastest rotators ($P < 1.2$ days) have very little or no excess at all. Using the same disk identification criteria ([3.6]–[8.0] > 1.0) and definition of "short" and "long" period stars adopted by Rebull et al. (2006), we find that only 12% ±7% (2/16) of the short-period ($P < 1.8$ d) stars in IC 348 have a disk, while 34% ±4% (32/95) of the long-period ($P > 1.8$ d) stars have a disk. These disk fractions are consistent with those seen in the ONC by Rebull and collaborators.

The low disk fraction of fast rotators is evident in Figure 4.11, where we plot angular velocity ($2\pi P^{-1}$) as a function of [3.6]–[8.0] color in order to better resolve the distribution of IR excesses at short periods. At first glance, the upper envelope of the IR excess seems to correlate with angular velocity. However, that is mostly due to the fact that most of the objects are concentrated at low angular velocity. The objects plotted in Figure 4.11 are the same objects plotted in Figure 4.10. From a statistical point of view, the significance in the correlation between period and IR excess is *identical* to that of the correlation between angular velocity and IR excess. The fact that very fast rotators tend to have little or no excess is also confirmed to a high level of significance by a preliminary analysis of *Spitzer* data on NGC 2264, which will be fully analyzed and presented in a follow-up paper (Paper II).

The low disk frequency of very fast rotators is the only feature of our sample that could *potentially* be interpreted as an evidence for disk braking. In the context of disk braking, stars that lost their disks very early in their evolution are expected to become very fast rotators. The main challenge for disk braking seems to be the large number of slow rotators without a disk. Qualitatively, it has been proposed that the large number of slow rotators that show no evidence of a disk are objects that have recently lost their disks and have not had enough time to spin up considerably (e.g. H02, Rebull et al., 2005, 2006). This scenario would require the spin-up timescale for the stars in the sample to be significantly longer than the transition timescale from a massive inner disk capable of disk braking to a disk tenuous enough to remain undetectable at IRAC wavelengths. However, we note that the population of fast rotators ($P < 1.8$ d) represents only a small fraction ($\sim 15\%$) of the entire sample of stars with rotation periods in both IC 348 and the ONC. In other words, the vast majority of stars with rotation periods, about 85% in each cluster, shows no correlation between their rotation period and the presence of a disk. This casts serious doubts on the explanation discussed by the three groups mentioned above that the large population of slow rotators with no mid-IR excess is populated by stars which have just lost their disks. This would require $\sim 50\%$ of the entire sample of periodic stars in each cluster to fall into this special regime. A more quantitative test of this scenario is underway and will be presented in Paper II.

Furthermore, we note that there are other possible explanations for the low disk fraction of very fast rotators besides disk braking. For instance, if the disk fraction of low mass stars, which tend to be very fast rotators, is significantly lower than that of higher mass stars, then an overall lower disk fraction of fast rotators is expected. Results from Lada et al. (2006) suggest that this might be the case. They find that the fraction of *optically thick* disks decreases from 47% ±12% for K6–M2 stars to 28% ±5% for M2–M6 stars. As discussed in Section 4.5.1 and illustrated by Figure 4.5, the criteria adopted by Rebull et al. (2006) for disk identification selects a sample which has almost a one-to-one correlation with the objects classified as optically thick disks by the Lada group. Also, as noted by Rebull and collaborators, an overabundance of close binaries among very fast rotators could account for their low disk fraction.

4.6.3 Are our results inconsistent with disk-braking?

How significant is the fact that we see no clear evidence of a correlation between rotation period and IR excess (with the exception of the fastest rotators as mentioned in the previous section)? Is the lack of evidence enough to exclude disk braking as a viable model? At least one line of argument suggests the contrary. Rebull et al. (2004) perform a series of Monte Carlo simulations of the evolution of rotation periods for stars in the context of the disk-braking model. They assume a Gaussian initial period distribution centered at 8 days with a $1\,\sigma$ dispersion of 4 days. In their models, they have a population of disk-locked stars that contract at constant angular velocity and a disk-free population which spins up as $\mathrm{P} \propto t^{-2/3}$ (appropriate for stars on convective tracks). The only free variables in their model relate to the fraction of disk-locked stars as a function of time.

After running a series of simulations, they perform K–S tests to constrain the circumstances under which a statistically significant correlation between period and IR excess would be expected. They conclude, given a broad distribution of initial periods, that the observational signatures of disk braking are much less conspicuous than is usually assumed, *even with a perfect knowledge of which stars have a disk.* They find that, unless the sample is very large (>500), the populations of stars with and without disks only become statistically different if a relatively large fraction ($\sim$30%) of the stars is released from their disks at an age <1 Myr. This is because the effect of disk locking is most important when the stars undergo rapid contraction at very young ages and becomes much less important later on as the contraction rate decreases. Furthermore, the Rebull et al. (2004) simulations can produce both a unimodal distribution of periods similar to the one seen in low-mass stars in IC 348 and a bimodal distribution similar to that of the higher-mass stars.

These caveats prevent us from drawing any categoric conclusion regarding the general validity of the disk-locking scenario. There is currently no alternative model to disk braking to explain the evolution of angular momentum of PMS stars, and there is some strong evidence that magnetic star–disk interaction actually occurs in early stages of the evolution of PMS stars (e.g. the presence of highly collimated jets in cTTs and deeply embedded objects). Therefore, we argue that a much more rigorous and quantitative analysis than that presented herein is required before the model can be regarded as inconsistent with the observational data. The fundamental question now becomes whether disk braking, which seems to be required to explain the angular momentum loss experienced by a large fraction of PMS stars between the birthline and the ZAMS, can occur early on in the evolution of PMS stars without leaving a clear correlation between rotation period and IR excess at the ages of clusters like IC 348.

To address this question, a more rigorous model than the one used by Rebull et al. (2004) could be created to investigate the range of disk-braking parameters (disk-braking efficiency and the fraction of regulated stars as a function of time) which would be allowed by the observed period distribution of stars with and without disks in clusters like IC 348 and NGC 2264. For instance, instead of starting from an initial distribution of rotation periods, one could use specific angular momentum, which is more physically meaningful and removes most of the dependence on the initial masses of the objects from the results. The initial angular momentum of the cluster can be constrained by the objects with a maximum current angular momentum (since they will have evolved with the lowest angular momentum loss). It would also be beneficial to incorporate into the models an age spread in the stellar population and observational constraints on the disk fraction as a function of age. Finally, instead of assuming a $\mathrm{P} \propto t^{-2/3}$ relation for all unregulated stars, the evolution of their periods can be calculated from the predicted evolution of their radii by theoretical evolutionary tracks.

In Paper II, we plan to perform Monte Carlo simulations to determine what initial conditions and disk-braking parameters might lead to the current lack of a correlation between rotation period and IR excess in PMS stars. We will use models similar to Rebull et al. (2004) with the improvements mentioned above to perform an analysis of the IC 348 cluster, using data presented in Table 4.1, and NGC 2264 and the ONC, combining *Spitzer* archival data and periods published in the literature.

4.7 Summary and Conclusions

We have obtained time series photometry of the young stellar cluster IC 348 and measured 74 new rotation periods. Our results increase the total number of known rotation periods in the cluster to 145. We combined all published rotation periods in IC 348 with *Spitzer* photometry (3.6, 4.5, 5.8, and 8.0 μm) in order to test the disk braking paradigm, constructing a new, more reliable set of criteria for disk identification with IRAC data.

We find that the IC 348 rotation period distribution resembles that seen in the heart of the ONC: Stars estimated to be less massive than $0.25\,M_{\odot}$ show a unimodal distribution dominated by fast rotators (P ~ 1–2 days) and a tail of slow rotators, while stars estimated to be more massive than $0.25\,M_{\odot}$ show a bimodal distribution with peaks at ∼2 and ∼8 days. We find no evidence that the tail of slow rotators in low-mass stars or the long-period peak of high-mass stars are preferentially populated by stars with disks, a correlation which is predicted by the current disk-braking paradigm. Also, we find no significant correlation between period and the *magnitude* of the IR excess, regardless of the mass range considered.

Given the large improvement of IRAC observations over near-IR disk indicators, our results support the claim made by Littlefair et al. (2005) that the correlation between period and (I–K) excess reported by several authors is a secondary manifestation of the correlation between near-IR excess and mass. We find that the disk properties of our sample are indistinguishable from the disk properties of the cluster as a whole and conclude that it is very unlikely that the lack of a correlation between rotation period and IR excess is due to a bias in the disk properties of our sample. Finally, we find some indication that the disk fraction might decrease significantly in stars with very short periods ($\mathrm{P} \lesssim 1.2$ days). The fact that very fast rotators tend to have little or no excess has already been shown by Rebull et al. (2005) for stars in the ONC and has been confirmed by a preliminary analysis of our ongoing work with objects in NGC 2264. The low disk fraction of these very fast rotators is the only feature of our sample that could *potentially* be interpreted as an evidence for disk braking.

However, the lack of evidence for disk braking (in the form of a correlation between PMS stellar rotation periods and IR excess) in all but the fastest rotators is not enough to rule out disk braking in PMS stars. As shown by Rebull et al. (2004), current observational signatures of disk braking may be hidden by an initial large distribution of rotation periods in PMS stars. Because there is currently no alternative mechanism for angular momentum loss in PMS stars and because there is evidence for star–disk interaction in very young stellar objects, a rigorous quantitative analysis of the effects of disk-braking parameters on current observational signatures is required to determine whether disk-braking may indeed play a significant role in the angular momentum evolution of these stars. Simulations similar to those run by Rebull et al. (2004), with the improvements suggested in Section 6.4 of this paper, can further constrain the importance of disk braking in the evolution of PMS stars. We are in the process of testing such models and will present our results in a follow-up paper.

4.8 Acknowledgments

We thank Luisa Rebull and Deborah Padgett for their careful reading of the paper and detailed suggestions. We also thank Paul Harvey, Daniel Jaffe and Neal Evans for their useful comments. We thank Judit Ries for obtaining R and I images and standards for absolute photometry. We also thank Luisa Rebull for providing a preprint of the paper Rebull et al. (2005) prior to publication. Support for this work, part of the Spitzer Legacy Science Program, was provided by NASA through contract 1224608 issued by the Jet Propulsion Laboratory, California Institute of Technology, under NASA contract 1407. This publication makes use of data products from the Two Micron All Sky Survey, which is a joint project of the University of Massachusetts and the Infrared Processing and Analysis Center funded by NASA and the National Science Foundation.

Table 4.1. Periodic Sample in IC 348

ID	Ra	Dec	P	PS ^{1}	Ref_P ^{2}	SpT	R_C ^{3}	I_C	J	H	K_S	[3.6]	[3.6] error	[4.5]	[4.5] error	[5.8]	[5.8] error	[8.0]	[8.0] error
	(deg)		(days)						(mag)						(mJy)				
1	55.5847	32.0919	7.7	44	1	—	—	—	13.04	11.96	11.47	1.18e+01	1.00e-01	9.33e+00	8.22e-02	7.48e+00	6.35e-02	9.03e+00	6.65e-02
2	55.6078	32.3506	17.7	61	1	—	16.74	15.30	13.29	12.32	12.00	—	—	—	—	—	—	—	—
3	55.6177	32.5133	4.3	47	1	—	16.78	15.25	13.18	12.31	11.99	—	—	—	—	—	—	—	—
4	55.6257	32.2471	26.9	24	1	—	17.29	16.30	14.64	13.88	13.62	—	—	—	—	—	—	—	—
5	55.6340	32.4914	2.3	30	1	—	14.51	13.60	12.33	11.67	11.45	—	—	—	—	—	—	—	—
6	55.6467	32.5651	0.2	35	1	—	16.12	15.42	14.63	14.24	14.03	—	—	—	—	—	—	—	—
7	55.6486	32.2888	1.2	43	1	—	15.89	15.02	13.84	13.14	12.95	—	—	—	—	—	—	—	—
8	55.6698	32.5729	5.8	45	1	—	—	—	13.34	12.45	12.11	—	—	—	—	—	—	—	—
9	55.6703	32.2263	0.5	30	1	—	16.81	15.07	12.75	11.85	11.52	9.55e+00	9.10e-02	—	—	4.58e+00	5.27e-02	—	—
10	55.6817	31.9875	2.2	60	1	—	15.03	13.76	11.79	10.85	10.53	2.22e+01	1.77e-01	1.40e+01	9.42e-02	9.37e+00	5.66e-02	5.36e+00	5.31e-02
11	55.7311	31.9534	1.9	26	1	—	15.90	14.67	13.28	12.54	12.29	3.95e+00	3.21e-02	2.56e+00	2.26e-02	1.79e+00	2.79e-02	9.82e-01	2.73e-02
12	55.7332	31.9783	22.1	29	1	—	—	—	10.55	9.73	9.02	3.84e+02	5.69e+00	3.23e+02	5.02e+00	3.69e+02	3.62e+00	4.88e+02	4.60e+00
13	55.7589	32.1243	17.3	31	1	—	17.20	15.30	12.83	12.05	11.69	8.59e+00	1.06e-01	6.00e+00	6.94e-02	3.79e+00	5.15e-02	2.12e+00	3.35e-02
14	55.7794	32.1718	6.2	55	1	—	16.22	14.79	12.71	11.71	11.37	1.00e+01	6.95e-02	—	—	4.43e+00	4.06e-02	—	—
15	55.7944	32.5923	6.0	34	1	—	16.44	14.98	12.98	12.04	11.71	—	—	—	—	—	—	—	—
16	55.7981	32.4422	7.5	23	1	—	16.79	15.79	14.33	13.57	13.35	1.52e+00	2.52e-02	1.01e+00	1.39e-02	6.56e-01	2.93e-02	3.35e-01	3.20e-02
17	55.8014	32.5698	0.2	23	1	—	16.14	15.20	14.35	13.75	13.56	—	—	—	—	—	—	—	—
18	55.8072	32.0125	7.8	24	1	—	23.28	19.96	14.26	12.57	11.76	1.26e+01	1.02e-01	1.12e+01	9.15e-02	1.10e+01	8.25e-02	1.32e+01	9.20e-02
19	55.8482	32.2072	3.0	36	1	—	18.84	16.79	14.09	13.15	12.72	4.16e+00	5.29e-02	3.26e+00	3.85e-02	2.82e+00	3.71e-02	2.30e+00	3.73e-02
20	55.8516	32.6421	1.3	54	1	—	16.13	14.56	12.25	11.28	10.92	—	—	—	—	—	—	—	—
21	55.8675	32.0331	8.8	30	1	—	14.94	13.61	11.76	10.72	10.11	4.45e+01	9.46e-01	5.06e+01	5.65e-01	3.85e+01	2.95e-01	3.35e+01	2.40e-01
22	55.8875	32.4674	12.2	27	1	—	17.47	15.81	13.44	12.42	12.08	5.32e+00	1.21e-01	3.52e+00	3.59e-02	2.54e+00	7.28e-02	1.31e+00	4.10e-02
23	55.9382	32.0663	27.6	52	1	—	19.29	17.70	13.78	12.15	11.01	2.35e+01	5.18e+00	1.45e+02	2.57e+00	6.61e+01	1.54e+00	1.03e+02	2.04e+00
24	55.9495	32.2991	9.8	54	1	—	15.79	14.44	12.59	11.68	11.39	9.19e+00	1.46e-01	6.21e+00	7.46e-02	4.28e+00	4.46e-02	2.48e+00	3.31e-02
25	55.9532	32.1259	20.3	27	1	M1.5	15.44	14.16	12.43	11.65	11.37	9.01e+00	1.79e-01	6.60e+00	7.88e-02	4.12e+00	5.04e-02	2.31e+00	4.18e-02
26	55.9534	32.2643	2.9	46	1	—	17.02	15.32	13.01	12.14	11.78	8.50e+00	1.52e-01	8.54e+00	9.87e-02	8.40e+00	7.56e-02	1.04e+01	7.31e-02
27	55.9558	32.1777	13.1	44	1	M3.5	16.36	14.76	12.68	11.85	11.56	7.51e+00	1.14e-01	5.42e+00	6.95e-02	3.55e+00	4.44e-02	2.12e+00	4.02e-02
28	55.9642	32.5302	3.8	60	1	—	15.62	14.18	12.03	11.12	10.80	—	—	—	—	—	—	—	—
29	55.9802	31.9256	9.6	26	1	—	20.92	18.30	14.22	12.31	11.39	2.35e+01	4.41e-01	2.18e+01	2.00e-01	1.80e+01	1.42e-01	1.19e+01	8.50e-02
30	55.9843	32.5050	8.1	52	1	—	15.89	14.51	12.49	11.62	11.33	—	—	—	—	—	—	—	—

Table 4.1 (cont'd)

ID	Ra	Dec	P	PS[1]	Ref_P[2]	SpT	R_C[3]	I_C	J	H	K_S	[3.6]	[3.6] error	[4.5]	[4.5] error	[5.8]	[5.8] error	[8.0]	[8.0] error
	(deg)		(days)						(mag)						(mJy)				
31	55.9940	32.2910	12.8	26	1	—	15.85	14.36	12.05	11.12	10.66	3.06e+01	4.63e-01	2.18e+01	4.05e-01	2.06e+01	1.60e-01	2.43e+01	1.70e-01
32	55.9962	32.2392	17.7	28	1	—	17.27	15.82	13.49	12.29	11.39	1.31e+01	2.03e-01	1.40e+01	1.76e-01	1.19e+01	9.46e-02	1.26e+01	9.91e-02
33	55.9981	32.2653	7.6	39	1	—	16.96	15.43	13.06	11.99	11.69	7.19e+00	1.24e-01	4.91e+00	5.29e-02	3.42e+00	4.47e-02	1.94e+00	3.30e-02
34	55.9988	32.2341	14.0	63	1,2	M0.75	15.50	14.19	12.30	11.40	11.06	1.29e+01	1.97e-01	8.97e+00	9.60e-02	6.17e+00	6.52e-02	3.43e+00	5.81e-02
35	56.0090	32.3278	6.2	63	1	—	15.73	14.41	12.51	11.64	11.38	8.84e+00	1.47e-01	6.48e+00	7.87e-02	4.48e+00	3.95e-02	2.62e+00	3.43e-02
36	56.0177	32.2305	1.2	32	1	M4.75	—	—	12.61	11.76	11.41	9.73e+00	1.41e-01	7.41e+00	8.13e-02	4.96e+00	4.95e-02	3.05e+00	5.64e-02
37	56.0283	32.1317	1.3	23	1	M4.25	17.27	15.48	13.03	12.14	11.75	1.01e+01	1.73e-01	8.91e+00	1.05e-01	7.53e+00	8.79e-02	8.11e+00	1.05e-01
38	56.0422	32.0679	2.2	–	3	M5.75	18.25	16.14	13.22	12.41	11.93	8.72e+00	1.14e-01	8.23e+00	8.07e-02	7.25e+00	1.17e-01	7.28e+00	1.22e-01
39	56.0468	32.1378	13.0	–	3	M5.25	17.38	15.39	12.84	12.09	11.75	7.36e+00	1.05e-01	5.35e+00	6.98e-02	3.72e+00	5.52e-02	2.27e+00	6.96e-02
40	56.0469	32.1034	9.1	29	1,2,3,4	M0	15.72	14.34	12.42	11.44	11.16	1.12e+01	1.41e-01	7.35e+00	8.22e-02	5.19e+00	7.27e-02	2.75e+00	7.99e-02
41	56.0476	32.3278	0.8	42	1,2	M3	16.13	14.65	12.56	11.78	11.51	8.94e+00	1.32e-01	6.19e+00	6.99e-02	4.51e+00	4.54e-02	2.42e+00	3.28e-02
42	56.0574	31.9263	8.3	39	1	—	19.31	17.13	13.68	12.19	11.64	1.14e+01	2.12e-01	7.98e+00	2.19e-01	5.13e+00	6.85e-02	3.64e+00	9.47e-02
43	56.0649	32.1561	0.6	–	3,	M7.5	20.94	18.18	14.59	13.78	13.30	2.11e+00	2.42e-02	1.52e+00	1.78e-02	1.11e-01	5.27e-02	4.77e-01	1.96e-02
44	56.0654	32.5245	13.7	44	1	—	14.21	13.07	11.72	10.98	10.75	—	—	—	—	—	—	—	—
45	56.0684	32.1653	3.0	33	1,2,3,4	K0	13.54	12.65	11.32	10.58	10.38	2.06e+01	2.90e-01	1.36e+01	1.54e-01	9.46e+00	8.43e-02	5.40e+00	7.21e-02
46	56.0746	32.2056	4.5	29	1	M2.5	15.59	14.10	12.16	11.35	11.07	1.17e+01	1.86e-01	8.08e+00	9.06e-02	5.55e+00	5.84e-02	3.06e+00	5.62e-02
47	56.0758	32.1665	2.7	27	1	M4.25	17.87	15.85	13.21	12.27	11.87	7.07e+00	1.09e-01	6.09e+00	7.55e-02	4.88e+00	5.76e-02	4.04e+00	6.86e-02
48	56.0761	32.1257	2.2	–	3	M4.75	18.27	16.30	—	—	—	3.74e+00	4.99e-02	2.79e+00	3.65e-02	1.94e+00	4.44e-02	2.00e+00	5.69e-02
49	56.0801	32.1262	7.6	–	4	M3.75	16.68	14.88	—	—	—	1.50e+01	2.29e-01	1.28e+01	1.40e-01	1.16e+01	1.53e-01	1.28e+01	1.42e-01
50	56.0834	32.1127	8.6	–	3,4	M3.5	17.77	16.04	13.58	12.61	12.23	4.66e+00	6.74e-02	3.41e+00	3.37e-02	2.18e+00	4.54e-02	8.11e-01	3.81e-02
51	56.0841	32.1491	2.2	–	3	M2	16.76	15.03	12.70	11.79	11.41	1.01e+01	1.69e-01	9.42e+00	1.03e-01	7.79e+00	9.73e-02	7.59e+00	1.51e-01
52	56.0843	32.5063	2.8	45	1	—	17.11	15.42	13.13	12.20	11.85	7.23e+00	7.55e-02	4.77e+00	7.92e-02	3.20e+00	4.29e-02	1.81e+00	5.97e-02
53	56.0857	32.4610	4.8	51	1	—	17.66	15.79	13.23	12.37	12.01	6.86e+00	9.46e-02	4.49e+00	5.25e-02	2.87e+00	5.34e-02	1.54e+00	4.43e-02
54	56.0886	32.0840	6.9	54	1,3	M2.5	16.82	15.17	12.74	11.73	11.40	9.64e+00	1.35e-01	7.12e+00	7.44e-02	4.79e+00	8.04e-02	2.20e+00	7.35e-02
55	56.0886	32.2103	2.3	30	1	M4.75	17.41	15.71	13.70	12.92	12.51	4.90e+00	5.86e-02	4.30e+00	3.88e-02	3.50e+00	3.99e-02	2.71e+00	6.23e-02
56	56.0898	32.1715	7.0	60	1,2,3,4	M1.5	16.20	14.71	12.62	11.66	11.35	1.02e+01	1.13e-01	7.13e+00	6.83e-02	4.88e+00	5.12e-02	2.68e+00	3.12e-02
57	56.0903	32.1069	8.4	–	2,4,	M2.75	16.21	14.65	12.54	11.60	11.31	9.91e+00	1.40e-01	6.67e+00	8.79e-02	4.74e+00	6.77e-02	2.72e+00	6.81e-02
58	56.0901	32.1771	2.8	26	1,2	K7	16.42	14.92	12.49	11.28	10.62	5.32e+01	5.84e-01	4.80e+01	5.73e-01	4.16e+01	2.42e-01	3.53e+01	2.36e-01
59	56.0913	32.2032	14.0	–	3	M4	16.37	14.57	12.28	11.40	11.09	1.43e+01	2.09e-01	8.91e+00	1.13e-01	6.13e+00	6.78e-02	4.04e+00	1.10e-01
60	56.0929	32.0952	30.0	25	1	K8	15.88	14.45	12.55	11.28	10.70	2.76e+01	3.23e-01	2.34e+01	2.51e-01	2.06e+01	1.54e-01	2.83e+01	2.95e-01

Table 4.1 (cont'd)

ID	Ra	Dec	P	PS [1]	Ref_P [2]	SpT	R_C [3]	I_C	J	H	K_S	[3.6]	[3.6] error	[4.5]	[4.5] error	[5.8]	[5.8] error	[8.0]	[8.0] error
	(deg)		(days)						(mag)						(mJy)				
61	56.0930	32.2002	8.4	–	3	M1	16.35	14.78	12.56	11.60	11.10	1.52e+01	2.96e-01	1.66e+01	1.93e-01	1.67e+01	1.41e-01	1.90e+01	2.11e-01
62	56.0941	32.0316	1.0	25	1	M2.5	16.01	14.40	12.12	11.15	10.79	1.35e+01	2.91e-01	1.10e+01	1.44e-01	8.44e+00	6.38e-02	6.76e+00	6.39e-02
63	56.0982	32.1594	1.7	–	3	M5	17.72	15.89	13.50	12.74	12.40	4.81e+00	5.23e-02	4.13e+00	3.72e-02	3.10e+00	4.29e-02	2.92e+00	7.73e-02
64	56.0986	32.1129	10.0	48	1,2,3,4	M2.5	15.83	14.27	12.23	11.38	11.07	1.30e+01	1.44e-01	8.89e+00	6.93e-02	6.19e+00	6.60e-02	3.27e+00	5.27e-02
65	56.1024	32.0659	4.9	57	1,3,4	M1	17.29	15.54	12.82	11.81	11.37	9.91e+00	1.41e-01	6.82e+00	7.41e-02	4.64e+00	7.81e-02	—	—
66	56.1065	32.1048	7.3	52	1,3	M2.25	17.85	15.98	12.98	11.70	11.14	1.55e+01	1.75e-01	1.25e+01	1.22e-01	9.82e+00	1.03e-01	1.05e+01	2.08e-01
67	56.1066	32.2083	8.4	–	1,2,4	M0.5	14.79	13.59	11.82	10.95	10.68	1.68e+01	2.56e-01	1.11e+01	1.34e-01	7.55e+00	7.55e-02	4.49e+00	6.18e-02
68	56.1065	32.1919	5.4	24	1,2,3	M0	16.47	14.85	12.48	11.27	10.64	4.36e+01	7.81e-01	4.11e+01	7.02e-01	3.58e+01	3.29e-01	4.81e+01	3.75e-01
69	56.1066	32.2083	8.4	63	1,2,4	M0.5	14.79	13.59	11.82	10.95	10.68	1.68e+01	2.56e-01	1.11e+01	1.34e-01	7.55e+00	7.55e-02	4.49e+00	6.18e-02
70	56.1110	32.0662	3.1	30	1,2,3,4	M4.75	16.20	14.33	11.80	10.94	10.59	1.93e+01	2.23e-01	1.26e+01	1.49e-01	8.79e+00	8.03e-02	5.22e+00	1.33e-01
71	56.1112	32.1390	8.9	29	1	M0.5	17.72	16.03	12.99	11.56	10.84	3.12e+01	4.26e-01	2.76e+01	3.01e-01	1.99e+01	1.94e-01	1.95e+01	2.54e-01
72	56.1126	32.0788	9.1	–	3	M1	15.07	13.77	11.95	11.14	10.85	1.44e+01	1.80e-01	9.96e+00	1.49e-01	6.82e+00	7.61e-02	3.88e+00	1.06e-01
73	56.1137	32.1216	1.5	–	3	M4.75	18.57	16.81	14.43	13.59	13.27	2.03e+00	2.77e-02	1.39e+00	1.76e-02	9.29e-01	2.54e-02	7.75e-01	5.00e-02
74	56.1153	32.5638	2.6	31	1	—	15.87	14.34	12.10	11.23	10.87	—	—	—	—	—	—	—	—
75	56.1162	32.1255	5.4	23	1,2,4	M2	15.80	14.23	12.13	11.27	10.97	1.40e+01	2.01e-01	9.78e+00	9.15e-02	6.30e+00	9.11e-02	3.39e+00	8.18e-02
76	56.1172	32.2667	2.7	52	1	M3.25	15.98	14.38	12.21	11.35	11.02	1.29e+01	1.97e-01	8.79e+00	1.10e-01	6.35e+00	7.15e-02	3.71e+00	8.04e-02
77	56.1186	32.1229	7.0	52	1,2,3,4	K6.5	14.44	13.30	11.67	10.85	10.58	1.65e+01	2.50e-01	1.12e+01	1.14e-01	7.29e+00	1.16e-01	4.04e+00	1.01e-01
78	56.1309	32.1915	1.4	–	3	M5.25	18.27	16.15	13.48	12.74	12.34	4.68e+00	7.17e-02	3.60e+00	7.48e-02	2.22e+00	9.20e-02	1.49e+00	1.70e-01
79	56.1314	32.1458	10.8	–	3,4	K2	12.98	12.15	10.69	9.97	9.72	3.89e+01	6.15e-01	2.66e+01	2.96e-01	1.80e+01	1.46e-01	1.05e+01	2.07e-01
80	56.1349	32.0576	1.6	–	3	M5.5	20.68	18.09	14.88	14.04	13.48	2.37e+00	2.96e-02	2.05e+00	2.29e-02	1.63e+00	6.07e-02	—	—
81	56.1357	32.1488	6.7	–	3	M3	16.05	14.43	12.11	11.13	10.76	1.77e+01	2.94e-01	1.40e+01	1.39e-01	1.09e+01	1.30e-01	9.29e+00	1.65e-01
82	56.1364	32.1437	2.6	–	3,4	G6	12.47	11.62	10.28	9.65	9.43	4.86e+01	6.93e-01	3.47e+01	2.77e-01	2.25e+01	2.15e-01	1.26e+01	2.76e-01
83	56.1365	32.1544	5.5	33	1,4	M3.25	16.14	14.68	12.35	11.37	11.01	1.39e+01	1.80e-01	1.00e+01	1.22e-01	7.12e+00	8.31e-02	4.88e+00	1.40e-01
84	56.1367	32.0704	5.3	23	1	M5	18.61	16.49	13.74	12.90	12.52	4.15e+00	5.86e-02	2.86e+00	4.19e-02	1.90e+00	5.41e-02	—	—
85	56.1388	32.1610	2.2	25	1	M2	15.10	13.99	12.33	11.37	11.06	2.13e+01	3.10e-01	1.62e+01	2.98e-01	1.20e+01	1.46e-01	7.49e+00	1.75e-01
86	56.1408	31.9751	3.9	27	1	—	18.13	16.23	13.49	12.27	11.61	1.13e+01	1.95e-01	9.15e+00	9.60e-02	6.87e+00	8.20e-02	6.63e+00	5.42e-02
87	56.1416	32.1484	16.4	–	2,4	M0	14.74	13.54	11.85	10.98	10.70	1.58e+01	2.32e-01	1.06e+01	1.18e-01	7.62e+00	1.00e-01	5.25e+00	1.65e-01
88	56.1419	32.1159	3.4	–	3	M7.25	19.47	17.26	—	—	—	4.67e+00	6.25e-02	4.28e+00	4.42e-02	4.28e+00	6.56e-02	4.86e+00	1.10e-01
89	56.1450	31.9487	3.5	35	1	—	16.82	15.17	13.03	12.09	11.62	1.26e+01	1.21e-01	8.60e+00	1.18e-01	6.43e+00	6.74e-02	5.19e+00	1.12e-01
90	56.1453	32.1094	5.4	–	2,3,4	K5.5	14.55	13.35	11.51	10.61	10.31	2.32e+01	3.68e-01	1.63e+01	1.91e-01	1.13e+01	1.30e-01	6.64e+00	1.27e-01

Table 4.1 (cont'd)

ID	Ra	Dec	P	PS[1]	Ref_P[2]	SpT	R_C[3]	I_C	J	H	K_S	[3.6]	[3.6] error	[4.5]	[4.5] error	[5.8]	[5.8] error	[8.0]	[8.0] error
	(deg)		(days)						(mag)						(mJy)				
91	56.1459	32.1493	1.8	–	3	M4.75	18.08	16.63	14.87	14.11	13.71	1.79e+00	4.59e-02	1.32e+00	3.15e-02	1.01e+00	1.04e-01	5.88e-01	2.12e-01
92	56.1460	32.1270	4.5	42	1,2	K6.5	14.22	15.14	10.99	10.07	9.76	4.18e+01	6.16e-01	2.80e+01	3.81e-01	1.81e+01	1.49e-01	1.17e+01	1.38e-01
93	56.1477	32.1490	1.9	–	3	M5.25	17.71	16.05	13.25	12.31	11.83	9.19e+00	1.78e-01	8.21e+00	1.22e-01	7.54e+00	1.48e-01	7.48e+00	1.86e-01
94	56.1480	32.1346	1.7	–	3	M5.25	18.26	16.39	13.64	12.72	12.33	4.72e+00	7.17e-02	3.38e+00	4.57e-02	2.35e+00	3.62e-02	1.14e+00	9.20e-02
95	56.1487	32.0510	12.0	34	1	M3.25	19.06	17.36	14.13	12.78	11.84	1.15e+01	1.96e-01	1.18e+01	1.63e-01	1.16e+01	9.46e-02	1.30e+01	1.35e-01
96	56.1539	32.1126	1.7	–	2,4	G3	11.83	10.80	9.21	8.48	8.19	1.85e+02	3.63e+00	1.03e+02	2.98e+00	1.15e+02	7.00e-01	8.48e+01	6.24e-01
97	56.1541	32.1429	2.5	–	3	M4.75	17.53	15.73	13.06	12.07	11.59	1.05e+01	1.62e-01	8.46e+00	1.08e-01	6.92e+00	1.27e-01	6.27e+00	1.59e-01
98	56.1558	32.2067	13.7	–	1,3	M2	17.89	16.02	13.07	11.84	11.28	1.32e+01	2.18e-01	1.15e+01	1.27e-01	8.93e+00	1.04e-01	1.15e+01	2.06e-01
99	56.1558	32.1033	6.2	–	2,4	K7	15.17	13.88	12.08	11.14	10.87	1.41e+01	2.05e-01	9.42e+00	1.10e-01	6.86e+00	8.12e-02	3.96e+00	1.28e-01
100	56.1558	32.2067	19.8	31	1,3	M2	17.89	16.02	13.07	11.84	11.28	1.32e+01	2.18e-01	1.15e+01	1.27e-01	8.93e+00	1.04e-01	1.15e+01	2.06e-01
101	56.1559	32.1502	8.4	38	1,4	M1	16.28	14.91	12.48	11.44	10.99	2.25e+01	4.00e-01	2.04e+01	3.67e-01	1.89e+01	2.91e-01	2.39e+01	3.96e-01
102	56.1574	32.2050	3.3	58	1,3,4	M4.5	17.69	15.68	13.04	12.15	11.79	8.40e+00	8.81e-02	5.95e+00	5.99e-02	4.12e+00	5.34e-02	1.97e+00	4.63e-02
103	56.1578	32.1345	8.2	30	1,3	K7	15.58	14.12	11.69	10.48	9.83	6.03e+01	1.51e+00	6.55e+01	8.83e-01	5.62e+01	4.69e-01	5.83e+01	5.54e-01
104	56.1583	32.0582	8.6	33	1,2	K6	14.66	13.35	11.45	10.44	9.87	6.15e+01	6.67e-01	4.52e+01	8.42e-01	4.40e+01	3.47e-01	5.27e+01	4.02e-01
105	56.1599	32.2166	13.5	–	4	M0	15.97	14.64	12.81	11.93	11.65	7.73e+00	1.08e-01	4.99e+00	4.89e-02	3.22e+00	4.41e-02	1.52e+00	6.94e-02
106	56.1602	32.1266	5.1	45	1,2,3,4	K6	14.52	13.21	11.18	10.23	9.85	3.77e+01	8.08e-01	3.67e+01	4.80e-01	3.81e+01	2.85e-01	5.69e+01	5.22e-01
107	56.1606	32.1335	7.3	29	1,2,3,4	M1.25	15.85	14.32	11.94	10.90	10.47	2.74e+01	4.85e-01	2.45e+01	2.55e-01	1.88e+01	2.27e-01	2.65e+01	3.43e-01
108	56.1612	32.1491	2.1	–	3	M3.25	15.99	14.45	12.45	11.57	11.28	1.18e+01	1.61e-01	7.93e+00	8.67e-02	5.09e+00	1.39e-01	3.13e+00	1.50e-01
109	56.1613	32.1450	2.4	31	1,3,4	K3	15.60	14.01	11.19	9.97	9.49	5.52e+01	9.19e-01	4.12e+01	3.49e-01	2.72e+01	2.71e-01	1.50e+01	2.52e-01
110	56.1616	32.3182	4.8	56	1	—	17.16	15.47	13.34	12.47	12.14	5.25e+00	8.46e-02	3.49e+00	5.26e-02	2.62e+00	7.57e-02	1.79e+00	1.08e-01
111	56.1632	32.1551	1.6	–	2,3,4	G8	13.51	12.15	10.07	9.14	8.77	9.01e+01	2.24e+00	7.49e+01	9.51e-01	5.02e+01	5.20e-01	2.87e+01	6.57e-01
112	56.1633	32.1625	3.9	52	1,3,4	M2	16.30	14.77	12.46	11.46	11.09	1.66e+01	2.69e-01	1.48e+01	1.71e-01	1.27e+01	1.47e-01	1.41e+01	3.25e-01
113	56.1643	32.1689	1.5	–	3	M5	17.60	16.06	13.85	13.10	12.72	3.16e+00	4.50e-02	2.33e+00	3.03e-02	1.37e+00	4.53e-02	1.28e+00	1.37e-01
114	56.1638	32.6037	0.2	24	1	—	19.75	18.64	16.28	15.33	15.12	—	—	—	—	—	—	—	—
115	56.1658	32.3012	9.5	38	1	M3.75	16.85	15.00	12.23	11.28	10.78	2.21e+01	3.09e-01	1.75e+01	2.43e-01	1.37e+01	1.10e-01	1.35e+01	1.05e-01
116	56.1692	32.3864	4.1	45	1	—	—	—	12.80	11.83	11.55	8.07e+00	1.24e-01	5.61e+00	5.73e-02	3.69e+00	4.76e-02	2.16e+00	3.49e-02
117	56.1721	32.1737	3.7	–	3	M4.75	16.05	14.76	12.56	11.77	11.44	9.64e+00	1.52e-01	7.34e+00	7.02e-02	4.75e+00	7.29e-02	1.86e+00	7.88e-02
118	56.1721	32.0815	1.6	–	3	M5	—	—	14.51	13.71	13.28	1.95e+00	2.96e-02	1.43e+00	1.77e-02	8.46e-01	3.85e-02	—	—
119	56.1732	32.1776	1.7	–	3	M5.75	19.07	18.16	15.46	14.86	14.25	1.02e+00	1.70e-02	7.93e-01	1.10e-02	5.05e-01	4.12e-02	3.60e-01	2.61e-02
120	56.1739	32.2006	2.1	28	1	M5	18.68	16.09	13.26	12.02	11.42	1.12e+01	1.16e-01	8.13e+00	7.94e-02	6.70e+00	7.23e-02	6.61e+00	1.46e-01

Table 4.1 (cont'd)

ID	Ra	Dec	P	PS [1]	Ref_P [2]	SpT	R_C [3]	I_C	J	H	K_S	[3.6]	[3.6] error	[4.5]	[4.5] error	[5.8]	[5.8] error	[8.0]	[8.0] error
	(deg)		(days)						(mag)							(mJy)			
121	56.1753	32.1503	16.0	38	1	—	16.27	14.21	11.79	10.67	10.13	2.47e+01	3.83e-01	2.21e+01	4.64e-01	2.61e+01	4.01e-01	2.10e+01	3.84e-01
122	56.1774	32.1674	3.6	–	3	M4.25	19.18	17.11	13.63	12.36	11.79	1.18e+01	1.33e-01	1.12e+01	1.02e-01	9.82e+00	9.29e-02	1.02e+01	1.64e-01
123	56.1776	32.1054	12.0	25	1,2,3,4	M1	15.10	13.95	12.52	11.77	11.54	8.41e+00	1.09e-01	5.26e+00	5.70e-02	3.51e+00	8.74e-02	2.64e+00	1.48e-01
124	56.1791	32.0259	1.0	24	1	—	—	—	15.22	14.66	11.74	—	—	—	—	—	4.39e-01	—	—
125	56.1824	32.1751	10.6	26	1,2	M1.25	15.92	14.40	12.29	11.25	10.83	1.82e+01	2.31e-01	1.85e+01	1.77e-01	2.08e+01	1.29e-01	3.27e+01	2.58e-01
126	56.1843	32.1465	1.8	–	3	M5.75	19.20	17.42	14.59	13.71	13.34	2.21e+00	2.77e-02	1.49e+00	1.78e-02	5.70e-01	4.44e-02	—	8.85e-02
127	56.1845	32.1769	1.5	–	3	M5.25	20.34	18.00	15.38	14.75	14.37	8.78e-01	1.18e-02	6.42e-01	1.35e-02	3.74e-01	3.87e-02	—	6.35e-02
128	56.1902	32.1863	1.3	–	3	M4.75	19.33	17.46	15.10	14.29	13.95	1.14e+00	2.28e-02	8.23e-01	1.39e-02	5.11e-01	4.84e-02	3.04e-01	1.36e-01
129	56.2034	32.2227	6.9	61	1	M2.75	16.80	15.20	13.10	12.24	11.94	5.62e+00	7.73e-02	3.86e+00	3.98e-02	2.63e+00	5.02e-02	1.57e+00	7.50e-02
130	56.2123	32.2693	13.1	45	1	M3.25	16.29	14.60	12.33	11.49	11.13	1.27e+01	1.62e-01	8.85e+00	7.72e-02	6.04e+00	6.75e-02	3.65e+00	1.13e-01
131	56.2240	32.1144	9.6	22	1	M4	18.04	16.03	13.33	12.37	11.96	6.04e+00	9.19e-02	4.42e+00	5.30e-02	3.16e+00	4.39e-02	1.52e+00	3.05e-02
132	56.2317	32.1555	3.1	60	1	K4	16.02	14.39	11.85	10.75	10.36	2.41e+01	3.83e-01	1.77e+01	1.75e-01	1.16e+01	9.29e-02	6.66e+00	9.29e-02
133	56.2338	32.0990	3.3	33	1	M2.75	16.50	14.95	13.07	12.27	11.99	5.57e+00	6.23e-02	3.54e+00	4.91e-02	2.54e+00	2.89e-02	1.42e+00	3.62e-02
134	56.2339	32.1542	2.5	29	1	K0	14.69	5.26	11.02	9.99	9.47	6.62e+01	1.06e+00	6.28e+01	9.42e-01	4.42e+01	3.45e-01	3.81e+01	2.56e-01
135	56.2563	32.1809	1.9	51	1,2	K0	14.26	13.26	11.86	11.13	10.88	1.36e+01	2.08e-01	9.33e+00	9.06e-02	6.29e+00	5.62e-02	3.77e+00	7.11e-02
136	56.2573	32.2410	16.4	55	1,2	K4	14.80	13.46	11.34	10.40	10.04	3.18e+01	4.26e-01	1.91e+01	2.68e-01	1.45e+01	9.37e-02	8.61e+00	6.94e-02
137	56.3166	32.5144	4.1	44	1	—	15.17	13.90	11.96	11.07	10.77	1.59e+01	1.28e-01	1.05e+01	7.09e-02	7.04e+00	6.04e-02	3.78e+00	4.31e-02
138	56.3250	32.3258	7.9	37	1	—	17.72	15.87	13.35	12.40	12.05	6.12e+00	6.11e-02	3.96e+00	5.11e-02	2.55e+00	3.59e-02	1.49e+00	3.48e-02
139	56.3353	32.1096	6.9	41	1	M1	14.90	13.42	11.12	9.98	9.35	7.93e+01	1.82e+00	8.07e+01	1.36e+00	7.68e+01	5.40e-01	7.31e+01	6.16e-01
140	56.3371	32.3034	5.0	28	1	—	18.43	16.67	15.59	14.70	14.46	5.55e-01	1.27e-02	3.86e-01	8.06e-03	2.38e-01	3.39e-02	1.65e-01	2.51e-02
141	56.3378	32.3049	5.0	58	1	—	17.70	15.72	12.87	11.82	11.40	1.17e+01	1.78e-01	7.51e+00	7.42e-02	5.26e+00	7.26e-02	2.81e+00	2.78e-02
142	56.3846	32.0542	0.7	31	1	M3	16.03	14.60	12.89	12.14	11.89	5.40e+00	8.36e-02	3.88e+00	4.46e-02	2.58e+00	3.46e-02	1.48e+00	2.55e-02
143	56.3980	31.9405	9.6	49	1	—	16.64	15.08	12.76	11.79	11.41	9.91e+00	1.95e-01	6.12e+00	1.74e-01	3.87e+00	7.50e-02	2.16e+00	4.20e-02
144	56.4327	32.4098	14.3	50	1	—	17.62	15.82	13.42	12.53	12.17	4.97e+00	4.36e-02	3.34e+00	3.24e-02	2.36e+00	2.40e-02	1.37e+00	2.43e-02
145	56.4448	32.4802	10.5	33	1	—	—	—	12.77	11.79	11.41	8.56e+00	8.15e-02	6.04e+00	5.06e-02	4.62e+00	8.24e-02	2.49e+00	3.74e-02

[1] Power spectrum peak

[2] Rotation period reported in this paper (1), Koziloglu et al. (2005) (2), Littlefair et al. (2005) (3), and Cohen et al. (2004) (4)

[3] The R_C and I_C photometry of the following stars have been taken from Cohen et al. (2004), ID=45,49,79,82,87,96,111

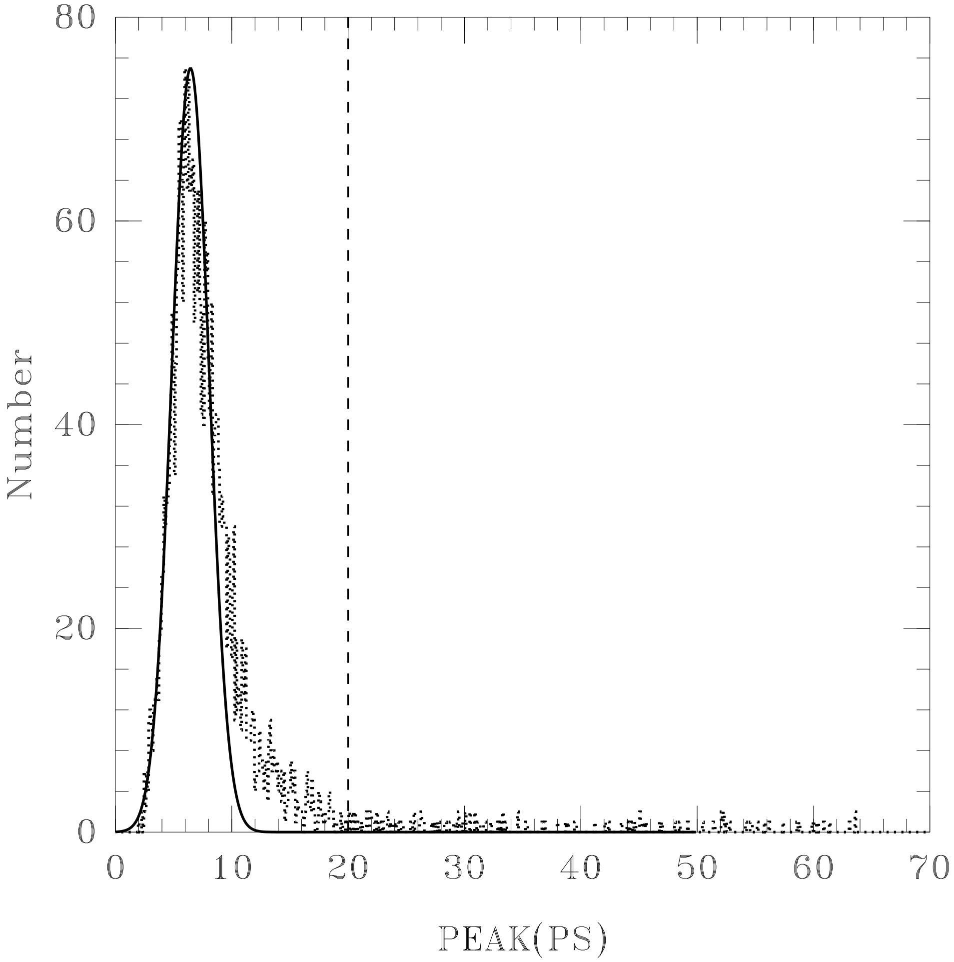

Figure 4.1 This is a plot of the distribution of power spectrum peaks for the entire sample of stars in the IC 348 data set. The dotted line is a histogram of the maximum power spectrum peak of each star, and the solid line is a Gaussian fit to the left side of the distribution of power spectrum peaks. Non-white noise is likely to raise a particular peak above what white noise alone would provide. Such systematic noise creates the shoulder above the Gaussian curve on the right wing of the distribution of peaks. This additional non-white noise makes period determinations for stars with power spectrum peaks lower than ∼20 unreliable.

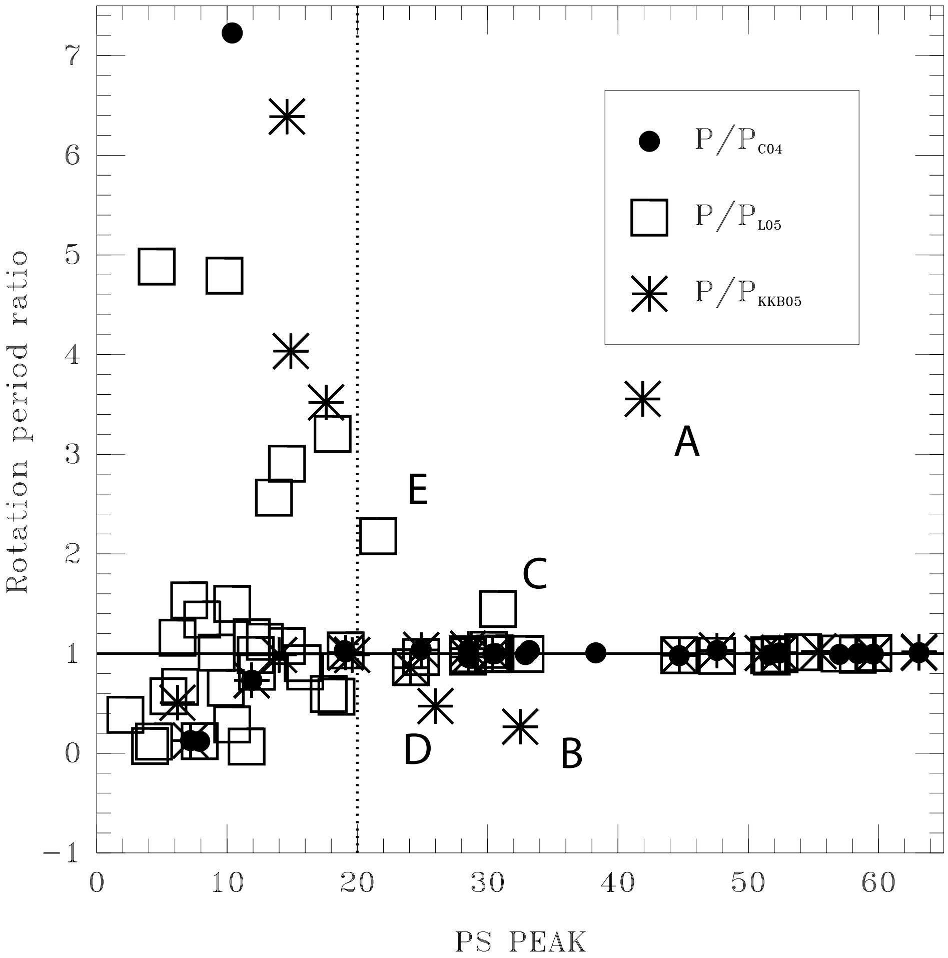

Figure 4.2 This is a plot of the ratio of our rotation periods to those from Cohen et al. (2004, C04), Littlefair et al. (2005, L05), and Kızıloğlu et al. (2005, KKB05) as a function of power spectrum peak from our light curves. The values start to diverge for power spectra peaks lower than ∼20. Based on the peak distribution from Figure 4.1 and these ratios, we adopt a power spectrum peak of 22.0 as the threshold above which we consider the measured periodic signal to be an accurate representation of the stellar rotation period. The disagreement with rotation periods from the literature for stars A through E is discussed in the text and in Figure 4.3.

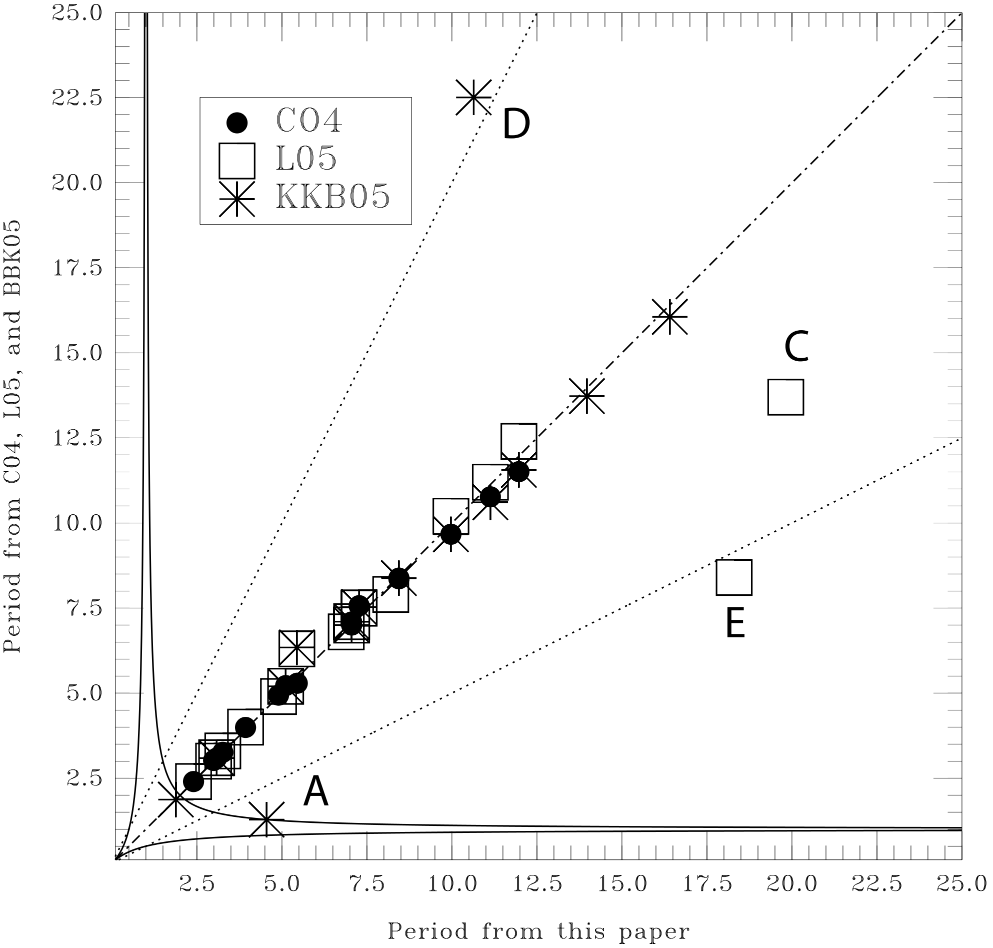

Figure 4.3 This figure is another comparison of our IC 348 periods to those obtained by other groups. Only five stars for which we measure power spectra peaks above 20 show significant discrepancies between our periods and those from the literature. For star A, Kızıloğlu et al. (2005, KKB05) find a period of 1.28 days, where we measure a period of 4.55 days. Their shorter period is a result of the beating of our period at a 1-day sampling interval, of the form $1/P_{\rm beating} = \pm 1 \pm (1/P)$ (plotted as a solid line). For object B and D, we find shorter periods than those found by KKB05; their periods are likely harmonics of the real periods (the two dotted lines represent factor-of-two harmonics). Our period for object C, 19.8 days, shows a discrepancy with the 13.4-day period found by Littlefair et al. (2005, L05) which cannot easily be explained. Longer periods have greater uncertainty, however, and since our observational baseline is twice as long as that of L05 (52 *versus* 26 days), we take our period to be closer to the correct value. Our period for object E is 18.3 days while L05 measured a period of 8.4 days. In this case, our period is likely a harmonic of the real period.

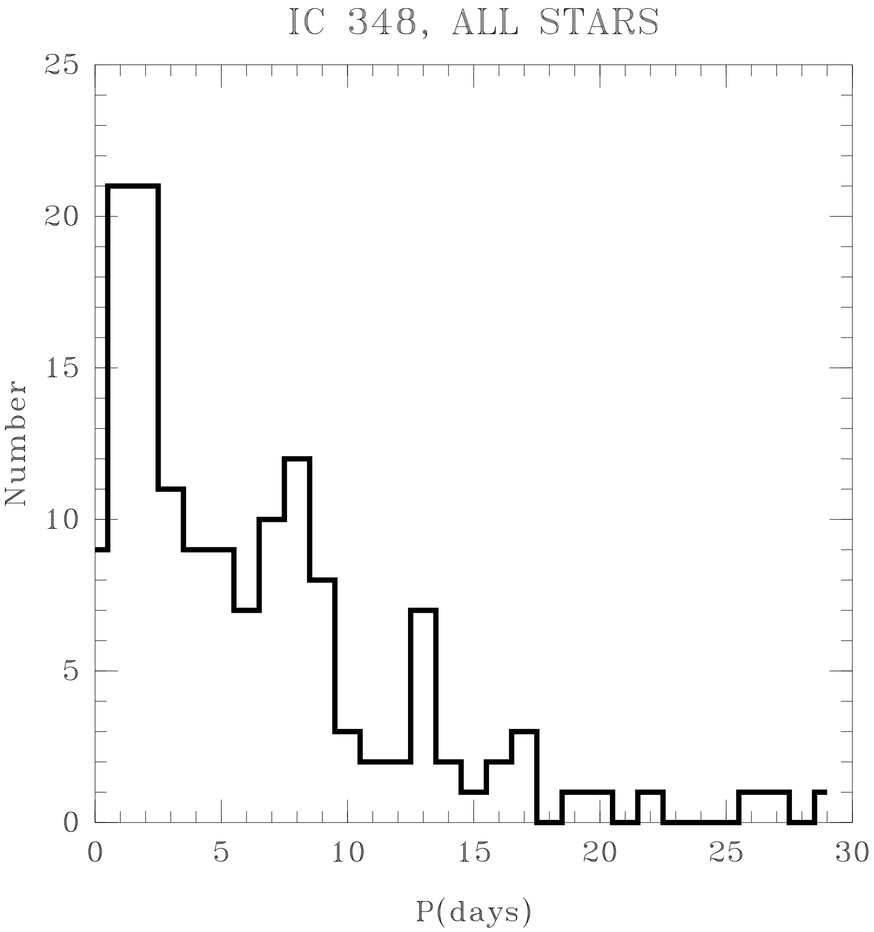

Figure 4.4 A histogram of all 145 know rotation periods in IC 348 from our data and the literature.

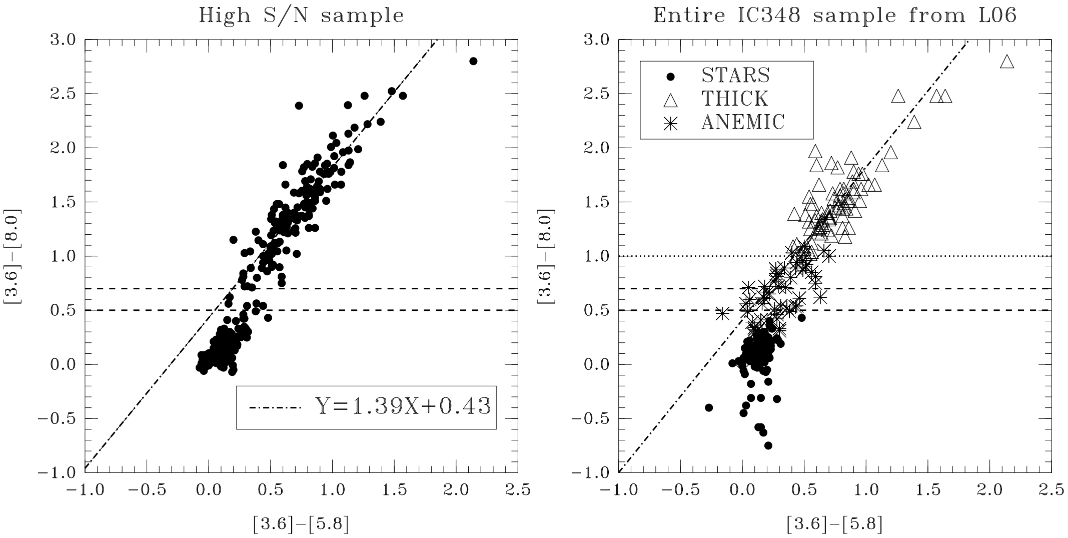

Figure 4.5 The plot on the left shows the [3.6]–[8.0] *vs.* [3.6]–[5.8] colors of 435 PMS stars collected from the literature with photometric errors less than 0.1 mag. Objects with [3.6]–[8.0] > 0.7 are stars with significant IR excess indicating the presence of a disk. Objects with [3.6]–[8.0] < 0.5 are consistent with stellar photospheres. Only ∼ 1% of the stars have 0.7 > [3.6]–[8.0] > 0.5. The dash-dotted line is a linear fit to the stars with disks. The plot on the right shows the entire sample of IC 348 members studied by Lada et al. (2006, L06 in this figure). Some of the objects classified as "anemic disks" by L06 seem to be photospheres of late type stars. The dotted line correspond to the disk identification criteria adopted by Rebull et al. (2006).

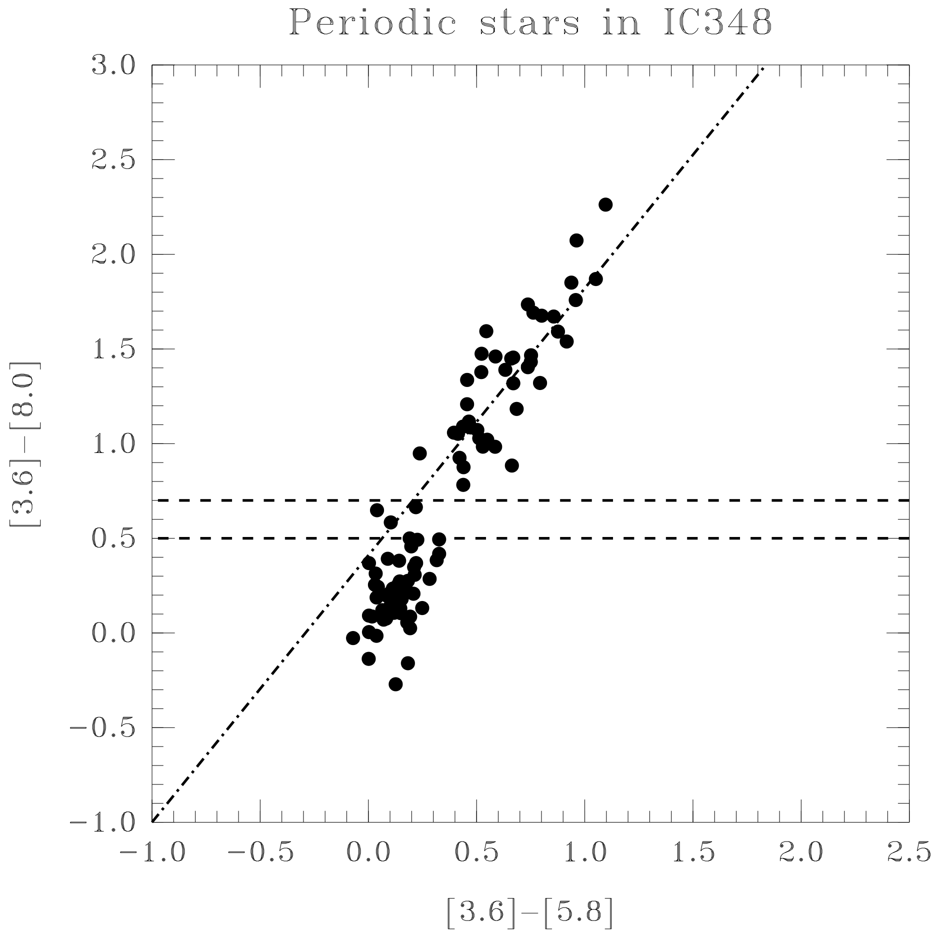

Figure 4.6 The [3.6]–[8.0] *vs.* [3.6]–[5.8] colors of the periodic stars in IC 348. Stars with [3.6]–[3.8] colors > 0.7 possess disks while stars with [3.6]–[3.8] colors < 0.5 are diskless. Only three objects show a somewhat ambiguous disk identification.

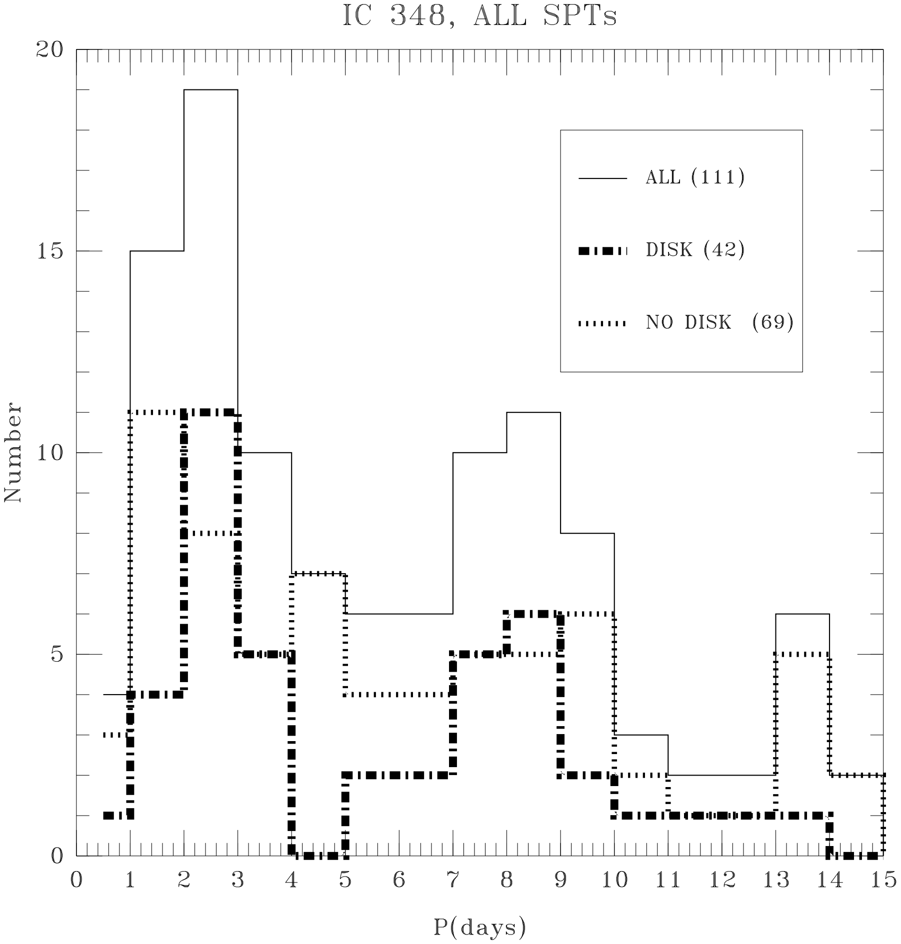

Figure 4.7 Period histogram for 111 IC 348 stars with rotation periods < 15 days and [3.6]–[8.0] data. The three different lines represent all stars (solid), stars with an IR excess indicating the presence of a disk (dot-dash line), and stars with no detected disk signature (dotted line). A very clear bimodal distribution is seen for stars with disks; there is no clear correlation between the presence of a disk and the rotation period for the stars in IC 348.

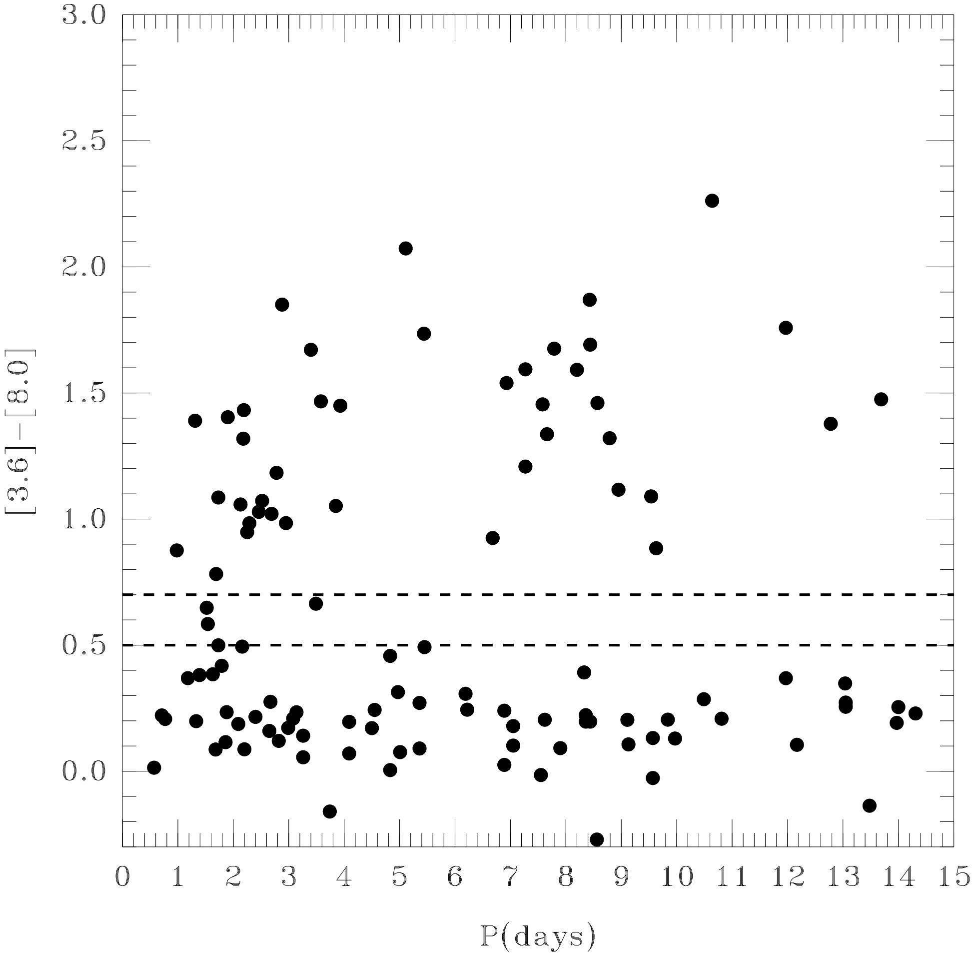

Figure 4.8 A plot of [3.6]–[8.0] color vs. period. We find no evidence for a correlation between period and the presence of an IR excess or the magnitude of the excess. A standard Spearman test yields over a 84% chance that the quantaties are completely uncorrelated.

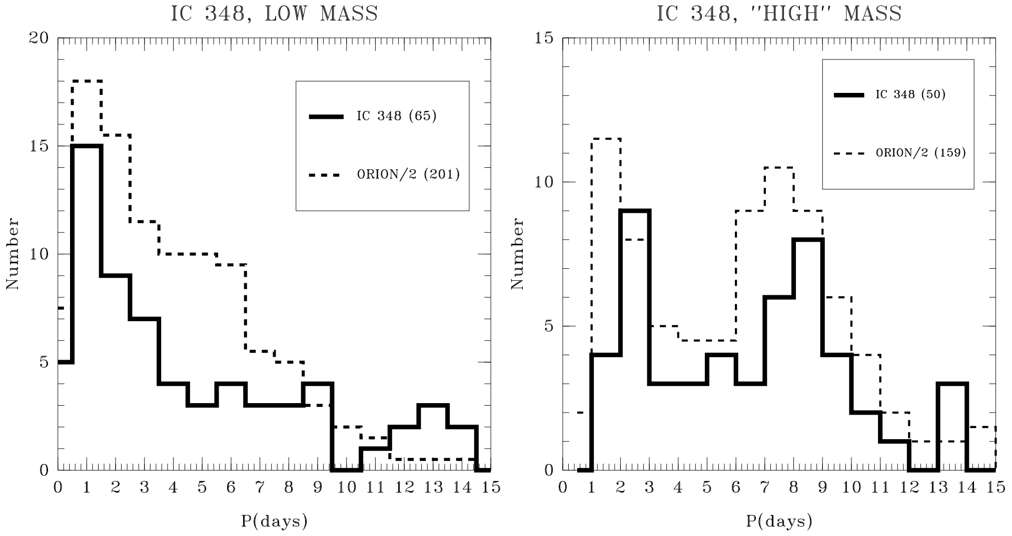

Figure 4.9 Period histograms for low and high mass stars in the IC 348 cluster with *Spitzer* data. The period distributions resemble those seen in the heart of the Orion Nebula Cluster (ONC) by H02, which are shown for comparison scaled down by a factor of two. Stars estimated to be less massive than $0.25\,M_\odot$ show a unimodal distribution dominated by fast rotators (P ~ 1–2 days), while stars estimated to be more massive than $0.25\,M_\odot$ show a bimodal distribution with peaks at ~2 and ~8 days.

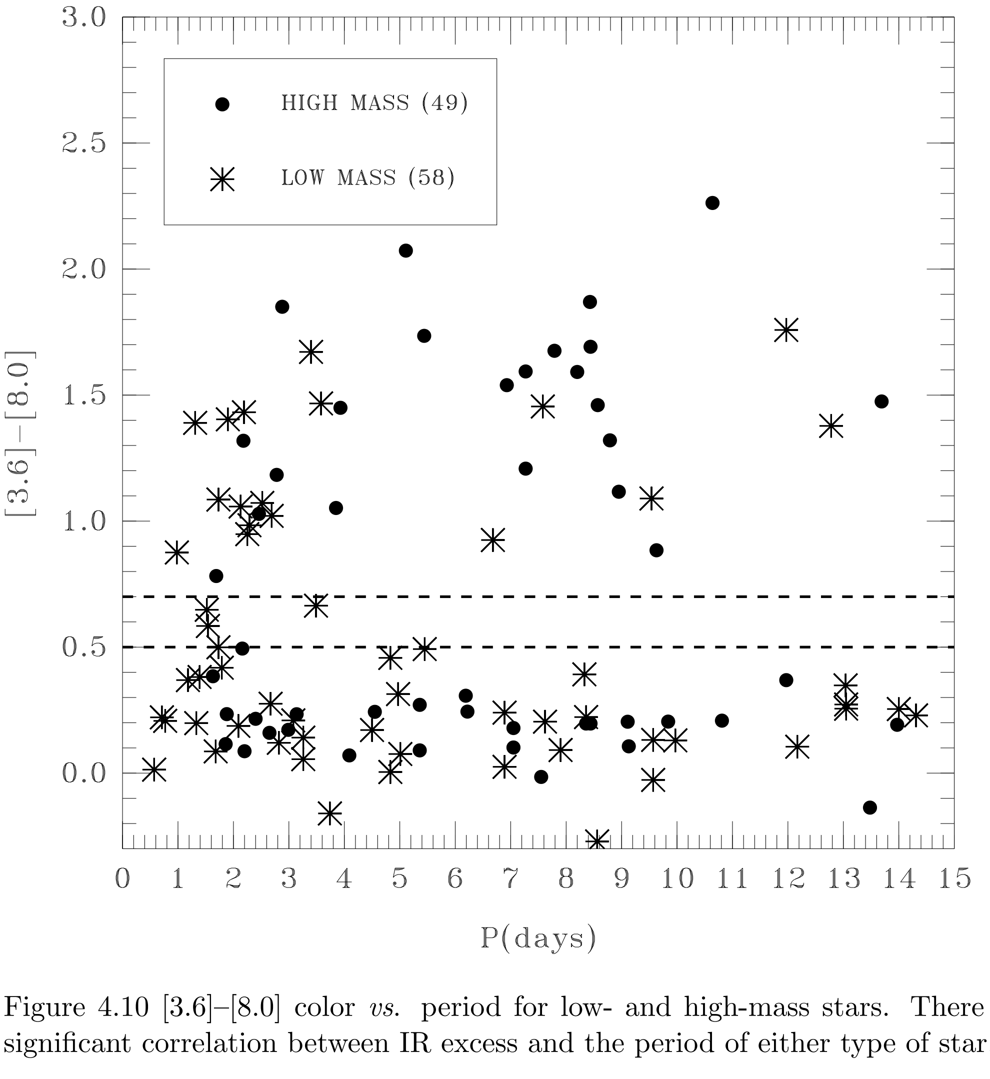

Figure 4.10 [3.6]–[8.0] color *vs.* period for low- and high-mass stars. There is no significant correlation between IR excess and the period of either type of star.

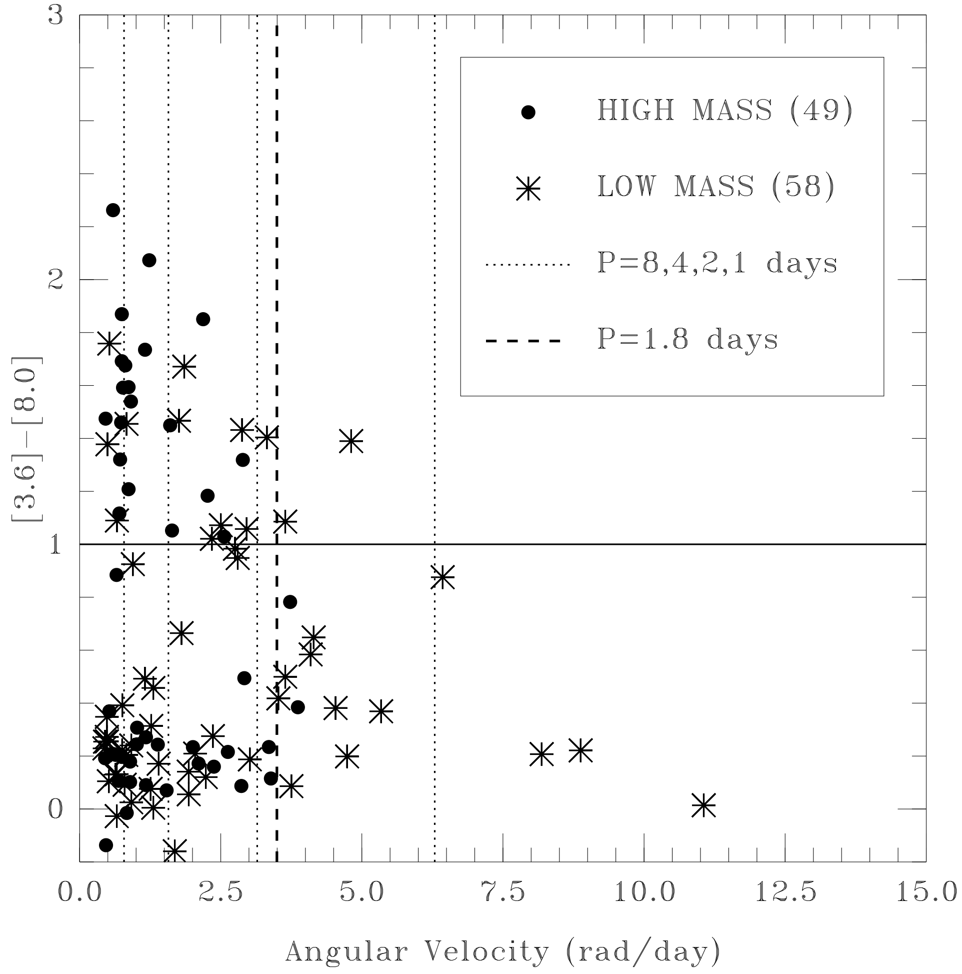

Figure 4.11 [3.6]–[8.0] color *vs.* angular velocity for low- and high-mass stars. Stars with periods $\lesssim$ 1.5 days are significantly less likely to have a disk than stars with longer periods. The low disk frequency of very fast rotators is the only feature of our sample that could *potentially* be interpreted as an evidence for disk braking, but a more rigorous analysis of this result is necessary to determine its significance.

Chapter 5

Testing the Disk Regulation Paradigm with Spitzer Observations. II. A Clear Signature of Star-Disk Interaction in NGC 2264 and the Orion Nebula Cluster

5.1 Abstract

[1] Observations of PMS star rotation periods reveal slow rotators in young clusters of various ages, indicating that angular momentum is somehow removed from these rotating masses. The mechanism by which spin-up is regulated as young stars

---

[1] based on Cieza, L. & Baliber, N. 2007, submitted to ApJ

contract has been one of the longest-standing problems in star formation. Attempts to observationally confirm the prevailing theory that magnetic interaction between the star and its circumstellar disk regulates these rotation periods have produced mixed results. In this paper, we use the unprecedented disk identification capability of the *Spitzer* Space Telescope to test the star-disk interaction paradigm in two young clusters, NGC 2264 and the Orion Nebula Cluster (ONC). We show that once mass effects and sensitivity biases are removed, a clear increase in the disk fraction with period can be observed in both clusters across the entire period range populated by cluster members. We also show that the long-period peak (P $\sim$8 days) of the bimodal distribution observed for high-mass stars in the ONC is dominated by a population of stars possessing a disk, while the short-period peak (P $\sim$2 days) is dominated by a population of stars without a disk. Our results represent the strongest evidence to date that star-disk interaction regulates the angular momentum of these young stars. This study will make possible quantitative comparisons between the observed period distributions of stars with and without a disk, as well as numerical models of the effects of protoplanetary disks on the young lives of their parent stars.

5.2 Introduction

For many years, the loss of angular momentum in the evolution of pre-main-sequence (PMS) stars was a fundamental problem in the theory of star formation. As PMS stars contract by a factor of $\sim 2-3$ during their first 3 Myrs of evolution, models assuming homologous contraction and conservation of angular momentum dictate that all stars less than $\sim 1.2\,\mathrm{M}_\odot$ should rotate with periods shorter than $\sim$2 days by an age of 2 Myrs (D'Antona & Mazzitelli, 1998; Herbst et al., 2000). However, observations of clusters determined to be $\sim$2 Myrs old or older show that most PMS stars rotate much slower than expected. Interaction between the magnetic field of a young star and the inner regions of its protoplanetary disk has been invoked by virtually every rotational evolution model as the mechanism by which the rotation periods of these stars are regulated as they evolve onto the main sequence (Königl, 1991; Shu et al., 1994; Hartmann, 2002; Matt & Pudritz, 2005).

A first-order prediction of these models is stars interacting with their disks should have longer rotation periods than stars that have already lost their disks, leaving them free to spin up as they contract (Herbst & Mundt, 2005). Early observations of rotation periods of PMS stars, obtained by monitoring the brightness modulation produced by stellar surface features, seemed to support the star-disk interaction scenario for angular momentum regulation.

Some studies showed correlations between rotation period and ground-based disk indicators (most commonly excess K-band emission, e.g. Herbst et al., 2002) and interpreted these results as strong evidence for star-disk interaction, claiming that stars with longer periods were rotating more slowly because they had transferred angular momentum to their disks (Edwards et al., 1993; Herbst et al., 2000, 2002; Lamm et al., 2005). This interpretation suffers from several problems as various issues can mask or mimic the correlation, such as sample size, sensitivity biases, mass effects, and, most importantly, ambiguous disk indicators. Therefore, the correlation between infrared (IR) excess and rotation period was challenged by studies which failed to find any correlation between rotation period and a range of disk and accretion indicators in various clusters (Stassun et al., 1999; Rebull, 2001; Rebull et al., 2004; Makidon et al., 2004; Littlefair et al., 2005). The current work presents conclusive evidence that star-disk interaction is the mechanism by which PMS angular momentum is regulated.

The ability to overcome the confusion surrounding the angular momentum problem arrived with the acquisition of *Spitzer* mid-IR observations sensitive enough to unambiguously determine the presence of a disk around PMS stars in the IRAC band passes. In a study of the young cluster IC 348 (Cieza & Baliber, 2006, hereafter, Paper I), we find that 8.0 μm data are needed to clearly identify all of the disks in a given sample of stars (fig. 5) (see also Hartmann et al., 2005; Rebull et al., 2006). Unlike those in ground-based studies, *Spitzer* mid-IR observations are sensitive enough in the IRAC bands to unambiguously determine the presence of a disk around PMS stars. This accurate disk identification allows proper sample separation of stars with and without disks, making it possible to study separately and compare the entire period distribution of each sample. As a result, quantitative analysis and modeling of the period distributions of stars with and without a disk can be performed to put further constraints on the angular momentum evolution of PMS stars and the disk-regulation mechanism.

In this paper, we present a new study of the angular momentum history of two young stellar clusters, the ONC (~1 Myr) and NGC 2264 (~2-3 Myrs). In §5.3, we discuss results from previous work on these two clusters and IC 348, the other well-studied PMS star cluster, detailing the important factors, such as accurate disk identification and sample selection, needed to isolate the effects of circumstellar disks on the current rotation period distributions of young clusters. In §5.5, we describe our new results from NGC 2264, using rotation periods from the literature and public *Spitzer* data, and a reanalysis of the data in the ONC study presented by Rebull et al. (2006), using the same mass sample for each study, with a stricter sample selection in the ONC because of the different extinction levels in that cluster. In §5.6, we compare the two results and discuss robust Monte Carlo simulations, already underway, which will determine what star and disk evolution parameters are allowed given the current rotation period distributions of stars with and without a disk in each cluster. Future work on the subject is also proposed. Our conclusions are summarized in §5.7.

5.3 Previous Observational Results

Three clusters have been studied extensively to produce rotation periods from photometric monitoring campaigns, spectral types from spectroscopy and photometric colors, and disk identification from various disk indicators. Until *Spitzer* mid-IR data became available, disk identification was limited to ground-based color excesses, mostly in the near-IR, and Hα equivalent widths.

These indicators, however, have not provided disk identification accurate and reliable enough to study the effect circumstellar disks have had throughout the lives of PMS stars at the age of these clusters. The correlation between rotation period and near-IR color excess can be masked by biases introduced by these data. For instance, it has been shown that the near-IR disk indicator misses 30% of the disks that can be detected at longer wavelengths (Hillenbrand et al., 1998). Also, the ground-based photometry used to calculate the excess most often comes from different epochs, which can affect the results due to the high photometric variability of these stars (Rebull, 2001).

Moreover, correlations between rotation period and near-IR excess can be caused by a secondary effect of the correlation between mass and rotation period, in a sense mimicking the result expected from star-disk interaction (Littlefair et al., 2005). As shown by previous work (Herbst et al., 2000, 2002; Lamm et al., 2005; Cieza & Baliber, 2006), rotation period distributions of PMS stars are highly dependent on mass. PMS stars of later spectral types behave differently than do stars M2 and earlier, corresponding to masses of $M \geq 0.25M_{\odot}$ at the ages of these clusters, according to theoretical evolutionary tracks (D'Antona & Mazzitelli, 1998) (hereafter, high-mass stars). ONC high-mass stars show a bimodal period distribution, while low-mass stars rotate more rapidly than the high-mass stars, with a unimodal distribution peaking at ∼2 days and a tail of longer periods (Herbst et al., 2001). In NGC 2264, the high-mass stars do not show a **clear** bimodal distribution, but they do rotate more slowly than the low-mass population. The low-mass period distribution is also more sharply peaked than the high-mass distribution. Due to the difference in the color contrast between the stellar photosphere and the inner disk, near-IR excess tends to be greater for high-mass stars than for low-mass stars (Hillenbrand et al., 1998), and since lower mass stars tend to rotate faster than higher mass stars, this can result in a correlation between near-IR excess and rotation period that is not necessarily connected to star-disk interaction. Therefore, these two different populations must be studied separately.

Spitzer's Infrared Array Camera (IRAC, 3.6–8.0 μm) (Fazio et al., 2004) allows the first observations sensitive enough at mid-IR wavelengths to accurately determine the presence of inner circumstellar disks for a statistically significant number of PMS stars with known rotation periods. The observations at every IRAC wavelength are also observed concurrently, overcoming previous limitations caused by stellar magnitude variations between observations. However, even with an accurate identification of circumstellar disks, biases and selection effects can still mask useful measurements of the effects of star-disk interaction on young stellar populations. As discussed in §5.4 and §5.5, selecting a uniform and complete sample of stars is critical in order to be able to detect the role star-disk interaction has on the angular momentum evolution of PMS stars. What follows is a more detailed discussion of the mixed results of previous searches for the effects of star-disk interaction on rotation period distributions in each cluster.

5.3.1 NGC 2264

Virtually all $\sim$500 known rotation periods in NGC 2264 can be collected from two studies (Makidon et al., 2004; Lamm et al., 2005). Makidon et al. (2004) conduct a study of 201 stars in this cluster. They examine the hypothesis that star-disk interaction regulates the angular momentum of PMS stars by searching for a correlation between rotation period and 4 different disk indicators (U-V, I_C–K_s, H–K_s, and Hα). They find "no conclusive evidence that more slowly rotating stars have disk indicators, or that faster rotating stars are less likely to have disk indicators." Lamm et al. (2005) investigate the disk regulation hypothesis in NGC 2264 by studying rotation period distributions of classical T Tauri stars (CTTS) and weak-lined T Tauri stars (WTTS) using a R_C–Hα vs. R_C–I_C color criterion to distinguish between the two populations. They find that the distribution of rotation periods of the high-mass CTTS and WTTS populations "looks quite different" even though "the statistics are poor." Namely, according a Kolmogorov-Smirnov test, they find that there is a 0.02 probability that the distribution of high mass CTTS and WTTS are equivalent. They attribute this marginally significant difference in the rotation period distribution to the fact that the stars classified as CTTS are more likely to have a disk than those classified as WTTS. Although they attempt to separate stars by both mass and disk presence, their results are hampered by an inefficient disk identifier. Fewer than half of their high-mass stars, for example, are used in their analysis (72 out of 184), leaving 112 stars as ambiguous disk identifications.

5.3.2 ONC

With over 900 known rotation periods, the ONC has been the focus of most studies of the angular momentum evolution of PMS stars. Edwards et al. (1993) conduct a study of 34 T Tauri stars from Taurus and the ONC, ranging in spectral type from K7 to M1 and in age from 1 to 10 Myrs. They show a correlation between H-K excess and rotation period for these stars; however, in a subsequent study by Stassun et al. (1999) for stars in the ONC, no such correlation was found. Herbst et al. (2000) find a strong period dependence on stellar mass and confirm the bimodal distribution for high-mass stars originally suggested by an earlier study from that group (Attridge & Herbst, 1992). They explain that the previous study by Stassun et al. (1999) did not exhibit the bimodal period distribution because its sample was dominated by low-mass stars. They find a "weak but significant" correlation with period among stars with $M > 0.25$ $M_\odot$, but argue that the strongest evidence for disk-locking is the bimodal distribution itself.

Rebull (2001) study 4 fields in the outer ONC, surrounding but not including the Trapezium region. They conclude that "There is no unambiguous correlation of period with I_C-Ks, H-Ks, and U-V color excesses or more indirect disk indicators; the slowest rotators are not necessarily the disk candidates, and the disk candidates are not necessarily the slow rotators, regardless of how one defines a disk candidate" (Rebull, 2001).

Subsequently, Herbst et al. (2002) show a correlation between rotation period and I-K excess for stars in the ONC which they claim has a "very high" level of significance. They find that slower rotators with periods >6.28 d show a mean IR excess emission, Δ(I–K) = 0.55 ±0.05, and more rapidly rotating stars with periods <3.14 d have a mean Δ(I–K) of 0.17 ±0.05. With this result, they claim, "The long-suspected, but somewhat controversial, correlation between rotation and excess infrared emission, which is relevant to the disk-locking hypothesis, is finally confirmed at a very high significance level. There is no doubt now that more slowly rotating stars in the ONC have, on average, greater infrared excess emission than do their more rapidly rotating counterparts" (Herbst et al., 2002). This correlation between rotation and the magnitude of the excess infrared emission has been interpreted by the Herbst group as conclusive support of the star-disk interaction hypothesis (Herbst et al., 2002, 2006).

However, having failed to find a correlation between period and disk indicators such as Hα emission, U-V color excess, and K-L color excess, other groups have a different interpretation of the Herbst et al. (2002) results and argue that the observed correlation between period and the magnitude of the infrared excess does not represent strong support for star-disk interaction. Makidon et al. (2004) state that "the size (and indeed the presence) of the near-IR excess need not be well correlated with the presence of a circumstellar disk owing to the combined effects of inclination and inner disk hole effects (see Hillenbrand et al. 1998; Mathieu 2003). Therefore, correlations between period and near-IR excess strength are not necessarily particularly meaningful" (Makidon et al., 2004). Littlefair et al. (2005) express similar concerns about the Herbst et al. (2002) result, and add an additional one: a mass effect. They argue that the "the level of I–K excess depends upon a number of factors: disc mass, inclination angle, inner disc hole size and disc structure. It also depends strongly upon stellar mass, with excesses around high-mass stars being much stronger than excesses around low-mass stars (Hillenbrand et al. 1998). What this means for the ONC is that the low-mass stars, which are rotating rapidly, will necessarily exhibit smaller I–K excesses than the high-mass stars, which rotate more slowly. Such an effect could easily be responsible for the apparent correlation between rotation rate and infrared excess. The claims that the ONC offers strong support for disc locking should therefore be interpreted with caution" (Littlefair et al., 2005).

We note that the slow and fast rotators ($\omega < 1$ radian/d and $\omega > 2$ radian/d, corresponding to periods longer than 6.28 days and shorter than 3.14 days, respectively), for which the Herbst et al. (2002) study finds very different IR-excess distributions, indeed have very different mass distributions. In their short-period sample, there are twice as many low-mass stars as high-mass stars (80 vs. 40), while in their long-period sample, there are only 34 low-mass stars vs. 84 high-mass stars. Moreover, the mean IR excess emission for long-period stars in the ONC found by the Herbst et al. study (Δ(I–K) = 0.55) is increased significantly by the 8 stars (all high-mass) with the highest excesses in the group.

Recently, using *Spitzer* IRAC data as a more reliable disk indicator, Rebull et al. (2006) studied the angular momentum problem in the ONC central and surrounding regions using periods from the literature. Having been able to accurately determine which stars have disks and which do not, they were able to show a connection between stellar rotation and the presence of a circumstellar disk. In particular, they show that stars with periods shorter than 1.8 days are significantly less likely to have a disk that stars with periods longer than 1.8 days. However, they also find that "among the slower rotators (stars with periods > 1.8 days), the period distributions for stars with and without disks ([3.6]–[8] > 1 and < 1, where bracketed notation indicates IRAC colors) are statistically indistinguishable." Though suggestive, by itself this result does not lend conclusive support to the star-disk interaction scenario because the short-period objects that represent the correlation make up less than 20% of the entire population, leaving over 80% of the objects showing no correlation. Also, this 1.8-day period cut is arbitrary, chosen in order to maximize the result rather than for a specific scientific reason. Other factors, such as an overabundance of close binaries among fast rotators, could also account for the low disk fraction in this population (Rebull et al., 2006; Cieza & Baliber, 2006). As shown in §5.4 and §5.5, even when using *Spitzer* colors as a disk indicator, a general correlation between disk fraction and rotation period can only be seen across the entire period range after the mass effects and sensitivity biases are removed from the sample.

5.3.3 IC 348

To date, only two groups have searched for a period-disk correlation in IC 348 (~3 Myrs). Littlefair et al. (2005) study a sample of 50 periodic stars and search for a correlation between period and K-L color excess (available for 30 stars) and Hα (available for 43 stars), but find no significant correlation.

Thanks to a very deep IRAC GTO survey (1600 sec exposures/pixel), of the three clusters discussed in this paper, IC 348 is the only cluster that currently has deep-enough observations to reach the photospheric level of the entire sample of periodic stars at all four IRAC wavelengths. In Paper I, a study of IC 348 using these *Spitzer* data, we find a similar result to the one reported by Rebull et al. (2006) in the ONC, although with a smaller level of significance given the size of our sample.

Namely, in a total sample of ∼130 stars with rotation periods, we find a small subset of cluster members that rotate with periods shorter than ∼2 days, showing a significantly lower disk fraction than the rest of the cluster population. We also find no statistically significant difference between the rotation period distribution of stars with and without disks at periods longer than ∼2 days. We analyze the populations of stars with and without disks regardless of stellar mass and the populations of high-mass and low-mass stars independently. When the entire sample is considered, we find a bimodal distribution of periods for the stars with disks which offers no support for star-disk interaction. However, after subdividing by mass the population of stars with and without a disk, there are too few stars in each mass bin for the disk and no-disk population to make the analysis as a function of period statistically meaningful (see §5.6.1).

5.4 The Data

5.4.1 NGC 2264

NGC 2264 Rotation Periods

Makidon et al. (2004) report rotation periods for 201 stars. Based on their false alarm probability levels, they divide their periods into two quality categories, 1 and 2. Lamm et al. (2005) report rotation periods for 405 stars. We combined the 114 "quality 1" rotation periods reported by Makidon et al. (2004) and the 405 rotation periods from Lamm et al. (2005). There were 74 stars in common between these two groups of 114 and 405 stars, which means that we have selected a total of 445 individual stellar rotation periods. We list the periods of these stars in Table 5.1, along with their coordinates and the R_C and I_C photometry reported by the two groups. We adopt the periods from the Lamm et al. (2005) study for the 74 stars common to both studies. Their work shows that ∼95% of these 74 stellar rotation periods are identical to those of the "quality 1" periods reported by the Makidon group, highlighting the reliability of all of the periods listed in Table 5.1.

NGC 2264 *Spitzer* data

NGC 2264 was observed with IRAC (Fazio et al., 2004) as part of the *Spitzer* Guaranteed Time Observation program "Disk Evolution in the Planet Formation Epoch" (PID=37). The observations consist of 4 dithers and were conducted in the High Dynamic Range mode which includes 0.4 sec observations before 10.4 sec exposures at each dither position. This mode allows photometry of both bright and faint stars at the same time. Each dither consists of 7×11 IRAC fields with $290''$ offsets, resulting in a total mapped area of $\sim 33' \times 51'$ at each of the IRAC wavelengths (3.6, 4.5, 5.8, and 8.0 μm). See Young et al. (2006) for a more detailed description of the IRAC observations of NGC 2264. We retrieved from the *Spitzer* Science Center (SSC) archive the Basic Calibrated data of NGC 2264 that was processed with the SSC pipeline version S11.0.2. The Astronomical Observation Request (AOR) Keys of the data are 0003956480, 0003956992, 0003956736, and 0003957248. We mosaicked the IRAC data and produced point-source catalogs for each band using the pipeline developed as part of the *Spitzer* Legacy Project, "From Molecular Cores to Planet-forming Disks" (c2d). See Evans et al. (2006) for a detailed description of the c2d pipeline.

NGC 2264 Sample Selection

Obtaining an unbiased sample is critical in order to be able to study the connection between circumstellar disks and PMS star angular momentum evolution. Using *Spitzer* data in our study of IC 348 (Paper I), we show that $\sim 40\%$ of the circumstellar disks identified with 5.8 and/or 8.0 μm excesses in IC 348 show no clear excess at shorter wavelengths.

We searched our point source catalogs for IRAC fluxes of the periodic stars in NGC 2264 listed in Table 5.1. We found 3.6 μm fluxes for all 445 of the objects, and data for 436, 371, and 229 stars at 4.5, 5.8, and 8.0 μm respectively. Following Paper I, we use the [3.6]-[8.0] colors for disk identification purposes ([3.6]-[8.0] $<$ 0.7 represents a bare stellar photosphere, and [3.6]-[8.0] $>$ 0.7 a star with a disk); therefore, in order to preserve the reliability of our disk identification, we restrict our analysis to the 229 stars with available 3.6 and 8.0 μm fluxes.

Mass Bias

Because IRAC 8.0 μm data are required for reliable disk identification, a mass bias can be introduced due to the sensitivity limits of those data in a magnitude-limited sample. To illustrate this effect, in Fig. 5.1 we plot histograms of the period distributions of the high- and low-mass stars in the NGC 2264 data set that were detected at 8.0 μm and those that were not. In the left panel, the period distribution of the high-mass stars detected at 8.0 μm is statistically indistinguishable from the distribution of stars with no 8.0 μm detection (P = 0.96, Kolmogorov-Smirnov two-sample test, n1 = 142, n2 = 70). In the right panel, on the other hand, the period distribution of low-mass stars detected at 8.0 μm is significantly different than that of the undetected stars (P = 1.6e-3, K-S two-sample test, n1 = 81, n2 = 142). The fraction of stars with periods $<$2 days detected at 8.0 μm is 26%, and the fraction with P $>$ 2 days detected is 46%. In the low-mass sample, there is a strong bias against the fastest rotators, which is expected if these stars are faint because they are the lowest-mass stars in the sample and/or they preferentially have no disks. Also, if optical colors are used to estimate mass, the low-mass sample can be contaminated by highly extincted high-mass stars, which have a different rotation period distribution than lower-mass stars.

Since low-mass stars suffer from these two effects which render the current sample unreliable, we must segregate the sample by spectral type (corresponding to masses given by evolutionary tracks). Since brighter high-mass stars do not suffer as much from these sources of sample bias and contamination (reddened low-mass stars cannot be mistaken for high-mass stars), in addition to requiring *Spitzer* 8.0 μm detection, we further restrict our study to the high-mass population.

Spectral types to estimate masses are available for only a fraction of the stars in NGC 2264. However, NGC 2264 has relatively low extinction ($A_V \sim 0.5$ mag) (Rebull, 2001), which is fairly uniform across the field of view covered by this study. This allows us to use R-I colors to make a mass cut and retain a relatively uncontaminated sample of high-mass stars. We use an R-I color < 1.3 (corresponding to unextincted M2 stars and stars with earlier spectral types (Kenyon & Hartmann, 1995)) as the cutoff for this sample. Restricting our sample, as discussed, based on *Spitzer* data and stellar mass, leaves a final sample of 142 high-mass stars with known rotation periods detected by IRAC at 8.0 μm with which we search for a correlation between rotation period and the presence of a circumstellar disk.

5.4.2 The ONC

For our analysis of the Orion Nebula Cluster and its surroundings, we combine in Table 5.2 the rotation periods and *Spitzer* data presented by Rebull et al. (2006) with spectral types from the literature (Rebull, 2001; Hillenbrand et al., 1998).

ONC Sample Selection

A large fraction of the stars in the Rebull et al. (2006) sample does not have measured spectral types. For stars with no spectral type measurement, Rebull et al. (2006) make a mass cut by placing these stars on I vs. (V-I) color-magnitude diagrams. Unlike in the case of NGC 2264, this method is unreliable for the ONC sample because the extinction is high and highly variable ($AV \sim 1-5$) across the entire field of view covered by the study (Hillenbrand, 1997). Using colors for spectral type classification can lead to a blending of the period distribution of the high- and low-mass stars (see §5.6.1 for a more detailed discussion). We therefore limit our analysis of the Rebull et al. (2006) sample of stars with known rotation periods to those with measured spectral types (M2 and earlier). This leaves 133 high-mass stars with which to monitor the effects of star-disk interaction.

5.5 Results

5.5.1 NGC 2264

When disk fraction is plotted as a function of period for all NGC 2264 members without separating the populations by spectral type (Fig. 5.2, left panel), we find that the only significant feature is a lower disk fraction (17±4%) for stars in the shortest period bin ($P \leq 2$ days) compared to that of the rest of the sample (45±4%). For periods longer than 2 days, the distributions of periods for stars with and without a disk (Fig. 5.2, right panel) are statistically indistinguishable (P=0.211, Kolmogorov-Smirnov two sample test, n1=76, n2=88). This is, in essence, an identical result to those found in the *Spitzer* studies of the ONC (Rebull et al., 2006) and IC 348 (Cieza & Baliber, 2006).

Using an R-I color < 1.3 (corresponding to unextincted M2 stars and stars with earlier spectral types (Kenyon & Hartmann, 1995)) as the cutoff for high-mass stars and plotting disk fraction as a function of period for the high-mass sample in NGC 2264 (Fig. 5.3, left panel), a clear increase in the disk fraction with period is revealed across the entire period range covered by the sample. The unambiguous disk identification from *Spitzer's* 8.0 μm IRAC band allows the populations of stars with and without disks to be separated and plotted individually for the first time. A histogram of the period distributions for high-mass stars with and without a disk (Fig. 5.3, right panel) shows that these distributions are significantly different (P=6.1e-05, Kolmogorov-Smirnov two sample test, n1=48, n2=94). Although there is a relatively flat distribution of stars with disks, there is a large peak of shorter-period stars (1-5 days) with no disks and far fewer with long periods. These different distributions are a clear indication that star-disk interaction regulates the angular momentum of stars as they contract onto the main sequence.

5.5.2 The ONC

The evidence for angular momentum regulation through star-disk interaction is equally dramatic in Orion if one restricts the sample studied by Rebull et al. (2006) by spectral types in the literature (Hillenbrand, 1997; Rebull, 2001) to stars of spectral type M2 and earlier, even though the sample of stars with rotation periods is cut in half as a result. Plotting disk fraction as a function of period for the restricted sample (Fig. 5.4, left panel), a clear increase in the disk fraction with period is revealed across the entire period range populated by the Orion stars. A histogram of the period distributions for high-mass stars with and without a disk (Fig. 5.4, right panel) shows that these distributions are dramatically different (P=9.99e-07, Kolmogorov-Smirnov two sample test, n1=58, n2=75).

Based on the star-disk interaction paradigm, Herbst et al. (2000) predict that the long-period peak (P $\sim$ 8 days) seen in the clear bimodal period distribution of the high-mass stars in the ONC should be dominated by stars with disks, while the short-period peak (P $\sim$ 2 days) should be dominated by stars without disks. Rebull (2001) include stars in the ONC and in surrounding regions termed the "Flanking Fields," which are composed of older stars than those in the younger central region of the cluster and do not show such a clear bimodal distribution as the ONC. If one further restricts their sample to stars in the ONC (84.1 dec $>$ RA $>$ 83.0 deg; 5.0 deg $>$ Dec $>$ -5.7 deg) with measured spectral types (Fig. 5.5, left panel), one recovers the bimodal distribution seen by earlier observations (Attridge & Herbst, 1992; Herbst et al., 2000, 2002). A period histogram of stars with disks over-plotted on a period histogram of stars without disks (Fig. 5.5, right panel) reveals two distinct and cohesive rotation period distributions, one populated by stars lacking disks peaked at P $\sim$ 2 days and the other by stars with disks peaked at P $\sim$ 8 days, which, blended together, form the bimodal distribution of the high-mass stars in the ONC. Separating and plotting individually these two populations of stars with and without disks results in an unambiguous indication that star-disk interaction has prevented the spin-up of PMS stars in the ONC.

5.6 Discussion

5.6.1 The Mass Effect

In §5.5, we have discussed the significant differences in the period distributions of low- and high-mass stars in NGC 2264 and the ONC. These differences are not fully understood but can be partially accounted for by the fact that lower mass stars of a given age have smaller radius, R. Thus, for a given specific angular momentum, j ($j \propto R^2/P$), they are in fact expected to have a a shorter period, P (Herbst et al., 2001). However, since j still seems to be higher for low mass stars than for the high mass counterparts, it has also been suggested that the disk regulation mechanism is less efficient in low mass stars than in high mass stars due to differences in the strength or structure of their magnetic fields (Lamm et al., 2005).

It is easy to show, by making a slightly different mass cut in our ONC analysis, that even small inaccuracies in spectral classification can lead to a severe blending of the period distributions of stars with and without disks. In Fig. 5.6, we compare the mass cut we use in our analysis (left panel) to a slightly different mass cut, including lower-mass stars by one spectral sub-type in the sample (right panel). Because low-mass stars inherently rotate faster than high-mass stars, regardless of the presence of a disk, contaminating the high-mass sample with low-mass stars will mask the effect star-disk interaction has on PMS star rotation periods. The extreme sensitivity of period distribution to mass supports the idea that a sudden change in the strength or structure of the magnetic field, happening at the boundary between M2 and M3 stars, is responsible for the observed differences in period distributions of low mass and high mass PMS stars.

The extreme sensitivity of period distribution to mass also explains previous *Spitzer* results that showed inconclusive evidence of the star-disk interaction scenario. Rebull et al. (2006) found a separate sub-population of fast rotators with $P \leq 2$ days with a low disk fraction (where there are few high- or low-mass stars with disks) and statistically indistinguishable period distributions for stars with and without disks at $P > 2$ days (as is the case with NGC 2264 when analyzing the entire sample instead of only high-mass stars). The longer-period stars in those results are a blend of high- and low-mass stars which have different period distributions, affected by something other than star-disk interaction alone.

In paper I, we obtain the same result for IC 348 because that cluster has too few member stars with known rotation periods to study the high- and low-mass samples separately (Fig. 5.7). As a result, after isolating the small sample, we find only a 1-σ hint that the high-mass stars rotating slower than the median (P = 6.2 days) have a higher disk fraction (50% ± 10% [12/24]) than the high-mass stars rotating faster than the median (39%± 10% [9/23]). We predict that once a significant number of rotation periods (100-150) become available for high-mass stars in IC 348 and its surroundings, the same clear increase in disk fraction with rotation period seen in NGC 2264 (Fig. 5.3) and the ONC (Figs. 5.4 and 5.5) will become evident in the IC 348 region as well.

5.6.2 Outstanding Questions

Quantitative models

Our results from §5.5 show that by restricting the sample of PMS stars studied to those with an accurately determined mass range, and by using a reliable disk indicator like the photometry from *Spitzer's* IRAC instrument, clear observational signatures of star-disk interaction become evident. Using *Spitzer* mid-IR data as a disk indicator, we can finally progress from first-order issues such as whether or not circumstellar disks regulate the angular momentum evolution of PMS stars to ones such as what initial conditions and PMS star and disk parameters are consistent with the observed period distributions of stars with and without a disk, or what constraints the observed distributions can place on disk evolution.

For instance, comparing the observed period distributions to Monte Carlo simulations (introduced by Rebull et al. (2004) and improved upon in the discussion in Paper I) can give us information about the disk-release time of PMS stars and the efficiency with which the disks drain their angular momentum. Results from Rebull et al. (2004) suggested that a significant fraction ($\sim$30%) of high-mass stars must evolve conserving angular momentum from the time they form in order to reproduce the bimodal distribution observed in the ONC. In the context of star-disk interaction, this implies an extremely short disk lifetime (< 1 Myr) for a significant number of stars. Preliminary comparisons of the period distributions of stars with and without a disk presented herein against much more detailed Monte Carlo models

(Cieza et al., 2006) confirm the Rebull et al. (2004) result. Short disk lifetimes are also detected independently in the results of recent *Spitzer* surveys (Padgett et al., 2006, Cieza et al. 2007 – submitted) that find that up to 50% of the youngest WTTS (age $\lesssim$ 1 Myr) show photospheric emission in the mid-IR (8.0-24.0 μm). Our Monte Carlo models show that the period distribution of the stars lacking disks is very sensitive to short disk dissipation timescales because the effects of star-disk interaction are more important at early ages when the stars undergo very rapid contraction.

The sensitivity of current PMS star rotation period distributions to short disk dissipation time scales allows this type of numerical analysis to put valuable constraints on both disk dissipation and planet formation time scales, and, hence, possibly formation mechanisms. A detailed comparison of the observed period distributions of NGC 2264 and the ONC presented herein to Monte Carlo models will be presented in a follow-up paper (Paper III).

Cluster to Cluster Comparisons

The high mass stars in the two clusters studied in this work, the ONC and NGC 2264, have substantially different rotation period distributions. In particular, NGC 2264 lacks the long period peak at $\sim$ 8 days and its stars with disks show a much flatter distribution than do those in the ONC. Lamm et al. (2005) argue that NCG 2264 is twice as old as the ONC and represents a later stage in rotational evolution. By assuming that at the age of the ONC, NGC 2264 had the exact period distribution as the ONC has today, they estimate that ~80% of the stars in NGC 2264 have spun up from the time it was the age of the present-day ONC until now, while only ~30% have remained locked to their disks.

However, the difference in rotation period distributions is also likely constrained by initial conditions and formation environment. Characteristics such as stellar density, cluster IMF, and overall cluster mass might play a role in the angular momentum evolution of PMS stars. The kind of numerical models described above can be used to test whether the period distributions observed in the ONC will naturally evolve into the period distributions observed in NGC 2264 or if different initial conditions and model parameters are required to reproduced the observed period distribution of each cluster.

The observations of NGC 2264 and the ONC studied here only represent a small fraction of the *Spitzer* data capable of playing a role in disentagling the steps in the evolution of PMS stars and their disks. *Spitzer* data currently exist for tens of young nearby clusters awaiting photometric monitoring campaigns to obtain rotation periods. Further studies of other clusters of different ages (from <1 to >10 Myrs) will provide a broader age baseline with which to study the evolution of angular momentum of PMS stars, while the study of clusters of different sizes will establish the importance of PMS stellar environment on this evolution.

Low-mass Population

The only current complete sample of stars with rotation periods in either of the well-studied clusters focused on in this work is the high-mass sample, or stars of spectral type M2 and earlier. Although these stars provide a very clear signature that star-disk interaction is regulating the spin-up of PMS stars as they contract onto the main sequence, the whole story is as yet untold. Lower mass stars, half of all stars with known rotation periods, cannot currently be studied to see if their rotation periods are similarly affected by their circumstellar disks as no cluster has *Spitzer* data deep enough to provide an unbiased sample of low-mass stars. It is clear that the rotation period behavior of these stars is very different from their high-mass counterparts, but the reason for this difference is still unknown. These stars might have a lower overall disk fraction than high-mass stars, which would explain the more rapid rotation of these objects. However, if there were no difference in the disk fraction of these stars, then something internal to the star itself, resulting in a different magnetic field structure for these objects, could prevent star-disk interaction from regulating their angular momentum in the same way it does for high-mass stars.

The only cluster currently suited to be studied in this way is NGC 2264, both because it is a rich cluster with many member stars with known rotation period, and because it has a low enough background brightness to allow deep *Spitzer* observations to detect bare stellar photospheres for the entire periodic sample.

5.7 Conclusions

We combined stellar rotation periods of the young cluster NGC 2264 from the literature with *Spitzer* photometry in order to search for the correlation between slow stellar rotation and mid-infrared excess predicted by disk regulation through star-disk interaction. We also re-analyzed results from the recent Rebull et al. (2006) study of the ONC using the similar criteria to those used in the NGC 2264 analysis. These two clusters combined contain the vast majority of all known rotation periods of PMS stars. Thanks to the unprecedented disk detection capabilities of *Spitzer*, our results provide the strongest observational evidence to date that star-disk interaction regulates PMS star angular momentum. Our main conclusions can be summarized as follows:

1) When stars of all masses in NGC 2264 are considered together, the only significant result is the lower disk fraction of objects with short periods (P $\leq$ 2 days), a range that contains only ~20% of the periodic stars, with respect to that of the rest of the sample. This is the same result found by Rebull et al. (2006) for the ONC, and by it self provides only ambiguous support for the disk regulation paradigm. However, we show that the apparent lack of a clear overall correlation between period and IR-excess across the entire period range is due to the strong

dependence of rotation period on stellar mass and a sensitivity bias against low-mass stars lacking disks.

2) When only the high-mass stars (R-I < 1.3) in our NGC 2264 sample are considered, the correlation between stellar rotation and IR-excess becomes evident across the entire period range of the sample.

3) The NGC 2264 periodic sample of low mass stars (R-I > 1.3) with 8.0 μm data (used for disk identification) is highly biased against the fastest rotators. The bias in the low-mass star sample can be explained if the fastest rotators are the lowest-mass stars in the sample and/or preferentially have no disk. This bias, which masks disk regulation signatures, does not exist in the high-mass star sample.

4) When the periodic sample of ONC stars presented by Rebull et al. (2006) is restricted to high-mass stars with reliable mass estimations, the correlation between stellar rotation and MID-IR-excess becomes apparent across the entire range of the period distribution in the ONC sample as well.

5) We show that the long-period peak (P$\sim$8 days) of the bimodal distribution observed for high-mass stars in the ONC is dominated by a population of stars with disks, while the short-period peak (P $\sim$ 2 days) is dominated by a population of stars without a disk. This result confirms one of the main predictions of the star-disk interaction scenario (Herbst et al., 2000).

6) We argue that a quantitative comparison between the period distribution of stars with and without a disk to numerical models is needed to constrain disk regulation parameters such as the angular momentum transfer efficiency, fraction of regulated stars as a function of time, etc. We will present such a quantitative comparison to Monte Carlo models in a follow up paper (Paper III).

7) The current samples of periodic high-mass stars in NGC 2264 and the ONC with reliable disk indicators (e.g. [3.6]-[8.0] colors) are fairly large and unbiased. However, accurate mass indicators (i.e., spectral types) and deeper *Spitzer*

observations are still needed for an unbiased quantitative study of the role star-disk interaction plays in the evolution of low-mass stars.

8) Photometric monitoring of the many other young clusters already observed by *Spitzer* will reveal the importance of age and stellar formation environments in the angular momentum evolution of PMS stars.

5.8 Acknowledgments

Support for this work, part of the *Spitzer* Legacy Science Program, was provided by NASA through contract 1224608 issued by the Jet Propulsion Laboratory, California Institute of Technology, under NASA contract 1407.

Table 5.1. NGC 2264 Stars with periods from the literature and Spitzer data

RA (J2000)	Dec (J2000)	Rc (mag)	Ic (mag)	Period (days)	Ref	Flux@3.6 (mJy)	$\mathrm{err}_{3.6}$ (mJy)	Flux@4.5 (mJy)	$\mathrm{err}_{4.5}$ (mJy)	Flux@5.8 (mJy)	$\mathrm{err}_{5.8}$ (mJy)	Flux@8.0 (mJy)	$\mathrm{err}_{8.0}$ (mJy)
99.94500	9.68167	13.26	12.69	3.84	2	1.06e+01	1.60e-01	6.29e+00	9.98e-02	4.65e+00	1.11e-01	2.56e+00	6.06e-02
99.95292	9.60983	15.69	14.49	4.01	2	4.62e+00	6.79e-02	3.03e+00	3.46e-02	1.88e+00	4.59e-02	1.16e+00	3.30e-02
99.96287	9.60922	17.16	15.84	1.36	1	2.15e+00	3.25e-02	1.40e+00	2.47e-02	1.45e+00	5.61e-02	5.89e-01	3.39e-02
99.96954	9.62714	19.37	17.49	2.14	1	6.69e-01	1.15e-02	5.21e-01	8.07e-03	0.00e+00	0.00e+00	2.62e-01	2.25e-02
99.97625	9.94092	17.55	15.70	0.58	2	2.45e+00	3.49e-02	1.84e+00	2.66e-02	0.00e+00	0.00e+00	7.91e-01	3.91e-02

Note. — [Reference (Ref) 1 indicates periods and optical photometry taken from Lamm et al. (2005), while Ref 2 indicates periods and optical photometry taken from Makidon et al. (2004). The complete version of this table is in the electronic edition of the Journal. The printed edition contains only a sample to illustrate its content.]

Table 5.2. Orion Stars detected in 3.6 and 8.0 microns with periods from the literature[1]

Name[2]	RA (J2000)			Dec (J2000)			F@3.6	$err_{3.6}$	F@4.5	$err_{4.5}$	F@5.8	$err_{5.8}$	F@8.0	$err_{8.0}$	Per	SpT	SpT-Ref[3]	Mass[4]
	(h	m	s)	(d	m	s)	(mag)	(mag)	(mag)	(mag)	(mag)	(mag)	(mag)	(mag)	(d)			
R01- 678	05	33	36.9	-05	23	06.2	11.52	0.006	11.52	0.008	11.47	0.027	11.44	0.119	7.23	——	——	NO
R01- 680	05	33	37.1	-05	23	07.0	11.52	0.006	11.52	0.008	11.47	0.027	11.44	0.119	7.20	——	——	NO
R01- 716	05	33	41.6	-04	55	59.9	11.91	0.006	11.90	0.009	11.78	0.018	11.88	0.027	7.55	M5.5	R01	L
R01- 739	05	33	43.3	-06	05	23.5	12.09	0.007	12.16	0.012	12.04	0.019	11.97	0.024	3.99	M3.5	R01	L
R01- 749	05	33	44.5	-06	05	20.5	12.39	0.009	12.36	0.011	12.36	0.020	12.36	0.031	15.42	——	——	NO
HBC 107	05	33	44.9	-05	31	08.6	9.92	0.002	9.97	0.003	9.89	0.007	9.82	0.039	2.64	——	——	NO
Par 1266	05	33	46.1	-05	34	26.5	10.84	0.003	10.84	0.004	10.84	0.011	10.90	0.039	4.65	K8	R01	H

Note. — The complete version of this table is in the electronic edition of the Journal. The printed edition contains only a sample to illustrate its content.

[1] With the exception of the last 3 columns, all data come from Rebull et al. (2006).

[2] R01 numbers come from Rebull (2001), HBC numbers from Herbig & Bell (1988), Par numbers from Parenago (1954), CHS numbers from Carpenter et al. (2001), H97 numbers from Hillenbrand (1997), HBJM numbers from Herbst et al. (2001), and JW numbers come from Jones & Walker (1988).

[3] R01 Spetral types come from Rebull (2001), while the H97 spectral types come from Hillenbrand (1997).

[4] Stars with M2 and earlier spectral types are considered high-mass stars, while stars with M2.5 and later spectral types are considered low-mass stars.

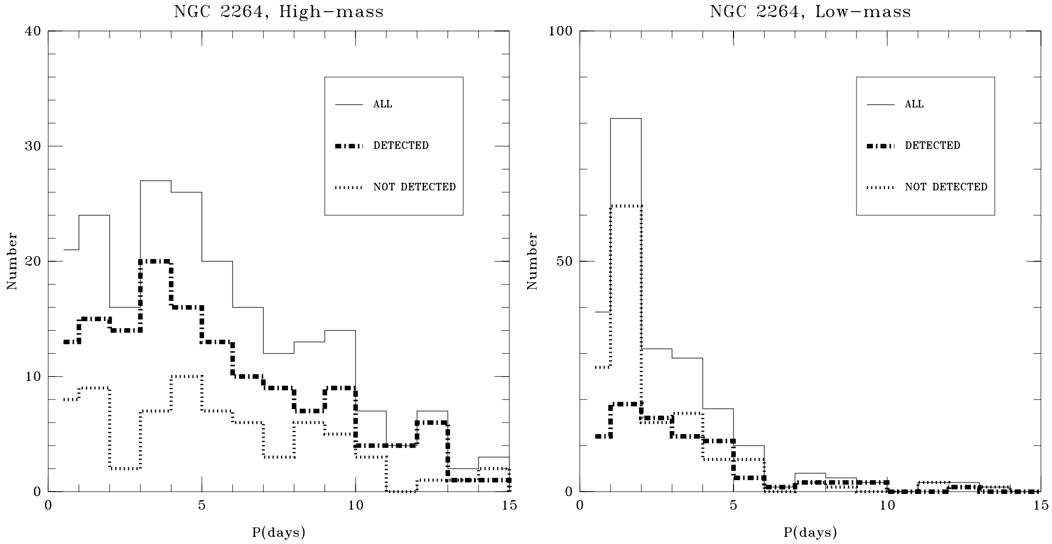

Figure 5.1 Mass-segregated period histograms for stars with and without 8.0 μm data in NGC 2264. (Left Panel) Period histogram for high-mass stars ([R-I] $<$ 1.3) in NGC 2264. The three different lines represent all stars (n=212, solid line), stars detected with *Spitzer's* IRAC instrument at 8.0 μm (n=142, dot-dash line), and stars not detected at 8.0 μm (n=70, dotted line). (Right Panel) Period histogram for low-mass stars ([R-I] $>$ 1.3) in the cluster. The three different lines represent all stars (n=223, solid line), stars detected with *Spitzer's* IRAC instrument at 8.0 μm (n=81, dot-dash line), and stars not detected at 8.0 μm (n=142, dotted line). As previously noted by Lamm et al. (2005) in NGC 2264 and Herbst et al. (2002) in the core of the ONC, low- and high-mass stars have clearly different period distributions. Since the 8.0 μm data is needed for a reliable disk identification (Rebull et al., 2006; Cieza & Baliber, 2006), our analysis is restricted to stars detected at this wavelength. The period distribution of the high-mass stars detected at 8.0 μm is statistically indistinguishable from that of the undetected stars (P = 0.96, Kolmogorov-Smirnov two-sample test, n1 = 142, n2 = 70). In contrast, the period distribution of low-mass stars detected at 8.0 μm is significantly different than that of the undetected stars (P = 1.6e-3, K-S two-sample test, n1 = 81, n2 = 142). As the low-mass sample has a much lower detected fraction of stars at shorter periods than at longer periods, the biases in this sample prevent us from using it.

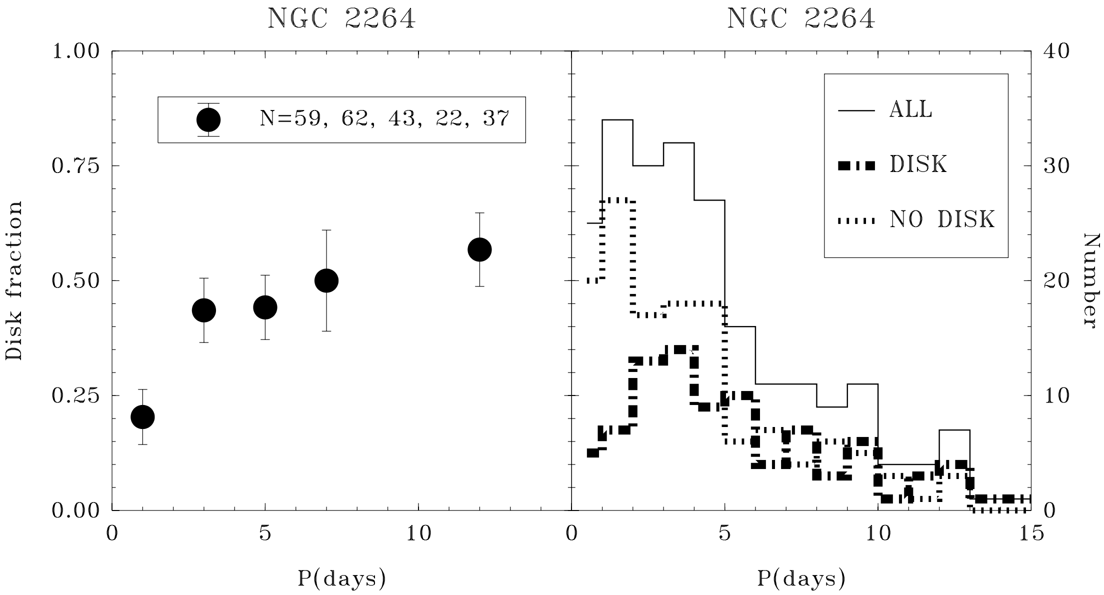

Figure 5.2 Results for all stars in NGC 2264. (Left Panel) The disk fraction as a function of period for the stars in NGC 2264 with rotation periods < 15 days and both 3.6 and 8.0 μm IRAC data, enough for an accurate disk identification. The error bars represent the 68% confidence level (1σ) of the measurements. The only significant feature is the lower disk fraction of the stars with shortest periods (P < 2 days) with respect to that of the rest of the sample. (Right Panel) The period histogram for the same sample of stars. The three different lines represent all stars (solid line), stars with IR-excess indicating the presence of a disk (dot-dash line) and stars with no detected disk signature (dotted line). For periods longer than 2 days, the distribution of periods for stars with and without a disk are statistically indistinguishable (P=0.211, Kolmogorov-Smirnov two sample test, n1=76, n2=88).

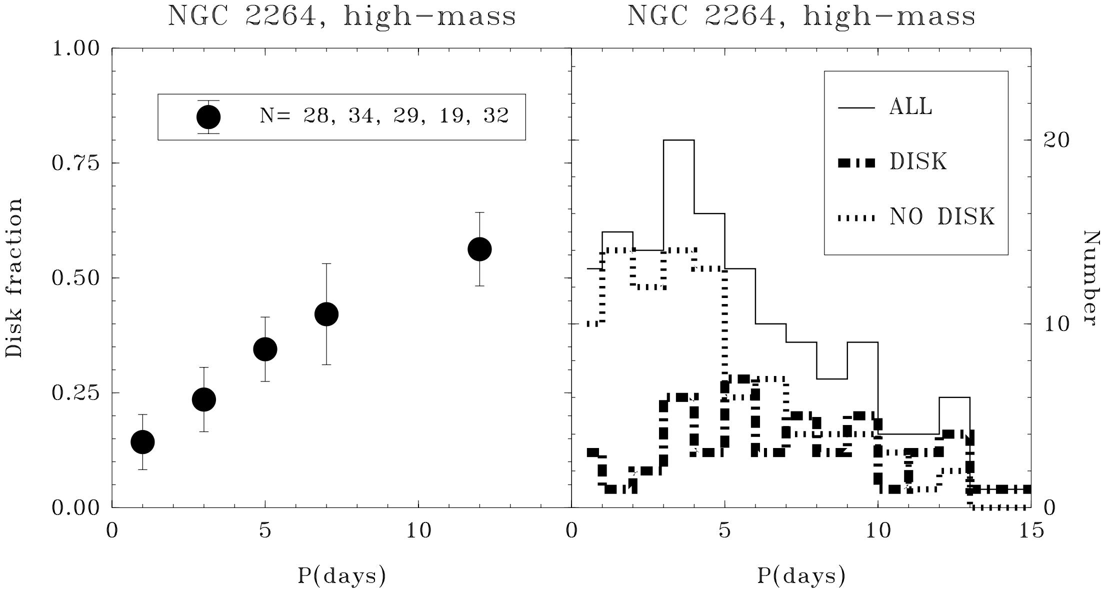

Figure 5.3 Results for high-mass stars in NGC 2264. (Left Panel) The disk fraction as a function of period for high-mass stars. The error bars represent the 68% confidence level (1σ) of the measurements. When only high-mass stars are considered, the connection between the presence of a disk and slow rotation becomes evident across the entire range of the period distribution. (Right Panel) The period histogram for high-mass stars. The three different lines represent all the stars (solid line) and stars with and without a disk (dot-dash line and dotted line, respectively). The period distribution of disk-less high-mass stars peaks at short periods ($P < 5$ days), while the periods of high-mass stars with disks are consistent with a flat distribution. These distributions are significantly different (P=6.1e-05, Kolmogorov-Smirnov two sample test, n1=48, n2=94). This result suggests that stars without disks are free to spin up faster than stars with disks.

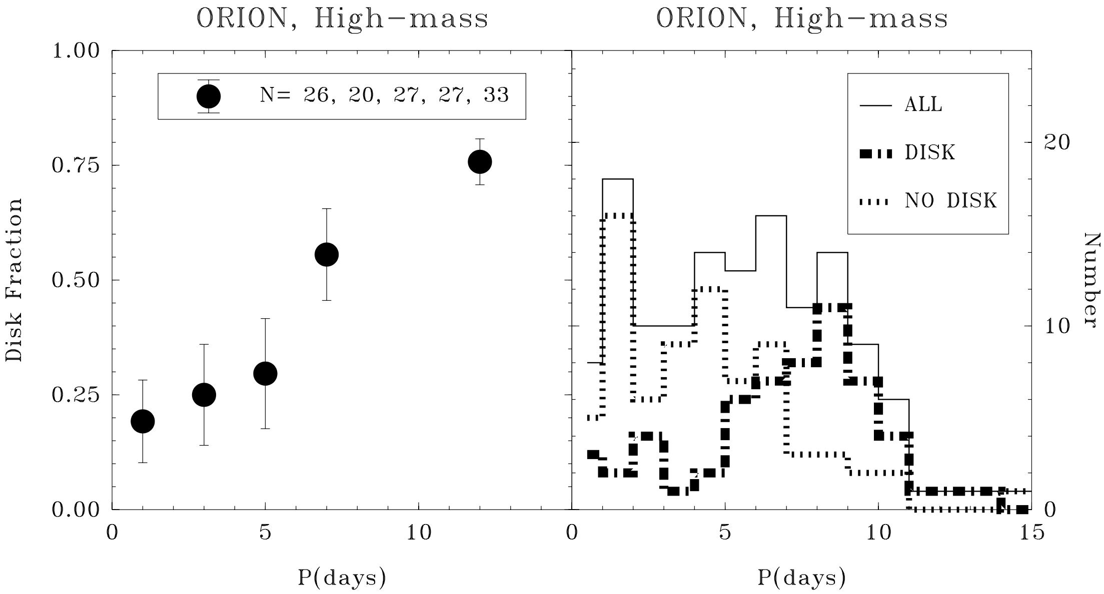

Figure 5.4 Results for high-mass stars in Orion. (Left Panel) The disk fraction as a function of period for high-mass stars with measured spectral types in the ONC and surrounding flanking fields. The error bars represent the 68% confidence level (1σ) of the measurements. As with NGC 2264, the disk fraction clearly increases with period across the entire period range covered by the data. (Right Panel) Period histograms for high-mass stars. The three different lines represent all the stars (solid line) and stars with and without a disk (dot-dash line and dotted line, respectively). The overall distribution is clearly a blend of the two distinct period distributions which are significantly different from one another (P=9.99e-07, Kolmogorov-Smirnov two sample test, n1=58, n2=75). The distribution of stars possessing a circumstellar disk is centered at a period much longer than the distribution of stars with no disk. Once again, the result from the high-mass stars in the ONC and surrounding regions clearly suggest that circumstellar disks are involved with angular momentum regulation in these young stars.

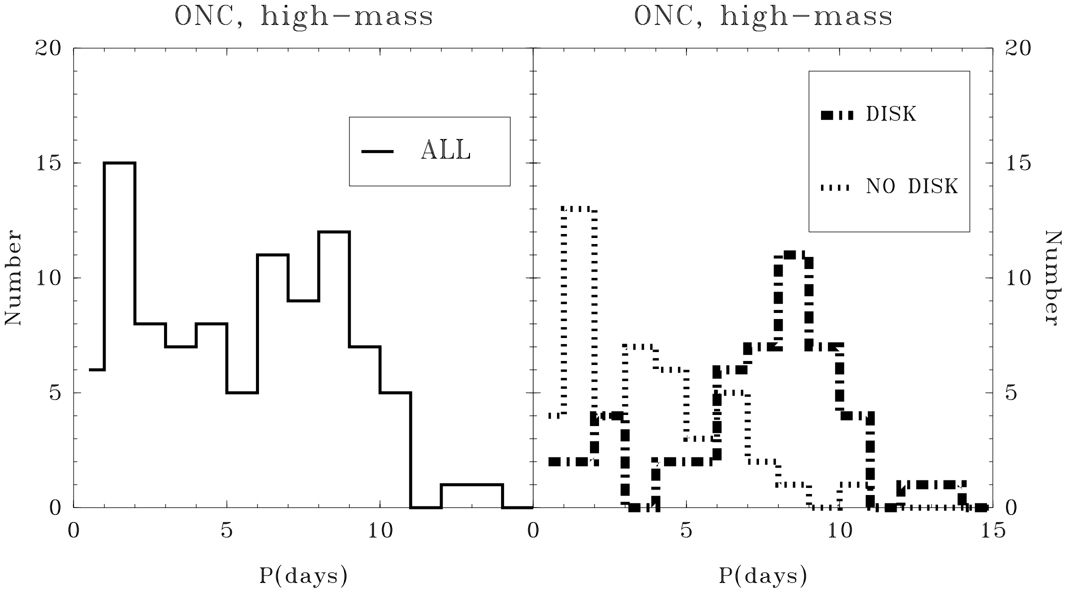

Figure 5.5 Results for high-mass stars in the central regions of the ONC. (Left Panel) The period histogram of all high-mass stars in the central region of the ONC that have measured spectral types. (Right Panel) The period histograms for the same stars with (dot-dashed line) and without (dotted line) a disk. When restricting the sample by not including the flanking fields, the bimodal period distribution seen by previous studies (Attridge & Herbst, 1992; Herbst et al., 2002) is recovered. With an accurate disk identifier and sample selection based on spectral types, one can see that the bimodal distribution is a blend of two dramatically different distributions, stars with and without protoplanetary disks (P=4.3e-08, Kolmogorov-Smirnov two-sample test, n1=49, n2=46). The disk-less, high-mass population is centered at a much shorter period that the population with disks, again unambiguously supporting the picture of angular momentum regulation through star-disk interaction.

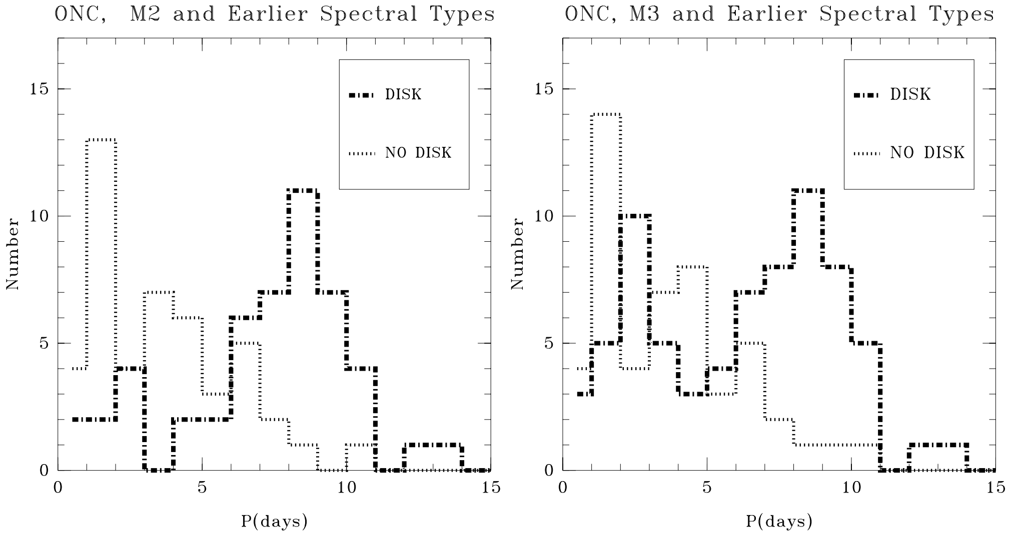

Figure 5.6 The effect of a different mass cut on the period distribution of stars with and without disks in the ONC. (Left Panel) Period histogram for high-mass stars (M2 and earlier spectral types) with (n = 49) and without (n = 46) a disk (dot-dash and dotted line, respectively). (Right Panel) The same plot with a slightly different mass cut. This histogram includes M3 stars (i.e. stars with slightly lower masses). Again, stars with disks (n=71) are represented by a dot-dash line, and stars without disks (n=50) by a dotted line. This panel shows that even a *small* contamination of the high-mass star sample by stars with slightly lower masses will result in a short-period ($P < 4$ days) peak of stars with disks that will weaken the observational signature of star-disk interaction on angular momentum (P increases from 4.3e-8 to 1.1e-4 in a Kolmogorov-Smirnov two sample test when comparing the disk and no-disk samples in the right panel to those in the left. This is due to the fact that low-mass stars (M3 and later spectral types) tend to have very short periods ($P < 4$ days) regardless of the presence of a disk.

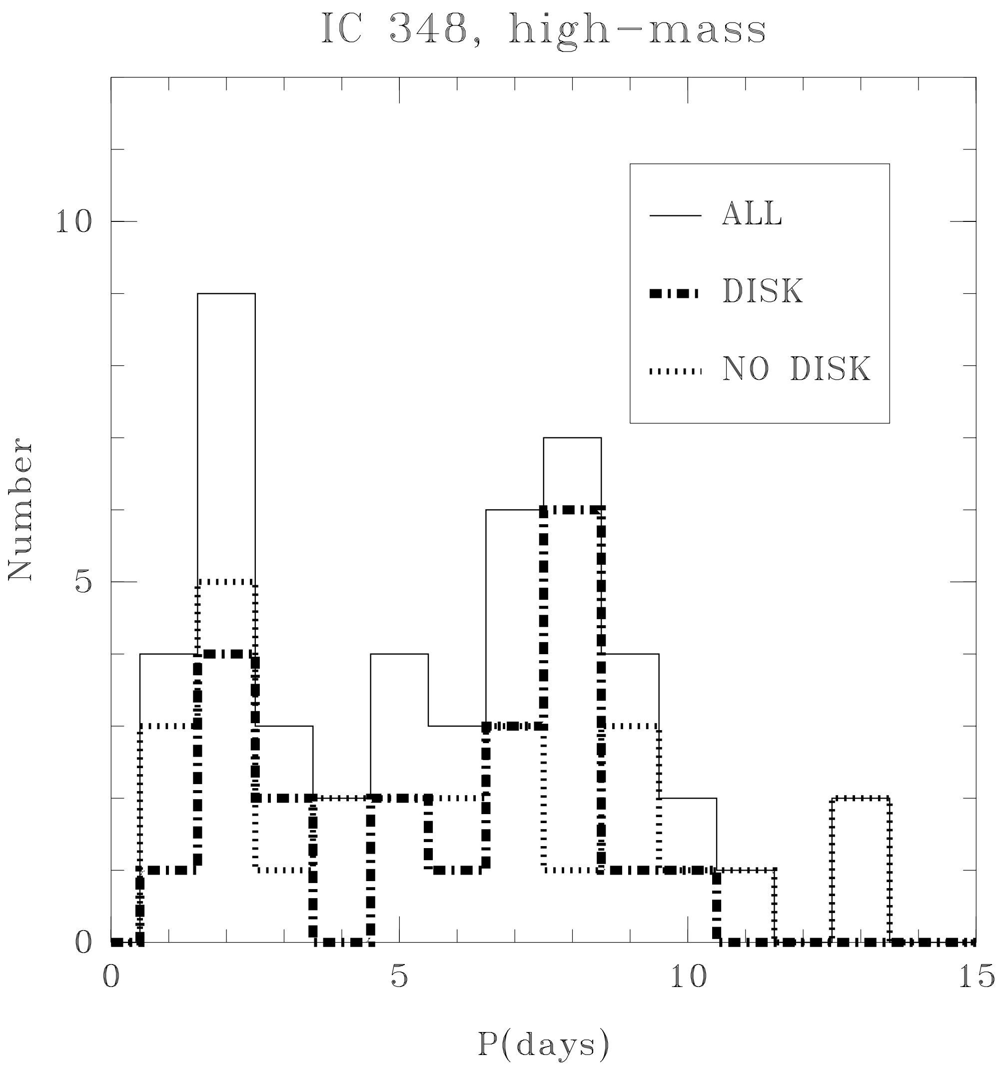

Figure 5.7 Histograms of high-mass stars in IC 348. After dividing the IC 348 sample of stars with known rotation periods by mass, there are too few stars to study the disk and no-disk populations separately. As seen in the figure, very few (or no) stars remain in each period bin. More rotation periods in that cluster would be needed to observe signatures of star-disk interaction affecting the period distributions.

Chapter 6

Spitzer observations of the Hyades: Circumstellar debris disks at 625 Myrs of age

6.1 Abstract

We use the *Spitzer* Space Telescope to search for infrared excess at 24, 70, and 160 μm due to debris disks around a sample of 45 FGK-type members of the Hyades cluster. We supplement our observations with archival 24 and 70 μm data of an additional 20 FGK-type and 11 A-type Hyades members in order to provide robust statistics on the incidence of debris disks at 625 Myrs of age, and era corresponding to the late heavy bombardment in the Solar System. We find that none of the 65 FGK-type stars in our sample show evidence for a debris disk, while 2 out of the 11 A-type stars do so. This difference in debris disks detection rate is likely to be due to a sensitivity bias in favor of early-type stars. The fractional disk

luminosity, L_{DUST}/L_*, of the disks around the two A-type stars is $\sim 4\times10^{-5}$, a level that is below the sensitivity of our observations toward the FGK-type stars. However, our sensitivity limits for FGK-type stars are able to exclude, at the 2-σ level, frequencies higher than 12% and 5% of disks with $L_{DUST}/L_* > 1\times10^{-4}$ and $L_{DUST}/L_* > 5\times10^{-4}$, respectively.

6.2 Introduction

Soon after IRAS discovered cold circumstellar disks around main-sequence (MS) stars (Aumann et al. 1984), it was realized that these disks could not be made of primordial material. Followup CO observations (e.g., Yamashita et al. 1993) showed that molecular gas was highly depleted around these disks. Since in the absence of gas, the survival time of dust to dissipation processes such as Poynting-Robertson effect is much shorter than the ages of MS stars, these systems are believed to be debris disks where dust is continuously replenished by collisions between planetesimals, the building blocks of planets. Because of their probable connection with the formation of planetary systems, debris disks rapidly became the subject of many studies. However, IRAS was only sensitive enough to study bright nearby objects and most of the pre-*Spitzer* statistics come from surveys performed by IRAS's successor, the ISO satellite. Habing et al. (2001) studied 84 nearby ($d < 25$ pc) A,F,G, and K stars for which ISO was sensitive to phoptospheric fluxes and detected 60 μm excess in ~50% of the stars younger than 400 Myrs and in 10% of the stars older than 400 Myrs. They suggest that this sudden decrease in the fraction of stars with disks around 400 Myrs is related to the lifetime of planetesimals that replenish the dust. Spangler et al. (2001) observed ~150 pre-main sequence stars and young main sequence stars and detected 60 μm excess in ~ 25% of the objects. Their observations do not confirm a sudden decrease in the disk fraction around 400 Myrs but rather suggest a power law relationship (index ~ –2) between the age of the star and the fractional dust luminosity, L_{DUST}/L_*. They argue that such a power law naturally arises in collisionally replenished debris disks.

The discrepancies in the results from these ISO surveys can probably be traced back to the different target selection criteria and observing strategies and to small number statistics. However, since conclusions from Habing et al. (2001) and Spangler et al. (2002) were not totally consistent, ISO was unable to provide a clear picture for the evolution of debris disks. Fortunately, *Spitzer*'s unprecedented sensitivity has recently allowed many studies of large samples of PMS and MS stars in the mid- and far-IR. These studies are rapidly providing important clues on the evolution of debris disks. The *Spitzer* study of the Hyades presented in this paper is intended to provide additional clues by giving robust statistics on the frequency of debris disks at 625 Myrs of age for a homogeneous sample of MS stars. At 46 pc, the Hyades is the nearest star cluster to the Sun, and represent a sample of stars formed at the same epoch with the same heavy element abundance ([Fe/H] = 0.13 ± 0.01) (Paulson et al. 2003).

The 625 Myrs age of the Hyades places them at an extremely interesting era in the evolution of planetary systems. This corresponds almost exactly to the era of the late heavy bombardment (Tera et al. 1973) in our Solar System about 3.9 Gyrs ago. The cratering record of the Moon, Mars, and Mercury all indicate that the inner planets experienced intense bombardment by large bodies at that time. There is still intense debate as to whether the late heavy bombardment represented merely the end of an exponential decrease in the impact rate from the formation of the terrestrial planets (Wetherill 1975, 1977; Neukum & Ivanov 1994), or was instead a short intense spike in the bombardment rate when the Solar System was about 600 Myrs old (Ryder 1990; Cohen 2002). In either case, the late heavy bombardment of our Solar System clearly indicates that at an age of ∼600 My there was still a major debris disk present that was undergoing a rapid evolution. Large, asteroidsize bodies had been built up during the early planet building era, but not all of these bodies had been incorporated into the planets. At the time of the late heavy bombardment, these bodies were undergoing an era of significant collisions with the inner planets, and presumably with each other as well. These collisions would have generated large amounts of smaller particles, ranging all of the way down to dust particles. It is quite reasonable to assume that other stellar systems might also have similar remnant debris disks at a similar age.

Here, we analyze deep MIPS (24, 70, 160 μm) observations for a sample of 76 Hyades stars, enough to provide robust statistics on the status of debris disks at 625 Myrs of age. In Section 6.3, we describe the sample of Hyades stars, our observations, and the data reduction procedures. In Section 6.4, we establish our disk identification criteria and present our detection statistics. In Section 6.5, we compare our detection statistics to recent *Spitzer* results and discuss their implications for debris disk evolution models and the late heavy bombardment in the Solar System.

6.3 Observations

6.3.1 *Spitzer* Sample

The majority of the 76 targets discussed in this paper were observed at 24, 70, and 160 μm with the Multiband Imaging Photometer for *Spitzer* (MIPS) as part of our Guest Observer (GO) program 3371. This program contains 45 FGK-type Hyades members from the radial velocity (RV) survey discussed by Cochran et al. (2002) and Paulson et al. (2004). We have also included MIPS 24 and 70 μm observations of Hyades members from the FEPS *Spitzer* Legacy Project (PID=148, 19 FGK-type stars), and two Guaranteed Time Observation (GTP) programs (PID=40, 11 A-type stars and PID = 71, 1 K0 star). Even though the MIPS photometry for some of the targets has already been published in the context of their respective programs (Su et al. 2006; Meyer et al. 2006), we have retrieved the MIPS data from the *Spitzer* archive and processed it ourselves for consistency. The Astronomical Observation Requests (AORs) keys, Program IDs, spectral types from the literature, and near-IR photometry (from 2MASS) for our entire sample of Hyades stars are listed in Table 6.1.

6.3.2 Data Reduction

We processed the 24 μm data using the mosaicking and source extraction software c2dphot, which was developed as part of the the *Spitzer* Legacy Project “From Molecular Cores to Planet Forming Disks” (c2d, Evans et al. 2003). This program is based on the mosaicking program MOPEX (MOsaicker and Point source EXtractor), developed by the *Spitzer* Science Center (SSC) and on the source extractor program DoPHOT (Schechter et al. 1993). The measured 24 μm fluxes and uncertainties for our entire sample are listed in Table 6.2.

For the 70 μm and 160 μm data, we used mopex to create mosaiced images. We started from the SSC pipeline version S14.4 of the median-filtered BCDs (basic calibrated data), which are optimized for point-source photometry. For each source, we created two versions of the 70 μm mosaic, one resampled to 8″pixels (close to the original size of the pixels in the detector) and the other resampled to 4″ pixels. We used the former to obtain the aperture photometry and the latter to visually inspect the images for background contamination (See section 6.4.2). The 160 μm data were resampled to mosaics with 16″ pixels.

For the 70 μm data, we use an aperture of 16″ in radius and a sky annulus with an inner and an outer radius of 48″ and 80″, respectively. From high S/N 70 μm point source observations we derive a multiplicative aperture correction, AC, of 1.8. Thus, we calculate the observed flux, F_{70}, as F_{70}=FA_{70} AC, where FA_{70} is the flux within the aperture. We estimate the 1-σ photometric uncertainty as $\sigma = \mathrm{AC} \times \mathrm{RMS}_{SKY} \times n^{1/2}$, where RMS_{SKY} is the flux RMS of the pixels in the sky annulus, and n is the number of pixels in our aperture. The 70 μm measurements for our entire sample are listed in Table 6.3. For the 160 μm data, we used an aperture with a radius of 32″ and a sky annulus with an inner and an outer radius of 48″ and 80″, respectively. The fluxes and uncertainty were calculated in the same way as for the 70 μm data, but adopting an aperture correction of 2.0, appropriate for the size of the aperture and sky annulus used [1]. The 160 μm measurements for the entire sample of FGK-type stars from program ID=3371 are listed in table 6.4 (the 160 μm data is not available for the Hyades stars from the other programs).

6.4 Results

6.4.1 MIPS 24 μm results

At 24 μm, all our targets are detected with very high signal to noise ratios (S/N $\sim$50-300). In order to establish whether or not our targets show IR-excess at a given wavelength, we first need to estimate the expected photospheric fluxes at that wavelength. We do so by normalizing NextGen Models (Hauschildt et al. 1999), corresponding to published spectral of our Hyades stars, to the near-IR data from 2MASS listed in Table 6.1. The expected 24 μm photospheric fluxes for our entire sample are also listed in Table 6.2.

The magnitude of the smallest 24 μm excess emission that we can identify depends on both the uncertainty of our photometry and on our ability to predict the photospheric flux. In Figure 6.1, we plot the distribution of observed 24 μm fluxes relative to predicted photospheric fluxes. After excluding a single outlier, this distribution can be characterized as a Gaussian distribution with a mean of 0.99

---

[1] See htt/ss.spitzer.caltech.edu/mips/apercorr.

and a 1-σ dispersion of 0.06. This dispersion is identical to that found by Bryden et al. (2006) for a sample of 69 FGK-type field stars and smaller than that obtained by Beichman et al. (2007) for a sample of 88 FGK, and M stars. However, it is significantly larger than the dispersion found by Su et al. (2006) for a sample of ∼160 A-type stars. As mentioned by Beichman et al. (2007), it seems to be a trend in the sense that the photospheric fluxes of stars with late spectral types are more difficult to predict than those of earlier spectral types.

Based on the analysis of Figure 6.1, we conclude that only one of the Hyades stars in our sample shows a significant (> 3-σ) 24 μm excess. This object is HD28355, an A-type star that was already identified by Su et al. (2006) as having a debris disk. According to the values listed in Table 6.2, we find that the 24 μm flux of HD28355 is 1.24 times the expected photospheric level, in good agreement with the 1.27 value found by Su et al (2006).

6.4.2 MIPS 70 μm results

We estimated the expected stellar photosphere fluxes at 70 μm, listed in Table 6.3, by extrapolating the values at 24 μm listed in Table 6.2. Unlike at 24 μm, the expected photospheric flux at 70 μm of all Hyades stars is at or below the noise of the observations, which is dominated by the sky pixel to pixel variations due to extragalactic source confusion and cirrus contamination (see Bryden et al. 2006 for a detailed analysis of the source of noise in deep 70 μm observations). This noise sets a firm limit to the sensitivity that can be achieved with MIPS at 70 μm and can not be reduced with longer integration times. Since the background noise is highly non-Gaussian, a simple 3-σ threshold is inappropriate to prevent spurious detections. Thus, the first step in our analysis is to establish a different detection criterion. In Figure 6.2, we plot the signal to noise ratio as a function of the measured 70 μm flux. We find that a similar number of negative and positive fluctuations exist at the

5-σ level; therefore, we considered objects with S/N ratios < 5 to be non-detections. We find that only two objects, HD28266 and HD28355, are unambiguously detected. In order to establish that the 70 μm emission is in fact associated with the Hyades targets, we inspect their mosaics, shown in Figure 6.3, and verify that the emission is centered on the targets. HD28266 and HD28355 are both A-type stars, which have been already identified by Su et al. (2006) as having a debris disk. As mentioned in Section 6.4.1, HD28355 also shows significant 24 μm excess.

Three objects, HD27962, HD29488, and HD33524, have S/N just above 5. We consider these objects to be possible detections that need further consideration. We inspect their high resolution ($4''$ pixel) mosaics (Figures 6.4 and 6.5) to establish the spatial distribution of the 70 μm emission. In the three cases, we find that even though it seems to be a source near the aperture, there is a significant offset ($\sim$10-$15''$) between the center of the 70 μm emission and the location of the Hyades targets. Therefore, we conclude that the 70 μm emission within the apertures, are likely to be due to background contamination.

We note that one of these objects, HD33524, has been identified by Su et al (2006) as having a weak 70 μm excess. For this object, they report a 70 μm flux of 21.46 ± 2.17 mJy as opposed to our 18.5 ± 3.25 mJy (i.e., the fluxes agree very well within the uncertainties). A similar situation occurs for HD28527. Su et al (2006) reports a 70 μm flux of 37.36 ± 5.94 mJy, which also is in relative agreement with our 25.1 ± 5.08 measurement (within $\sim$ 2-σ). However, since the 70 μm emission does not seem to be centered at the target (Figure 6.5), we do not consider this detection to be real either. Our conservative detection criterion is supported by the presence of negative fluctuations at the 5-7-σ level at the location of some of the targets, such as HD28430 shown in Figure 6.6.

We conclude that none of the 55 FGK-type Hyades stars in our sample are detected at 70 μm, while 2 of the 11 A-type stars are. The measured 70 μm fluxes for these two objects, HD28266 and HD28355, are 13.9 and 11.5 times the values predicted for their respective photospheres (Table 6.3). We attribute these excesses, as Su et al. (2006) did, to the presence of debris disks around both of these sources.

6.4.3 MIPS 160 μm results

At 160 μm, the expected photospheric levels are significantly below the noise of the observations (which are only available for the 45 FGK-type stars from the program ID=3371). In order to establish the detection of any of our targets, we follow the same approach as for the 70 μm data. In Figure 6.7, we plot the the signal to noise ratio as a function of the measured 160 μm flux. As for the 70 μm observations, we find that a similar number of negative and positive fluctuations exist at the 5-σ level; therefore, we considered all the 160 μm measurements to be non-detections.

6.5 Discussion

6.5.1 Comparison to Recent Spitzer Results

Recent *Spitzer* surveys have provided robust statistics on the debris disk frequencies around nearby stars against which our results can be compared. In order to make more meaningful comparisons, we divide the sample into FGK-type stars (65 objects) and A-type stars (11 objects). There are two motivations for doing so. First, most of the previous studies are restricted to either one of these groups. Second, given the strong luminosity dependence on spectral type, the 70 μm observations are sensitive to much smaller 70 μm excesses (in units of photospheric fluxes) and L_{DUST}/L_* values for A-type stars than for FGK-type stars.

FGK-type vs A-type stars

To estimate the sensitivity difference between the 70 μm observations of A-type stars and FGK-type stars, we calculate the ratio of 5 times the flux uncertainties to the estimated photospheric values (from Table 6.3). A cumulative histogram of this ratio is shown in Figure 6.8 for FGK and A-type stars. For A-type stars, the 70 μm observations can detect fluxes that are ~1-2× those of the expected photospheres. However, for most of the FGK-type stars, the 70 μm observations are only sensitive enough to detect fluxes that are ~15× the expected photospheric values.

The difference in 70 μm sensitivity is even larger when it is calculated in terms of minimum detectable disk luminosity, L_{DUST}/L_*. The minimum disk luminosity as a function of 70 μm excess flux can by calculated, by setting the emission peak at 70 μm ($T_{DUST} = 52.5K$), according to:

$$\frac{L_{DUST}}{L_*}(minimum) = 10^{-5}\left(\frac{5600K}{T_*}\right)^3 \frac{F_{DUST,70}}{F_{*,70}} \tag{6.1}$$

Where, $F_{DUST,70}$ is the flux of the dust and $F_{*,70}$ is the flux of the stars, both at 70 μm. By setting $F_{DUST,70} = 5\sigma_{70}$–$F_{*,70}$, we calculate the minimum L_{DUST}/L_* values that are detectable for A-type and FGK-type stars. The results are shown in Figure 6.9, which demostrates that the 70 μm observations of A-type stars are sensitive enough to detect disk with L_{DUST}/L_* values in the 10^{-6}-10^{-5} range. However for most of the FGK-type stars, the 70 μm observations are only sensitive enough to detect disks with $L_{DUST}/L_{STAR} \gtrsim$ 1-2×10^{-4}. We also use equation 6.1 to estimate L_{DUST}/L_* values of 3.4×10^{-5} and 4.7×10^{-5} for the debris disks around HD28226 and HD28355, respectively. Since there are only 2 FGK-type objects for which the 70 μm observations are sensitive enough to detect disks fainter than L_{DUST}/L_* ~4.0×10^{-4}, we conclude that the difference in the detection rate of debris disks around A-type stars and FGK-type stars is the result of a sensitivity bias rather than real effect.

Comparison to FGK-type field stars

Bryden et al. (2006) present 24 and 70 μm observations for 69 FGK nearby (distance $\sim$10-30 pc) field stars with a median age of $\sim$4 Gyrs. They find 24 μm excess around only one of their targets. This is consistent with the 24 μm excess rate of 0% we find for our 65 FGK-type stars. At 70 μm, they identify 7 debris disks. This excess rate ($\sim$10%), if taken at face value, seems inconsistent with our results. However, given the smaller distances involved, their survey was more sensitive than ours to faint disks. They also find that the disk frequency increases from 2% ± 2% for disks with $L_{DUST}/L_* \geq 10^{-4}$ to 12% ± 5% for disks with $L_{DUST}/L_* \geq 10^{-5}$.

Figure 6.9 shows that there are only 23 objects for which our 70 μm observations are sensitive enough to detect a debris disk with $L_{DUST}/L_* \geq 10^{-4}$. We use binomial statistics to show that if the incidence of disks brighter than $L_{DUST}/L_* = 10^{-4}$ is in fact 2% as found by Bryden et al. (2006), there was a 63% probability that our survey would find zero disks. Also, given the cumulative distribution of sensitivities shown in Figure 6.9, we use binomial statistics to calculate the minimum disk frequencies, as a function of L_{DUST}/L_*, that would be *excluded* at the 1 and 2-σ level (i.e., the disk frequencies that would give our survey a 32 and 5 % chance to result in zero detections). These disk frequencies are tabulated in Table 6.5.

Based on the statistics for disks with $L_{DUST}/L_* \geq 10^{-4}$, Table 6.5 suggests that a debris disk fraction in the Hyades $\sim$2.5 and $\sim$6 larger than in the field can be excluded at the 1 and 2-σ level, respectively. Thus, we conclude that the debris disk fraction of the FGK-type Hyades stars (age $\sim$625 Myrs) is consistent with that in the field (age $\sim$ 4 Gyrs), but that $\sim$4× higher values can not excluded from the currently available data.

6.5.2 Debris disk evolution and the Late Heavy Bombardment

Steady State vs. Stochastic Evolution

Rieke et al. (2005) studied a sample of 266 A-type stars with *Spitzer*, ISO, or IRAS 24 or 25 μm data. They used this very large sample to establish statistically significant trends of IR-excess with age. They find that (1) at all ages, the population is dominated by stars with little or no IR excess, (2) stars with a wide range of excesses are seen at every age, and (3) both the frequency and the magnitude of the IR excess decreases with time. In particular, they find that the upper envelope of the evolution of the excess ratio with time can be fitted by t_o/t, with t_o ~150 Myrs. Similar trends are seen in the 70 μm excesses of A-type stars (Su et al. 2006), with the difference that the decay time seems to be considerably larger, $t_o \gtrsim$ 400 Myrs.

Based on these results, Rieke et al. (2005) argue that the evolution of debris disks is the convolution of a stochastic and a steady component. They suggest that, at any given age, the debris disks detected are those that have experienced large planetesimal collisions in the recent past. This stochastic evolution is on top of steady decrease in the number of parent bodies in the belts of planetesimals where the dust is produced, which would explain the overall decrease of IR excess with age. However, it has also been argued that a stochastic component in the evolution of debris disk is not necessary to explain the diversity of disk properties observed at a given age. Wyatt et al. (2007a) construct a simple collisional model, where the mass of planetesimals is constant until the largest ones reach collisional equilibrium, at which point mass falls as 1/time. They propose that the large spread in IR properties observed at any given age can be explained in terms of the initial distributions of masses and temperatures of the planetesimal belts producing the dust. They argue that their simple model can account for the 24 and 70 μm statistics presented by Rieke et al. (2005) and Su et. all (2006) using realistic belt parameters, and thus that transient events are not *required* to explained the observations. Given the limited observational constraints available, the models presented by Wyatt et al. (2007) do not rule out the possibility that stochasticity plays an important role in the evolution of most debris disks. Our results could provide additional constrains to these kinds of models because, unlike the studies by Rieke et al. (2005) and Su et. all (2006), our study provides robust statistics for the debris disks at a single, well defined age.

Implications for the Late Heavy Bombardment in the Solar System

The 625 Myr age of the Hyades corresponds almost exactly to the era of the late heavy bombardment (LHB, Tera et al. 1973, Gomes et al. 2005). Thus, *If* the Solar-type (FGK) Hyades stars resemble the Sun at 625 Myrs of age, our statistics could provide valuable clues on this important event in the history of the Solar System.

The cause and the duration of the LHB is still a matter of debate. Proposed causes for a intense spike in the impact rate include the formation of Uranus and Neptune (Levison et al. 2001), the presence of a fifth terrestrial planet in a low-eccentricity orbit which became dynamically unstable at an age of about 600 Myrs (Chambers & Lissauer 2002), or impacts by bodies left over from planetary accretion (Morbidelli et al. 2001). More recently, Gomes et al. (2005) propose that the LHB was triggered by the sudden migration of the giant planets that occurred after a long quiescent period of time. In their model, soon after the dissipation of the solar nebula, the orbits of Jupiter and Saturn started to slowly diverge due to the interaction with the massive disk of planetesimals that was still present. They argue that ~700 Myrs later, when Jupiter and Saturn crossed their mean motion resonance, their orbits became eccentric and temporally destabilized those of Uranus and Neptune. The reconfiguration of the orbits of the giant planets resulted in the perturbation and massive delivery of planetesimals to the inner Solar System, which according to their models, lasted between 10-150 Myrs.

The observational signatures of a LHB-type event as seen from a distance of 46 pc are not known, but it as been suggested that they could be those of a family of rare Solar-type stars characterized by the presence of a bright "hot disk" around an object hundreds of million years old. These objects present excess 24 μm emission, originating in the terrestrial planet regions, with $F_{DUST}/F_{*} > 10^{-4}$, a level that is $>$ 1000 times larger than steady state evolution models can explain (Wyatt et al. 2007b). There are currently only 4 known objects that fall into this category of "hot transient disks": BD +20 307 (Age ∼300 Myrs, Song et al. 2005), HD72905 (Age ∼400 Myrs, Beichman et al. 2006), η Corvi (Age ∼1000 Myrs Wyatt et al. 2005), and HD69830 (Age ∼2000 Myrs, Beichman et al. 2005), which represent ∼2% of all the Solar-type stars surveyed. *If* this group of objects corresponds to those that are currently experiencing events similar to the LHB and the Hyades stars resemble the Sun at 625 Myrs of age, then the fact that none of the 65 Solar-type stars in our Hyades sample has a "hot transient disk" implies one of two possibilities: (1) the likelihood of an event similar to the LHB is not significantly higher at ∼625 Myrs than it is at any other age, or (2) events like the LHB are very short spikes with a duration much closer to the lower limit of 10 Myrs suggested by Gomes et al. (2005) than to their 150 Myr upper limit. If the likelihood of a LHB-type event is approximately constant with time, then a 2% incidence in the Solar neirghborwood (median age ∼4000 Myrs) would imply a total duration of ∼80 Myrs. However, if such an event is more likely to occur around an age of ∼625 Myrs, then our non detections would only be consistent with a much shorter duration. Thus, the implication of our results on the LHB could depend on the age distribution of these "hot transient disks", which still remains largely unconstrained since only 4 of such examples are currently known. Fortunately, as more *Spitzer* observations are reported, this distribution will become better constrained.

Understanding the debris disk phenomenon has been a high priority of the *Spitzer*'s mission. As a result, the number of debris disk studies has increased dramatically over the last few years. Each of these studies is providing new clues and constraints, from which it will eventually emerge a much clearer picture of the evolution of debris disks and its connection to the history of the Solar System.

Table 6.1. Sample of Hyades Stars

Star Name	Ra (J2000.0)	Dec (J2000.0)	AOR	PID	Spectral Type	J (mag)	H (mag)	K (mag)
BD+17 455	43.81800	17.89170	10853888	3371	G7	7.56	7.21	7.18
BD+29 503	44.44480	29.66140	10841856	3371	K0	7.38	7.00	6.91
HD18632	45.01220	7.74980	10842112	3371	K2	6.32	5.95	5.84
vB 1	49.35990	7.65580	05403904	148	F8	6.29	6.05	5.99
BD+07 499	50.12200	8.45440	12289280	3371	K5	7.54	6.96	6.88
BD+23 465	53.20890	23.69240	10842624	3371	K1	7.37	7.02	6.91
HIP 17766	57.04970	7.14620	10843648	3371	K6	8.27	7.62	7.51
BD+23 571	57.76320	23.90360	10843904	3371	K7	8.11	7.54	7.39
HD286363	58.75610	12.48560	10854144	3371	K4	8.18	7.69	7.57
HD285252	58.77730	16.99840	10844160	3371	K2	7.41	7.04	6.91
BD+19 650	60.91280	19.45500	10847232	3371	K4	8.21	7.71	7.60
HIP 19082	61.35720	19.44210	10847232	3371	K7	8.89	8.26	8.11
HD285367	61.41550	17.93770	10847232	3371	K1	7.75	7.37	7.25
HD25825	61.56740	15.69810	12290560	3371	K1	6.75	6.53	6.45
HD286554	62.11140	12.19180	10847744	3371	K7	8.82	8.17	8.05
BD+08 642	62.45580	9.30550	10848000	3371	K5	7.91	7.34	7.26
HD26767	63.61380	12.43530	10847744	3371	G2	6.86	6.61	6.53
HD26784	63.64330	10.70130	10848000	3371	F8	6.13	5.92	5.86
HD285690	64.58050	16.08810	10848512	3371	K3	7.88	7.42	7.32
HD27250	64.74170	19.90660	10848768	3371	G9	7.29	7.00	6.92
HD27282	64.78350	17.52470	10848512	3371	G8	7.13	6.87	6.79
HD27406	65.05420	19.23340	10848768	3371	G0	6.39	6.18	6.12
HD27628	65.51470	14.07720	03980032	40	A3	5.05	5.02	4.96
vB 39	65.68650	16.79090	05376256	148	G4	6.58	6.33	6.20
HD27732	65.84320	21.37900	10849536	3371	G9	7.53	7.20	7.12
HD27749	65.85440	16.77720	03980288	40	A1	5.04	5.01	4.95

Table 6.1 (cont'd)

Star Name	Ra (J2000.0)	Dec (J2000.0)	AOR	PID	Spectral Type	J (mag)	H (mag)	K (mag)
HD27771	65.88490	14.67040	10849280	3371	K1	7.61	7.25	7.14
HD286734	65.97690	14.05210	10849280	3371	K6	8.51	7.92	7.79
vB 49	66.05320	16.37890	05376768	148	G0	7.08	6.88	6.80
HD27808	66.06090	21.73620	10849536	3371	F7	6.15	5.95	5.87
vB 52	66.11800	16.88610	05377280	148	G2	6.66	6.40	6.29
HD27962	66.37240	17.92790	03980544	40	A3	4.34	4.38	4.10
vB 63	66.60250	16.85330	05377792	148	G1	6.84	6.56	6.44
vB 64	66.66710	16.74690	05378304	148	G6	6.89	6.64	6.55
HD286789	66.72660	13.13810	12290304	3371	K4	8.43	7.92	7.79
HD28205	66.89950	15.58920	12289024	3371	F8	6.38	6.17	6.14
vB 66	66.94200	11.73640	05368064	148	F8	6.42	6.22	6.16
HD285830	66.94610	14.41770	10849280	3371	K2	7.89	7.46	7.35
HD28226	67.00330	21.61990	03980800	40	A5	5.16	5.10	5.05
HD28258	67.01860	13.86790	10849280	3371	K0	7.51	7.14	7.00
vB 73	67.20120	17.28550	05378816	148	G2	6.70	6.46	6.40
HD28355	67.20900	13.04760	03981056	40	A7	4.79	4.66	4.53
HD283704	67.37830	26.67150	10846720	3371	G5	7.84	7.53	7.46
vB 79	67.38170	17.89320	05379328	148	K0	7.52	7.15	7.05
vB 180	67.49060	16.67280	05383424	148	K1	7.62	7.21	7.14
HD28527	67.64010	16.19400	03981312	40	A6	4.77	4.68	4.36
HD28546	67.66200	15.69190	03981568	40	A5	5.46	4.97	4.90
HD28593	67.81550	20.13310	10850816	3371	G8	7.26	6.96	6.88
vB 88	67.87220	13.90340	05397760	148	F9	6.73	6.57	6.46
HD285876	67.96880	15.49940	12290048	3371	K5	8.67	8.03	7.89
HIP21179	68.10710	13.11330	04543232	72	K0	8.42	7.79	7.65
vB 91	68.20870	16.00580	05379840	148	K1	7.29	6.86	6.77

Table 6.1 (cont'd)

Star Name	Ra (J2000.0)	Dec (J2000.0)	AOR	PID	Spectral Type	J (mag)	H (mag)	K (mag)
vB 92	68.24760	15.81900	05380352	148	G8	7.32	7.02	6.94
HD284552	68.40510	21.15080	10850816	3371	K7	8.43	7.83	7.69
vB 93	68.40800	16.76240	05380864	148	K2	7.84	7.42	7.35
vB 96	68.49370	15.16370	05381376	148	K0	6.99	6.58	6.46
vB 183	68.63400	15.82750	05383936	148	K2	8.06	7.67	7.55
vB 97	68.64700	15.50460	05381888	148	G1	6.75	6.55	6.45
vB 99	69.02190	15.68400	05382400	148	K1	7.86	7.50	7.37
HD29388	69.53940	12.51080	03981824	40	A3	4.12	4.08	4.11
HD29488	69.81880	15.91800	03982080	40	A7	4.68	4.55	4.23
HD286929	69.96250	12.72850	10844928	3371	K4	8.09	7.60	7.48
HD30210	71.50720	11.70560	03982336	40	A5	5.00	5.02	4.97
HIP 22177	71.57840	3.63640	10845184	3371	K6	8.57	7.98	7.83
HD284653	71.85920	23.05090	10845440	3371	K2	8.69	8.13	8.00
HD30505	72.26480	18.64120	10852352	3371	K0	7.49	7.14	7.06
HD30589	72.38400	15.88870	10852096	3371	F9	6.64	6.43	6.36
vB 143	72.84670	15.43340	05406976	148	F8	6.93	6.69	6.67
HD30809	72.84690	15.43340	10852096	3371	F7	6.93	6.69	6.67
HD284930	73.09820	18.99690	10852352	3371	K4	8.38	7.88	7.74
HD31609	74.45630	14.00210	10852608	3371	G8	7.57	7.27	7.24
BD+04 810	75.20380	4.73310	10845952	3371	K2	8.11	7.69	7.59
HD32347	75.78200	13.73040	10852608	3371	G9	7.63	7.30	7.23
HD240648	76.57510	17.81640	10846208	3371	G9	7.51	7.22	7.13
HD33254	77.33180	9.82960	03983104	40	A2	4.96	4.93	4.86
HD242780	80.10600	11.60980	10846464	3371	G9	7.70	7.40	7.30

Table 6.2. 24 μm Photometry

Star name	24 μm Flux (mJy)	σ (mJy)	Photosphere (mJy)	S/R	R_{24}
BD+17 455	9.72e+00	9.56e-02	1.04e+01	101.67	0.94
BD+29 503	1.22e+01	9.37e-02	1.40e+01	130.20	0.87
HD18632	3.38e+01	1.71e-01	3.31e+01	197.66	1.02
vB 1	2.81e+01	9.74e-02	2.93e+01	288.50	0.96
BD+07 499	1.33e+01	9.67e-02	1.38e+01	137.54	0.96
BD+23 465	1.24e+01	9.38e-02	1.32e+01	132.20	0.94
HIP 17766	7.89e+00	8.00e-02	7.31e+00	98.62	1.08
BD+23 571	8.23e+00	8.68e-02	9.15e+00	94.82	0.90
HD286363	7.06e+00	6.08e-02	7.06e+00	116.12	1.00
HD285252	1.22e+01	9.28e-02	1.24e+01	131.47	0.99
BD+19 650	6.85e+00	7.03e-02	6.89e+00	97.44	0.99
HIP 19082	4.46e+00	7.05e-02	4.75e+00	63.26	0.94
HD285367	9.26e+00	7.31e-02	9.59e+00	126.68	0.97
HD25825	1.89e+01	1.08e-01	2.02e+01	175.00	0.94
HD286554	4.91e+00	9.08e-02	5.02e+00	54.07	0.98
BD+08 642	9.81e+00	9.52e-02	9.70e+00	103.05	1.01
HD26767	1.75e+01	1.06e-01	1.67e+01	165.09	1.05
HD26784	3.51e+01	1.47e-01	3.31e+01	238.78	1.06
HD285690	9.91e+00	9.72e-02	8.47e+00	101.95	1.17
HD27250	1.24e+01	1.02e-01	1.26e+01	121.57	0.98
HD27282	1.37e+01	1.02e-01	1.49e+01	134.31	0.92
HD27406	2.64e+01	1.29e-01	2.56e+01	204.65	1.03
HD27628	7.27e+01	2.77e-01	7.99e+01	262.45	0.91
vB 39	2.42e+01	8.17e-02	2.27e+01	296.21	1.07
HD27732	1.05e+01	9.79e-02	1.05e+01	107.25	1.00
HD27749	7.31e+01	2.40e-01	6.59e+01	304.58	1.11

Table 6.2 (cont'd)

Star name	24 μm Flux (mJy)	σ (mJy)	Photosphere (mJy)	S/R	R_{24}
HD27771	1.01e+01	9.78e-02	1.06e+01	103.27	0.95
HD286734	6.01e+00	9.29e-02	5.66e+00	64.69	1.06
vB 49	1.50e+01	1.02e-01	1.38e+01	147.06	1.09
HD27808	3.17e+01	1.36e-01	3.28e+01	233.09	0.97
vB 52	2.24e+01	8.17e-02	2.09e+01	274.17	1.07
HD27962	1.51e+02	4.88e-01	1.77e+02	309.43	0.85
vB 63	1.95e+01	7.67e-02	1.89e+01	254.24	1.03
vB 64	1.69e+01	7.82e-02	1.65e+01	216.11	1.02
HD286789	6.53e+00	6.39e-02	5.76e+00	102.19	1.13
HD28205	2.49e+01	1.16e-01	2.56e+01	214.66	0.97
vB 66	2.45e+01	8.14e-02	2.52e+01	300.98	0.97
HD285830	8.49e+00	9.49e-02	8.27e+00	89.46	1.03
HD28226	7.43e+01	2.50e-01	7.11e+01	297.20	1.05
HD28258	1.19e+01	1.03e-01	1.28e+01	115.53	0.93
vB 73	2.00e+01	7.54e-02	1.88e+01	265.25	1.06
HD28355	1.39e+02	4.70e-01	1.12e+02	295.74	1.24
HD283704	7.68e+00	9.32e-02	7.11e+00	82.40	1.08
vB 79	1.12e+01	7.60e-02	1.22e+01	147.37	0.92
vB 180	1.03e+01	7.03e-02	1.07e+01	146.51	0.97
HD28527	1.35e+02	5.04e-01	1.33e+02	267.86	1.02
HD28546	8.10e+01	2.69e-01	8.17e+01	301.12	0.99
HD28593	1.26e+01	9.97e-02	1.36e+01	126.38	0.93
vB 88	1.88e+01	7.65e-02	1.91e+01	245.75	0.98
HD285876	5.21e+00	6.56e-02	5.43e+00	79.42	0.96
HIP21179	8.40e+00	3.41e-02	7.05e+00	246.92	1.19
vB 91	1.48e+01	7.82e-02	1.50e+01	189.26	0.99

Table 6.2 (cont'd)

Star name	24 μm Flux (mJy)	σ (mJy)	Photosphere (mJy)	S/R	R_{24}
vB 92	1.32e+01	7.60e-02	1.29e+01	173.68	1.02
HD284552	6.78e+00	1.22e-01	7.00e+00	55.57	0.97
vB 93	8.45e+00	6.61e-02	8.25e+00	127.84	1.02
vB 96	2.03e+01	8.19e-02	2.10e+01	247.86	0.97
vB 183	6.99e+00	6.38e-02	6.85e+00	109.56	1.02
vB 97	1.88e+01	7.82e-02	1.87e+01	240.41	1.00
vB 99	8.16e+00	6.47e-02	8.59e+00	126.12	0.95
HD29388	1.86e+02	6.24e-01	1.76e+02	298.08	1.06
HD29488	1.41e+02	5.19e-01	1.48e+02	271.68	0.95
HD286929	7.42e+00	9.06e-02	7.70e+00	81.90	0.96
HD30210	7.14e+01	2.40e-01	7.66e+01	297.50	0.93
HIP 22177	5.68e+00	5.68e-02	5.46e+00	100.00	1.04
HD284653	4.99e+00	7.42e-02	4.56e+00	67.25	1.10
HD30505	1.21e+01	8.13e-02	1.21e+01	148.83	1.00
HD30589	2.00e+01	1.05e-01	2.10e+01	190.48	0.95
vB 143	1.56e+01	9.97e-02	1.57e+01	156.47	0.99
HD30809	1.56e+01	9.97e-02	1.57e+01	156.47	0.99
HD284930	6.25e+00	6.98e-02	6.05e+00	89.54	1.03
HD31609	9.53e+00	9.31e-02	9.85e+00	102.36	0.97
BD+04 810	6.82e+00	6.01e-02	6.62e+00	113.48	1.03
HD32347	9.00e+00	9.05e-02	9.52e+00	99.45	0.95
HD240648	1.10e+01	1.06e-01	1.04e+01	103.77	1.06
HD33254	7.69e+01	3.19e-01	8.83e+01	241.07	0.87
HD242780	7.90e+00	8.86e-02	8.88e+00	89.16	0.89

Table 6.3. 70 μm Photometry

Star name	70 μm Flux (mJy)	σ (mJy)	Photosphere (mJy)	S/R
BD+17 455	-9.70e-01	3.00e+00	1.22e+00	-0.32
BD+29 503	-5.07e+00	2.82e+00	1.64e+00	-1.80
HD18632	5.96e+00	4.31e+00	3.90e+00	1.38
vB 1	1.11e+01	4.58e+00	3.45e+00	2.42
BD+07 499	8.13e-01	2.98e+00	1.62e+00	0.27
BD+23 465	-1.97e+00	2.37e+00	1.55e+00	-0.83
HIP 17766	-8.01e+00	2.55e+00	8.59e-01	-3.14
BD+23 571	3.07e+00	2.55e+00	1.08e+00	1.20
HD286363	7.67e-01	1.69e+00	8.30e-01	0.45
HD285252	-2.04e+00	3.22e+00	1.46e+00	-0.63
BD+19 650	-1.99e+00	1.63e+00	8.10e-01	-1.22
HIP 19082	9.09e+00	2.51e+00	5.58e-01	3.62
HD285367	-6.44e+00	2.41e+00	1.13e+00	-2.67
HD25825	-1.11e+00	5.37e+00	2.37e+00	-0.21
HD286554	-1.34e+01	3.36e+00	5.91e-01	-3.99
BD+08 642	-5.66e+00	3.02e+00	1.14e+00	-1.87
HD26767	-9.88e-01	3.37e+00	1.96e+00	-0.29
HD26784	1.72e+01	3.52e+00	3.89e+00	4.89
HD285690	-5.01e+00	2.76e+00	9.96e-01	-1.82
HD27250	8.03e+00	3.11e+00	1.48e+00	2.58
HD27282	-3.45e+00	2.43e+00	1.75e+00	-1.42
HD27406	9.62e+00	3.72e+00	3.01e+00	2.59
HD27628	9.12e+00	3.84e+00	9.39e+00	2.38
vB 39	-4.65e+00	4.42e+00	2.66e+00	-1.05
HD27732	-1.26e+01	3.92e+00	1.23e+00	-3.21
HD27749	9.81e+00	3.76e+00	7.74e+00	2.61

Table 6.3 (cont'd)

Star name	70 μm Flux (mJy)	σ (mJy)	Photosphere (mJy)	S/R
HD27771	-1.19e+01	2.75e+00	1.25e+00	-4.33
HD286734	-8.38e+00	2.93e+00	6.66e-01	-2.86
vB 49	-6.36e+00	3.46e+00	1.62e+00	-1.84
HD27808	-1.50e+01	3.87e+00	3.85e+00	-3.88
vB 52	-8.06e+00	4.47e+00	2.46e+00	-1.80
HD27962	4.48e+01	7.10e+00	2.08e+01	6.31
vB 63	3.19e+00	4.24e+00	2.22e+00	0.75
vB 64	-1.90e+00	5.34e+00	1.94e+00	-0.36
HD286789	9.92e-01	2.62e+00	6.77e-01	0.38
HD28205	1.15e+01	3.96e+00	3.01e+00	2.90
vB 66	1.01e+01	4.25e+00	2.96e+00	2.38
HD285830	3.77e+00	3.57e+00	9.72e-01	1.06
HD28226	9.58e+01	4.89e+00	8.35e+00	19.59
HD28258	2.87e+00	2.68e+00	1.50e+00	1.07
vB 73	-1.68e+00	3.96e+00	2.21e+00	-0.42
HD28355	1.83e+02	5.63e+00	1.31e+01	32.50
HD283704	-7.86e-01	2.71e+00	8.35e-01	-0.29
vB 79	-6.83e+00	3.16e+00	1.43e+00	-2.16
vB 180	-3.29e+00	2.76e+00	1.25e+00	-1.19
HD28527	2.51e+01	5.08e+00	1.56e+01	4.94
HD28546	8.10e+00	4.37e+00	9.61e+00	1.85
HD28593	3.93e-01	4.34e+00	1.60e+00	0.09
vB 88	-1.12e+01	4.88e+00	2.25e+00	-2.30
HD285876	-5.70e+00	3.28e+00	6.38e-01	-1.74
HIP21179	-5.24e+00	3.16e+00	8.24e-01	-1.66
vB 91	-1.38e+00	5.12e+00	1.76e+00	-0.27

Table 6.3 (cont'd)

Star name	70 μm Flux (mJy)	σ (mJy)	Photosphere (mJy)	S/R
vB 92	7.24e-01	4.47e+00	1.52e+00	0.16
HD284552	-8.42e+00	3.62e+00	8.23e-01	-2.33
vB 93	4.86e+00	3.19e+00	9.69e-01	1.52
vB 96	-1.19e+01	5.08e+00	2.46e+00	-2.34
vB 183	-1.11e+01	4.41e+00	8.05e-01	-2.52
vB 97	-4.57e-01	5.62e+00	2.20e+00	-0.08
vB 99	-1.77e+00	4.84e+00	1.01e+00	-0.37
HD29388	2.34e+01	5.00e+00	2.06e+01	4.68
HD29488	3.01e+01	4.14e+00	1.74e+01	7.27
HD286929	5.52e+00	3.13e+00	9.05e-01	1.76
HD30210	1.60e+01	3.54e+00	9.00e+00	4.52
HIP 22177	3.91e+00	1.95e+00	6.41e-01	2.01
HD284653	-3.88e-01	2.49e+00	5.36e-01	-0.16
HD30505	-5.40e+00	2.18e+00	1.43e+00	-2.48
HD30589	1.30e+01	3.28e+00	2.47e+00	3.96
vB 143	2.67e+00	4.43e+00	1.84e+00	0.60
HD30809	-8.62e+00	3.52e+00	1.84e+00	-2.45
HD284930	-1.40e+01	2.02e+00	7.11e-01	-6.93
HD31609	-6.50e-01	2.94e+00	1.16e+00	-0.22
BD+04 810	-9.98e-01	1.97e+00	7.79e-01	-0.51
HD32347	-4.02e+00	3.27e+00	1.12e+00	-1.23
HD240648	1.25e+01	3.29e+00	1.22e+00	3.80
HD33254	1.85e+01	3.25e+00	1.04e+01	5.69
HD242780	-8.78e+00	5.39e+00	1.04e+00	-1.63

Table 6.4. 160 μm Photometry

Star name	160 μm Flux (mJy)	σ (mJy)	Photosphere (mJy)	S/R
BD+17 455	2.11e+01	1.25e+01	2.33e-01	1.69
BD+29 503	7.84e+00	3.06e+01	3.15e-01	0.26
HD18632	8.29e+01	2.25e+01	7.46e-01	3.68
vB 1	———	———	6.60e-01	—-
BD+07 499	-3.93e+01	3.30e+01	3.11e-01	-1.19
BD+23 465	-2.06e+01	3.69e+01	2.97e-01	-0.56
HIP 17766	-1.10e+01	1.26e+01	1.64e-01	-0.87
BD+23 571	-1.57e+01	1.77e+01	2.06e-01	-0.89
HD286363	-2.36e+01	9.89e+00	1.59e-01	-2.39
HD285252	-5.35e+01	2.56e+01	2.79e-01	-2.09
BD+19 650	4.35e+00	1.16e+01	1.55e-01	0.38
HIP 19082	6.06e+01	1.81e+01	1.07e-01	3.35
HD285367	-1.05e+00	1.44e+01	2.16e-01	-0.07
HD25825	-2.85e+01	2.26e+01	4.54e-01	-1.26
HD286554	3.64e+01	2.09e+01	1.13e-01	1.74
BD+08 642	-3.06e+00	1.18e+01	2.18e-01	-0.26
HD26767	-5.07e+01	2.96e+01	3.76e-01	-1.71
HD26784	4.98e+01	5.45e+01	7.44e-01	0.91
HD285690	-2.93e+01	4.33e+01	1.91e-01	-0.68
HD27250	4.05e+01	2.17e+01	2.84e-01	1.87
HD27282	-3.09e+01	2.40e+01	3.35e-01	-1.29
HD27406	2.10e+01	3.96e+01	5.76e-01	0.53
HD27628	———	———	1.80e+00	—-
vB 39	———	———	5.10e-01	—-
HD27732	-4.53e+01	2.68e+01	2.36e-01	-1.69
HD27749	———	———	1.48e+00	—-

Table 6.4 (cont'd)

Star name	160 μm Flux (mJy)	σ (mJy)	Photosphere (mJy)	S/R
HD27771	-8.95e+00	2.00e+01	2.38e-01	-0.45
HD286734	2.25e+01	4.03e+01	1.27e-01	0.56
vB 49	———	———	3.10e-01	—-
HD27808	-1.13e+02	2.69e+01	7.38e-01	-4.20
vB 52	———	———	4.71e-01	—-
HD27962	———	———	3.98e+00	—-
vB 63	———	———	4.25e-01	—-
vB 64	———	———	3.71e-01	—-
HD286789	-4.08e+01	2.96e+01	1.30e-01	-1.38
HD28205	1.35e+01	2.94e+01	5.75e-01	0.46
vB 66	———	———	5.66e-01	—-
HD285830	-2.88e+01	1.98e+01	1.86e-01	-1.45
HD28226	———	———	1.60e+00	—-
HD28258	-5.39e+00	2.33e+01	2.87e-01	-0.23
vB 73	———	———	4.24e-01	—-
HD28355	———	———	2.52e+00	—-
HD283704	-4.69e+01	2.71e+01	1.60e-01	-1.73
vB 79	———	———	2.74e-01	—-
vB 180	———	———	2.40e-01	—-
HD28527	———	———	2.99e+00	—-
HD28546	———	———	1.84e+00	—-
HD28593	1.72e+01	2.11e+01	3.06e-01	0.82
vB 88	———	———	4.31e-01	—-
HD285876	-1.49e+02	3.53e+01	1.22e-01	-4.22
HIP21179	———	———	1.58e-01	—-
vB 91	———	———	3.37e-01	—-

Table 6.4 (cont'd)

Star name	160 μm Flux (mJy)	σ (mJy)	Photosphere (mJy)	S/R
vB 92	———	———	2.90e-01	—-
HD284552	-6.79e+01	4.81e+01	1.58e-01	-1.41
vB 93	———	———	1.86e-01	—-
vB 96	———	———	4.72e-01	—-
vB 183	———	———	1.54e-01	—-
vB 97	———	———	4.22e-01	—-
vB 99	———	———	1.93e-01	—-
HD29388	———	———	3.95e+00	—-
HD29488	———	———	3.33e+00	—-
HD286929	4.29e+01	3.67e+01	1.73e-01	1.17
HD30210	———	———	1.72e+00	—-
HIP 22177	3.64e+00	9.63e+00	1.23e-01	0.38
HD284653	6.93e+00	1.72e+01	1.03e-01	0.40
HD30505	-3.79e+01	2.72e+01	2.73e-01	-1.39
HD30589	3.84e+01	3.21e+01	4.72e-01	1.20
vB 143	———	———	3.53e-01	—-
HD30809	-2.15e+01	2.67e+01	3.53e-01	-0.81
HD284930	-2.65e+01	1.82e+01	1.36e-01	-1.46
HD31609	1.03e+00	1.99e+01	2.22e-01	0.05
BD+04 810	1.94e+01	1.23e+01	1.49e-01	1.58
HD32347	-4.95e+00	2.44e+01	2.14e-01	-0.20
HD240648	-1.02e+01	3.77e+01	2.34e-01	-0.27
HD33254	———	———	1.99e+00	—-
HD242780	-1.90e+02	5.13e+01	2.00e-01	-3.70

Table 6.5. Disk Frequency Limits

$L_{DUST}/L_* \geq$	Number of stars above limit	1-σ	2-σ
1×10^{-4}	23	4.8%	12 %
2×10^{-4}	45	2.5%	6.3%
5×10^{-4}	61	2.0%	4.8%
1×10^{-3}	65	1.7%	4.5%

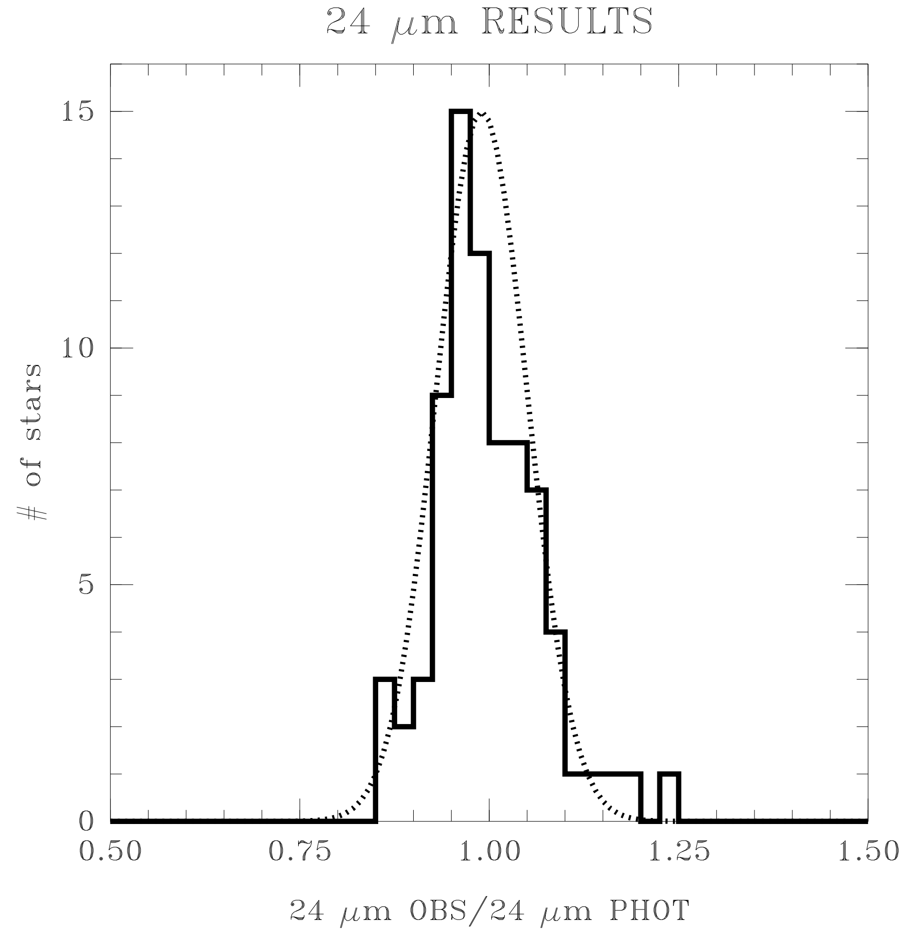

Figure 6.1 Distribution of the observed 24 μm fluxes in units of the expected photospheric fluxes. A Gaussian distribution with centered at 0.99 with 1-σ dispersion of 0.06 (dotted line) is shown for comparison. Only one object, HD28355, shows a significant ($>$ 3-sigma) 24 μm excess above the predicted stellar photosphere. HD28355 is an A-type star whose excess was already identified by Su et al. (2006).

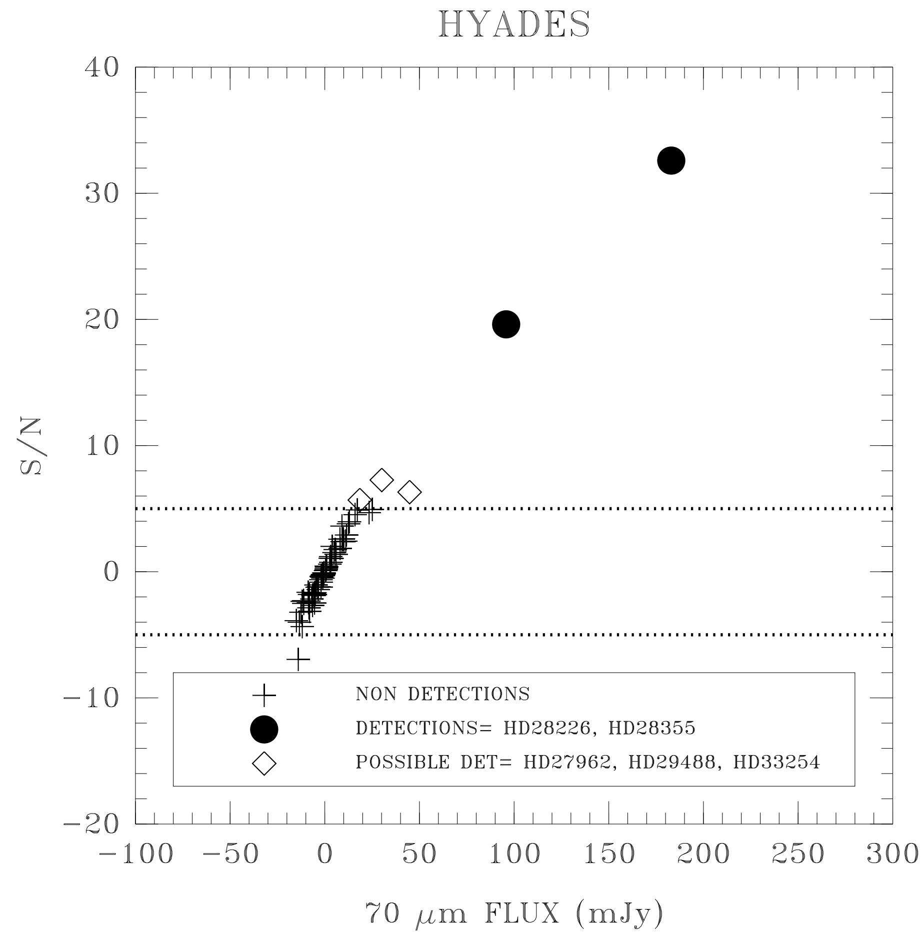

Figure 6.2 The signal to noise ratio versus the measured 70 μm flux for our sample of Hyades stars. Two objects shown as filled circles, HD28226 and HD28355, clearly stand out as robust detections. The horizontal dotted lines delimit the $5 > S/N > -5$ interval. For the deep 70 μm observations considered in this paper, the noise is dominated by the sky background variations. This variations are highly none Gaussian and primarily due to extragalactic source confusion and cirrus contamination. As a result, there is a similar number of objects with $S/N \sim 5$ and with $S/N \sim -5$ and we consider objects $S/N < 5$ to be none detections. Three objects, HD27962, HD29488, and HD33524, have S/N just above 5. We consider these objects to be possible detections that need further consideration.

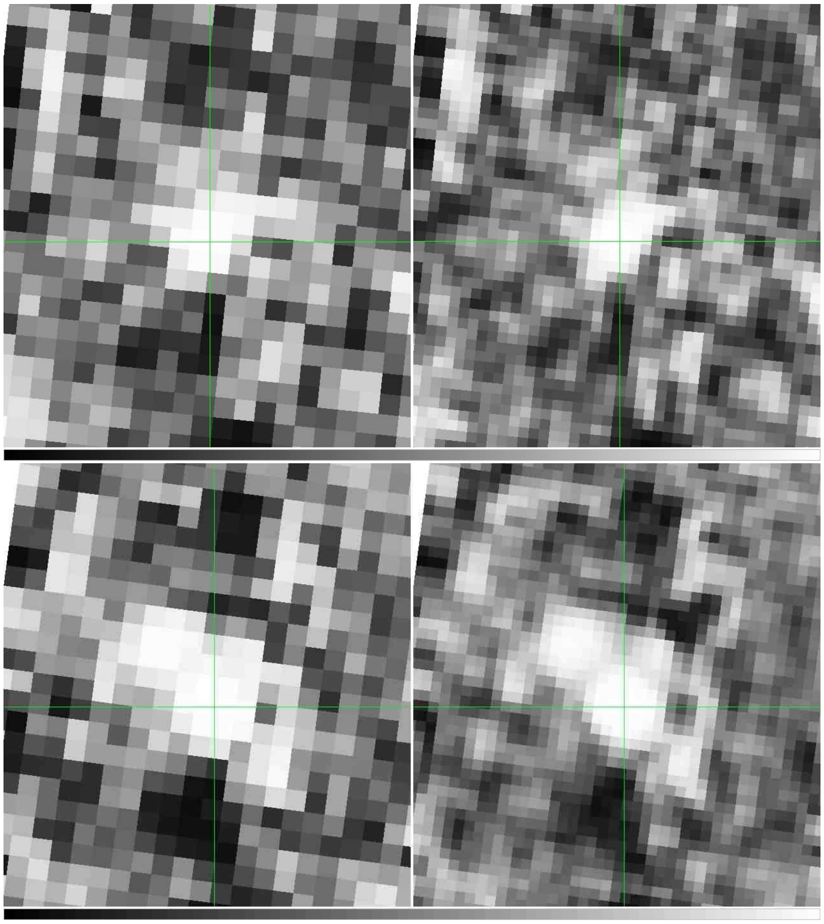

Figure 6.3 The 70 μm mosaics of HD28226 (top) and HD28355 (bottom). The images on the left correspond to the mosaics with $8''$ pixels (close to the physical size of the detector). The images on the right correspond to the mosaics resampled to $4''$ pixels ($\sim$half the physical size). The 70 μm emission is centered at the position of the objects (marked by the crosshairs) and is detected with signals to noise ratios $\sim$20-30. Both objects are A-type stars already identified by Su et al. (2006) as having debris disks.

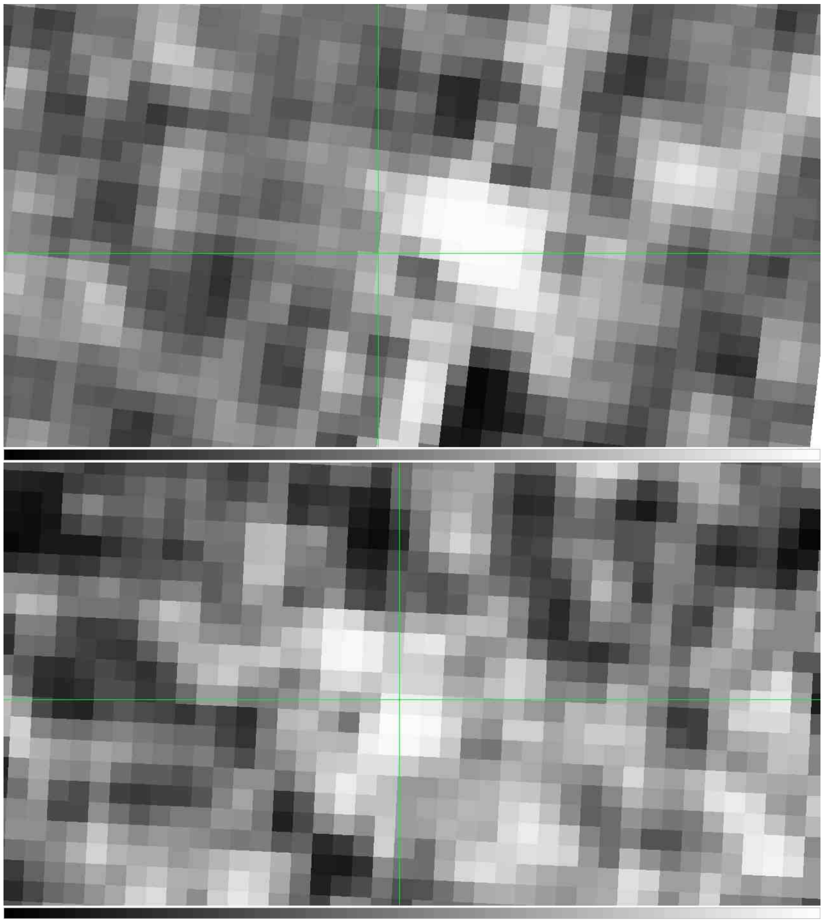

Figure 6.4 The 70 μm mosaics of HD27962 (top) and HD29488 (bottom) resampled to $4''$ pixels in order to gain spatial resolution. We find that 70 emission is detected at a S/N level $\sim$6-7 within the our aperture (radius=$16''$). However, since the emission is not centered at the position of the targets (marked by the crosshairs), we conclude that it is not likely to be associated with them.

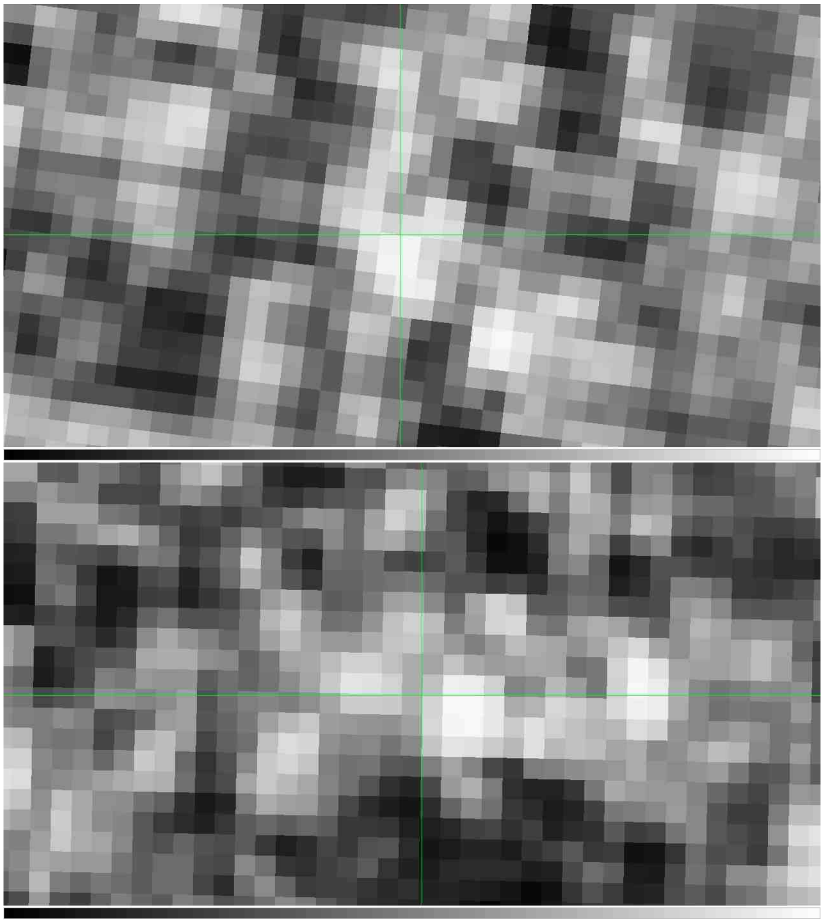

Figure 6.5 The 70 μm mosaics of HD28527 (top) and HD33254 (bottom) resampled to 4$''$ pixels in order to gain spatial resolution. Both objects are A-type stars identified by Su et al. (2006) as having small 70 μm excess (L_{disk} /L_* ~2.7-2.9). However, since we detect these objects at a marginal level (S/N = 4.9 and 5.6, respectively) and the emission is not centered at the location of the objects (marked by the crosshairs), we don not consider the detections to be real.

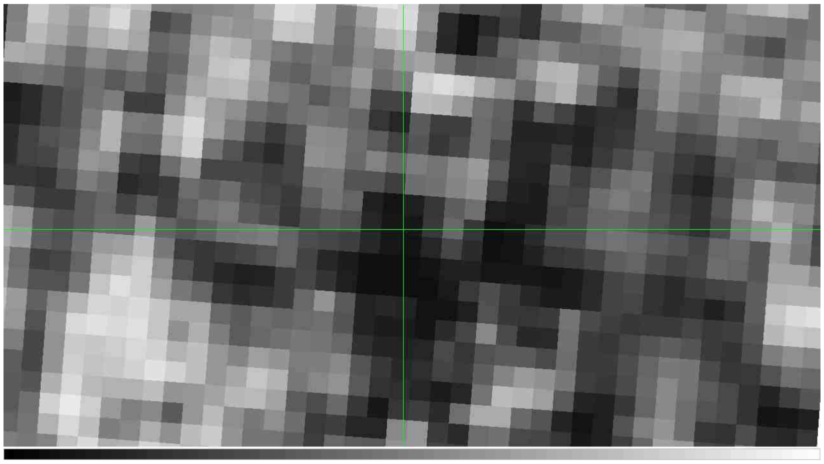

Figure 6.6 The 70 μm mosaics of HD28430 resampled to $4''$ pixels. Within the aperture centered at the target, there is a flux deficit that is significant at the 6.9 σ level. The existence of this kind of minima strongly suggests that "detections" at the 5-7-σ level should be interpreted with caution.

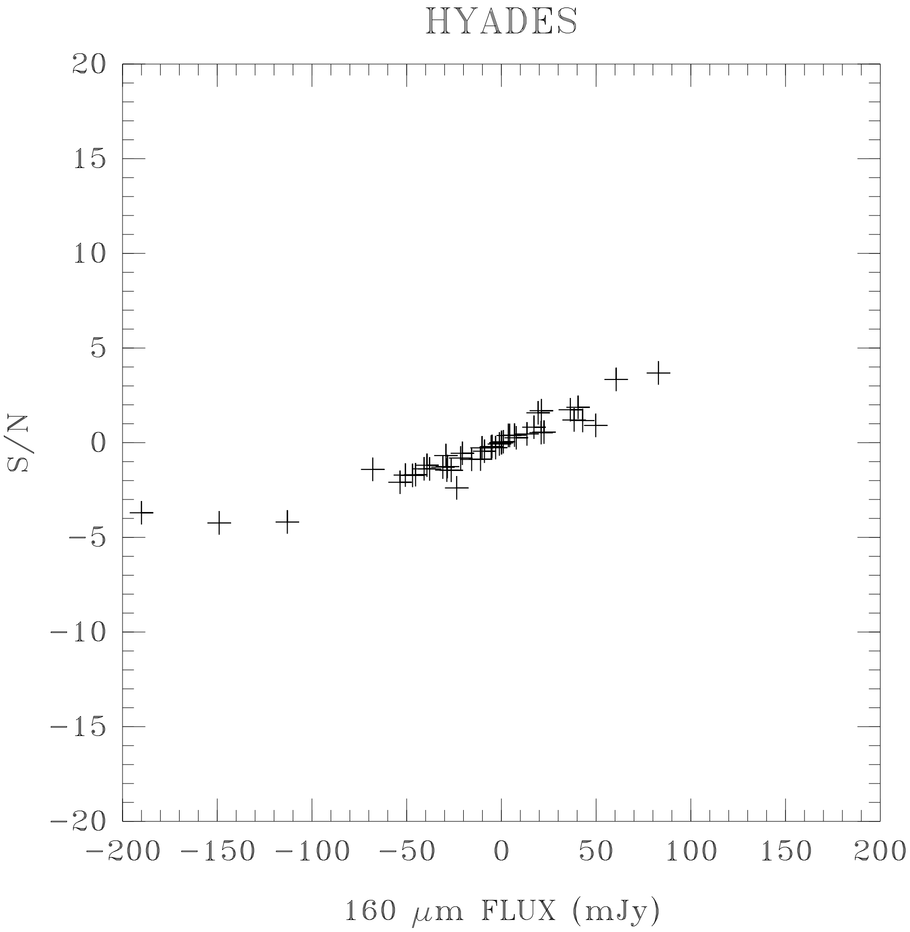

Figure 6.7 The signal to noise ratio versus the measured 160 μm flux for our sample of Hyades stars. We find no obvious 160 μm detections. At 160 μm, as at 70 μm, the noise is dominated by the extragalactic source confusion and cirrus contamination. Thus, positive and negative fluctuations at the $\sim$5-σ level are not uncommon.

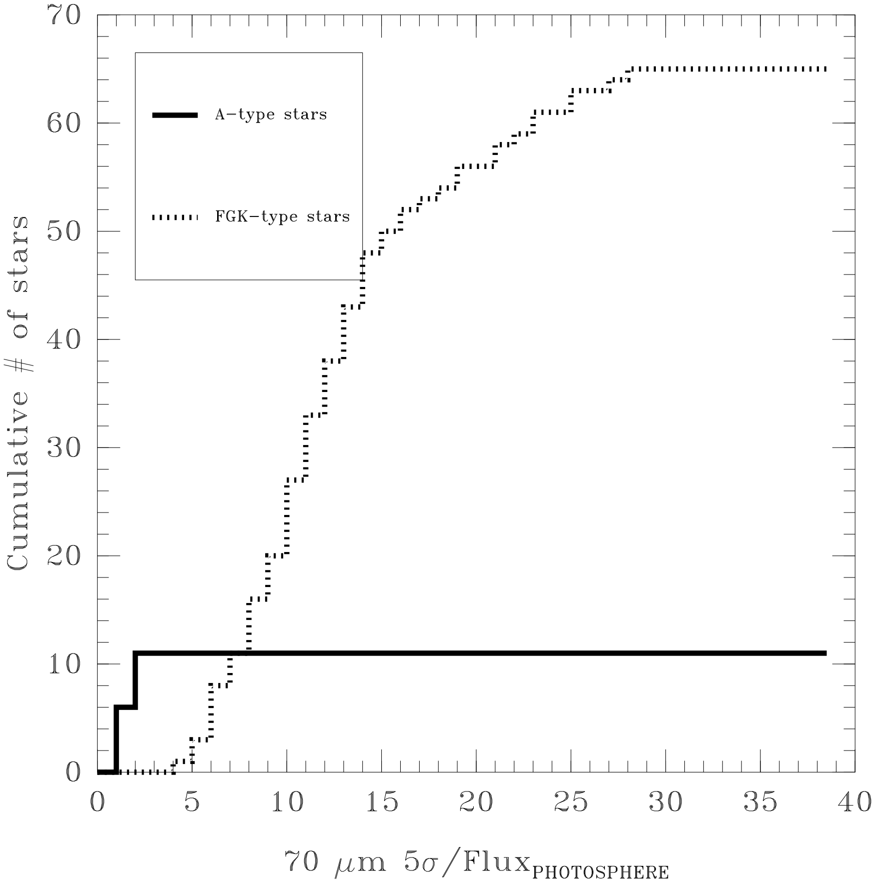

Figure 6.8 Cumulative distribution of 70 μm 5-σ sensitivities in units of the expected photospheric fluxes for FGK-type Hyades stars (dotted line) and A-type Hyades stars (solid line). For A-type stars, the 70 μm observations can detect, at the 5-σ level, fluxes that are ∼1-2 × that of the expected photospheres. In contrast, for most of the FGK-type stars, the 70 μm observations are only sensitive enough to detect fluxes that are ∼15 × the expected photospheric values.

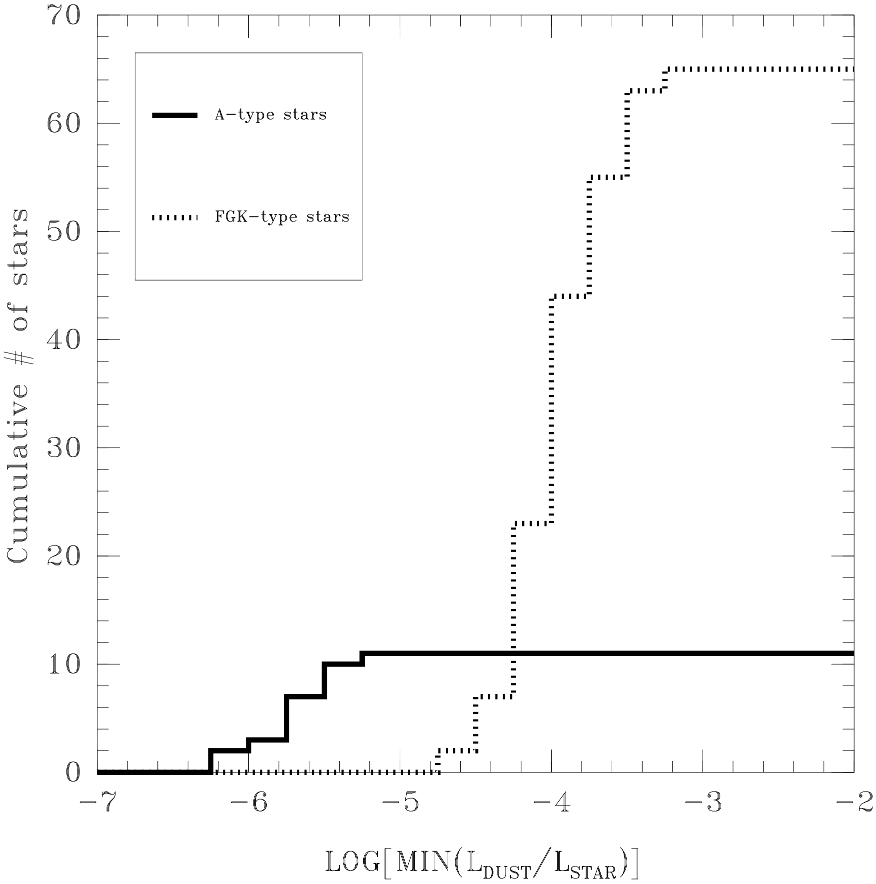

Figure 6.9 Cumulative distribution of 70 μm 5-σ sensitivities translated into fractional disks luminosities for FGK-type Hyades stars (dotted line) and A-type Hyades stars (solid line). For A-type stars, the 70 μm observations are sensitive to disks with fractional disk luminosities, L_{DUST}/L_{STAR}, $\sim 5\times10^{-6}$. In contrast, for most of the FGK-type stars, the 70 μm observations are only sensitive enough to detect disks with $L_{DUST}/L_{STAR} \gtrsim 2\times10^{-4}$

Chapter 7

Conclusions

The projects presented in this dissertation sample several aspects of an extremely active field in astronomy, the structure and evolution of circumstellar disks. In what follows, I summarize the main conclusions that arise from each one of the projects and from the dissertation as a whole. I also highlight some of the key outstanding questions, some of which I hope to tackle in the near future.

In Chapter 2, we find that cTTs show significant J and H-band color excesses in addition to the well studied K-band excess. We interpret these color excesses as evidence for non-photospheric emission originating at an inner rim which is physically narrow but has a gradient of temperatures several hundreds of degrees wide, analogous to those suggested to explain the "near-IR bump" in the SEDs of Herbig Ae/Be stars. Such an inner rim has become a central part of most models of circumstellar disks around cTTs. In section 2.8, we calculated stellar luminosities from the I_C and J-band, and used these luminosities to estimate stellar ages from 3 different sets of evolutionary tracks. We argued that normalizing the luminosity of cTTs to the J-band, which is the standard procedure, systematically overestimates their luminosities. These overestimated luminosities translate into underestimated ages when the stars are placed in the H-R diagram. When the ages are derived from I_C-band luminosities, cTTs and wTTs show a larger age overlap with respect to ages derived from the J-band. If wTTs are descendants of cTTs, as suggested in Chapter 3, this large overlap implies a wide diversity in the duration of the cTTs phase.

In Chapter 3, we find that ~20% of the wTTs have a circumstellar disk, as indicated by the presence of IR-excesses at IRAC wavelengths. We also find that the disk frequency is a function of stellar age. It is ~50% for the youngest wTTs and close to 0% for objects $\gtrsim$ 10 Myrs old. Since cTTs disks older than 10 Myrs are also very infrequent, 10 Myrs seems to be a general upper limit for the survival time of primordial disks around PMS stars. In Section 3.5.3, we estimate mass upper limits of dust within the inner 10 AU of $10^{-4} M_{\oplus}$ for the objects in our sample with 24 μm fluxes consistent with stellar photospheres. Also, we find that the wTTs disks in our sample exhibit a wide range of properties (SED morphology, inner radius, L_{DISK}/L_*, etc) intermediate between those observed in the cTTs and the debris disk stages. This strongly suggests that wTTs disks are in fact the link between the massive primordial disks found around cTTs (Chapter 2) and the debris disks observed around main-sequence stars (Chapter 6).

Taken together, the results from Chapter 2 and 3, imply that the inner 1-10 AU of a sizable fraction of all PMS stars become extremely depleted of dust before the star reaches an age of ~1 Myr, while some cTTs maintain a healthy accretion disk for up to ~10 Myrs. The reason why, within the same molecular cloud or stellar cluster, some primordial disks survive over 10 times longer than others is still unknown. The spread in disk lifetimes could be related to the wide range of initial conditions, the presence of unseen companions, and/or the planet formation process.

Since recent core accretion models can accommodate planet formation within the 10 Myrs observational limit, our results can not distinguish between the competing planet formation mechanisms, core accretion and gravitational instability. On one hand, it is possible that planets form through core accretion around the few cTTs disks that manage to survive for ∼5-10 Myrs. On the other hand, is is also possible that the youngest wTTs *without* a disk are objects that have already formed planets through gravitational instability. Thus, establishing the incidence of planets around "young wTTs" and "old cTTs" could provide a key observational discriminant between the core accretion and the gravitational instability model and is one of the central goals of the "Young Stars and Planets" Key Project of the Space Interferometry Mission.

In Chapter 4 and 5, we take advantage of the unprecedented disk identification capabilities of *Spitzer* to test the predictions of the disk-braking paradigm, according to which the rotational evolution of PMS stars is regulated through magnetic interactions between the stellar magnetosphere and the inner disk. In Chapter 4, we find that the "high-mass" stars in IC 348 show a bimodal period distribution similar to that seen in the Orion Nebular Cluster, but due the small size of our sample, we find no general correlation between rotation period and IR-excess. However, in Chapter 5 we study larger sample of objects in NGC 2264 and the Orion Cluster and show that the disk fraction of "high-mass" stars increases with rotation period across the entire period range. We also show that the long-period peak (P∼8 days) of the bimodal distribution observed for high-mass stars in the ONC is dominated by a population of stars with disks, while the short-period peak (P ∼ 2 days) is dominated by a population of stars without a disk. This result confirms one of the main predictions of the star-disk interaction scenario.

Even though the presence of IRAC excess does not guarantee that a star is *currently* accreting and transferring angular momentum to its disk, the success of the projects described in Chapters 4 and 5 is mainly due to two facts that render IRAC photometry a very powerful tool for the study of the effect that star-disk interactions have on the angular momentum evolution of young stars. First, as shown in Chapter 2, both near-IR and IRAC wavelengths trace the inner rim. However, since the magnitude of the IR excess over the stellar photosphere is much larger at IRAC wavelengths than it is in the NIR, *Spitzer* observations, unlike previous ground-based studies, are sensitive enough to unambiguously determine the presence of a disk around PMS stars. Second, as shown in Chapter 3, the transition timescale from an optically thick accretion disk to a disk undetectable at IRAC wavelengths is a factor of $\sim$10 smaller than typical accretion disk lifetimes. Also, once star-disk interaction stops, it takes some time for stars to spin-up significantly. This "reaction lag-time" will tend to compensate for the "detectability lag-time" (the time between the end of star-disk interaction and the time the disk is no longer detectable at IRAC wavelengths). As a result, IRAC 8 μm excess is arguably the best current method with which to reliably detect the presence of an inner circumstellar disk and study the effect of star-disk interaction on the angular momentum of young stars.

The period distributions of stars with and without 8 μm excess contain enough information to provide important constraints on the angular momentum history of PMS stars. For instance, preliminary Monte Carlo models (described in Appendix A) suggest that the bimodal distribution observed in the rotation period of "high mass" stars in the Orion Nebula Cluster and IC 348 can *only* be reproduced adopting a bimodal distribution of disk lifetimes, where a fraction of the disks are lost almost simultaneously very early on, while the remaining disks have a much wider distribution of lifetimes. In particular, the models are very sensitive to the effects of star-disk interactions at early ages, when the stars undergo very rapid contraction, and suggest that $\sim$30% of the stars become decoupled from their disks by an age $\ll$ 1 Myr. This result is very consistent with those of Chapter 3, where we show that $\sim$50% of the youngest wTTs (age $\lesssim$ 1 Myrs) have already lost their disks. It is tempting to speculate that such a bimodal distribution of disks lifetimes could naturally arise if giant planets form through gravitational instability. In this scenario, those disks undergoing gravitational instability would evolve in *much* shorter timescales than those where such instabilities do not occur. However, as mentioned above, the presence of companions at certain distances could also be responsible for the very early dissipation of a significant fraction of circumstellar disks. The circumstellar disks around the individual stars in a binary system are expected to be tidally truncated at a fraction of the binary separation. It has been suggested that the truncation of the disk limits the amount of material that can be accreted and effectively shortens the accretion time scale in close binaries. The effect that companions have on the evolution of circumstellar disks is currently not well established, but it could be studied with a combination of radial velocity and adaptive optics observations to search for companions around a large sample of PMS stars with available *Spitzer* data.

A major unresolved question in the study of the angular momentum evolution of PMS stars is the difference in behavior of “low-mass” and “high-mass” stars. Since low-mass stars are smaller than high-mass stars, a shorter period is expected for a given specific angular momentum. It has also been suggested that the disk regulation mechanism is less efficient in low mass stars than it is in high mass stars due to differences in the accretion rates and in the strength or structure of their magnetic fields. The extreme sensitivity of period distribution to mass, described in Chapter 5, is difficult to explain in terms of slowly varying quantities such as radius and accretion rates. Instead, the observed dependence of rotation periods on mass is more consistent with the idea that a *sudden* change in the strength or structure of the magnetic field at the boundary between M2 and M3 stars is responsible for the observed differences in period distributions of “low-mass” and “high-mass” PMS stars.

In Chapter 6, we search for infrared excess at MIPS wavelengths due to debris disks around a sample of Hyades cluster members in order to provide robust statistics on the incidence of debris disks at 625 Myrs of age, an era corresponding to the late heavy bombardment in the Solar System. We find that none of the 65 FGK-type stars in our sample show evidence for a debris disk, while 2 out of the 11 A-type stars do so. This difference in debris disks detection rate is likely to be due to a sensitivity bias in favor of early-type stars. Our detection statistics for solar-type stars suggest either that the likelihood of an event similar to the LHB is not significantly higher at $\sim$625 Myrs than it is at any other age or that events like the LHB are very short spikes (duration $\lesssim$ 10 Myrs).

Many questions on the debris disk phenomenon still remain. It is still unclear whether the diversity of disks properties observed at a given age is a result of the wide range of initial distributions of masses and temperatures of the planetesimal belts or the manifestation of an stochastic process where the IR-luminosity is dominated by single large collisions. Another key outstanding issue is the question of when the transition from the primordial to the debris disk stage actually occurs. In Chapter 3, we found that some of the wTTs disks have very small fractional luminosities and thus seem to be optically thin. These objects *could* be younger analogs of the β Pic and AU Mic debris disks, and thus some of the youngest debris disks ever observed. However, this interpretation depends on the assumption that these young wTTs disks are gas poor. It is also possible that some of the wTTs disks have very low fractional disk luminosities as a result of most of their grains growing to sizes $\gg$10-20 μm, in which case they would still be primordial disks. Since a real debris disks requires the presence of second generation of dust produced by the collision of much larger objects, the ages of the youngest debris disks can constrain the time it takes for a disk to form planetesimals.

It has even been proposed that detectable second generation dust is not produced until Pluto-sized objects form and trigger a collision cascade (Dominik &

Decin (2003). In that case, the presence of debris disks around ∼1-3 Myrs old stars would have even stronger implications for planet formation theories. The fact that, as discussed in Chapter 3, the incidence of 24 μm excesses around low-mass PMS stars with ages $\gtrsim$ 10 Myrs is ∼0 %, is consistent with the idea that a quiescent period exists between the dissipation/coagulation of the primordial dust and the onset of the debris phenomenon. However, the confirmation of such scenario will require far-IR observations sensitive enough to detect, at the distance of the nearest star-forming regions (150-200 pc), debris disks as faint as those observed in the solar neighborhood (10-30 pc). In the near future, *Herschel* will provide such sensitivity. It will also provide the information on the gas content and grain size distribution of optically thin disks around wTTs required to establish whether they represent the end of the primordial disk phase or the beginning of the debris disk stage.

Appendix A

Monte Carlo Simulations Of The Rotational Evolution Of PMS Stars

A.1 Abstract

[1] We describe a Monte Carlo code that simulates the evolution of angular momentum of pre-main-sequence stars in the context of the disk-braking paradigm. The code is similar to that presented by Rebull et al. (2004), but includes several improvements. The code allows us to set parameters such as the distributions of masses, ages, and disk dissipation timescales, all of which are constrained by observations. Also, we use the evolution of stellar radii predicted by theoretical tracks to evolve the periods of disk-less/unregulated stars and to calculate the amount of angular momentum drained as a function of time from disked/regulated stars. We present quantitative comparisons between models and recent observations of young stellar clusters in

---

[1] based on Cieza, L., Baliber, N., Counselor, N. 2006, American Astronomical Society Meeting Abstracts, 209

order to constrain disk-braking parameters.

A.2 The Monte Carlo code:

For each simulation, we generate probability distributions of initial angular momentum, mass, stellar age, and disk-braking timescale. We generate a synthetic cluster by evolving one star at a time following evolutionary tracks (e.g. D.Antona & Mazzitelli 1998, Siess et al. 2000). The properties of each star are randomly drawn from the probability distributions of the cluster, and we use its initial angular momentum and stellar radius to calculate its initial period. Then, we compare each age step given by evolutionary tracks to the disk-braking timescale until we reach the stellar age assigned to the particular star. While the stellar age is smaller than the disk-braking timescale, the angular momentum is drained from the star to the disk with an efficiency given by the Disk-Braking Efficiency parameter. Once the stellar age reaches the disk-braking timescale, angular momentum is conserved, and we evolve the period from the evolution of radius given by the evolutionary tracks. A star has a disk at the end of the simulation only if its age is smaller than its disk-braking timescale plus the disk dissipation Lag Time parameter. This Lag Time parameter allows us to account for a period of time when stellar rotation is not longer regulated by a dissipating disk that could be still detected by Spitzer.

A.3 Models vs. Observations:

In order to constrain the disk-braking parameters in young stellar clusters, we use our Monte Carlo (MC) code to reproduce the observed period distributions of stars with and without disks in the Orion Nebula Cluster (ONC) and NGC 2264 (Fig. A.1 and Fig A.2.) presented in the Spitzer study by Cieza & Baliber 2007. These distributions are limited to "high-mass" stars (spectral types M2 and earlier).

For each cluster, we run a series of MC simulations, each one consisting of 600 stars. At the end of each simulation, we perform a K-S test to determine the probability (P) that the simulated period distributions of stars with and without a disk are drawn from the same parent population as the observed period distributions. By maximizing P, we determine the "Best Values" listed in Tables A,1 and A,2.

Starting from the "Best Values", we vary one parameter at a time by increasing amounts until the simulated period distributions are no longer statistically consistent with the observations ($P < 0.01$). The minimum and maximum allowed values for each parameter are also listed in Tables A.1 and A,2.

A.4 Preliminary results:

- Our MC simulations can reproduce the period distributions of stars with and without a disk (and disk fractions) observed in the ONC and NGC 2264.
- We can constrain disk-braking parameters
  - Disk braking efficiency = 1.0 (i.e. disk-locking)
  - Early disk dissipation fraction ~30%
  - Disk-locking timescale agrees with inner disk dissipation timescales (~2-4 Myrs)

A.5 Future Work

We will run a much larger grid of models varying more than one parameter at the time. This will allow us to explore a larger parameter space and study parameter degeneracies

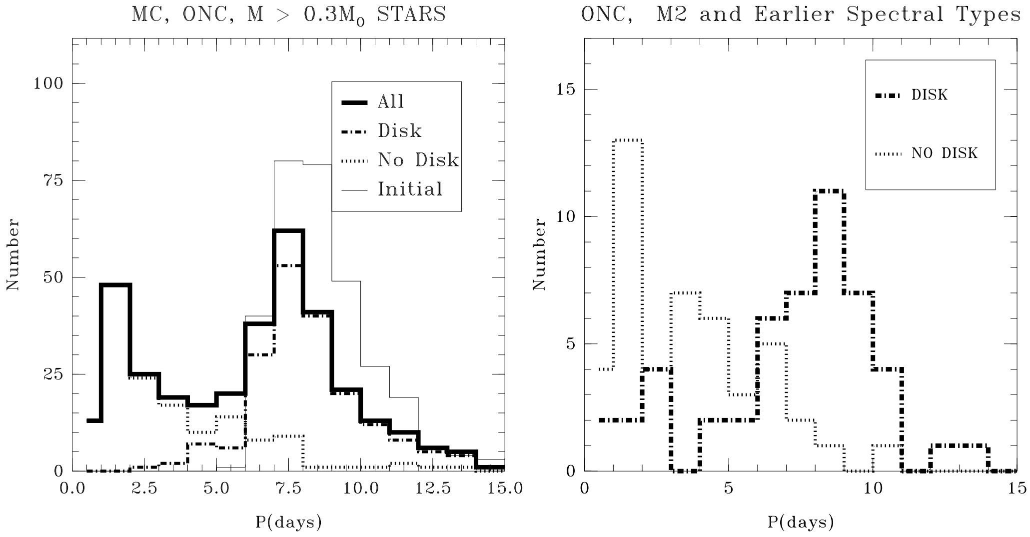

Figure A.1 (Left panel) Period histogram for a Monte Carlo simulation of the ONC. (Right panel) Observed period histogram for "high-mass" stars with and without a disk from Cieza & Baliber 2007. The period distributions of stars with and without a disk obtained in the simulation are statistically indistinguishable from those observed.

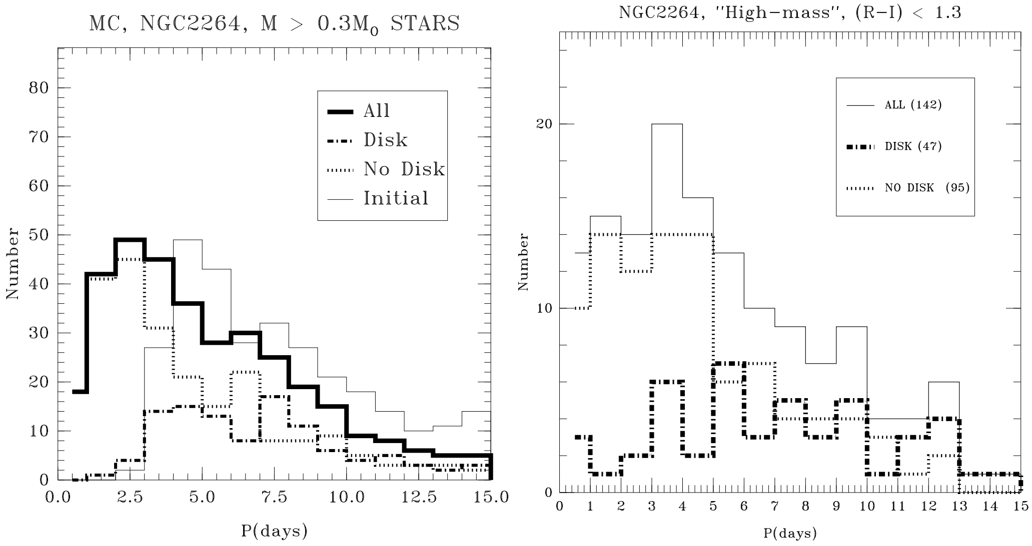

Figure A.2 Same as Fig. A.1, but for NGC 2264

Table A.1. Results from Monte Carlo simulations of the ONC using the evolutionary tracks presented by D'Antona & Mazzitelli (1998)

Parameter	"Best Value"	Min Allowed Value	Max allowed value
Mean Initial Angular Momentum	25	23	28
Mean Disk Braking Timescale (Myrs)	2	1	3
Sigma Disk Braking Timescale (Myrs)	1.3	0.5	3
Mean Stellar Age (Myrs)	1	0.5	1.5
Sigma Stellar Age (Myrs)	1.5	0.5	2.5
Disk Braking Efficiency	1	1	1
Lag Time (Myrs)	0.55	0.45	0.75
Early Disk Dissipation Fraction [1]	0.35	0.25	0.40
Early Dissipation Age (Myrs)	0.07	0.06	0.08

[1] Rebull et al. (2004) found that in order to reproduce the bimodal period distribution observed in the ONC, a significant fraction of the stars (∼30%) must evolve conserving angular momentum from a very early age. The last two parameters in Tables A.1 and A.2 are designed to account for this population.

Table A.2. Results from Monte Carlo simulations of NGC 2264 using the evolutionary tracks presented by D'Antona & Mazzitelli (1998)

Parameter	"Best Value"	Min Allowed Value	Max allowed value
Mean Initial Angular Momentum	38	28	41
Mean Disk Braking Timescale (Myrs)	4	3	5
Sigma Disk Braking Timescale (Myrs)	2	0.5	3
Mean Stellar Age (Myrs)	4.5	3	6.5
Sigma Stellar Age (Myrs)	4	0.5	4.5
Disk Braking Efficiency	1	1	1
Lag Time (Myrs)	1.5	0	2.0
Early Disk Dissipation Fraction [1]	0.35	0.25	0.40
Early Dissipation Age (Myrs)	1.5	0.95	2.5

[1] Rebull et al. (2004) found that in order to reproduce the bimodal period distribution observed in the ONC, a significant fraction of the stars (∼30%) must evolve conserving angular momentum from a very early age. The last two parameters in Tables A.1 and A.2 are designed to account for this population.

Bibliography

Akeson, R. L., Ciardi, D. R., van Belle, G. T., Creech-Eakman, M. J., & Lada, E. A. 2000, ApJ, 543, 313

Akeson, R. L., Ciardi, D. R., van Belle, G. T., & Creech-Eakman, M. J. 2002, ApJ, 566, 1124

Alard, C. 2000, A&AS, 144, 363

Alard, C., & Lupton, R. H. 1998, ApJ, 503, 325

Alcala, J. M., Krautter, J., Covino, E., Neuhaeuser, R., Schmitt, J. H. M. M., & Wichmann, R. 1997, A&A, 319, 184

Alibert, Y., Mordasini, C., & Benz, W. 2004, A&A, 417, L25

Allen, L. E., et al. 2004, ApJS, 154, 363

Andrews, S. M., & Williams, J. P. 2005, ApJ, 631, 1134

Armitage, P. J., Clarke, C. J., & Tout, C. A. 1999, MNRAS, 304, 425

Attridge, J. M., & Herbst, W. 1992, ApJ, 398, L61

Augereau, J. C., Lagrange, A. M., Mouillet, D., Papaloizou, J. C. B., & Grorod, P. A. 1999, A&A, 348, 557

Augereau, J.-C., & Beust, H. 2006, A&A, 455, 987

Aumann, H. H., et al. 1984, ApJ, 278, L23

Backman, D. E., & Paresce, F. 1993, Protostars and Planets III, 1253

Baliber, N. R., & Cochran, W. D. 2001, Bulletin of the American Astronomical Society, 33, 1112

Baraffe, I., Chabrier, G., Allard, F., & Hauschildt, P. H. 1998, A&A, 337, 403

Barnes, S. A., Sofia, S., Prosser, C. F., & Stauffer, J. R. 1999, ApJ, 516, 263

Barnes, S., Sofia, S., & Pinsonneault, M. 2001, ApJ, 548, 1071

Barnes, S. A. 2003, ApJ, 586, 464

Basri, G., & Batalha, C. 1990, ApJ, 363, 654

Beckwith, S. V. W. 1999, Star Formation 1999, Proceedings of Star Formation 1999, held in Nagoya, Japan, June 21 - 25, 1999, Editor: T. Nakamoto, Nobeyama Radio Observatory, p. 211-211, 211

Beichman, C. A., et al. 2005, ApJ, 622, 1160

Beichman, C. A., et al. 2006, ApJ, 652, 1674

Beichman, C. A., Fridlund, M., Traub, W. A., Stapelfeldt, K. R., Quirrenbach, A., & Seager, S. 2007, Protostars and Planets V, 915

Bessell, M. S. 1979, PASP, 91, 589

Bodenheimer, P., & Pollack, J. B. 1986, Icarus, 67, 391

Boss, A. P. 2000, ApJ, 536, L101

Blum, J., & Wurm, G. 2000, Icarus, 143, 138

Bouvier, J., & Appenzeller, I. 1992, A&AS, 92, 481

Bouvier, J., Forestini, M., & Allain, S. 1997, A&A, 326, 1023

Briceno, C., Hartmann, L. W., Stauffer, J. R., Gagne, M., Stern, R. A., & Caillault, J.-P. 1997, AJ, 113, 740

Bryden, G., et al. 2006, ApJ, 636, 1098

Butler, R. P., Tinney, C. G., Marcy, G. W., Jones, H. R. A., Penny, A. J., & Apps, K. 2001, ApJ, 555, 410

Calvet, N., & Gullbring, E. 1998, ApJ, 509, 802

Calvet, N., D'Alessio, P., Hartmann, L., Wilner, D., Walsh, A., & Sitko, M. 2002, ApJ, 568, 1008

Cambrésy, L., Petropoulou, V., Kontizas, M., & Kontizas, E. 2006, A&A, 445, 999

Carpenter, J. M., Hillenbrand, L. A., & Skrutskie, M. F. 2001, AJ, 121, 3160

Carpenter, J. M., Mamajek, E. E., Hillenbrand, L. A., & Meyer, M. R. 2006, ApJ, 651, L49

Chen, C. H., et al. 2005, ApJ, 634, 1372

Chiang, E. I., & Goldreich, P. 1997, ApJ, 490, 368

Chiang, E. I., & Goldreich, P. 1999, ApJ, 519, 279

Chiang, E. I., Joung, M. K., Creech-Eakman, M. J., Qi, C., Kessler, J. E., Blake, G. A., & van Dishoeck, E. F. 2001, ApJ, 547, 1077

Cieza, L. A., Kessler-Silacci, J. E., Jaffe, D. T., Harvey, P. M., & Evans, N. J. 2005, ApJ, 635, 422

Cieza, L., & Baliber, N. 2006, ApJ, 649, 862

Cieza, L. A., Baliber, N., & Counselor, N. 2006, in American Astronomical Society Meeting Abstracts, Vol. 209, American Astronomical Society Meeting Abstracts

Claver, C. F. 1992, Bulletin of the American Astronomical Society, 24, 1282

Cochran, W. D., Hatzes, A. P., & Paulson, D. B. 2002, AJ, 124, 565

Cohen, M. 1983, ApJ, 270, L69

Cohen, R. E., Herbst, W., & Williams, E. C. 2004, AJ, 127, 1602

Colavita, M., et al. 2003, ApJ, 592, L83

Covey, K. R., Greene, T. P., Doppmann, G. W., & Lada, C. J. 2005, AJ, 129, 2765

Covino, E., Alcala, J. M., Allain, S., Bouvier, J., Terranegra, L., & Krautter, J. 1997, A&A, 328, 187

D'Alessio, P., Calvet, N., & Hartmann, L. 2001, ApJ, 553, 321

D'Alessio, P., et al. 2005, ApJ, 621, 461

D'Antona, F., & Mazzitelli, I. 1994, ApJS, 90, 467

D'Antona, F., & Mazzitelli, I. 1998, in ASP Conf. Ser. 134: Brown Dwarfs and Extrasolar Planets, 442–+, d94

Doppmann, G. W., & Jaffe, D. T. 2003, AJ, 126, 3030

Duchêne, G., Ménard, F., Stapelfeldt, K., & Duvert, G. 2003, A&A, 400, 559

Dullemond, C. P., Dominik, C., & Natta, A. 2001, ApJ, 560, 957

Dullemond, C. P., & Dominik, C. 2005, A&A, 434, 971

Durisen, R. H., Boss, A. P., Mayer, L., Nelson, A. F., Quinn, T., & Rice, W. K. M. 2007, Protostars and Planets V, 607

Duschl, W. J., Gail, H.-P., & Tscharnuter, W. M. 1996, A&A, 312, 624

Edwards, S., Ray, T., & Mundt, R. 1993, in Protostars and Planets III, ed. E. H. Levy & J. I. Lunine, 567–602

Evans, N. J., Allen, L. E., Blake, G. A., Boogert, A. C. A., Bourke, T., Harvey, P. M., Kessler, J. E., Koerner, D. W., Lee, C. W., Mundy, L. G., Myers, P. C., Padgett, D. L., Pontoppidan, K., Sargent, A. I., Stapelfeldt, K. R., van Dishoeck, E. F., Young, C. H., & Young, K. E. 2003, PASP, 115, 965

Evans, N. J., Harvey, P. M., Dunham, M. M., Mundy, L. G., Lai, S., Chapman, N., Huard, T., Brooke, T. Y., & Koerner, D. W. 2006, Delivery of Data from the c2d Legacy Project: IRAC and MIPS (Pasadena,SSC), Pasadena, SSC, http://ssc.spitzer.caltech.edu/legacy/original.html

Fazio, G. G., Hora, J. L., Allen, L. E., Ashby, M. L. N., Barmby, P., Deutsch, L. K., Huang, J.-S., Kleiner, S., Marengo, M., Megeath, S. T., Melnick, G. J., Pahre, M. A., Patten, B. M., Polizotti, J., Smith, H. A., Taylor, R. S., Wang, Z., Willner, S. P., Hoffmann, W. F., Pipher, J. L., Forrest, W. J., McMurty, C. W., McCreight, C. R., McKelvey, M. E., McMurray, R. E., Koch, D. G., Moseley, S. H., Arendt, R. G., Mentzell, J. E., Marx, C. T., Losch, P., Mayman, P., Eichhorn, W., Krebs, D., Jhabvala, M., Gezari, D. Y., Fixsen, D. J., Flores, J., Shakoorzadeh, K., Jungo, R., Hakun, C., Workman, L., Karpati, G., Kichak, R., Whitley, R., Mann, S., Tollestrup, E. V., Eisenhardt, P., Stern, D., Gorjian, V., Bhattacharya, B., Carey, S., Nelson, B. O., Glaccum, W. J., Lacy, M., Lowrance, P. J., Laine, S., Reach, W. T., Stauffer, J. A., Surace, J. A., Wilson, G., Wright, E. L., Hoffman, A., Domingo, G., & Cohen, M. 2004, ApJS, 154, 10

Feigelson, E. D. 1996, ApJ, 468, 306

Fiorucci, M., & Munari, U. 2002, Ap&SS, 280, 77

Fiorucci, M., & Munari, U. 2003, A&A, 401, 781

Folha, D. F. M., & Emerson, J. P. 1999, A&A, 352, 517

Furlan, E., et al. 2005, ApJ, 628, L65

Ghez, A. M., Neugebauer, G., & Matthews, K. 1993, AJ, 106, 2005

Goldreich, P., & Ward, W. R. 1973, ApJ, 183, 1051

Gomes, R., Levison, H. F., Tsiganis, K., & Morbidelli, A. 2005, Nature, 435, 466

Gullbring, E., Hartmann, L., Briceno, C., & Calvet, N. 1998, ApJ, 492, 323

Habing, H. J., et al. 2001, A&A, 365, 545

Haisch, K. E., Jr., Lada, E. A., & Lada, C. J. 2001, ApJ, 553, L153

Hartigan, P., Kenyon, S. J., Hartmann, L., Strom, S. E., Edwards, S., Welty, A. D., & Stauffer, J. 1991, ApJ, 382, 617

Hartigan, P., Strom, K. M., & Strom, S. E. 1994, ApJ, 427, 961

Hartmann, L. W., & Kenyon, S. J. 1990, ApJ, 349, 190

Hartmann, L., Calvet, N., Gullbring, E., & D'Alessio, P. 1998, ApJ, 495, 385

Hartmann, L. 2001, AJ, 121, 1030

Hartmann, L. 2002, ApJ, 566, L29

Hartmann, L., Megeath, S. T., Allen, L., Luhman, K., Calvet, N., D'Alessio, P., Franco-Hernandez, R., & Fazio, G. 2005, ApJ, 629, 881

Harvey, P., Cieza, L., Spiesman, W., & c2d Team. 2004, American Astronomical Society Meeting Abstracts, 204,

Harvey, P. M., et al. 2006, ApJ, 644, 307

Hauschildt, P. H., Allard, F., & Baron, E. 1999, ApJ, 512, 377

Herbig, G. H. 1960, ApJS, 4, 337

Herbig, G. H., & Bell, K. R. 1988, Catalog of emission line stars of the orion population : 3 : 1988 (Lick Observatory Bulletin, Santa Cruz: Lick Observatory, —c1988)

Herbig, G. H. 1998, ApJ, 497, 736

Herbst, W., Rhode, K. L., Hillenbrand, L. A., & Curran, G. 2000, AJ, 119, 261

Herbst, W., Maley, J. A., & Williams, E. C. 2000, AJ, 120, 349

Herbst, W., Bailer-Jones, C. A. L., & Mundt, R. 2001, ApJ, 554, L197

Herbst, W., Bailer-Jones, C. A. L., Mundt, R., Meisenheimer, K., & Wackermann, R. 2002, A&A, 396, 513

Herbst, W., & Mundt, R. 2005, ApJ, 633, 967

Herbst, W., Eisloffel, J., Mundt, R., & Scholz, A. 2006, in Protostars and Planets V, ed. V. Mannings, in press

Hillenbrand, L. A. 1997, AJ, 113, 1733

Hillenbrand, L. A., Strom, S. E., Calvet, N., Merrill, K. M., Gatley, I., Makidon, R. B., Meyer, M. R., & Skrutskie, M. F. 1998, AJ, 116, 1816

Hillenbrand, L. A., & White, R. J. 2004, ApJ, 604, 741

Hogerheijde, M. R., Jayawardhana, R., Johnstone, D., Blake, G. A., & Kessler, J. E. 2002, AJ, 124, 3387

Hollenbach, D., et al. 2005, ApJ, 631, 1180

Horne, J. H., & Baliunas, S. L. 1986, ApJ, 302, 757

Hughes, J., & Hartigan, P. 1992, AJ, 104, 680

Johns-Krull, C. M., & Valenti, J. A. 2001, ApJ, 561, 1060

Jones, B. F., & Walker, M. F. 1988, AJ, 95, 1755

Jorgensen, J. K., Harvey, P. M., Evans, N. J., Huard, T. L., Allen, L. E., Porras, A., Blake, G. A., Bourke, T. L., Chapman, N., Cieza, L., Koerner, D. W., Lai, S.-P., Mundy, L. G., Myers, P. C., Padgett, D. L., Rebull, L., Sargent, A. I., Spiesman, W., Stapelfeldt, K. R., van Dishoeck, E. F., Wahhaj, Z., & Young, K. E. 2006, ArXiv Astrophysics e-prints

Kenyon, S. J., & Hartmann, L. W. 1990, ApJ, 349, 197

Kenyon, S. J., Dobrzycka, D., & Hartmann, L. 1994, AJ, 108, 1872

Kenyon, S. J., & Hartmann, L. 1995, ApJS, 101, 117

Kenyon, S. J., & Bromley, B. C. 2004, ApJ, 602, L133

Kenyon, S. J., & Bromley, B. C. 2005, AJ, 130, 269

Kitamura, Y., Kawabe, R., & Saito, M. 1996, ApJ, 465, L137

Kızıloğlu, Ü., Kızıloğlu, N., & Baykal, A. 2005, AJ, 130, 2766

Kleinmann, S. G. 1992, Robotic Telescopes in the 1990s, 34, 203

Kohler, R., & Leinert, C. 1998, A&A, 331, 977

Königl, A. 1991, ApJ, 370, L39

Krautter, J., Wichmann, R., Schmitt, J. H. M. M., Alcala, J. M., Neuhauser, R., & Terranegra, L. 1997, A&AS, 123, 329

Kurucz, R. L. 1993, VizieR Online Data Catalog, 6039, 0

Lachaume, R., Dominik, C., Lanz, T., & Habing, H. J. 1999, A&A, 348, 897

Lada, C. J., Muench, A. A., Haisch, K. E., Jr., Lada, E. A., Alves, J. F., Tollestrup, E. V., & Willner, S. P. 2000, AJ, 120, 3162

Lada, C. J., Muench, A. A., Luhman, K. L., Allen, L., Hartmann, L., Megeath, T., Myers, P., Fazio, G., Wood, K., Muzerolle, J., Rieke, G., Siegler, N., & Young, E. 2006, AJ, 131, 1574

Lamm, M. H., Mundt, R., Bailer-Jones, C. A. L., & Herbst, W. 2005, A&A, 430, 1005

Landolt, A. U. 1992, AJ, 104, 340

Levison, H. F., Dones, L., Chapman, C. R., Stern, S. A., Duncan, M. J., & Zahnle, K. 2001, Icarus, 151, 286

Lissauer, J. J. 1993, ARA&A, 31, 129

Lissauer, J. J., & Stevenson, D. J. 2007, Protostars and Planets V, 591

Littlefair, S. P., Naylor, T., Burningham, B., & Jeffries, R. D. 2005, MNRAS, 358, 341

Luhman, K. L., Stauffer, J. R., Muench, A. A., Rieke, G. H., Lada, E. A., Bouvier, J., & Lada, C. J. 2003, ApJ, 593, 1093

Lumsden, S. L., Hoare, M. G., Oudmaijer, R. D., & Richards, D. 2002, MNRAS, 336, 621

Makidon, R. B., Rebull, L. M., Strom, S. E., Adams, M. T., & Patten, B. M. 2004, AJ, 127, 2228

Mamajek, E. E., Meyer, M. R., & Liebert, J. 2002, AJ, 124, 1670

Marcy, G. W., & Butler, R. P. 1998, ARA&A, 36, 57

Martin, E. L. 1997, A&A, 321, 492

Martin, E. L., Montmerle, T., Gregorio-Hetem, J., & Casanova, S. 1998, MNRAS, 300, 733

Martín, E. L., & Magazzù, A. 1999, A&A, 342, 173

Matt, S., & Pudritz, R. E. 2005, ApJ, 632, L135

McCaughrean, M. J., & O'dell, C. R. 1996, AJ, 111, 1977

Mendoza V., E. E. 1966, ApJ, 143, 1010

Mendoza V., E. E. 1968, ApJ, 151, 977

Meyer, M. R., Calvet, N., & Hillenbrand, L. A. 1997, AJ, 114, 288

Meyer, M. R., & Beckwith, S. V. W. 2000, ISO Survey of a Dusty Universe, 548, 341

Meyer, M. R., et al. 2006, PASP, 118, 1690

Morbidelli, A., Petit, J.-M., Gladman, B., & Chambers, J. 2001, Meteoritics and Planetary Science, 36, 371

Muzerolle, J., Hartmann, L., & Calvet, N. 1998, AJ, 116, 2965

Muzerolle, J., Calvet, N., Hartmann, L., & D'Alessio, P. 2003, ApJ, 597, L149

Muzerolle, J., et al. 2006, ApJ, 643, 1003

Nelson, R. P., Papaloizou, J. C. B., Masset, F., & Kley, W. 2000, MNRAS, 318, 18

Osterloh, M., & Beckwith, S. V. W. 1995, ApJ, 439, 288

Padgett, D. L., et al. 2006, ApJ, 645, 1283

Padgett, D. L., Cieza, L., Stapelfeldt, K. R., Evans, N. J., Koerner, D., Sargent, A., Fukagawa, M., van Dishoek, E. F., Augereau, J., Allen, L., Blake, G., Brooke, T., Chapman, N., Harvey, P., Porras, A., Lai, S., Mundy, L., Myers, P. C., Spiesman, W., & Wahhaj, Z. 2006, astro-ph/0603370

Papaloizou, J. C. B., & Terquem, C. 1999, ApJ, 521, 823

Parenago, P. P. 1954, Trudy Gosudarstvennogo Astronomicheskogo Instituta, 25, 1

Pascucci, I., et al. 2006, ApJ, 651, 1177

Paulson, D. B., Sneden, C., & Cochran, W. D. 2003, AJ, 125, 3185

Paulson, D. B., Saar, S. H., Cochran, W. D., & Henry, G. W. 2004, AJ, 127, 1644

Pollack, J. B., Hubickyj, O., Bodenheimer, P., Lissauer, J. J., Podolak, M., & Greenzweig, Y. 1996, Icarus, 124, 62

Press, W. H., Teukolsky, S. A., Vetterling, W. T., & Flannery, B. P. 1992, Cambridge: University Press, —c1992, 2nd ed.,

Quillen, A. C., Blackman, E. G., Frank, A., & Varnière, P. 2004, ApJ, 612, L137

Lyo, A.-R., Lawson, W. A., Mamajek, E. E., Feigelson, E. D., Sung, E.-C., & Crause, L. A. 2003, MNRAS, 338, 616

Rebull, L. M. 2001, AJ, 121, 1676

Rebull, L. M., Wolff, S. C., Strom, S. E., & Makidon, R. B. 2002, AJ, 124, 546

Rebull, L. M., Wolff, S. C., & Strom, S. E. 2004, AJ, 127, 1029

Rebull, L. M., Stauffer, J. R., Megeath, T., Hora, J., & Hartmann, L. 2005, in Protostars and Planets V, Proceedings of the Conference held October 24-28, 2005, in Hilton Waikoloa Village, Hawai'i. LPI Contribution No. 1286., p.8264, 8264–+

Rebull, L. M., Stauffer, J. R., Megeath, S. T., Hora, J. L., & Hartmann, L. 2006, ApJ, 646, 297

Rebull, L. M., Stauffer, J. R., Megeath, S. T., Hora, J. L., & Hartmann, L. 2006, astro-ph/0604104, ApJ– in press

Richter, M. J., Jaffe, D. T., Blake, G. A., & Lacy, J. H. 2002, ApJ, 572, L161

Rieke, G. H., et al. 2005, ApJ, 620, 1010

Scargle, J. D. 1982, ApJ, 263, 835

Schechter, P. L., Mateo, M., & Saha, A. 1993, PASP, 105, 1342

Sekiya, M. 1998, Icarus, 133, 298
bibitem[Song et al.(2005)]2005Natur.436..363S Song, I., Zuckerman, B., Weinberger, A. J., & Becklin, E. E. 2005, Nature, 436, 363

Shu, F. H., Adams, F. C., & Lizano, S. 1987, ARA&A, 25, 23

Shu, F., Najita, J., Ostriker, E., Wilkin, F., Ruden, S., & Lizano, S. 1994, ApJ, 429, 781

Shu, F. H., Najita, J. R., Shang, H., & Li, Z.-Y. 2000, Protostars and Planets IV, 789

Siess, L., Dufour, E., & Forestini, M. 2000, A&A, 358, 593

Silverstone, M. D., et al. 2006, ApJ, 639, 1138

Skrutskie, M. F., Dutkevitch, D., Strom, S. E., Edwards, S., Strom, K. M., & Shure, M. A. 1990, AJ, 99, 1187

Spangler, C., Sargent, A. I., Silverstone, M. D., Becklin, E. E., & Zuckerman, B. 2001, ApJ, 555, 932

Stassun, K. G., Mathieu, R. D., Mazeh, T., & Vrba, F. J. 1999, AJ, 117, 2941

Stassun, K. G., Mathieu, R. D., Vrba, F. J., Mazeh, T., & Henden, A. 2001, AJ, 121, 1003

Stassun, K. G., & Terndrup, D. 2003, PASP, 115, 505

Stepinski, T. F., & Valageas, P. 1996, A&A, 309, 301

Stepinski, T. F., & Valageas, P. 1997, A&A, 319, 1007

Stetson, P. B. 1987, PASP, 99, 191

Strom, K. M., Strom, S. E., Edwards, S., Cabrit, S., & Skrutskie, M. F. 1989, AJ, 97, 1451

Strubbe, L. E., & Chiang, E. I. 2006, ApJ, 648, 652

Su, K. Y. L., et al. 2006, ApJ, 653, 675

Tera, F., Papanastassiou, D. A., & Wasserburg, G. J. 1973, Lunar and Planetary Institute Conference Abstracts, 4, 723

Thi, W. F., et al. 2001, ApJ, 561, 1074

Weidenschilling, S. J. 1997, Lunar and Planetary Institute Conference Abstracts, 28, 1517

Weingartner, J. C., & Draine, B. T. 2001, ApJ, 548, 296

Wichmann, R., Krautter, J., Covino, E., Alcala, J. M., Neuhaeuser, R., & Schmitt, J. H. M. M. 1997, A&A, 320, 185

Wichmann, R., et al. 2000, A&A, 359, 181

White, R. J., & Basri, G. 2003, ApJ, 582, 1109

White, R. J., & Hillenbrand, L. A. 2004, ApJ, 616, 998

Wyatt, M. C., Dent, W. R. F., & Greaves, J. S. 2003, MNRAS, 342, 876

Wyatt, M. C., Greaves, J. S., Dent, W. R. F., & Coulson, I. M. 2005, ApJ, 620, 492

Wyatt, M. C., Smith, R., Su, K. Y. L., Rieke, G. H., Greaves, J. S., Beichman, C. A., & Bryden, G. 2007, ApJ, 663, 365

Wyatt, M. C., Smith, R., Greaves, J. S., Beichman, C. A., Bryden, G., & Lisse, C. M. 2007, ApJ, 658, 569

Yamashita, T., Handa, T., Omodaka, T., Kitamura, Y., Kawazoe, E., Hayashi, S. S., & Kaifu, N. 1993, ApJ, 402, L65

Yi, S. K., Demarque, P., & Kim, Y.-C. 2003, Extragalactic Globular Cluster Systems, 255

Youdin, A. N., & Shu, F. H. 2002, ApJ, 580, 494

Young, E. T., Teixeira, P. S., Lada, C. J., Muzerolle, J., Persson, S. E., Murphy, D. C., Siegler, N., Marengo, M., Krause, O., & Mainzer, A. K. 2006, apj, 642, 972

Zuckerman, B., & Becklin, E. E. 1993, ApJ, 414, 793

Vita

Lucas Alejo Cieza-Gonzalez was born in La Plata, Buenos Aires, Argentina on December 17, 1978, the son of Daniel Alejandro Cieza, a lawyer, and Ana Isabel Gonzalez, an anthropologist. He was raised in the city of Quilmes, Buenos Aires, where he lived until graduating from High School. In August 1998, he entered the Space Sciences program at the Florida Institute of Technology, in Melbourne, FL, where he obtained a Bachelor of Science with the Highest Honors in May 2002. As an undergraduate student he participated in the 2001 Visiting Summer Student program at the Space Telescope Science Institute in Baltimore, MD. In August 2002, he began graduate studies in Astronomy at the University of Texas at Austin and started working for the Spitzer Legacy Project "From Molecular Cores to Planet Forming Disks". He received a Masters of Arts in Astronomy in August 2005 and a PhD in Astronomy in August 2007 from the University of Texas at Austin. He will start working, as a *Spitzer* Fellow, at the Institute for Astronomy at the University of Hawaii in September 2007.

Permanent Address: Peru 857 5to Piso
Buenos Aires CP 1068
Argentina

This dissertation was typeset with LaTeX 2$_\varepsilon$[2] by the author.

---

[2] LaTeX 2$_\varepsilon$ is an extension of LaTeX. LaTeX is a collection of macros for TeX. TeX is a trademark of the American Mathematical Society. The macros used in formatting this dissertation were written by Dinesh Das, Department of Computer Sciences, The University of Texas at Austin, and extended by Bert Kay, James A. Bednar, and Ayman El-Khashab.